Proceedings Book Series -PBS-

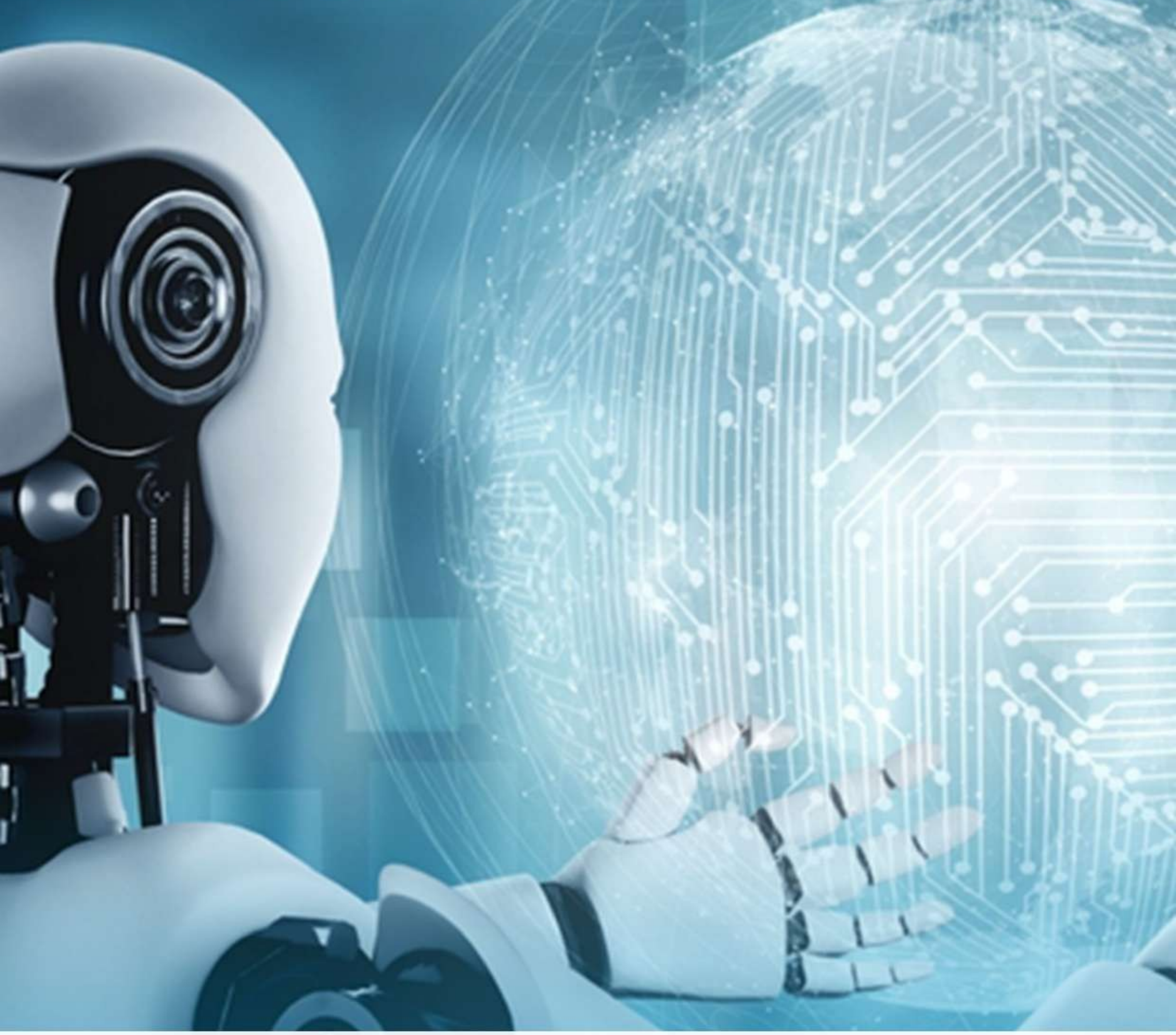

-CISAI-

2ème Conférence Internationale sur les Sciences Appliquées et l'Innovation

Special Session
« La Revue des Sciences Appliquées »

Editor : Dr. Ahmed Rhif (Tunisia)

CNPSI

Centre National de la Promotion Scientifique et de L'innovation

Proceedings Book Series -PBS-

Special Session : « La Revue des Sciences Appliquées »

-CISAI-

2ème Conférence Internationale sur les Sciences Appliquées et l'Innovation

PBS-Vol. 14
ISSN: 2961-6611

Editor : Dr. Ahmed Rhif (Tunisia)

Committes

Scientific Partners
Aissa Keffous (CRTSE, ALG)
Bechir Chaouachi (LEEEP, TUN)
Hamouine Abdelmadjid (ARCHIPEL, ALG)
Messaoud Hamouda (LDDI, ALG)
Mohamed Asri NOOr (UPSI, MYS)
Mohamed Yussof Ghazali (NUSATEK, MYS)

Honorary Presidents
Abdenasser El Figha (MAR)
Mihoub Ouahiba (ALG)
Nabila Guerfi (ALG)
Walid Hassen (TUN)

General Presidents
Ahmed Rhif (TUN)
Afef Khalil (TUN)
Laoudj Ouardia (ALG)
Sara Zatir (ALG)

Steering Committee
Abdoulaye Bouya Diop (SEN)
Abdoulaziz Alhassane (SEN)
Akrouch Soukaina (MAR)
Allé Dioum (SEN)
Amer Zerek (LYB)
Bendifallah Leila (ALG)
Bouazouni Omar (ALG)
Bouslah Naima (ALG)
Chettat Yacine (ALG)
Fatima Zohra Boufadi (ALG)
Fatoumata GAYE (SEN)
Gharbi Sonia (ALG)
Gherbi Mohamed (ALG)
Hadiza Moussa-Saley (SEN)
Hanaa Benchrifa (MAR)
Jeru Achyl Hounogbe (SEN)
Merchichi Amira (CAN)
Mohammed Baroudi (ALG)
Mounsi Demmouche Nedjoua (ALG)
Nawel Seddiki (ALG)
Ndeye Astou Manel Fall (SEN)
Ouadjaout Djamel (ALG)
Ould Hamou Malek (ALG)
Seddiki Nesrinne (ALG)
Zohra Haouam (MAR)

Technical Committee
Djalila Boudemagh (ALG)
Fateh Mebarek-Oudina (ALG)
Hadja Fatima Mehnane (ALG)
Harrizi Driss (MAR)
Hayani Mechkouri Meriem (MAR)
Méziane Aïder (ALG)
Mohamed Boukherouk (MAR)
Rachid Benchrifa (MAR)
Serigne Moussa Dia (SEN)

Summary

Investigating Current-Voltage Characteristics of MIS Devices under Elevated Temperatures: A Study of TiN/Al_2O_3/p-Si Structures

Slah Hlali*(1), Neila Hizem(1), Liviu Militaru(2), Adel Kalboussi(1)
and Abdelkader Souifi(2)

[1]*Laboratoire de Microélectronique et Instrumentation (LR13ES12), Faculté des Sciences de Monastir,*
Avenue de l'environnement, Université de Monastir, 5019 Monastir, Tunisie
[2]*Institut des Nanotechnologies de Lyon - site INSA de Lyon, UMR CNRS 5270, Bât. Blaise Pascal,*
7 avenue Jean Capelle, 69621 Villeurbanne Cedex, France

*Corresponding author: hlalislah@yahoo.fr

***Abstract*—This research explores the current-voltage (*I-V*) behaviors of a Schottky Metal-Insulator-Semiconductor (MIS) structure featuring a TiN/p-Si interface, incorporating a high-k oxide layer (ranging from 5 to 500 nm in thickness) composed of Al_2O_3. The study covers a temperature spectrum from 270 to 450 Kelvin, and the analysis, based on thermionic emission (TE) theory, yields crucial electrical parameters like reverse saturation current (I_0), ideality factor (n), zero bias barrier height (Ψ_{B0}), series resistance (R_s), and rectification rate (RR) from the *I–V* data.**

***Keywords*—Temperature Dependence, MIS device, I-V-T characteristics, high-k (Al_2O_3), reverse saturation current**

I. INTRODUCTION

Schottky-type structures incorporating a high-*K* oxide interfacial layer commonly referred to as metal-insulator-semiconductor (MIS) or metal–oxide–semiconductor (MOS), exhibit rectification features attributed to the formation of a barrier between the metal and semiconductor interface. The nature and magnitude of this barrier height (BH) typically rely on the selected work-function metal (Φm) and semiconductor (Φs) [1–3]. The effectiveness and quality of these structures are influenced by various factors, including the nature of the interface, the thickness and uniformity of the interfacial layer, the homogeneity of the barrier height (BH) at the metal/semiconductor (MS) interface, and the presence of interface traps between the metal and semiconductor materials [4-6].

Therefore, understanding both potential current transport mechanisms and the characteristics of the barrier height becomes of paramount importance. Various mechanisms contribute to carrier transition, encompassing thermionic emission, thermionic field emission, and field emission (TE, TFE, FE), as well as tunneling via interface traps or dislocations, generation-recombination processes, and specialized distributions of barrier heights. It is essential to consider these factors for a comprehensive understanding of the electrical behavior of Schottky-type structures with oxide interfacial layers.

It is noteworthy that specific mechanisms may dominate within particular temperature and voltage ranges [7–11]. Typically, *I–V* measurements are carried out at a single temperature or within a limited temperature range, often centered around room temperature or higher. This approach inherently constrains the extent to which we can fully grasp potential mechanisms for current transport (CT) and the makeup of the barrier height (BH) at the interface between the metal and semiconductor.

However, when these measurements are extended across an extensive spectrum of temperatures and bias voltages, they have the potential to provide significant data, enabling the identification of potential CT mechanisms and the intrinsic characteristics of the BH [12, 13]. Therefore, the primary technological and scientific challenge lies in enhancing the quality and performance of metal–semiconductor (MS) and metal/insulator/semiconductor (MIS) structures while simultaneously reducing production costs, surface states, series resistance, and leakage current.

ISSN: 2961-6611

Nevertheless, the exploration of CT mechanisms in these structures based on thermionic emission (TE) theory typically reveals a decrease in ideality factor (n) and an increase in barrier height (BH) with rising temperature. The Richardson plot, especially at low temperatures, deviates from linearity and provides a relatively low value for the Richardson constant (A*), when compared to its theoretical counterpart [14, 15]. The TiN/Al_2O_3 combination has been identified as a promising and especially reliable candidate, thanks to its chemical compatibility and thermal stability, good adhesion properties on various substrates and low interface trap densities in TiN/Al_2O_3/p- Si devices [16, 17].

Recently, there has been notable enthusiasm surrounding the exploration and application of high-dielectric constant (high-k) gate dielectric materials like HfO_2, ZrO_2, TiO2 and Al_2O_3. These materials are being investigated as potential replacements for SiO_2 in gate dielectric applications, offering advantages such as higher capacitance and reduced leakage current [18–22]. In the literature, it has been reported that the use of high-k materials enhances the capacitance properties of transistors by 60% and can reduce leakage current by up to 100 times compared to conventional SiO_2 materials [23]. Consequently, MOSFETs can operate at significantly higher speeds, and power loss in MOSFETs can be minimized due to the reduction in leakage current [24]. Among the high-k materials, Al_2O_3 has emerged as a particularly stable and robust oxide. It has undergone extensive scrutiny for diverse applications, especially in the fields of optoelectronics and microelectronics. Al_2O_3 exhibits noteworthy characteristics, including a high dielectric permittivity (>9), a substantial band gap (9 eV) [25], significant band offset with silicon (crucial for maintaining low leakage currents in devices), kinetic stability, thermodynamic stability on silicon at high temperatures, favorable interface properties with silicon, low bulk defect density, and amorphous behavior under relevant conditions [26, 27].

In this study, our primary goal was to comprehensively explore the fundamental electrical parameters and charge transport mechanisms in the TiN/p-Si structure featuring an interfacial layer of aluminum Oxide (Al_2O_3). This investigation was carried out within the temperature range of 270 K to 450 K. The aim was to obtain precise and dependable insights amidst diverse thermal conditions. To accomplish this goal, we systematically analyzed the current-voltage-temperature (I–V–T) characteristics of TiN/Al_2O_3/p-Si semiconductor devices. Our experimental observations from these analyses suggested that the charge transport mechanism could be effectively elucidated using thermoelectric theory, specifically involving generation-recombination centers, even at elevated temperatures. This stands in contrast to relying on conventional tunneling mechanisms such as field and thermionic-field emission.

.

II. EXPERIMENTAL DETAILS

The TiN/Al_2O_3/p-Si MIS structure used in this study was fabricated at Sherbrook University, engineered on a ⟨100⟩ p-type substrate with a carrier concentration of around $10^{10} cm^{-3}$ and surface area of $100 * 100\ \mu m^2$.

I–V measurements were conducted using a Keithley 236 source meter. Precise temperature control of the sample was achieved with the Janis VPF-800 cryostat, maintained under a vacuum of $10^{-3} bar$, in conjunction with Lake Shore 331S temperature control systems.

.

III. RESULTS

The current–voltage (*I–V*) characteristics of the TiN/Al_2O_3/p-Si structure were examined across a high-temperature spectrum ranging from 270 K to 450 K. The findings are visually represented in Fig. 1.

ISSN: 2961-6611

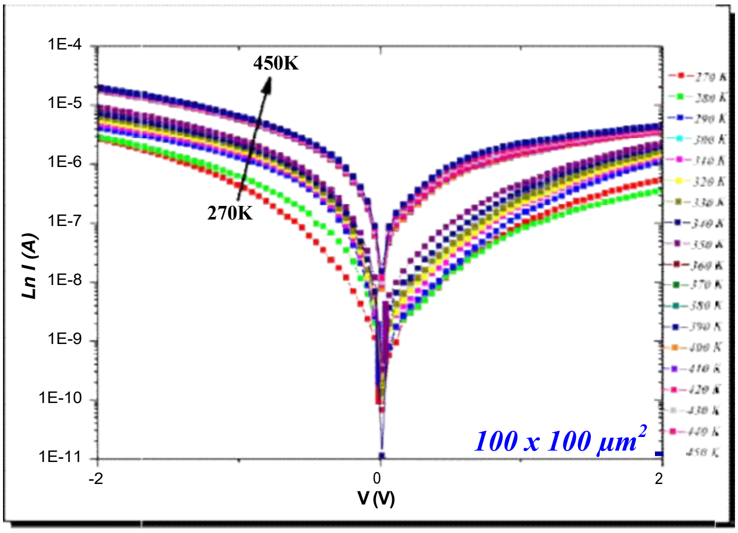

Fig. 1 the semi-logarithmic I–V curves of the TiN/Al_2O_3/p-Si structure, analyzed at temperatures range of 270–450 K.

The semi-logarithmic *I-V* plots clearly depict rectifying behavior, where the current magnitude increases as temperature rises. This phenomenon is likely due to the reduction in the bandgap of silicon (Si) and the increased thermal energy of charge carriers. In simpler terms, the TiN/Al_2O_3/p-Si structure demonstrates a remarkably strong sensitivity to temperature across different applied bias voltages or current conditions, resembling that of a temperature sensor. This behavior suggests that the device could potentially be utilized as a temperature-sensitive component, leveraging its inherent response to temperature changes for various sensing applications. Investigation of the semi-logarithmic *I-V* curves, a linear region is discernible under reverse bias conditions. However, this linearity tends to deviate at higher reverse bias voltages. Such deviation is primarily attributed to the influence of series resistance (Rs) and the effects induced by the interfacial high-k oxide layer.

The presence of series resistance and the interfacial high-k oxide layer introduces complexities in the *I-V* characteristics, leading to deviations from ideal linear behavior, particularly at lower bias voltages. Understanding and mitigating these effects are essential for accurate interpretation and utilization of the device in practical applications.

According to TE theory, when a diode includes a series resistance (Rs) and demonstrates an ideality factor exceeding unity, the linear relationship persists under the condition of qV ≥ 3kT [1–4].

$$I = AA^{*}T^{2}exp\left(-\frac{q}{KT}\phi_{B0}\right)\left[exp\left(\frac{q(V-IR_{S})}{nkT}\right)-1\right] = I_{0}[exp(q(V-IR_{S})/nkT)-1] \quad (1)$$

Where I_o is the reverse-saturation current derived from the linear region of the intercept of ln*I* vs *V* at zero bias, and is given by

$$I_0 = AA^{*}T^{2}exp\left(-\frac{q\phi_{Bo}}{KT}\right) \quad (2)$$

In Eq. 1, The variables A, A*, k, ϕ_{B0}, T, and I_0 represent the contact area, Richardson constant, Boltzmann constant, zero-bias barrier height, temperature in Kelvin, and reverse-saturation current, respectively.

At each temperature point, the values of ideality factor were calculated from the slope of the linear region of the forward bias ln I–V plots for each temperature by using following equation [28]:

$$n = \frac{q}{KT}\left(\frac{dV}{dlnI}\right) \quad (3)$$

The saturation current versus temperature is shown in Fig. 2. The values of *Io* were obtained by extrapolating the linear part of *ln I–V* plots at intermediate voltage region.

Copyright © 2024
ISSN: 2961-6611

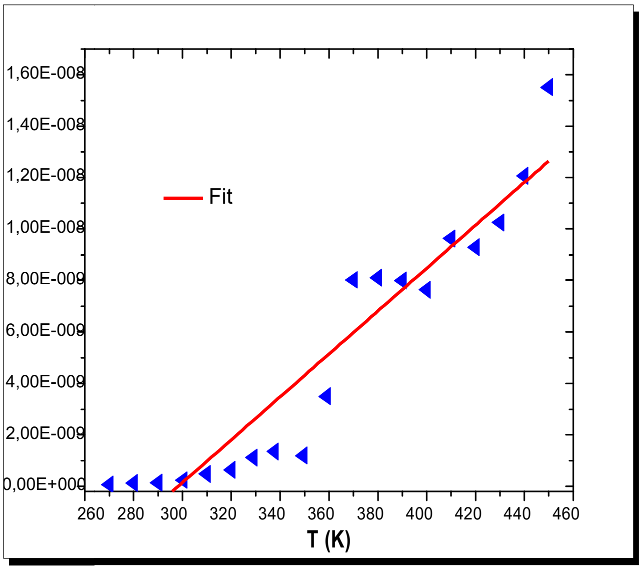

Fig.2: Variation of the experimental saturation current as a function of the temperature.

Since current transport across the device interface is produced by temperature, high temperature carriers (electrons) can overcome the upper barriers. Conversely, at low temperatures, the main current transport will be dominated by the current flowing through the lower barrier height layers of the Schottky diode [29]. As the temperature of the structure increases, many electrons have enough energy to overcome the upper barrier and then the barrier height will increase with polarization and temperature [30].

Forward bias *I–V* measurements were made to determine the saturation current *Io* from which the zero bias BH ϕ_{B0} was defined in terms of the TE theory [1– 4, 31].

$$\phi_{B0} = \frac{kT}{q} ln\left(\frac{AA^{*}T^{2}}{I_0}\right) \qquad (4)$$

The values of ϕ_{B0} and n can be determined from intercepts and slopes of the forward bias *ln I–V* plot at each temperature using Eqs. (3) and (4), respectively.

Furthermore, Fig. 3 illustrates both the value of n and the correlation between ϕ_{B0} and temperature.

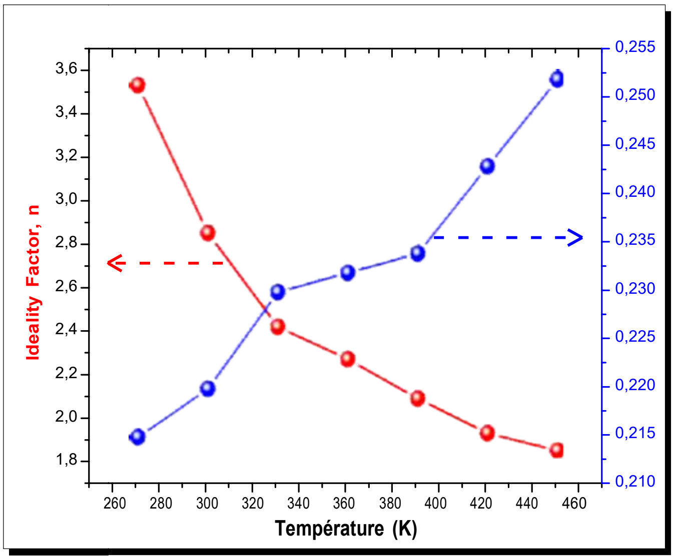

Fig. 3: Ideality factor and barrier height variation with temperature in TiN/Al_2O_3/p-Si structure.

The electrical characteristics of I_0, n, and Φ_{B0} were determined as 0.03×10^{-9} A, 3.54, and 0.215 eV at 270 K, and 10.54×10^{-9} A, 1.86, and 0.252 eV at 450 K, respectively.
These parameters exhibit a strong dependence on temperature. As shown in Fig. 3, the ideality factor (n) decreases with rising temperature, while the barrier height (Φ_{B0}) increases. Notably, even at room temperature, its value significantly surpasses unity. It's noteworthy that this increase in barrier height does not adhere to the negative temperature coefficient commonly associated with the forbidden bandgap of semiconductors (e.g., -0.473 meV/K for Si). Conversely, in the case of an ideal semiconductor diode (where $\alpha = dE_g/dT$), the change in barrier height, as inferred from the forward bias *I-V* data, correlates with the negative temperature coefficient of E_g or BH. Another approach for assessing BH involves using the traditional Richardson or Arrhenius plot. To determine the activation energy, denoted as Ea = Φ_{B0}, we constructed a $\ln(I_0/T^2)$ versus q/kT plot, as demonstrated in Fig. 4. [15, 16].

$$\ln\left(\frac{I_0}{T^2}\right) = \ln(AA^*) - \frac{q\Phi_{B0}}{KT} \qquad (5)$$

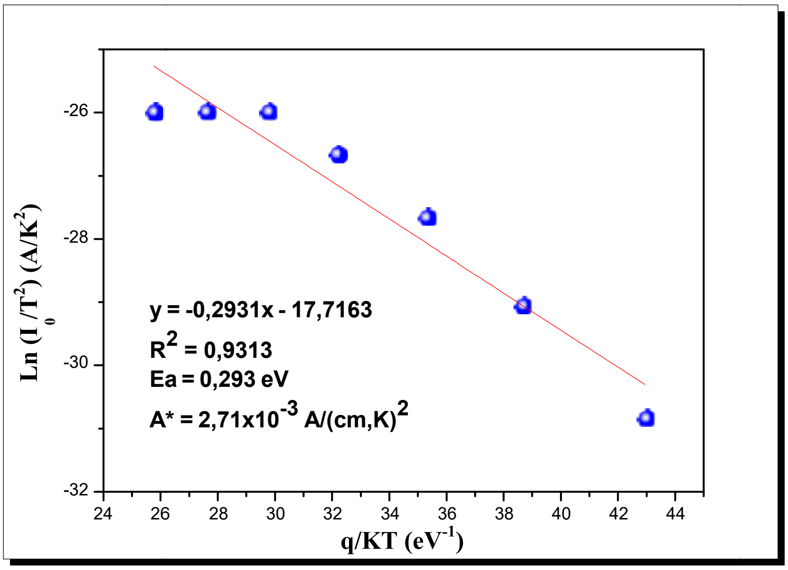

Fig. 4: $\ln(I_0/T^2)$ vs. q/KT curve of the TiN/Al_2O_3/p-Si structure.

The values of E_a and A* for TiN/Al_2O_3/p-Si structure were determined as 0.293 eV and 2.71×10^{-3} A/ (cm. K) ^{2}, respectively, extracted from the slope and intercept of the linear segment of the $\ln(I_0/T^2)$ versus q/KT curve.

The observed value of A* is approximately 1.18×10^4 times lower than its theoretical counterpart, which is 32 A/ (cm K) ^{2} for p-Si [32]. Moreover, the E_a value is below the mid-gap energy of silicon. This difference can be explained by the diminished effective contact or diode area, caused by spatially distributed variations in barrier height or potential fluctuations at the metal-semiconductor interface. To put it simply, due to these fluctuations, which encompass both regions with lower and higher barriers, electron flow across the barrier becomes biased towards regions with lower barriers, like patches. Recent studies have begun to address these disparities, including discrepancies between theoretical and practical A* values, higher ideality factor (n) values, and non-linear trends in the conventional Richardson plot [33].

The lateral heterogeneity in barrier height likely exerts influence on the determined A* value derived from the *I-V-T* characteristics. As temperature increases, the enlarged size of the homogeneous region offsets the lower barrier height of patches at the metal-semiconductor interface; thereby channeling most of the current flow through it. This suggests that temperature-dependent changes in barrier height distribution play a significant role in modulating electrical conduction characteristics within the material.
As illustrated in Fig.5, the parameter *n* was observed to exhibit an inverse relationship with temperature, as described by this Eq.6 [34]:

$$n(T) = n_0 + T_0/T. \qquad (6)$$

ISSN: 2961-6611

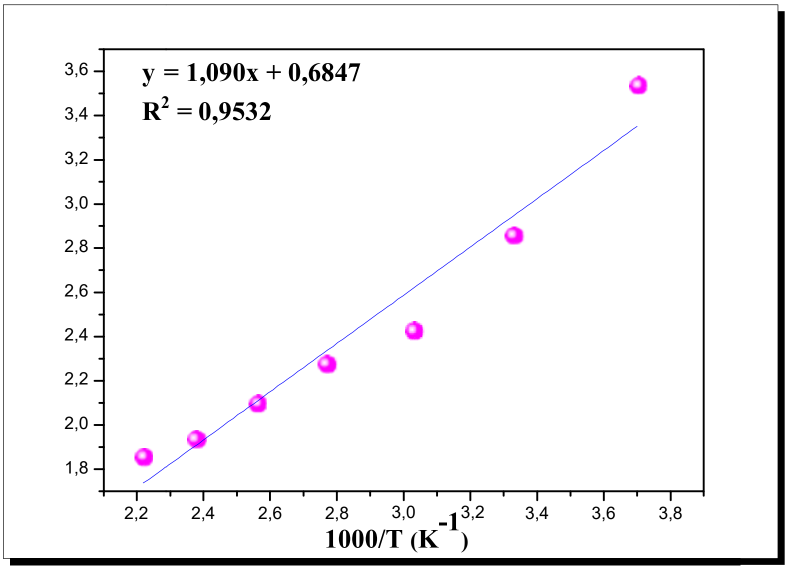

Fig.5: Ideality factor n variation as a function of *1000/T* in the TiN/Al_2O_3/p-Si structure.

In this equation, n_0 and T_0 represent constants with values of 0.68 and 1090 K, respectively. This phenomenon, where n increases as temperature decreases, is commonly referred to as the anomaly effect.
The phenomenon where the parameter n increases as temperature decreases are commonly known as an anomaly effect.

IV. CONCLUSIONS

In this study, we investigate the impact of temperature on the *I-V* characteristics of a TiN/p-Si metal-oxide-semiconductor (MOS) structure featuring an interfacial layer of Al_2O_3. The examination spans temperatures ranging from 270 to 450 Kelvin. It was observed that both at forward and reverse bias, the values of zero bias barrier heights derived from the *I-V* data exhibit an increase with rising temperature in a consistent manner. This suggests that the *I-V* mechanisms remain unchanged at both biases, particularly at low voltages. The ideality factor n of the diode decreases with increasing temperature, transitioning from 3.54 at 270 Kelvin to 1.86 at 450 Kelvin. Additionally, the T_0 effect value for the structure was determined as 1090 Kelvin based on the nT versus T plot. The conventional Richardson plot ($\ln(I_0/T^2)$ vs. q/kT) exhibited noticeable deviations from linearity at low temperatures, and the determined value of A* (2.71×10^{-3} A/ (cm. K) ^{2}) was notably lower than its theoretical prediction. The decrease in the value of series resistance (Rs) with increasing temperature can be attributed to the reduction in the forbidden bandgap (Eg) and the subsequent rise in conductivity.

ACKNOWLEDGMENT

This work benefited from the support of the Microelectronic and Instrument Laboratory (LMI) in Monastir, Tunisia, and the Lyon Institute of Nanotechnologies (INL) in Lyon, France, providing essential resources and expertise.

REFERENCES

[1] Sze, Simon M., Yiming Li, and Kwok K. Ng. *Physics of semiconductor devices*. John wiley & sons, 2021.

[2] Sharma, B. L., ed. Metal-semiconductor Schottky barrier junctions and their applications. Springer Science & Business Media, 2013.

[3] Padovani, F. A., and R. Stratton. "Field and thermionic-field emission in Schottky barriers." *Solid-State Electronics* 9.7 (1966): 695-707.

[4] Sreenu, K., C. Venkata Prasad, and V. Rajagopal Reddy. "Barrier parameters and current transport characteristics of Ti/p-InP Schottky junctionmodified using orange G (OG) organic interlayer." *Journal of Electronic Materials* 46 (2017): 5746-5754.

[5] Rajagopal Reddy, V., et al. "Electrical properties and current transport mechanisms of the Au/n-GaN Schottky structure with solution-processed high-k BaTiO 3 interlayer." *Journal of electronic materials* 43 (2014): 3499-3507.

[6] Ertap, Hüseyin, et al. "Analysis of temperature dependent electrical characteristics of Au/GaSe Schottky barrier diode improved by Ce-doping." *Sensors and Actuators A: Physical* 315 (2020): 112264.

[7] Werner, Jürgen H., and Herbert H. Güttler. "Barrier inhomogeneities at Schottky contacts." *Journal of applied physics* 69.3 (1991): 1522-1533.

[8] Lakshmi, B. Prasanna, et al. "Electrical transport properties of Au/SiO2/n-GaN MIS structure in a wide temperature range." *Current applied physics* 12.3 (2012): 765-772.

[9] Sullivan, J. P., et al. "Electron transport of inhomogeneous Schottky barriers: A numerical study." *Journal of applied physics* 70.12 (1991): 7403-7424.

[10] Song, Y. P., et al. "On the difference in apparent barrier height as obtained from capacitance-voltage and current-voltage-temperature measurements on Al/p-InP Schottky barriers." *Solid-State Electronics* 29.6 (1986): 633-638.

[11] Mönch, Winfried. "Barrier heights of real Schottky contacts explained by metal-induced gap states and lateral inhomogeneities." *Journal of Vacuum Science & Technology B: Microelectronics and Nanometer Structures Processing, Measurement, and Phenomena* 17.4 (1999): 1867-1876.

[12] Schmitsdorf, R. F., T. U. Kampen, and W. Mönch. "Correlation between barrier height and interface structure of AgSi (111) Schottky diodes." *Surface Science* 324.2-3 (1995): 249-256.

[13] Reddy, M. Siva Pratap, et al. "Electrical properties and the role of inhomogeneities at the polyvinyl alcohol/n-inp schottky barrier interface." *Journal of Applied Polymer Science* 131.2 (2014).

[14] Tung, Raymond T. "Recent advances in Schottky barrier concepts." Materials Science and Engineering: R: Reports 35.1-3 (2001): 1-138.

[15] Durmuş, Haziret, et al. "The effect of temperature on the electrical characteristics of Ti/n-GaAs Schottky diodes." Current Applied Physics 44 (2022): 85-89.

[16] Cho, Moonju, et al. "Thermal annealing effects on the structural and electrical properties of HfO_2/Al_2O_3 gate dielectric stacks grown by atomic layer deposition on Si substrates." Journal of applied physics 94.4 (2003): 2563-2571.

[17] Hlali, S., N. Hizem, and A. Kalboussi. "Investigation of capacitance characteristics in metal/high-k semiconductor devices at different parameters and with and without interface state density (traps)." Bulletin of Materials Science 40.5 (2017): 1035-1041.

[18] Joo-Hyung Kim, Velislava A. Ignatova, Peter Kücher, et al., Post annealing effect on ultra-thin Hf-based high-k gate oxides on Si, Curr. Appl. Phys. 9 (2) (2009) e104ee107.

[19] J.H. Choi, Y. Mao, J.P. Chang, Development of hafnium based high-k materialsda review, Mater. Sci. Eng. R Rep. 72 (6) (2011) 97e136.

[20] S. Rudenja, A. Minko, D.A. Buchanan, Low-temperature deposition of stoichiometric HfO 2 on silicon: analysis and quantification of the HfO_2/Si interface from electrical and XPS measurements, Appl. Surf. Sci. 257 (1) (2010) 17e21.

[21] Tao Yu, Chenggang Jin, Xumin Yang, et al., The structure and electrical properties of HfTaON high-k films prepared by DIBSD, Appl. Surf. Sci. 258 (7) (2012) 2953e2958.

[22] Park, Jae Beom, et al. "Atomic layer etching of ultra-thin HfO2 film for gate oxide in MOSFET devices." *Journal of Physics D: Applied Physics* 42.5 (2009): 055202.

[23] Wu, Mo, Y. I. Alivov, and Hadis Morkoç. "High-κ dielectrics and advanced channel concepts for Si MOSFET." *Journal of Materials Science: Materials in Electronics* 19 (2008): 915-951.

[24] Özden, Şadan, et al. "Temperature dependent current transport mechanism of photopolymer based Al/NOA60/p-Si MPS device." Journal of Inorganic and Organometallic Polymers and Materials 32.5 (2022): 1810-1818.

[25] Hlali, Slah, Neila Hizem, and Adel Kalboussi. "High-k dielectric materials for the gate oxide of a MIS capacitor: effect of interface states on the C–V characteristics." Journal of computational electronics 15 (2016): 1340-1350.

[26] Hlali, Slah, et al. "High temperature and voltage dependent electrical and dielectric properties of TiN/Al2O3/p-Si MIS structure." Journal of Alloys and Compounds 713 (2017): 194-203.

[27] Glen D. Wilk, Robert M. Wallace, J.M. Anthony, High-k gate dielectrics: current status and materials properties considerations, J. Appl. Phys. 89 (10) (2001) 5243e5275.

[28] Badali, Yosef. "Electrical properties of PVC: BN nanocomposite as interfacial layer in metal-semiconductor structure." Journal of Materials Science: Materials in Electronics 35.7 (2024): 1-13.

[29] Korucu, Demet, Abdulmecit Turut, and Hasan Efeoglu. "Temperature dependent I–V characteristics of an Au/n-GaAs Schottky diode analyzed using Tung's model." *Physica B: Condensed Matter* 414 (2013): 35-41.

[30] Aydoğan, Şakir, Mustafa Sağlam, and A. B. D. U. L. M. E. C. İ. T. Türüt. "On the some electrical properties of the non-ideal PPy/p-Si/Al structure." *Polymer* 46.24 (2005): 10982-10988.

[31] Güçlü, Ç. Ş., et al. "A comparison of electrical characteristics of the Au/n-Si Schottky diodes with (ZnCdS: GO (1: 1) and (ZnCdS: GO (1: 0.5) doped PVP interlayer using current–voltage (I–V) and impedance–voltage (Z–V) measurements." Journal of Materials Science: Materials in Electronics 34.28 (2023): 1909.

[32] Dökme, Ilbilge, and Şemsettin Altindal. "On the intersecting behaviour of experimental forward bias current–voltage (I–V) characteristics of Al/SiO2/p-Si (MIS) Schottky diodes at low temperatures." Semiconductor science and technology 21.8 (2006): 1053.

[33] Güçlü, Ç. Ş., et al. "A comparison of electrical characteristics of the Au/n-Si Schottky diodes with (ZnCdS: GO (1: 1) and (ZnCdS: GO (1: 0.5) doped PVP interlayer using current–voltage (I–V) and impedance–voltage (Z–V) measurements." Journal of Materials Science: Materials in Electronics 34.28 (2023): 1909.

[34] Buyukbas-Ulusan, A., A. Tataroglu, and Seçkin Altındal-Yerişkin. "Analysis of the Current Transport Characteristics (CTCs) in the Au/n-Si Schottky diodes (SDs) with Al2O3 interfacial layer over wide temperature range." ECS Journal of Solid State Science and Technology 12.8 (2023): 083010.

A move toward green agriculture: Discovery of novel environmental-friendly insecticidal ''ulvan'' from the renewable bioresource *Ulva lactuca*; effect of the extraction processes on the chemical-physical, and insecticidal properties

Mariem Guidara [a*], Hela Yaich [a], Aurore Richel [b], Christophe Blecker [c], Slim Tounsi [d], Hamadi Attia [a], Haikel Garna [e].

[a] Laboratoire de Valorisation, Analyses et Sécurité des Aliments, École Nationale d'Ingénieurs de Sfax, Route de Soukra, 3038 Sfax, Tunisia.

[b] Unité de Chimie Biologique Industrielle, Université de Liège – Gembloux Agro – Bio Tech, passage des Déportés 2 - 5030 Gembloux, Belgium.

[c] Unité de Science des Aliments et Formulation, Université de Liège – Gembloux Agro – Bio Tech, passage des Déportés 2 - 5030 Gembloux, Belgium.

[d] Laboratoire de Biopesticides, Centre de Biotechnologie de Sfax, Université de Sfax, P.O. 1177, 3018 Sfax, Tunisie

[e] Laboratoire de Biotechnologie et Valorisation des Bio-Géo-Ressources, Institut Supérieur de Biotechnologie de Sidi Thabet, BP-66, 2020 Ariana, Tunisia

Email1 : mariem.guidara@gmail.com

Email2 : hela_yaich@yahoo.fr

Email3 : Hamadi.Attia@gmail.com / Hamadi.Attia@enis.rnu.tn

Introduction :

The research on effective insecticidal agents is important challenging to limit the insecticide resistance of many larvae insect populations. This study aimed not only, to discover the insecticidal efficiency of the sulphated polysaccharide 'ulvan' from the green seaweed *Ulva lactuca,* as a novel environmental-friendly insecticidal agent; but also, to investigate an alternative strategy for insecticide production and to improve the effective control of *Spodoptera littoralis* larvae.

ISSN: 2961-6611

Résultats :

This aim reached by the investigation of the enzymatic chemical extraction and acid extractions effects on physical properties and insecticidal activities of ulvan extract; for further, feasible and optimal application of ulvans, as insecticidal agent. The study demonstrated that ulvans were characterized by an anionic stable structure and molecular weight distribution; varied between 1.77 and 7.21 (×102 kDa), as well as, specific particle sizes, which were affected by the extraction processes. Ulvan will be a valuable candidate due to its bioactivity and environmental safety. The extraction procedure effects were observed in the chemical composition, molecular weight, particle size, surface charge and insecticidal activities of ulvans. At high concentrations, the enzymatic-chemical (EE) and acidic (CA1) extraction processes successfully produced ulvans with the greatest insecticidal activities against *S. littoralis* larvae. The mortality rate of larvaes after treatments with a concentration at 100 (mg/ml), achieved 75 % of larvae's mortality. LC 30, LC50 and LC 90 evidenced the expected outcome of the insecticidal ability of ulvans.

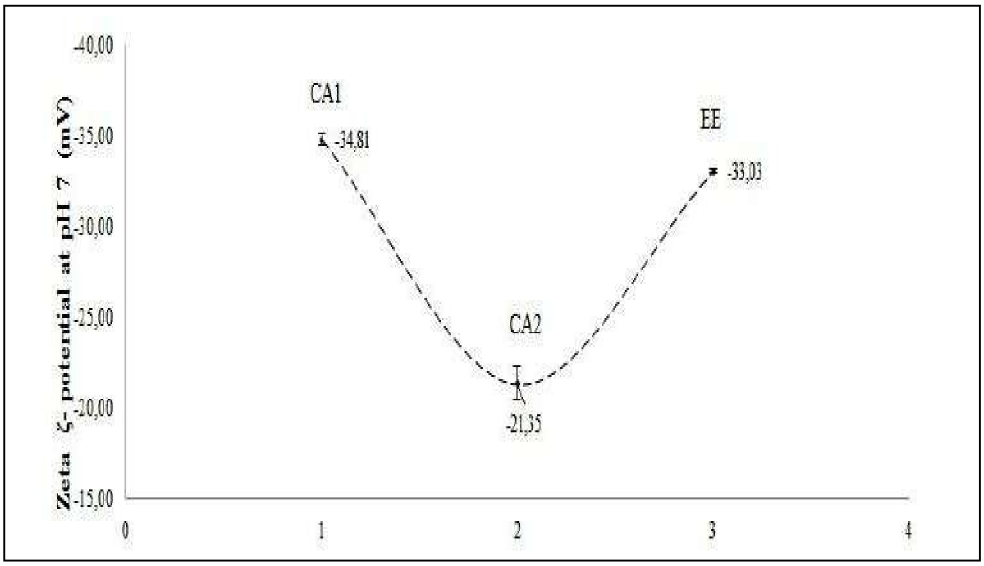

Fig. 2. The effect of extraction processes on the ζ-potential of ulvans at pH 7. All values given are means of three determinations (X ±SD) ; SD: standard deviation

ISSN: 2961-6611

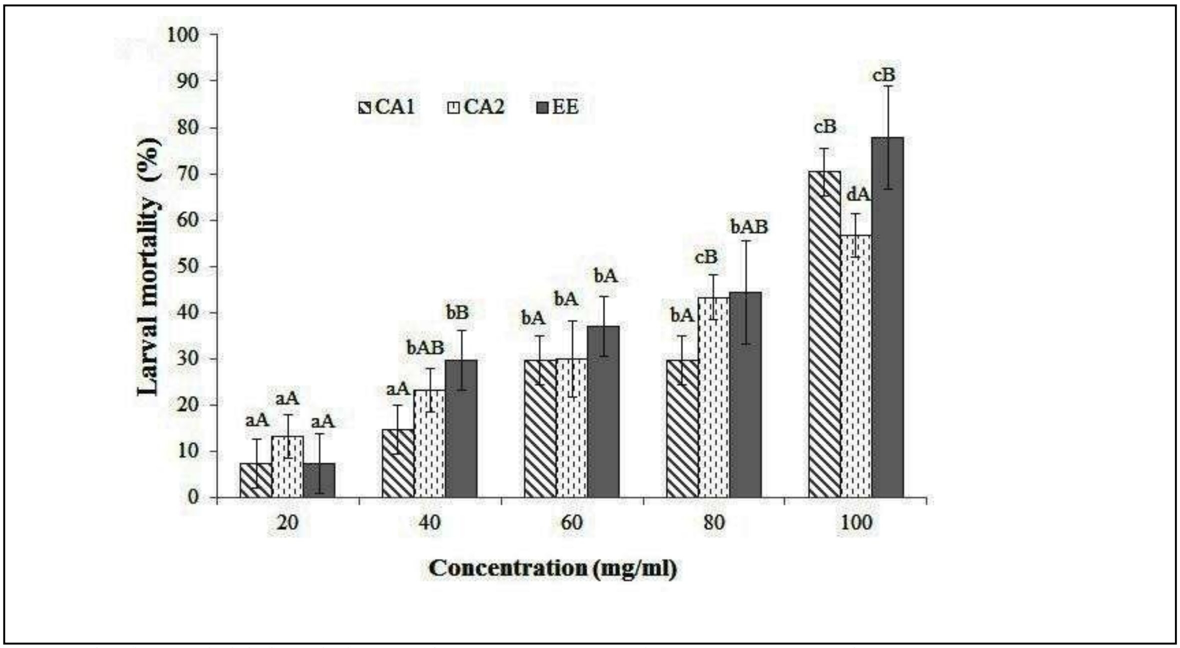

Fig. 2. The insecticidal activity of ulvan extracts against *S. littoralis* larvae.

All values given are means of three determinations (X ±SD) ; SD: standard deviation.

Means with different small letters are significantly different ($p < 0.05$) for the same extraction condition and at different concentration of extract.

Means with different capital letters are significantly different ($p < 0.05$) for the same concentration of extract, and at different extraction conditions

Conclusion :

The insecticidal efficiency of ulvans with a dose-dependent manner promotes their use as novel eco-friendly bio-insecticidal agent suitable for the agriculture systems needs and technology trends. This strategy of (EE) and (CA1) extraction processes can considerably improve the economic and environmental benefits.

Références :

Abbassy, M. A., et al., 2014. Insecticidal and fungicidal activity of Ulva lactuca Linnaeus (Chlorophyta) extracts and their fractions. Annual Research & Review in Biology. 2252-2262.

Carneiro-da-Cunha, M. G., et al., 2011. Influence of concentration, ionic strength and pH on zeta potential and mean hydrodynamic diameter of edible polysaccharide solutions envisaged for multinanolayered films production. Carbohydrate polymers. 85, 522-528.

Elleuch, J., et al., 2014. New Bacillus thuringiensis toxin combinations for biological control of lepidopteran larvae. International Journal of Biological Macromolecules. 65, 148-154.

Guidara, M., et al., 2021. Effect of extraction procedures on the chemical structure, antitumor and anticoagulant properties of ulvan from Ulva lactuca of Tunisia coast. Carbohydrate Polymers. 253, 117283.

Ismail, S. M., et al., 2022. Bio-residual activity of novel insecticides in Spodoptera littoralis (boisaduval, 1833) throughout its life cycle. Egyptian Academic Journal of Biological Sciences, F. Toxicology & Pest Control. 14, 149-158.

Robic, A., et al., 2009a. Structure and interactions of ulvan in the cell wall of the marine green algae Ulva rotundata (Ulvales, Chlorophyceae). Carbohydrate Polymers. 77, 206-216.

Yin, Y., et al., 2020. A sodium alginate-based nano-pesticide delivery system for enhanced in vitro photostability and insecticidal efficacy of phloxine B. Carbohydrate polymers. 247, 116677.

Sliding Mode Control Associated with Robust Observer of a Drone Quadrotor

Abderrahim BENFEKIR[#1], Taha BENARBIA[*2]

[#]*Laboratory of Industrial Safety Engineering and Sustainable Development*
Institute of Maintenance and Industrial Safety, University'Oran-2 Ahmed Ben-Ahmed, Oran, Algeria
`benfkir.abderrahim@univ-oran2.dz`
`taha05@yahoo.fr`

***Abstract*— This paper develops a nonlinear observer and controller applied to a helicopter with 4 rotors. We are interested in dynamic modelling while taking into account the various physical phenomena, which can influence the dynamics of a flying structure. These permit us to introduce a new state-space representation and new control scheme. We present after the development and the synthesis of a stabilizing control laws design based on sliding mode in order to perform best tracking results. It ensures locally asymptotic stability and desired tracking trajectories. In addition, this technique allows reducing the number of sensors to be embedded in the flying system by observing non available or non measurable entities. Finally simulation results are also provided in order to illustrate the performances of the proposed controllers.**

***Keywords*— Dynamic modelling, Lyapunov function, Quadrotor, Robust observer, Sliding mode control**

I. INTRODUCTION

The miniature rotary wing UAVs are a new class of flying machines subject to a growing interest in both academic and industrial. Indeed, thanks to capabilities hover and vertical takeoff or landing in tight spaces, many applications are possible: video monitoring of traffic, location of victims during natural disasters, inspection of structures for maintenance tasks, etc… The need for autonomy during these missions requires the development of control algorithms implemented in an embedded system with artificial intelligence. In this paper, we focus on the miniature aerial vehicles or mini-UAV (Unmanned Autonomous Vehicles), especially quadrotor, capable of hovering knowing that this feature is very useful for aerial surveillance. The purpose of this study is to develop new techniques to be applicable to guide the development of control laws for a model of UAV Quadrotor.

Moreover, they used a new Lyapunov function, which leads to a controller base on the PD2 exponentially stable.

While in [11] the authors develop a PID controller to stabilize the altitude. Other papers, the authors present the sliding mode control [5] and high order sliding mode [8] with an observer to estimate the immeasurable states and the effects of external disturbances such as wind and noise.

In this paper, we are based on the vector model presented in [11, 4], the authors are interested primarily modelled quadrotor and are explained the various parameters that affect the dynamic structure of flight such as friction couples due to aerodynamic forces by resistance axis (x, y, z) and gyroscopic effects that are identified in [11].

Accordingly, in [4] the authors presented a new state representation more complete and realistic system, being interested in the synthesis of control laws based on sliding mode choosing a stabilizing function of Lyapunov. Next, we present a control technique based on the development and synthesis of stabilizing control law for the sliding mode approach ensures the local asymptotic stability of desired trajectory expressed in of centre of mass coordinates (x, y, z) and yaw angle, while the desired angles of roll and pitch are deducted. However, the synthesis of the observer nonlinear high gain is necessary to estimate the immeasurable states and the effects of additive uncertainties. Finally, the synthesized control laws are validated by simulations in Matlab / Simulink, which gave results considered satisfactory.

II. MODELLING SYSTEM

In this section we have established a complete model of the system quadrocopters. First, we propose a theoretical model of the propulsion system shown in Fig. 1, which shows a circuit diagram of a DC motor (CMC), connected by a propeller through a gearbox G. This complete system is derived from linear and nonlinear rotor gear ratio and engine [2, 5]. The reactive torque caused by the propeller and the rotor thrust f are proportional to the angular velocity of the rotor.

$$f = k_l\,\omega^2 \;,\quad \tau_R = k_d\,\omega^2 \tag{1}$$

The speed reduction ratio G as well as the total torque inertia $\tilde{J}_{tot}$ of the motor side are given by:

$$G = \frac{\omega_M}{\omega} = \frac{\tau_M}{\tilde{\tau}_M\,\eta_G} \quad \text{and} \quad \tilde{J}_{tot} = \frac{J_R}{G^2} + J_M \tag{2}$$

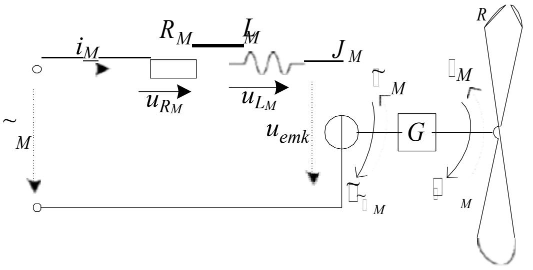

Fig. 1 Propulsion System

Where η_G is the efficiency factor.

Le modèle de commande du moteur à C.C est donné par :

$$\dot{\omega} = -A\omega + Bu_M + C \tag{3}$$

$$A = \frac{1}{\tau} + \frac{2c_t\omega_0}{\eta_G G^3 J_t}\;;B = \frac{1}{k_m\tau}\;;C = \frac{2c_t\omega_0^2}{\eta_G G^3 J_t}$$

k_m is the torque constant, τ is the time constant and c_t is the drag coefficient.

The quadrotor consists of four parallel bars placed crosswise at the ends of which are placed the four motors controlling vertical axis rotors for sustenance. To centred the yaw moment, it is necessary to turn two propellers (which are opposite each other) in one direction and two in the other direction Fig. 2. Indeed, when projected aerodynamic forces caused by the air on the blade, we see that the rotor always tends to rotate the quadrotor in the opposite direction of its rotation [3]. The control of the four engines will be used to alter the vertical acceleration (power control) and to rotate the quadrotor around the vertical axis (Yaw control (ψ)).Only the control of two opposing motors allow rotation around the longitudinal axis. (Roll control (ϕ)). Similarly, the control of two others motors allow rotation around the lateral axis. (Pitch control (θ)).To model the gear, we define two frame shown in Fig.2. An inertial frame of reference linked to earth (E) and a marker binds to the body of the drone (B). The model developed assumes the following assumptions :

- The structure of quadrotor rigid and symmetrical
- The centre of mass coincides with G.
- The propellers are rigid.
- The lift and drag are proportional to the square of angular velocity of the motors.

Under these assumptions, it is possible to describe the dynamic model of the equivalent system. Using the formalism of Newton-Euler [1, 6], the dynamic equations are written as follows:

$$\begin{cases} \dot{\xi} = v \\ m\dot{v} = F_f + F_t + F_g \\ \dot{R} = R\,S(\Omega) \\ J\dot{\Omega} = -\Omega \wedge J\Omega + \Gamma_f - \Gamma_a - \Gamma_g \end{cases} \tag{4}$$

Copyright © 2024
ISSN: 2961-6611

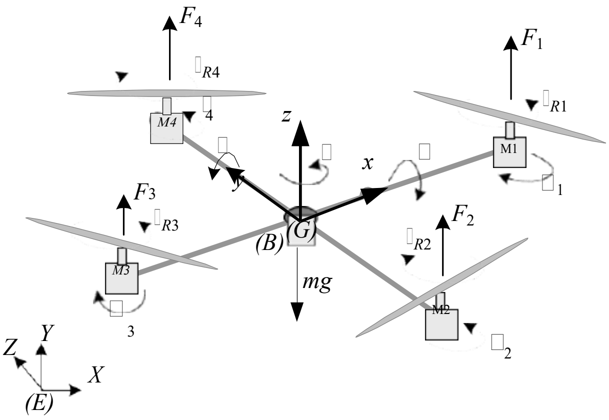

Fig.2 Quadrotor representation, coordinate, torques and forces.

$\xi = (x, y, z)^T$ is quadrotor position of centre mass in the inertial reference frame. m is the total mass of structure and $j \in R^{3\times 3}$ diagonal inertial matrix, constant and

$$. \quad J = \begin{bmatrix} I_x & 0 & 0 \\ 0 & I_y & 0 \\ 0 & 0 & I_z \end{bmatrix}$$

$\Omega = (\Omega_1, \Omega_2, \Omega_3)^T$ is the angular velocity defined as follows:

$$\Omega = \begin{bmatrix} 1 & 0 & -sin\theta \\ 0 & cos\phi & sin\phi\, cos\theta \\ 0 & -sin\phi & cos\phi\, cos\theta \end{bmatrix} \begin{bmatrix} \dot{\phi} \\ \dot{\theta} \\ \dot{\psi} \end{bmatrix} \tag{5}$$

Where, the quadrotor performs many angular movements of low amplitude. Ω can be assimilated by $\left[\dot{\phi} \;\; \dot{\theta} \;\; \dot{\psi}\right]^T$.

The two frame ((E_x, E_y, E_z) ; (E_X, E_Y, E_Z)) are relate by the rotation matrix defined by: $R(\phi, \theta, \psi)$:

$$R = \begin{bmatrix} C\psi C\theta & C\psi S\theta S\phi - S\psi C\phi & C\psi S\theta C\phi + S\psi S\phi \\ C\theta S\psi & S\psi S\theta S\phi + C\psi C\phi & S\psi S\theta C\phi - S\phi C\psi \\ -S\theta & C\theta S\phi & C\theta C\phi \end{bmatrix}$$

Where C and S are trigonometric functions Sin and Cos, respectively. $S(\Omega)$ is the symmetric matrix defined as follows:

$$S(\Omega) = \begin{bmatrix} 0 & -\Omega_3 & \Omega_2 \\ \Omega_3 & 0 & -\Omega_1 \\ -\Omega_2 & \Omega_1 & 0 \end{bmatrix} \tag{6}$$

F_f is the resultant of forces produced by the four rotors.

$$F_f = \begin{bmatrix} \cos\phi \sin\theta \cos\psi + \sin\phi \sin\psi \\ \cos\phi \sin\theta \sin\psi - \sin\phi \cos\psi \\ \cos\phi \cos\theta \end{bmatrix} \sum_{i=1}^{4} F_i \tag{7}$$

$$F_i = K_p \omega_i^2 \tag{8}$$

where K_p is the surge coefficient and ω_i is the angular velocity of rotor F_t is the forces resultant along the axes (X,Y,Z).

$$F_t = \begin{bmatrix} -K_{ftx} & 0 & 0 \\ 0 & -K_{fty} & 0 \\ 0 & 0 & -K_{ftz} \end{bmatrix} \dot{\xi} \tag{9}$$

ISSN: 2961-6611

where, K_{ftx}, K_{fty} et K_{ftz} are the coefficients of drag.

F_g is the force of gravity:

$$F_g = \begin{bmatrix} 0 & 0 & -mg \end{bmatrix}^T \tag{10}$$

Γ_f is moment developed by the rigid body of quadrotor. It is expressed as follows:

$$\Gamma_f = \begin{bmatrix} d\,(F_3 - F_1) \\ d\,(F_4 - F_2) \\ K_d\,(\omega_1^2 - \omega_2^2 + \omega_3^2 - \omega_4^2) \end{bmatrix} \tag{11}$$

d is the distance between the center of mass of quadrotor and the axis of rotation of the propeller. K_d is the coefficient of drag. Γ_a is the resultant of aerodynamic friction couples.

$$\Gamma_a = \begin{bmatrix} -K_{fax} & 0 & 0 \\ 0 & -K_{fay} & 0 \\ 0 & 0 & -K_{faz} \end{bmatrix} \Omega^2 \tag{12}$$

K_{ftx}, K_{fty} et K_{ftz} sont les coefficients de frottement aérodynamique. Γ_g is the result of gyroscopic torques due to the effects of rotation of the armature and the four rotors.

$$\Gamma_g = \sum_{i=1}^{4} \Omega \wedge J_r \begin{bmatrix} 0 \\ 0 \\ (-1)^{i+1}\omega_i \end{bmatrix} \tag{13}$$

J_r is the inertia of the rotor.

Consequently, the complete dynamic model governing quadrotor is as follows:

$$\begin{cases} \ddot{x} = (\cos\phi \sin\theta \cos\psi + \sin\phi \sin\psi)\,\frac{1}{m} U_1 - \frac{K_{ftx}}{m}\dot{x} \\ \ddot{y} = (\cos\phi \sin\theta \sin\psi - \sin\phi \cos\psi)\,\frac{1}{m} U_1 - \frac{K_{fty}}{m}\dot{y} \\ \ddot{z} = (\cos\phi \cos\theta)\,\frac{1}{m} U_1 - \frac{K_{ftz}}{m}\dot{z} - g \\ \ddot{\phi} = \frac{I_y - I_z}{I_x}\dot{\theta}\dot{\psi} - \frac{J_r}{I_x}\bar{\Omega}\dot{\theta} - \frac{K_{fax}}{I_x}\dot{\phi}^2 + \frac{d}{I_x} U_2 \\ \ddot{\theta} = \frac{I_z - I_x}{I_y}\dot{\phi}\dot{\psi} + \frac{J_r}{I_y}\bar{\Omega}\dot{\phi} - \frac{K_{fay}}{I_y}\dot{\theta}^2 + \frac{d}{I_y} U_3 \\ \ddot{\psi} = \frac{I_x - I_y}{I_z}\dot{\theta}\dot{\phi} - \frac{K_{faz}}{I_z}\dot{\psi}^2 + \frac{K_d}{I_z} U_4 \end{cases} \tag{14}$$

.

with U_1, U_2, U_3 et U_4 are the control inputs of the system, written by the four rotors angular velocities as follows:

$$\begin{bmatrix} U_1 \\ U_2 \\ U_3 \\ U_4 \end{bmatrix} = \begin{bmatrix} K_p & K_p & K_p & K_p \\ -K_p & 0 & K_p & 0 \\ 0 & -K_p & 0 & K_p \\ K_d & -K_d & K_d & -K_d \end{bmatrix} \begin{bmatrix} \omega_1^2 \\ \omega_2^2 \\ \omega_3^2 \\ \omega_4^2 \end{bmatrix} \tag{15}$$

et $\bar{\Omega} = \omega_1 - \omega_2 + \omega_3 - \omega_4$

From the dynamic equations (14) we can extract the high order terms of pitch angles (θ) and roll (ϕ), which depend not only on the angle of yaw (ψ) but also dynamic movements of the axes (x, y, z) as follows:

$$\begin{cases} \tan\theta = \dfrac{\left(\ddot{x}+\dfrac{K_{ftx}}{m}\dot{x}\right)Cos\psi + \left(\ddot{y}+\dfrac{K_{fty}}{m}\dot{y}\right)Sin\psi}{\ddot{z}+g+\dfrac{K_{ftz}}{m}\dot{z}} \\ S\phi = \dfrac{\left(\ddot{x}+\dfrac{K_{ftx}}{m}\dot{x}\right)Sin\psi - \left(\ddot{y}+\dfrac{K_{fty}}{m}\dot{y}\right)Cos\psi}{\sqrt{\left(\ddot{x}+\dfrac{K_{ftx}}{m}\dot{x}\right)^2+\left(\ddot{y}+\dfrac{K_{fty}}{m}\dot{y}\right)^2+\left(\ddot{z}+g+\dfrac{K_{ftz}}{m}\dot{z}\right)^2}} \end{cases}$$

III. SYNTHESIS OF ROBUST OBSERVER

In this section we present the nonlinear observer high gain [7, 10, 12] on our process. The model (14) developed in the first part of this article can be rewritten in the state representation as follows:

$$\begin{cases} \dot{X} = f(X,U) \\ Y = h(X) \end{cases} \tag{16}$$

$$X = [x_1 \ldots x_{12}]^T = [\phi\ \dot{\phi}\ \theta\ \dot{\theta}\ \psi\ \dot{\psi}\ x\ \dot{x}\ y\ \dot{y}\ z\ \dot{z}]^T \tag{17}$$

From (14) and (17) we obtain the following state representation:

$$\begin{aligned} &\dot{x}_1 = x_2;\ \dot{x}_2 = a_1x_4x_6 + a_2x_2^2 + a_3\bar{\Omega}x_4 + b_1U_2;\ \dot{x}_3 = x_4 \\ &\dot{x}_4 = a_4x_2x_6 + a_5x_4^2 + a_6\bar{\Omega}x_2 + b_2U_3;\ \dot{x}_5 = x_6 \\ &\dot{x}_6 = a_7x_2x_4 + a_8x_6^2 + b_3U_4 \\ &\dot{x}_7 = x_8;\ \dot{x}_8 = a_9x_8 + U_x\frac{U_1}{m};\ \dot{x}_9 = x_{10} \\ &\dot{x}_{10} = a_{10}x_{10} + U_y\frac{U_1}{m};\ \dot{x}_{11} = x_{12} \\ &\dot{x}_{12} = a_{11}x_{12} + \frac{Cx_1Cx_3}{m}U_1 - g \end{aligned} \tag{18}$$

$$a_1 = \left(\frac{I_y - I_z}{I_y}\right), a_2 = \frac{-K_{fax}}{I_x}, a_3 = \frac{-J_r}{I_x}, a_4 = \left(\frac{I_z - I_x}{I_y}\right)$$

$$a_5 = \frac{-K_{fay}}{I_y}, a_6 = \frac{-J_r}{I_y}, a_7 = \left(\frac{I_x - I_y}{I_z}\right), a_8 = \frac{-K_{faz}}{I_z}$$

$$a_9 = \frac{K_{ftx}}{m}, a_{10} = \frac{-K_{fty}}{m}, a_{11} = \frac{-K_{ftz}}{m}$$

$$b_1 = \frac{d}{I_x}, b_2 = \frac{d}{I_y}, b_3 = \frac{1}{I_x}$$

$$\begin{cases} U_x = cos\phi\ sin\theta\ cos\psi + sin\phi\ sin\psi \\ U_y = cos\phi\ sin\theta\ sin\psi - sin\phi\ cos\psi \end{cases} \tag{19}$$

To achieve the high gain observer in most of the work covered at high gain [7, 10, 12], the authors introduce a change of variable appropriate to facilitate the synthesis of the observer. We operate the structure (18) as follows:

$$\begin{cases} \dot{z} = Az + \varphi(U,z) \\ y = Cz \end{cases} \tag{20}$$

Where,

$$z_1 = \begin{pmatrix} z_{11} \\ z_{12} \end{pmatrix} = \begin{pmatrix} x_1 \\ x_2 \end{pmatrix},\ z_2 = \begin{pmatrix} z_{21} \\ z_{22} \end{pmatrix} = \begin{pmatrix} x_3 \\ x_4 \end{pmatrix},\ z_3 = \begin{pmatrix} z_{31} \\ z_{32} \end{pmatrix} = \begin{pmatrix} x_5 \\ x_6 \end{pmatrix}\ z_4 = \begin{pmatrix} z_{41} \\ z_{42} \end{pmatrix} = \begin{pmatrix} x_7 \\ x_8 \end{pmatrix}, z_5 = \begin{pmatrix} z_{51} \\ z_{52} \end{pmatrix} = \begin{pmatrix} x_9 \\ x_{10} \end{pmatrix}, z_6 = \begin{pmatrix} z_{61} \\ z_{62} \end{pmatrix} = \begin{pmatrix} x_{11} \\ x_{12} \end{pmatrix}$$

$$A_i = \begin{pmatrix} 0 & 1 \\ 0 & 0 \end{pmatrix},\ y = (x_1, x_3, x_5, x_7, x_9, x_{11})^T,\ C_i = (1\quad 0).$$

ISSN: 2961-6611

$$\Phi_1 = \begin{pmatrix} \varphi_{11} = 0 \\ \varphi_{12} = a_1x_4x_6 + a_2x_2^2 + a_3\Omega x_4 + b_1U_2 \end{pmatrix}, \quad \Phi_2 = \begin{pmatrix} \varphi_{21} = 0 \\ \varphi_{22} = a_4x_2x_6 + a_5x_4^2 + a_6\Omega x_2 + b_2U_3 \end{pmatrix}, \quad \Phi_3 = \begin{pmatrix} \varphi_{31} = 0 \\ \varphi_{32} = a_7x_2x_4 + a_8x_6^2 + b_3U_4 \end{pmatrix}$$

and

$$\Phi_4 = \begin{pmatrix} \varphi_{41} = 0 \\ \varphi_{42} = a_9x_8 + U_x\dfrac{U_1}{m} \end{pmatrix}, \quad \Phi_5 = \begin{pmatrix} \varphi_{51} = 0 \\ \varphi_{52} = a_{10}x_{10} + U_y\dfrac{U_1}{m} \end{pmatrix}, \quad \Phi_6 = \begin{pmatrix} \varphi_{61} = 0 \\ \varphi_{62} = a_{11}x_{12} + \dfrac{Cx_1Cx_3}{m}U_1 - g \end{pmatrix}$$

Theorem. 1 : The system (20) is uniformly observable if it satisfies the following structural property: exist p couples $(\delta_i, \eta_i), \delta_i \in N$, and $\eta_i \in N^*$ $\forall i,k = 1,\ldots,p$ and $j = 1,\ldots,n_i$ $\forall l = 1,\ldots,n_k$:

$$\frac{\partial \varphi_{ij}}{\partial z_{kl}} \neq 0 \Rightarrow \delta_i + (j-1)\eta_i + \frac{\eta_i}{2} > \delta_k + (l-1)\eta_k + \frac{\eta_k}{2} \tag{21}$$

After applying théorème1 we found:

$$\delta_4 + \frac{3}{2}\eta_4 > \delta_1 + \frac{\eta_1}{2}, \quad \delta_5 + \frac{3}{2}\eta_5 > \delta_1 + \frac{\eta_1}{2}$$

$$\delta_6 + \frac{3}{2}\eta_6 > \delta_1 + \frac{\eta_1}{2}, \quad \delta_1 = \delta_2 = \delta_3, \eta_1 = \eta_2 = \eta_3$$

With : $n = 1,\ldots,12$, $p = 1,\ldots,6$, $k = \{1,2\}$.

(**H**)-The function $\varphi(z,u)$ is globally Lipschitz with respect to z: $\exists\rho > 0; \forall(z,u) \in \mathbb{R}^{kl} \times U$, $\left\| \frac{\partial \varphi_{ij}}{\partial z_{kl}} \right\| \leq \rho$.

Theorem.2: If the system (20) is uniformly observable and it satisfies condition (**H**) then $\exists\theta_0 > 0$ as $\theta > \theta_0$, thefollowing system:

$$\dot{\hat{z}} = A\hat{z} + \varphi(\hat{z},u) - S_\theta^{-1}C^T(C\hat{z} - y) \tag{22}$$

Is an exponential observer for (20) and S_θ is a block matrix that depends only on the setting parameters of the dynamics of the observer (δ_i, η_i) and θ with :

$$S_\theta = \begin{pmatrix} S_{\theta^{\delta_1}} & & 0 \\ & \ddots & \\ 0 & & S_{\theta^{\delta_p}} \end{pmatrix}$$

Where S_{θ_k} are positive definite matrices which are solutions of Lyapunov relationship given by:

$$\theta^{\eta_k} S_{\theta_k} + A^T S_{\theta_k} + S_{\theta_k} A - C^T C = 0$$

$$S_{\theta_k} = \begin{pmatrix} \dfrac{1}{\theta_k} & -\dfrac{1}{\theta^{2}_k} \\ -\dfrac{1}{\theta^{2}_k} & \dfrac{2}{\theta^{3}_k} \end{pmatrix}, \ k = 1,\ldots,6.$$

The structure of the observer designed for the system (20) is described by the following system:

$$\begin{cases} \dot{\hat{z}} = A\hat{z} + \varphi(\hat{z},u) - S_\theta^{-1}C^T(C\hat{z} - y) \\ \hat{y} = C\hat{z} \end{cases} \tag{23}$$

The first term of the first equation of system (23) constitutes a prediction phase the second is a correction phase.

$$S_\theta^{-1}C^T(C\hat{z} - y) = \begin{pmatrix} 2\theta^{\eta_k}(\hat{L} - L) \\ \theta^{2\eta_k}(\hat{L} - L) \end{pmatrix}$$

with $L = (\phi \ \theta \ \psi \ x \ y \ z)^T$

IV. SYNTHESIS OF SLIDING MODE CONTROL

The method was chosen after considering the following main benefits:

- Lyapunov stability.

- Ensuring the robustness and all the properties of the dynamics desired.
- Safe handling nonlinear system.
- However, the control strategy is summarized in the control of two subsets: the first relates to the position control while the second is that of attitude.

In this section, the goal is to design a sliding mode control [2, 4]. The purpose of this order in our case is performed in two stages. First, synthesize a variety (the choice of sliding surface) *S(X, t)* such that all trajectories of the system obeys a desired behaviour tracking, control and stability. As the second step, determine a control law (switching) *U(X,t)*, which is able to attract all the trajectories of the green state sliding surface and remain on that surface. Involves the design of a Lyapunov function which can satisfy the necessary condition of sliding ($SS < 0$). Control laws are summarized as follows:

$$\begin{cases} U_1 = \frac{m}{C\square C\square}\left(k_6\, sign(S_z) \square a_{11} x_{12} + g + \ddot{z}_d + \square_6 e_{12}\right) \\ U_2 = \frac{1}{b_1}\left(k_1\, sign(S_\square) \square a_1 x_4 x_6 \square a_2 x_2^2 \square a_3 \underline{\square} x_4 + \ddot{\square}_d + \square_1 e_2\right) \\ U_3 = \frac{1}{b_2}\left(k_2\, sign(S_\square) \square a_4 x_2 x_6 \square a_5 x_4^2 - a_6 \underline{\square} x_2 + \ddot{\square}_d + \square_2 e_4\right) \\ U_4 = \frac{1}{b_3}\left(k_3\, sign(S_\square) \square a_7 x_2 x_4 \square a_8 x_6^2 + \ddot{\square}_d + \square_3 e_6\right) \\ U_x = \frac{m}{U_1}\left(k_4\, sign(S_x) \square a_9 x_8 + \ddot{x}_d + \square_4 e_8\right) \quad /U1 \square 0 \\ U_y = \frac{m}{U_1}\left(k_5\, sign(S_y) \square a_{10} x_{10} + \ddot{y}_d + \square_5 e_{10}\right) \quad /U1 \square 0 \end{cases} \tag{24}$$

Proof: *Choose the sliding surfaces given by*:

$$S_\square = e_2 + \square_1 e_1; S_\square = e_4 + \square_2 e_3; S_\square = e_6 + \square_3 e_5$$
$$S_x = e_8 + \square_4 e_7; S_y = e_{10} + \square_5 e_9; S_z = e_{12} + \square_6 e_{11}$$

As

$$\square_i > 0 \quad et \quad \begin{cases} e_i = x_{id} \square x_i \quad i = 1,\cdot,11 \\ e_{i+1} = \dot{e}_i \end{cases} \tag{25}$$

We assume that:

$$V(S_\square) = \frac{1}{2} S_\square^2 \tag{26}$$

If $\dot{V}(S_\square) < 0$, thus $S_\square \dot{S}_\square < 0$ therefore, the necessary condition for slip is checked and the Lyapunov stability is guaranteed. The law chosen for the attractive surface is derived from the time (26) satisfying ($S_\square \dot{S}_\square < 0$):

$$\begin{aligned} \dot{S}_\square &= \square k_1\, sign(S_\square) \\ &= \dot{x}_{1d} \square \dot{x}_2 + \square_1 \dot{e}_1 \\ &= \square a_1 x_4 x_6 \square a_2 x_2^2 \square a_3 \bar{\square} x_4 \square b_1 U_2 + \ddot{\square}_d + \square_1 (\dot{\square}_d \square x_2) \end{aligned}$$

So

$$U_2 = \frac{1}{b_1}\left(k_1\, sign(S_\square) \square a_1 x_4 x_6 \square a_2 x_2^2 \square a_3 \bar{\square} x_4 + \ddot{\square}_d + \square_1 e_2\right) \tag{27}$$

The same steps are followed to extract *U_1 ,U_3, U_4, U_x* and *U_y* with $k_j \square R^+$, $j = 1,\ldots,6$.

To validate the nonlinear control algorithm proposed above, we have performed simulations in the Matlab-Simulink. In which we added white noise on the signals from the sensors.

TABLE I- THE CHARACTERISTICS OF THE UAV USED ARE GIVEN AS FOLLOWS [11,4].

Symbol	Parameters of the UAV	Value (unit)
Kp	Lift coefficient	2.984 e-5 (N.m/r.s)
Kd	Drag coefficient	3.232 e-7 N.m/r.s

m	The total mass	0.486 Kg
d	Distance	0.25 m
Jr	Rotor inertia	2.838 e-5 N.m/r.s2
J	Inertial matrix	3.827 e-3 N.m/ r.s2
Kfa	Aerodynamic coefficients of friction	5.567 e-4 N.m/r.s2
Kft	Result of couples Gyros	5.670 e-4 N.m/r.s2

N =Newton, *m* = meter, ***s*** = second;

To further analyze the performance of the proposed model of orders, we have chosen trajectories level types. The parameters of our control were set as follows $\square_i = 10, k_i = 10^3$ for $i = 1,\cdot,6$.

Generally, there is no definite method for adjusting gains of the observer, however, the gains are set to values well chosen in order to neglect.

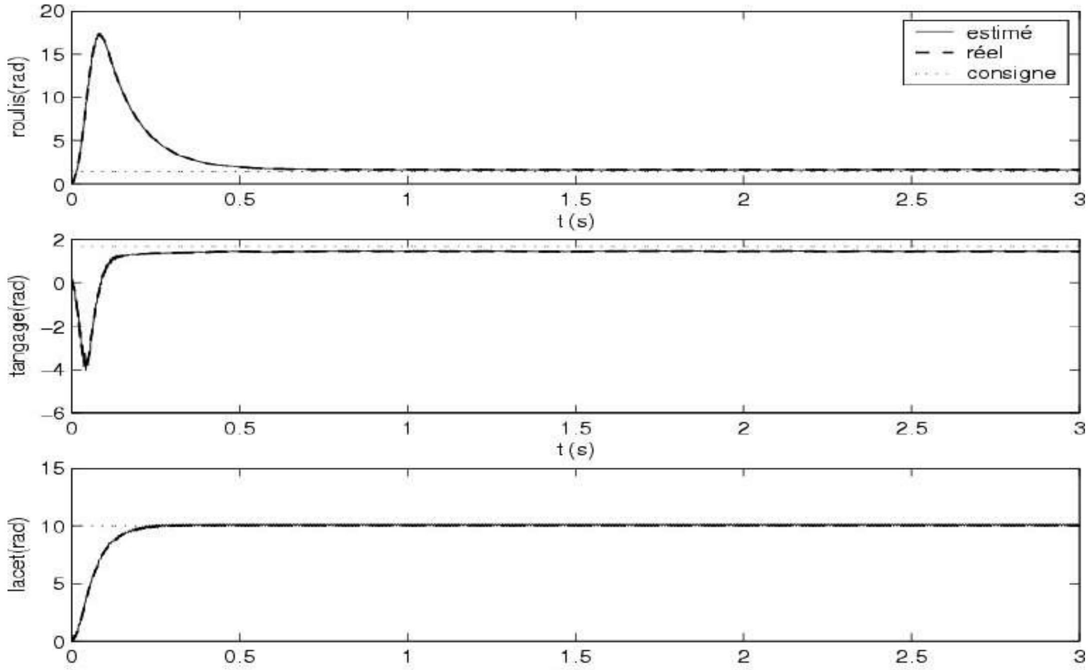

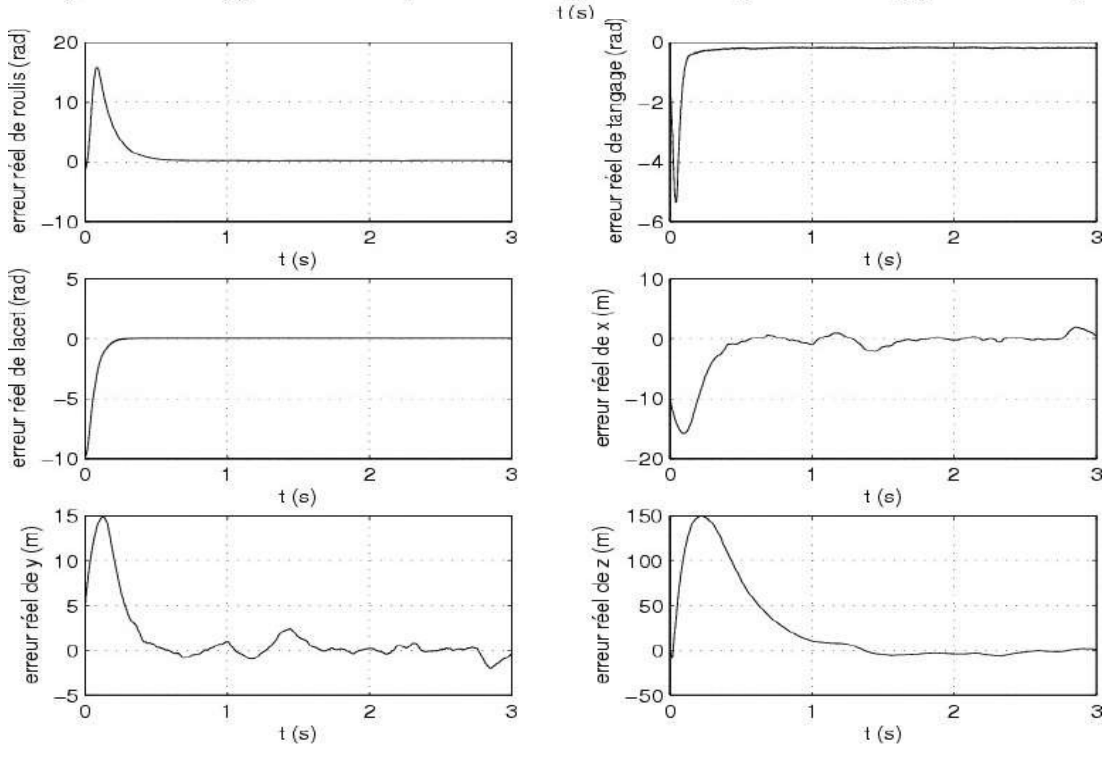

ISSN: 2961-6611

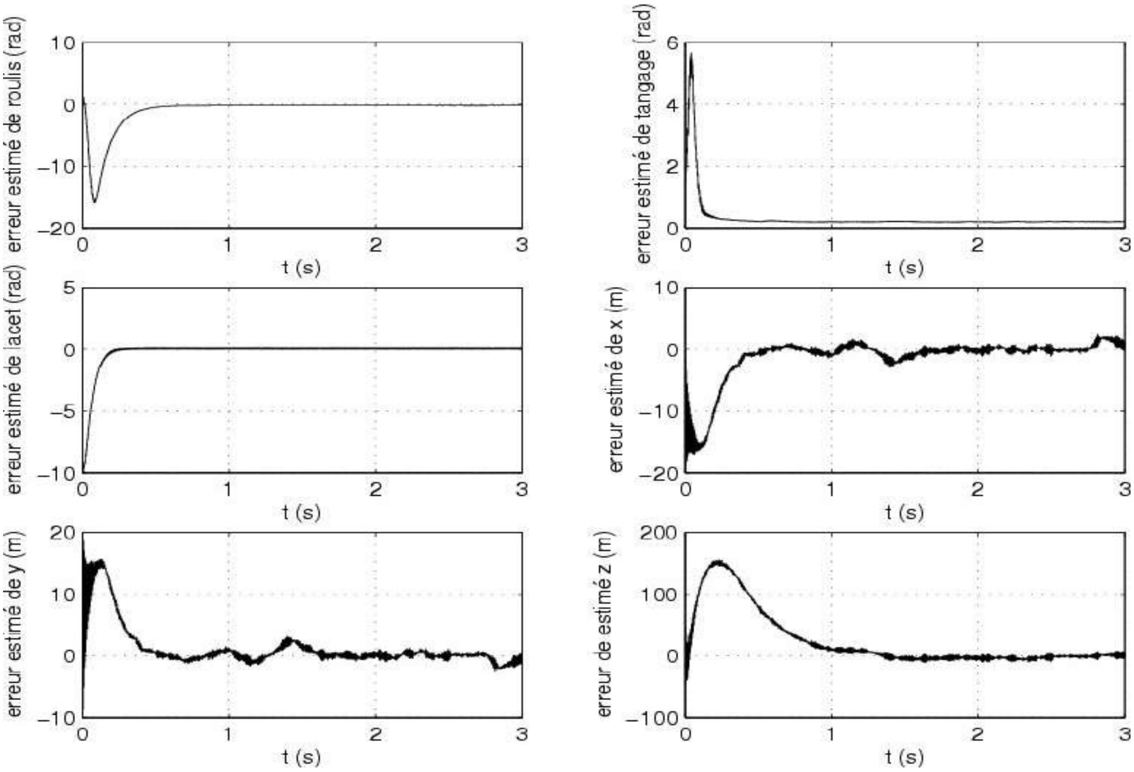

Fig.3. Simulation results

V. CONCLUSIONS

In this paper, we demonstrated the richness and simplicity of the sliding mode control with nonlinear switching surface. We are interested in closer to the application of this type of control on quadroror, considering the simplified nonlinear model obtained in the first part. With this model, we developed the control structure based on the observer presented in the second part, to estimate all immeasurable states of our system for attitude control and position.

The sliding mode control showed good dynamic performance and high tracking ability of the set of desired trajectories, the disturbance rejection and insensitivity vis-à-vis the changes in measurements from the position sensors yaw angle. These performances are better for a good selection of tuning parameters and the observer, in order to eliminate grazing affect the trajectories, such as large ranges of variation of the deposit. Finally, we hope to develop other nonlinear control techniques to improve performances and good navigation systems in the environment such evolutionary constraint.

REFERENCES

[1] M. Ckerrow, “Modelling the Draganflyer four rotor helicopter”, IEEE International Conference on Robotics and Automation, 2004, pp. 3596– 3601.

[2] P. Adigbli. “Nonlinear Attitude and Position Control of a MicroQuadrotor using Sliding Mode and Backstepping Techniques”. European Micro Air Vehicle Conference and Flight Competition. EMAV2007), 17-21 September 2007, Toulouse, France.

[3] T. Hamel. P. Souères ’’Modélisation, estimation et contrôle des drones à voilures tournantes’’ : Un aperçu des projets de recherche français UNSA-CNRS, LAAS-CNRS, Toulouse, France (2003).

[4] H. Bouadi, and M. Tadjine, “Nonlinear Observer Design and Sliding Mode Control of Four Rotors Helicopter”. Proceedings of World Academy of Science, Engineering and Technology volume 25 November 2007 ISSN 1307-6884.

[5] A. Mokhtari, A.Benallegue and A.Belaidi “polynomial linear quadratic Gaussian and sliding mode observer for a quadrotor unmanned aerial vehicle” Journal of Robotics and Mechatronics Vol.17 No.4, 2005.

[6] P. Castillo, R. Lozano and A. Dzul, "Modelling and Control of Mini- Flying Machines", Springer-Verlag in Advances in Industrial Control July 2005.

[7] M. Farza.‘’Modelisation et synthèse d’observateurs pour des classes de systèmes non linéaire Application aux procèdes (Bio) chimique’’. Habitation a dirigé des recherches. L’INPG. Déc. 2000.

[8] A. Mokhtari, N.K.M’sirdi, K. Meghriche and A. Belaidi “feedback linearization and linear observer for a quadrotor unmanned aerial vehicle” Advanced Robotics, Vol.20, No.1, pp. 71-91, 2006.

[9] A.Tayebi. “Unit quaternion observer based attitude stabilization of a rigid spacecraft without velocity measurement”. Proceedings of the 45th IEEE Conference on Decision & Control. San Diego, CA, USA, December, 2006.

[10] A. Mansouri, M. Chnafa, A. bouhanna, E. Etien‘’ powerful nonlinear observer associated with field-oriented control of an induction motor’’. Int. Appl. Math. Comput. Sci., 2004, vol. 14, No. 2, 209-220.

[11] Derafa L. Madani t. and Benallegue A, 2006 ‘’ dynamic modelling and experimental identification of four rotor helicopter parameters’’ ICIT Mumbai, India.

[12] A.Benfekir, A.Mansouri, A.Bouhenna, M.Chenafa ‘’Synthèse d'un observateur non linéaire pour un drone de type mico-hélicoptère à 4 rotors’’. EMP d'Alger Algérie, SSNE08, mais 2008.

[13] A. Tayebi, S. Mcgilvray, 2004 “Attitude stabilisation of a four rotor aerial robot”, IEEE conference on decision and control, December 14-17, Atlantis Paradise Island, Bahamas 1216-1217.

Effect of Surfactants on double diffusive natural convection of CNT water-based micropolar nanofluids

Awatef Abidi [a,b,c], , Nessrin Manaa[b], Mohammed Naceur Borjini [b]

[a] *Physics Department, College of Sciences Abha , King Khalid University, Saudi Arabia.*
[b] *Research Laboratory of Metrology and Energy Systems, National Engineering School, Energy Engineering Department, Monastir University , Monastir City, Tunisia.*
[d]*Higher school of Scienecs and Technology of Hammam Sousse, Sousse University, Tunisia.*
[d]*Univ Rennes, LGCGM, F-35000, Rennes, France.*
`Email1 : abidiawatef@yahoo.fr`
`Email 2 : manaa_nessrin@outlook.com`
`Email 3 : borjinimn@yahoo.com`

Abstract :

This paper presents numerical simulations of double diffusive natural convective heat and mass transport in a cubic cavity filled with micropolar nanofluid and micropolar hybrid nanofluid. The governing equations are stated in vorticity stream function formulations and numerically solved using the control volume approach. The effect of hybrid nanofluids and the significance of micropolar theory are investigated. Furthermore, the influence of nanoparticle volume fraction, Rayleigh number, Nusselt number, Sherwood number, buoyancy ratio, and micropolar vortex parameter on the flow field and the rate of heat and mass transfer is studied. The micropolar hypothesis played a role in lowering the Nusselt and Sherwood values. The rise in micropolar viscosity parameter affects the rates of heat and mass transfer, as well as the three-dimensional structure of the flow, which is more visible in regions dominated by thermal buoyancy. Heat and mass transfer rates rose when hybrid nanofluids were used instead of single nanofluids, but stayed constant when the Rayleigh number grew in regions dominated by thermal buoyancy. The kind of hybrid nanofluid has a considerable influence on heat and mass transfer rates, as well as the 3D aspect of the flow.

I. INTRODUCTION

Many fluids like water, ethylene glycol, kerosene, engine oil and acetone used in the industrial applications have low thermal conductivity. Due to this, the capital and operation costs of thermal systems become uneconomical. Hence highly thermal conductive nanoparticles are added to the afore-mentioned fluids to boost their thermal conductivities. Choi and Eastman [1] were the first who introduced this idea and used the term nanofluids to denote the fluids with suspended nanoparticles. Thereafter, a significant amount of research has been carried out on the nanofluids because of their important practical applications in microelectronics, solid-state lighting, detergency, and manufacturing. Heat transfer characteristics of the nanofluids are significantly improved because of an increase in surface area and heat capacity of the fluid, increase in thermal conductivity, interaction, and collision among nanoparticles, intensification in fluid turbulence, and flattening of the transverse temperature gradient across the fluid. Few investigators analyzed the convective heat transfer characteristics of nanofluids confined in enclosures with different models and those prominent researchers are When and Ding [2], Abouali and Falahatpishe [3], Jou and Tzeng [4], Abu Nada et al. [5], Kolsi et al. [6], Bouhalleb and Abbassi[7].Hybrid nanofluid is a new type of advanced working fluids, engineered with enhanced thermophysical properties. The hybrid nanofluids profit from the thermo-physical properties of more than one type of nanoparticles.

In the last few decades, many studies were being conducted to explore the preparation procedure, enhancement in properties, and challenges encountered in various stages of hybrid nanofluids preparation. Momin [8] experimentally investigated the mixed convection through Al_2O_3 water nanofluid inside an inclined copper tube surface by analysing the effects of nanoparticle concentration and power supply on the development of the thermal field under laminar flow

ISSN: 2961-6611

condition. He also presented a fully developed laminar convective heat transfer through a uniformly heated circular tube using Al_2O_3–Cu/water hybrid nanofluid.

Afrand et al. [9] carried out an experimental investigation on the rheological behavior of Fe_3O_4–Ag/EG hybrid nanofluid with the influence of temperature and nanoparticles' concentration. Their results reveal that the dynamic viscosity of the hybrid nanofluid increases with the increase in nanoparticles' volume fraction and the same decreases with the increase in temperature. Dalkılıç et al. [10] synthesized the hybrid nanofluids by dispersing silicon dioxide and graphite nanoparticles in distilled water and analyzed its viscosity variation with respect to nanoparticles' volume fraction ratio and temperature. It is found that the highest percentage increase in viscosity is 36.12% with nanoparticles' volume fraction ratio of 2 at 15 °C. Takabi and Salehi [11] numerically analyzed the laminar natural convection in a sinusoidal corrugated enclosure with a discrete heat source on the bottom wall, filled by pure water, Al_2O_3/water nanofluid, and Al_2O_3-Cu/water hybrid nanofluid. Their results indicate that hybrid nanofluid shows better heat transfer characteristics when compared to simple nanofluid.

The rotating micro-constituents' effects in nanofluids should be carefully analyzed to understand the nature of fluid flow effectively and the same was originally proposed by Eringen [12] to elucidate fluid particle's micro-motions which cannot be explained by the classical models. The model of micropolar fluid represents fluids consisting of rigid, randomly oriented (or spherical) particles suspended in a viscous medium where the deformation of the particles is ignored. Micropolar fluids have been well adhered to precisely simulate the flow characteristics of polymeric additives, geomorphological sediments, colloidal suspensions, haematological suspensions, liquid crystals, lubricants, etc. The main advantage of using a micropolar fluid model compared to other non-Newtonian fluids' models is that the former takes into account the rotation of fluid particles employing an independent kinematic vector called the microrotation vector. The above-mentioned applications demand critical research efforts on flow behavior and heat and mass transfer characteristics of micropolar fluids. Further, the findings of Eringen [12] were critically reviewed by Ariman et al. [13] and found it accurate. Lukaszewics [14] presented a detailed comprehensive analysis of micropolar fluids and their applications. It is vivid that the micropolar fluids have many engineering applications, such as liquid crystal solidification, colloidal and suspension solutions, exotic lubricants, animal blood, and polymer fluids extrusion.

Abidi and Borjini [15] analyzed the influence of micro-constituents in micropolar fluid on the three-dimensional double-diffusive natural convection. They established that the deterioration in three-dimensional features of the flow with a significant decrease in heat and mass transfer rates with an increase in the vortex viscosity parameter. The extensive use of colloidal suspensions in modern engineering industries along with the limitations of its modelling due to its non-Newtonian nature demands a more sophisticated micropolar nanofluid model.

Bourantas and Loukopoulos [16] proposed a theoretical micropolar model to investigate natural convection in nanofluidic suspensions based on a micropolar theory with its genuine validation. The presence of nanoparticles' microrotation well explains the controversial theoretical numerical results and experimental data on the natural convection of nanofluids (Putra et al. [17]). The results show that nanoparticles' microrotation decreases overall heat transfer rate with an increase in average Nusselt number. It was also observed that the variation of Rayleigh number and Nusselt number were in similar agreement for a constant microrotation number. Hussanan et al. [18] used five types of oxide nanoparticles on a vertical plate to explore the transient natural convection in a micropolar nanofluid. They concluded that the temperature of nano-fluid is much higher with graphene oxide.It is worth mentioning that the current literature does not give a substantial contribution to the analysis of flow and heat transfer in the micropolar hybrid nanofluid model. Mollamahdi et al. [19] studied the forced convection in Al_2O_3-Cu/water micropolar nanofluid in a porous channel under the effect of a magnetic field. The authors analyzed the consequences of utilizing hybrid nanofluid with the application of micropolar theory on flow field and heat transfer rate.

The focus of the present study is on the analyses of the influences of relevant parameters such as Rayleigh number, buoyancy ratio, nanoparticles' volume fraction, and vortex viscosity parameter on flow behavior and heat and mass transfer rates. The effects of type of hybrid nanoparticles on the rate of heat and mass transfer and flow structure are also analyzed.

II. MATHEMATICAL MODELING

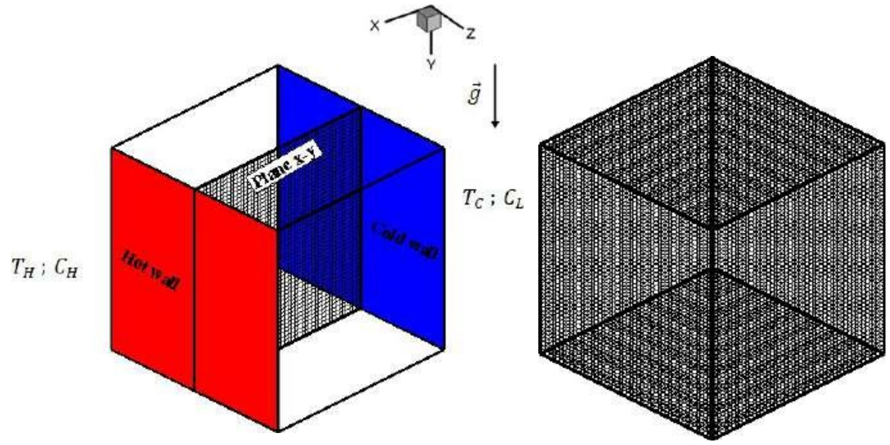

(a) **(b)**

Fig.1 (a) Schematic of the considered problem, **(b)** Mesh surfaces

A simple schematic view of the thermo-solutal natural convection problem under study is described in Fig. 1. The cube is filled with multi-walled CNT water-based micropolar nanofluid stabilized with two types of surfactants lignin and sodium polycarboxylate respectively. The two vertical walls parallel to the plane (y-z) are subject to constant temperatures (T_H>T_C) and constant concentrations (C_H>C_L). The other walls are supposed to be impermeable and adiabatic. The dynamic and thermal slips between nanoparticles and the base fluid are negligible. During the process of the natural convection, all the properties of the base fluid and nanoparticles are unchangeable except the density in the buoyancy term in momentum equation, its variations being modeled using Boussinesq approximation. The effects of Soret and Dufour are assumed to be negligible.

The vorticity–vector potential formulation is used in the present study to eliminate the pressure term and makes easier the numerical treatment. The vorticity and vector potential are respectively defined by the following two relations: $\vec{U} = \nabla \times \vec{\psi}$ and $\vec{\omega} = \nabla \times \vec{U}$.

The system of governing equations of the phenomenon is:

$$\nabla^2 \vec{\psi} = -\vec{\omega} \tag{7}$$

$$\frac{\partial \vec{\omega}}{\partial t} + (\vec{U}.\nabla)\vec{\omega} - (\vec{\omega}.\nabla)\vec{U} = Pr\left(\frac{\mu_{nf}}{\mu_f} + K\right)\left(\frac{\rho_f}{\rho_{nf}}\right)\nabla^2\vec{\omega} - PrK\left(\frac{\rho_f}{\rho_{nf}}\right)\nabla^2\vec{H}$$
$$+RaPr\left(\frac{(\rho\beta_T)_{nf}}{(\rho\beta_T)_f}\right)\left(\frac{\rho_f}{\rho_{nf}}\right)\left(\left[\frac{\partial T}{\partial z}, 0, -\frac{\partial T}{\partial x}\right] - N\left[\frac{\partial C}{\partial z}, 0, -\frac{\partial C}{\partial x}\right]\right) \tag{8}$$

$$\left(\frac{\partial \vec{H}}{\partial t} + (\vec{U}.\nabla)\vec{H}\right) = Pr\left(\frac{\mu_{nf}}{\mu_f} + \frac{K}{2}\right)\left(\frac{\rho_f}{\rho_{nf}}\right)\nabla^2\vec{H} + K\left(\frac{\rho_f}{\rho_{nf}}\right)(\vec{\omega} - 2\vec{H}) \tag{9}$$

$$\frac{\partial T}{\partial t} + (\vec{U}.\nabla)T = \left(\frac{(\rho C_P)_f}{(\rho C_P)_{nf}}\right)\left(\frac{k_{nf}}{k_f}\right)\nabla^2 T \tag{10}$$

$$\frac{\partial C}{\partial t} + (\vec{U}.\nabla)C = \frac{1}{Le}\left(\frac{(\rho C_P)}{(\rho C_P)_f}\right)\left(\frac{k_f}{k_{nf}}\right)\nabla^2 C \tag{11}$$

The local Nusselt and Sherwood numbers on the isothermal walls are defined by:

$$Nu = \frac{k_{nf}}{k_f}\left.\frac{\frac{\partial T'}{\partial x'}}{\frac{T'_H - T'_C}{L}}\right)_{x'=0,1} = -\left.\frac{k_{nf}}{k_f}\frac{\partial T}{\partial x}\right)_{x=0,1} \tag{12}$$

ISSN: 2961-6611

$$Sh = \left.\frac{D\frac{\partial C'}{\partial x'}}{D\frac{C'_H - C'_L}{L}}\right)_{x'=0,1} = \left.\frac{\partial C}{\partial x}\right)_{x=0,1} \tag{13}$$

The average Nusselt and Sherwoood numbers, on the isothermal walls of the enclosure are defined as follows:

$$\overline{Nu} = \int_0^1\int_0^1 Nu\,dy\,dz \tag{14}$$

$$\overline{Sh} = \int_0^1\int_0^1 Sh\,dy\,dz \tag{15}$$

For each time step, the following convergence criterion is satisfied:

$$\sum_{1,2,3}\frac{\max|\psi^n - \psi^{n+1}|}{\max|\psi^n|} + \max|\,-T^{n+1}| + \max|C^n - C^{n+1}| \le 10^{-5} \tag{16}$$

III. RESULTS AND DISCUSSION:

To highlight the influence of using Cu-Al_2O_3/water MHNF on HMT characteristics, the variations of $\overline{Nu}$ and $\overline{Sh}$ for different values of N for both Cu/water MNF and Cu-Al_2O_3/water MHNF are presented in Fig 6. It is increasingly obvious that both the cases have a quasi-similar pattern for different values of $\overline{Nu}$ and $\overline{Sh}$.

It is also seen that for both the cases, $\overline{Nu}$ and $\overline{Sh}$ decreases, as N value increases in the negative sense. And for N value above -1, $\overline{Nu}$ and $\overline{Sh}$ rises. However, when contrasted to Cu/water MNF in the thermally dominated zone, the values of $\overline{Nu}$ and $\overline{Sh}$ for Cu-Al_2O_3/water MHNF are larger. The values of $\overline{Nu}$ and $\overline{Sh}$ are lower for HN when compared with Cu/water MNF, conflicting to the thermally dominated region.

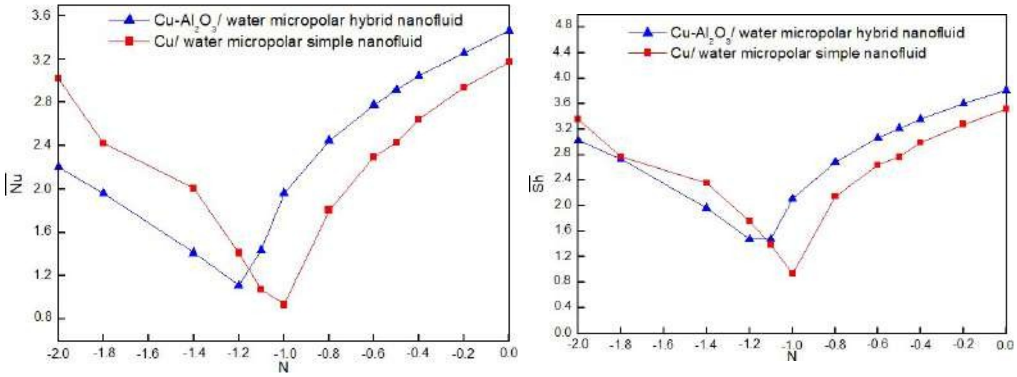

Figure 1 : $\overline{Nu}$ and $\overline{Sh}$ for different N using Cu-Al_2O_3/water MHNF and Cu/water MNF atRa=10^5, $Le = 1$, $Pr = 6.2$, $\varphi = 0.01$, and $K = 1$.

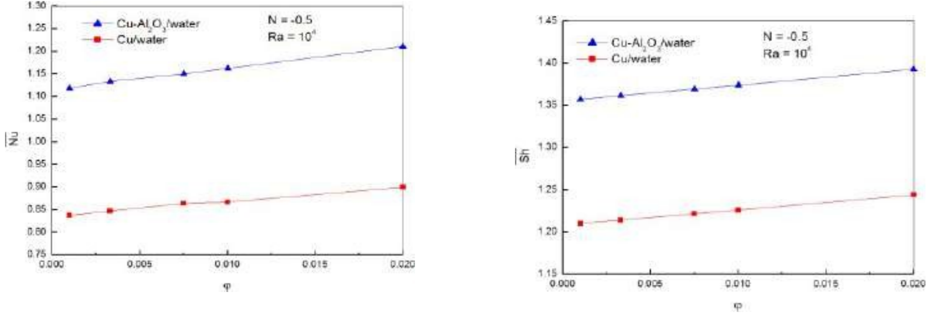

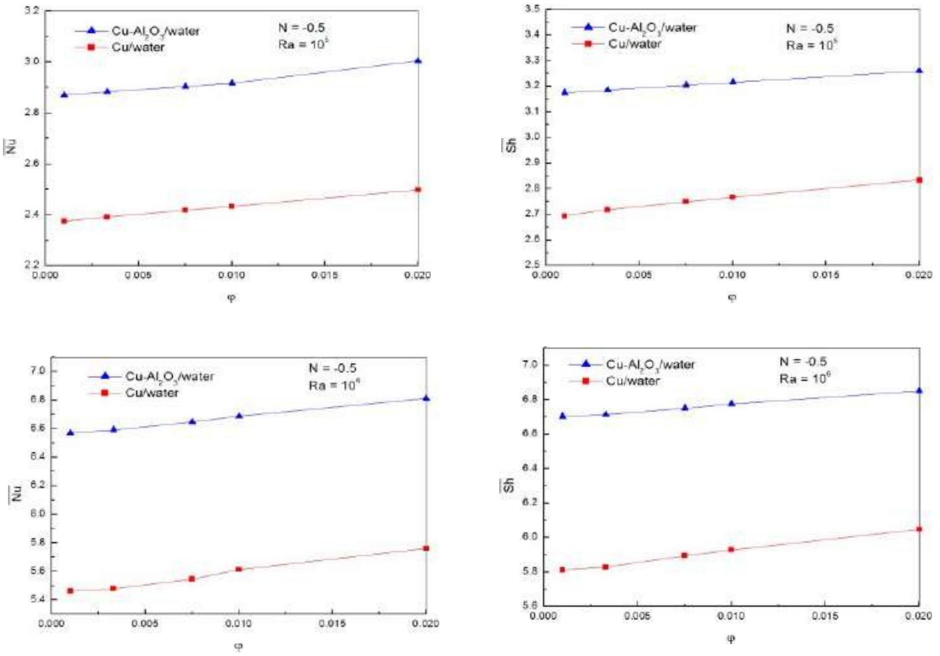

Figure 2: $\overline{Nu}$ and $\overline{Sh}$ variations versus volume fraction of nanoparticles (φ) for Cu-Al$_2$O$_3$/water MHNF and Cu/water MNF at N = - 0.5 at Le = 1, Pr = 6.2, φ = 0.01, and K = 1.

It can also be noticed that a lowest value for $\overline{Nu}$ and $\overline{Sh}$ exists for Cu/water MNF at N ≈ −1. By using Cu-Al$_2$O$_3$/water MHNF, this minimum value moves towards the left side of the y axis (N ≈ 0) and is equal to -1.2. As an interesting result in Figure 6, when using Cu-Al$_2$O$_3$/water MHNF, the heat and mass transfer in the thermally dominated region of the cavity is highest. Therefore, it can be inferred that both N and the hybridity may be important in the performance of heat and mass transfer within the cavity.

The variations of $\overline{Nu}$ and $\overline{Sh}$ versus volume fraction of nanoparticles for both classical nanofluid (Cu/water) and hybrid nanofluid (Cu-Al$_2$O$_3$/water) models are shown in Figure 2. For all cases, the increase of nanoparticles volume fraction increases $\overline{Nu}$ and $\overline{Sh}$ numbers for both working fluids. Besides, the hybrid nanofluid possesses better heat transfer characteristics for a given *Ra*. As expected, the influence of hybrid nanoparticles is more pronounced at high volume fractions due to high thermal conductivity. Therefore, the enhancement of heat and mass transfer characteristics using hybrid nanofluid becomes more prominent at high *Ra* cases.

IV. CONCLUSION:

Numerical investigation of heat and mass transfer in double-diffusive natural convection is performed in three-dimension. Single nanofluid (Cu /water) and hybrid micropolar nanofluid (Cu-Al$_2$O$_3$/water) filled in a cubic cavity is considered for the analysis. Following are the important conclusions arrived in this work:

1. The rates of heat and mass transfer considering the model of micropolar nanofluid is lower compared to the model of pure nanofluid.
2. The rates of heat and mass transfer are enhanced by using hybrid Cu-Al2O3/water compared to Cu /water nanofluid. These rates were true for any values of volume fractions of nanoparticles. However, these rates remained same at all Rayleigh numbers considered.

ISSN: 2961-6611

REFERENCES :

[1] D. Wen, Y. Ding, Formulation of nanofluids for natural convective heat transfer applications, Int. J. Heat and Fluid Flow 26 (6) (2005) 855–864.

[2] O. Abouali, A. Falahatpisheh, Numerical investigation of natural convection of Al2O3 nanofluid in vertical annuli, Int. J. Heat Mass Transf. 46 (1) (2009) 15–23.

R.Y. Jou, S.-C. Tzeng, Numerical research of nature convective heat transfer enhancement filled with nanofluids in rectangular enclosures, Int. Commun. Heat Mass Transf. 33 (6) (2006) 727–736.

[3] E. Abu-Nada, Z. Masoud, H.F. Oztop, A. Campo, Effect of nanofluid variable properties on natural convection in enclosures, Int. J. Therm. Sci. 49 (3) (2010) 479–491.

[4] L. Kolsi, A.A.A.A. Alrashed, K. Al-Salem, H.F. Oztop, M.N. Borjini, Control of natural convection via inclined plate of CNT-water nanofluid in an open sided cubical enclosure under magnetic field, Int. J. Heat Mass Transf. 111 (2017) 1007–1018.

[5] M. Bouhalleb, H. Abbassi, Numerical Investigation of Heat Transfer by CuO–Water Nanofluid in Rectangular Enclosures, Heat Transf. Eng. 37 (1) (2015) 13–23.

[6] G.G. Momin, Experimental investigation of mixed convection with water–Al2O3& hybrid nanofluid in inclined tube for laminar flow, Int. J. Scientific Technol. Res. 2 (2013), 195–202.

[7] M. Afrand, D. Toghraie, B. Ruhani, Effects of temperature and nanoparticles concentration on rheological behavior of Fe3O4 –Ag/EG hybrid nanofluid: An experimental study, Exp. Therm. Fluid Sci. 77 (2016) 38–44.

[8] A.S. Dalkılıç, Ö. Açıkgöz, B.O. Küçükyıldırım, A.A. Eker, B. Lüleci, C. Jumpholkul, S. Wongwises, Experimental investigation on the viscosity characteristics of water based SiO2-graphite hybrid nanofluids, Int. Commun. Heat Mass Transf. 97 (2018) 30–38.

[9] B. Takabi S. Salehi, Augmentation of the Heat Transfer Performance of a Sinusoidal Corrugated Enclosure by Employing Hybrid Nanofluid, Adv. Mechanical Eng. 6 (2014) 147059.

[10] A. Eringen, Theory of Micropolar Fluids, Indiana University Mathematics Journal, 16 (1) (1966) 1–18.

[11] T. Ariman, M.A. Turk, N.D. Sylvester, Applications of microcontinuum fluid mechanics, Int. J. Eng. Sci. 12 (4) (1974) 273–293.

[12] G. Lukaszewicz Birkhauser,Micropolar Fluids: Theory and Applications. 1999. 252 pp. ISBN 3 7643 4008 8. DM 14, J. Fluid Mechanics 401 (1999) 378–381.

[13] A. Abidi, M.N. Borjini, Effects of Microstructure on Three-Dimensional Double-Diffusive Natural Convection Flow of Micropolar Fluid, Heat Transf. Eng. (2018) 1–48.

[14] G.C. Bourantas V.C. Loukopoulos, Modeling the natural convective flow of micropolar nanofluids, Int .J. Heat Mass Transf. 68 (2014) 35–41.

[15] N. Putra, W. Roetzel, S.K. Das, Natural convection of nano-fluids, Heat Mass Transf. 39 (8–9) (2002) 775–784.

[16] A. Hussanan, M.Z. Salleh, I. Khan, and S. Shafie, Convection heat transfer in micropolar nanofluids with oxide nanoparticles in water, kerosene and engine oil, J. Mol. Liq. 229 (2017) 482–488.

[17] M. Mollamahdi, M. Abbaszadeh, G.A. Sheikhzadeh, Flow Field and Heat Transfer in a Channel with a Permeable Wall Filled with Al2O3-Cu/Water Micropolar Hybrid Nanofluid, Effects of Chemical Reaction and Magnetic Field, J. Heat Mass Transf. Res. 3 (2016) 101-114.

Large Eddy Simulation of natural exhaustion effect in a corridor fire using vertical duct

Imen Ben Abdellaziz[#1, *1], Mourad Bouterra[#2], Afif El Cafsi[#3]

[#1]*Physics Department, Laboratory of Energetics, Thermal and Mass Transfers (LETTM),*
University of Tunis El Manar, Faculty of Sciences of Tunis, El Manar II, 2092, Tunis, Tunisia.

[*1]*Hafr Al Batin University, Kingdom of Saudi Arabia*

benabdellazizimen@gmail.com, Mourad.Bouterra@gmail.com;elafif.k@gmail.com

Abstract— **Both numerical and theoretical study on a vertical exhaustion efficiency in a corridor fire and state stratification behaviours of the smoke under different duct sections and heights were conducted. Results show that the mixing process, the stack effect and the plug-holing are the dominating factors on the natural ventilation efficiency. There exists an optimal duct section, such as the hot smoke will be adhered to the upstream and the downstream walls of the duct. The 2D flow pattern in near region could be used to improve the efficiency process of the natural disastrous smoke exhaustion. In this case we obtained the maximum efficiency at about 82.1 %. It was found also that during the plug-holing effect, the smoke layer is completely destroyed were the downstream layer is predicted by the stratification parameter evolution. The temperature at upper height approachs to the lower temperature layer and the "$S_{nw,dow}$" shows an important decreasing ("$S_{nw,dow} < 1$"). So, the stratification become unstable. This work is beneficial for safety evaluation and optimization design of tunnel safety engineering using natural exhausting duct effect.**

Keywords— Tunnel fires, natural smoke exhaustion, LES, Stratification.

I. INTRODUCTION

Several catastrophic fires have occurred in the past decade. Examples of such fires include the corridor-like structures [1-3] and other include the tunnel fire. Generally, a tunnel fire is a complex flow phenomenon that depends on many factors as the geometry of tunnel and the ventilation system. It can be considered as a possible idea of applying similar a model to the corridor modeling structure. In case of tunnel fire, the hazardous gas diffuses and spreads widely over this confined space, causing a disastrous suffocations and leading to catastrophic loss of human lives. Statistics have shown that smoke is the most hazardous factor in tunnel fires as it was even the cause of dramatic events such as the case of the Mont-Blanc (39 deceases), the Tauern (11 decades) and the Gotthard (12 decades) tunnels [4]. The propagation of smoke combustion is likely depending on the ventilation systems that are set up in the tunnel. Tunnel ventilation systems fall into two main categories. The natural ventilation and the mechanical ventilation. The design of mechanical ventilation system needs more place for the installation and increases the operation of the utility bills. However, the natural ventilation using vertical duct consumes less power in addition of naturally-occurring forces employment.

In tunnel fire research, the buoyancy-driven smoke flow layering length beneath the ceiling by point extraction and longitudinal ventilation combination [5], the ventilation performance realization by mechanical exhaust system [6, 7] have been widely studied. The temperature distribution and stratification of smoke in a tunnel at 1-D propagation phase with variation of

ISSN: 2961-6611

the ventilation strategy are conducted by Kalech et al. [8]. They found that in case of a transversal ventilation strategy, the smoke layer is maintained below the ceiling, between the two openings A and D, at height 20% of h from the ceiling. The smoke flow is perfectly stratified. Vauquelin and Mégret [9], have investigated experimentally the smoke extraction of a transverse ventilation system. The tunnel is equipped with two ducts located one on either side of a fire source in order to study the influence of their location and their shape on the exhaust system efficiency in a first step, then the effect of the fire heat release. They conclude that the efficiency of 100 % is reached for 10 and 20 MW.

With the methods development used to design a ventilation system, the benefit characteristic of the natural ventilation system with vertical duct has become more and more attractive. The position of ventilation system can be conducted using full-scale tests which require very large.

Ji et al. [10], were analyzed numerically by Large Eddy Simulation (LES), the influence of cross-sectional area and aspect ratio of duct on natural ventilation. He demonstrated that when the cross-sectional aspect ratio increases to a certain value, the hot smoke will be adhered to the upstream wall of the duct that will be exhausted through the upstream region and this latter is predicted by using the 2D flow pattern interpretation. Zhong et al. [11] numerically analyzed (by the code Fire Dynamic Simulator (FDS.5)) the smoke flow characteristics of a road tunnel fire under the combined function of a longitudinal wind and stack effect of duct. The effect of vertical duct height on natural ventilation is investigated experimentally by Ji et al. [3], two special phenomena plug-holing and turbulent boundary-layer-separation was influenced by the effect of smoke exhaustion. He et al. 2023 [12] studied the behaviour of air supply in tunnels with multiple vertical shafts during fire incidents, focusing on natural ventilation dynamics. Result show that the position of the smoke front significantly influences the direction and flow rate of gases during fire development. The mass flow rate of air supply during the stable fire development stage is influenced by the geometric size and positioning of vertical shafts, with shafts closer to the fire source exhibiting higher air flow rates.

Currently, many studies have conducted a particular research on stratification state based on natural exhaustion effect by vertical duct. The buoyant flow stratification behaviour is studied by Tang et al. [13] based on instability criterion for the smoke layer in tunnel fire with complex combination of longitudinal ventilation and ceiling extraction. The Richardson number is predicted where the buoyancy and inertial forces are the two important factors influencing the buoyancy stratification. They found that the stratification became unstable with a strong mixing flow when $(Ri < 1.4 \; or \; Fr > 0.8)$. The smoke stratification behaviors caused by fire and outdoor wind is experimentally predicted by Huang and Li [14]. In order to to describe the layering properties, Froude number was proposed and a correlation for the stratification characteristic of smoke was defined as follow:

$$\frac{\Delta T_{cf}}{\Delta T_{avg}} = 70.43 \, exp\left(-\left(\frac{Fr+4.357}{2.427}\right)^{2}\right) \qquad (1)$$

In all the previously cited results, the parametric conditions of a vertical duct system in the tunnel roof on natural ventilation efficiency have not been completely addressed and discussed. Therefore, in order to investigate the natural ventilation efficiency using vertical duct, the method of Large Eddy Simulation (LES) was adopted and two scenarios were stimulated respectively: The variation of the duct section and the duct height. The term of efficiency is calculated first with the flow field pattern description. Then, a criterion for the stratification state is also studied were critical conditions to maintain the downstream smoke stratification are numerically analyzed. The objective of this research is to focus on the smoke exhaustion efficiency by natural ventilation and improve the best duct parametrical condition to obtain an excellent performance for the vertical duct control respecting the state stratification of the smoke based on a new criterion for the smoke stability control.

II. NUMERICAL TECHNIQUES

A. *Physical Model Setup*

The physical domain under investigation is shown in Fig. 1, which simulated a fire in a tunnel and consisted of two principal units, the tunnel and the duct (Fig. 1 (b)). For the realization of their numerical experiments, the authors used the geometry shown in fig. 1 [3]. Initially, we follow the same pattern with the same boundary conditions for the comparison of results. The experiments were conducted in a small-scale model with a ratio of 1:6 [3]. The tunnel is 6 m long, 2 m wide and 0.9 m high. The duct is set up 4.2 m away from the left side (Fig. 1) and is topped vertically in the ceiling with a size of (0.3 m, 0.3 m, 0.8 m). The internal lining of the tunnel and duct are specified as ‘‘CONCRETE’’. The physical properties of this material are specified in the FDS model based on data provided by FDS. The top of the duct and tunnel entrance are naturally open, without initial speed. The initial temperature of tunnel wall is set to be 20 °C. Fire is simulated by a source placed at 1.2 m (Fig. 1) away from the left opening of the tunnel. Fire power is determined by the command heat release rate per unit area “HRRPUA’’ provided in FDS. The dimension of the source of fire is (0.2 m × 0.2 m) with a size HRR (The heat release rate of the fire) of 20.21 KW [3]. In this study, the HRRPUA is steady for all simulations.

Figure 1 (b) illustrates the duct provision in the tunnel ceiling and the schematic diagram of the model with FDS simulation is shown in Fig. 2. As it is shown in Fig. 2, the total area of the tunnel with the duct system, the “OPEN” boundary condition for the left direction of the tunnel and the fire source (with the color red) localization are very clearly illustrated by FDS simulation. Fig. 2 presents also the different transverse planes (with the color green) for several longitudinal displacements along the tunnel which are required to calculate the convective HRR in the upstream (the left direction of the source zone) and the downstream directions (the right direction of the source zone) of the source zone in addition the upstream (the left direction of the duct) and the downstream (the right direction of the duct) directions of the duct emplacement. The objective is to prove the efficiency of an exhaust duct (see part 3) by changing its geometry.

In order to investigate respectively, the influences of the duct section and height, we are simulated two series of fire-scenarios. First, we fixed the duct height as 0.8 m and we will be varied the section from 0.01 m^2 to 0.36 m^2. Second, the section is fixed 0.09 m^2 (0.3 * 0.3), then, the height is changed from 0.1 m to 1 m.

B. *Fire Dynamics Simulator*

The application of the computational fluid dynamics (CFD) technology to analyze problems involved in three-dimensional flows in tunnel fire [15] has become possible with the development of (CFD) and the advent of increasing computer power. CFD codes such as FDS was previously used for tunnel issues (fire and ventilation) [11]. The Fire Dynamics Simulator (FDS) [16, 17], developed at NIST (National Institute of Standards and Technology), USA, is a model of fire-driven fluid flow, coded for this work in Fortran input record and run from the command prompt. Its accuracy has been validated in many tests [18, 19]. The mathematical description refers to the FDS technical guide [17]. Based on the Hydrodynamic Model [16, 17], FDS solves numerically a form of the Navier-Stokes equations appropriate for low speed, thermally-driven flow with an emphasis on smoke and heat transport from fires.

ISSN: 2961-6611

The turbulence model of FDS includes Direct Numerical Simulation (DNS) and Large Eddy Simulation (LES). In this study, we chose the LES model, due to its intensive user to simulate the problem of the tunnel fire and the development of the disaster smoke.

The Smagorinsky in LES simulation is flow dependent and sets as low as possible to maintain numerical stability. It has been optimized over a range from 0.1 to 0.25 for various flow fields [20]. Two points should be considered in the prediction of the smoke movement by LES [16, 17]: The fine enough grids and the suitable sub-grid model (SGM) on small eddies. The Sub-Grid-Model (SGM) which is applied in LES, is carried out by Smagorinsky [21]. The eddy viscosity is defined as the equilibrium between the energy production and dissipation (the small scales). The turbulent viscosity defined in FDS by [16,17]:

$$\square_{LES} = \square(c_s\square)^2[2\bar{S}_{ij} : \bar{S}_{ij} \; \square \; \frac{2}{3}(\square.u)^2]^{1/2} \qquad (2)$$

Where C_s is the empirical Smagorinsky constant, Δ is $(\delta x \delta y \delta z)^{1/3}$ and the term $\bar{S}$ consists of second-order spatial differences averaged at the grid centre.

The thermal conductivity k_{LES} and material diffusivity D_{LES} of the fluid are related to the viscosity μ_{LES} in term of the Prandtl and Schmidt numbers by:

$$k_{LES} = \frac{c_p \, \mu_{LES}}{Pr}, \qquad (\rho D)_{l,LES} = \frac{\mu_{LES}}{Sc} \qquad (3a, 3b)$$

The numbers of Prandtl and Schmidt are assumed to be constant. The specific heat, c_p is taken to be that of the dominant species of the mixture [16, 17]. According to many validation works, the constants C_s, Pr and Sc are defaulted in FDS as 0.2, 0.2 and 0.5 [16], respectively. In our study, and in order to set these parameters, we tested many values. The 0.2 for the C_s number and 0.2 for the Pr number allowed for a fusty convergence of the model [11, 22].

The Courant-Friedrichs-Lewy (CFL) criterion is used in FDS for justifying numerical convergence. It is more important for large-scale calculations where the time step is constrained by the convective and diffusive transport speeds. So, the estimated velocities are tested at each time step to ensure that the CFL is satisfied via this condition [17]:

$$\delta t.\max\left(\frac{|U_{ijk}|}{\delta X}, \frac{|V_{ijk}|}{\delta Y}, \frac{|W_{ijk}|}{\delta Z}\right) \cdot 1 \qquad (4)$$

Where U_{ijk}, V_{ijk} and W_{ijk} are respectively the velocity vector in x, y and z-axis direction. δX, δY and δZ present the dimensions of the smallest grid cell in x, y and z direction.

The time step is eventually changed to a quasi-steady value when the fire burns steadily. The numerical analysis results are sensitive to the grid size used.

C. Validation of Results

FDS is a fire spreading and smoke transport simulation software widely used in tunnel, corridor and stations. Engineers must have a good understanding on the physics behind, so that results can be judged appropriately. Therefore, before making the numerical simulation, it is necessary to make the validation of the numerical code and to analyze the mesh nature because it presents a key parameter to be considered. Also, it is necessary to make a sufficiently fine mesh in order to obtain a more accuracy results. However, an excessively fine mesh leads to a long time step. Certain rules are applied here in terms of the sizes and the shapes of the cells in order to limit the numerical errors.

The $\frac{D^*}{\delta x}$ criterion has been widely used for assessing the grid resolution [16, 23]. The characteristic length of D^* is calculated by:

$$\left(\frac{\dot{Q}}{\rho_\infty c_p T_\infty \sqrt{g}}\right)^{2/5} \tag{5}$$

c_p is the specific heat capacity and $\dot{Q}$ is the heat release rate. The quantity $\frac{D^*}{\delta x}$ can be thought of as the number of computational cells spanning the characteristic diameter of the fire. According to a large number of domestic and foreign scholars, the values of $\frac{D^*}{\delta x}$ ranging from 4 to 16 give good simulation results [16, 24]. Also the grid size of the finest mesh for a 4 MW fire was calculated to be between 0.1 m and 0.4 m [25].

In this paper, four different mesh sizes ranging from 0.1–0.2 m are chosen for comparison. Figure 3 illustrates the distribution of the vertical temperature in the corridor with different grid sizes. It presents the confrontation of our numerical simulation to the experimental result [3]. It is very clear that with the mesh density increasing, the temperature curve trends to be uniform. The result of mesh (A) with 0.2 m is the lowest (A1). The numerical points are far from the experimental points. A2 is the higher curve, with 0.1 m mesh density. There is here more time consuming. The mesh with 0.187 m (A4) provide a good confrontation between the point measurements. A multi-mesh system (A3) with grid size of 0.2 m at the zone source and the duct-system and 0.187 m in the other regions, presents the best curve. There is more coincidence between the experimental and the numerical points. Also, less time consuming is obtained. Hence, we choose this multi-mesh system (A3).

It is very clear that in case of thermocouple tree at h = 0.85 m, the temperatures rise sharply from the ambient temperature to the values of (52 °C - 59 °C) at about 150 s. Then, it keeps stable at the range of (60 °C – 65°C) until 300 s. This latter can be explained by the fact that the upper part of the thermocouple is located in the smoke layer at the upper part of the tunnel. For example, we can notice that the temperature achieves at about 60°C at 300 s [3]. However, our numerical result finds out 64°C. A good agreement was obtained.

It can be conducted also from this Fig. 3 that the total time step is 300 s. The time step is eventually changed to a quasi-steady value when the fire burns steadily. The steady state corresponds to 180 s - 300 s. The regime is realized under this period. So, all our results are extracted and so examined in this time (between 180 s - 300 s).

III. NATURAL EXHAUSTING EFFICIENCY

In order to ameliorate the natural extraction process during tunnel fire, the separation interface between the tunnel and the exhaustion system should be reduced as little as possible. So, the amount of air which is penetrated into the smoke or drawn directly into the duct from the lower layer must be very small. In case of natural ventilation control, the 100% efficiency will be achieved only by increasing the convective heat release rate (convective HRR) of the smoke extract system. So, the convective HRR of smoke exhausted by the duct can be regarded as a key factor to judge if the natural ventilation process is effective.

Vauquelin and Mégret [9], defined the efficiency of an extract duct to characterize the transverse ventilation system. It constitutes the ratio of the extracted smoke VFR (Volume Flow Rate) to the produced smoke VFR and can be expressed as follows:

$$\varepsilon = \frac{Q_{es}}{Q_s} \tag{6}$$

ISSN: 2961-6611

In this study, a simple definition will be conducted for the design of the smoke exhausting effect. It has similar physical meaning with Vauquelin and Mégret application. However, there is an evidently new modification. The objective is to evaluate the natural performance effect of a vertical duct in a corridor fire.

The method is based on convective HRR calculation under different planes for several transversal displacements along the tunnel. Each plane is illustrated by a matrix for component of temperature and velocity calculation in the j and k direction (T_{jk} , V_{jk}) as it is presented in Fig. 2.

The term of ''efficiency'' of the smoke exhaustion can be calculated through the following equation:

$$Ef = \frac{HRR_{exh}}{HRR_{pro}} \quad (7)$$

Were, $$HRR = \iint U\,[T - T_a]\,d\sigma = \sum_{jk} U_{jk}\,[T_{jk} - T_a]\,\Delta Y \Delta Z \quad (8)$$

The different quantities can be calculated are:

- The $HRR_{pro\,(ups)}$ is the produced HRR calculated in the upstream (the left direction of the zone source) direction.
- The $HRR_{pro\,(dow)}$ is the produced HRR calculated in the downstream (the right direction of the zone source) direction.
- The HRR_{exh} is the exhaust HRR calculated under the smoke vent (the limit area between the duct and the tunnel roof).
- The HRR_{rsd} is the residual HRR calculated in the downstream direction of the duct location.

Where U_{jk} and T_{jk} are the longitudinal component velocity and the temperature respectively calculated in each plane, T_a is the ambient temperature and σ is the cross-section area for each considered plane.

For each simulated case, we kept the same measurement point to calculate the $HRR_{pro\,(ups)}$ (1.7 m), and the $HRR_{pro\,(dow)}$ (3.85 m), however, the HRR_{exh} and the HRR_{rsd} will be changed from one case to another.

So, for the two different fire scenarios, the duct efficiency is determined depending on the (HRR_{exh}) and is calculated using the Eq. 10.

IV. RESULTS AND DISCUSSIONS

A. *Influence of the Duct Section*

1) Exhaust efficiency of duct

Figure 4 presents the efficiency of the duct at different cross-sections of 0.01 m^2, 0.04 m^2, 0.09 m^2, 0.16 m^2, 0.25 m^2 and 0.36 m^2. From the figure, we can observe that the efficiency increases with the increase of the duct section. This rising features an exponential behavior. This is well observed in the study of Vauquelin and Mégret [9] in order to investigate the efficiency and the relative VFR for different duct locations. It is very clear that the maximum efficiency is reached in case of the bigger duct (s = 0.36 m^2) and it is far from being obtained (82.1 %). It can be noticed that there exists a low entrainment effect of air fresh through the limit area between the tunnel roof and the duct bottom. This can be explained by the fact that when the horizontal velocity of the smoke flowing into the duct becomes higher, the stack effect causes a weaker induction of a vertical inertia force and the smoke flow becomes controlled by the horizontal component. As a result, a small quantity of fresh air will be extracted from the duct were the active smoke exhausting region can slightly decrease. Consequently, 4/5 of the total efficiency of the smoke exhausting is obtained.

ISSN: 2961-6611

2) Flow field pattern

In this sub-section, we will intend to examine the flow field pattern in the tunnel and the duct in order to improve the phenomena that are occurred along the smoke exhausting effect with the duct section variation and caused the decrease of the natural smoke extraction process.

Figure 5 shows the distribution of the temperature for three different section (s = 0.04 m^2, s = 0.16 m^2, and s = 0.36 m^2) in tunnel and the duct were the left side presents the duct-system.

As shown in Figs.5(a), when the disturbance on smoke layer interface starts to break the stability of the smoke induced by the smaller vertical inertia force effect, a bit quantity of fresh air mixed into the smoke layer and a very small hollow (leakage area) under the smoke vent appears. The particles of smoke found a big problem to enter in to the duct because the upper point of leakage region is still smaller than the installing point in the downward ceiling part. The only small quantities that can include it are founded so closed to each other and will be blocked in the bottom and the middle section. The smoke is unable to separate from this region and then to exhaust through the duct section of 0.04 m^2. So, this is the cause of the smoke exhausting inefficiency in this case as it is shown in Fig.4. However, in case with duct section larger than 0.04 m^2, and under the average driving effect of the vertical inertia force, it is very clear that the highest points of the smoke-hollow (hollow in the smoke layer) appear more clearly (Figs.5(b) and 5(c)). These leakage areas are circulated with the color red in Fig. 5 and namely “the sunken areas”. The lower limit layer starts to interact with the upper area of the tunnel center where the flow speed increases rapidly with the duct section increasing and leads to the mixture process between the two species. When the smoke layer thickness below duct weakness, the highest point enters into the middle of the duct and the mixed fresh air with smoke is drawn into the duct bottom. As it is shown in Fig.5(b) and in the lower part of the duct section of 0.16 m^2, the temperature in the left region from the tunnel ceiling and the lower duct area are about 61°C and 60°C respectively. There exists also an area where the thermal field reaches the 39°C value in the right region of the tunnel roof. However, the temperature keeps the value of 36°C in the lower duct from the right area. We can easily confirm an entrainment of a proportion of fresh air from the tunnel center into the right duct region which will be the cause of the temperature decrease in this area. Consequently, we obtain an average smoke exhausting efficiency in case of the average duct section (Fig. 4 and Fig.5(b)).

As shown in Fig.5(c), the temperature at the ceiling level is almost equal to that at the duct bottom. For example, we can notice that the temperature reaches 61°C and 39°C in the left and in the right parts of the sunken area, respectively (case for S = 0.36 m^2). The lower part of the duct is also characterized by a similarity from the thermal field (61°C in the left and 39°C in the right sides). It is very clear that the smoke layer stratification is stable under the duct because there is a thicker smoke layer and the horizontal inertia force is high. That stability limits the mixed air penetration into the smoke layer from the left and the right direction and avoids the occurrence of the stack effect. However, under the action of the weak vertical disturbance, the mixture process becomes a bit stronger due to the smoke exhausting of the duct, and a portion of fresh air will be flowing into the duct center. An amount of air is exhausted through it and the other part remains stable between the thicker smoke layers in the medium. The rest keep spreading along the tunnel ceiling. Therefore, the smoke efficiency is relatively large in this case (See Fig.4).

So, when the higher hot smoke flows inside the duct without mixture with cold air (both the left and the right direction of the duct), it illustrates the shape of the adhered behavior of spill plume. It is similar to the adhered form of spill plume in big region of building. It can be regarded as the 2D flow pattern in near region.

Therefore, various cross-sections of duct issue in tunnel roof have been envisaged and have obvious influence on the flow field pattern behavior and natural ventilation performance of the duct. A small duct section will inhibit the smoke exhausting effect process, resulting in poor natural ventilation performance. With a medium duct section, we achieve the 60 %. While the duct with a large section, will bring a better exhaust effect. However, the 100 % of smoke exhausting process is not achieved because of the mixing phenomena emergence which leads to the hot smoke dilution.

B. Influence of the Duct Height

1) Exhaust efficiency of duct

Figure 6 shows the duct efficiency for different duct height. It can be observed that the efficiency seems to be varied linearly with the vertical height and slightly increased with the duct height increases. For the duct height bellow 0.7 m, the efficiency does not exceed the 36 %, indicating that the exhaust smoke efficiency based on height vertical duct below 0.7 m is not significant. When the duct reaches the height of 1 m, we obtained the maximum percentage (62.35 %) and the efficiency seems to be with an average value. It is very clear that the flow motion is controlled by the vertical inertia force of the smoke. The smoke layer interface is totally broken and a lot of fresh air can easily draw through the larger duct. So, the flowing smoke to the duct weakness progressively. The reason is that when the vertical inertia force is large, the fresh air beneath smoke layer is directly exhausted and plug-holing occurs, resulting in the duct efficiency reduction.

In the next part, we will prove the process of the plug-holing (based on the flow pattern analyses) and its impact on the smoke exhausting effect (reduction of the smoke exhausting effect).

2) Flow field pattern

In this sub-section, we will interest to plot the same contour as it is discussed in part 4.1.2, however with respecting the duct height variation. The temperature contours in the tunnel are located at a fixed plan (Y = 1) along the total length (X: 0 m – 6 m) and height (Z: 0 m - 0.9 m). In the duct, they are located at a fixed plan (Y = 1) along the total length (4.2 m – 4.5 m). However, the height is varied.

Figure 7 presents the distribution of temperature for different duct heights under S = 0.09 m^2. Results for duct heights of 0.4 m, 0.6 m, 0.8 m and 1 m are selected here. As it is observed in Figs. 7(a) and 7(b), the hollow form and the height of the sunken point progressively rises with the increasing of the duct height. When the height is 0.4 m, a weak vertical stream of air appears at the medium duct level where the temperature is about 24°C. However, it seems at about 29 °C at the top of the duct level. For H = 0.6 m, the limit area of the smoke layer interacts with the center area of the tunnel. The sunken area appears more again were a secondary vertical stream of air emerges progressively. In this case the smoke is naturally exhausted from the upstream and the downstream direction of the duct along the penetration effect. This exhausting is predicted as an adhered behavior of spill plume as it is presented in part 4.2.1. With the duct height increase, Figs.7(c) and 7(d) show that the disturbances on smoke layer interface are strong and the intensity of vertical stack effect involved by the current of toxic gas from the roof of tunnel into the duct-system is gradually increased. The smoke layer under the duct- tunnel contact becomes very thin and the stratification is broken. When a strong “sunken area” appears (a large hollow along the smoke layer) and the thickness of smoke layer under the contact area decreases to 0, the apex of the depression enters into the duct and the plug-holing occurs immediately, i.e. the fresh air is drawn directly into the duct from the lower area.

Fig.7(c) indicates the presence of two vertical air-streams which spread along the duct top and promote the weakness of the adhered spill plumes. There exists an area in the duct bottom were the temperature is about 25°C and about 36°C in the top area.

In Fig.7(d), the two vertical air-streams start to interact with each other at the upper part of the duct where the downstream adhered spill plume weakens more once again. Therefore, a lot of air is easily exhausted by the duct.

Thus, we can conclude that the flow pattern with duct height variation is immediately determined with the combined function of the assumption of 2D flow pattern in near region and the two vertical air-streams. These two effects are defined to improve the phenomenon of natural smoke extraction process in case of a vertical duct provision in the tunnel ceiling after the entrainment observed through the upstream and the downstream directions.

C. Smoke Stratification State

Smoke stratification is an important issue for evacuation and fire fighting in tunnel fires. If the smoke stratification in a tunnel section dissolves, tunnel users in this region could be in great danger. In no ventilation conditions by vertical duct-system, smoke exists on both sides of the fire, and good stratification could exist at the early stages. In the presence of natural duct provision, different mechanisms can disturb the stability of the smoke stratification as the mixing and the plug-holing effects which will be decrease the performance of the exhausting-duct. An empirical model for the smoke stratification in tunnels is studied by Demouge [26]. He presents the theory of the stratification state based on temperature distribution and he defined a stratification parameter as follow:

$$S = \frac{T_{ac} - T_{af}}{T_{avg} - T_0} \tag{9}$$

Where T_{ac} is the temperature of fluid at the hot layer level, T_{af} is the temperature at the cold layer level, T_{avg} is the average temperature and T_0 is the ambient temperature. He prove that the stratification parameter is a key factor to judge if the smoke stratification is stable and the critical condition to determine the stable smoke stratification is $S > 1.1$.

In this study, a new model of the stratification parameter is conducted. This model is based on temperature calculation at a level height of the person and the exactely layers disposition of the fresh air and the dangerous smoke. From this point of view, the temperature variation as a function of the tunnel height for the duct height of 0. 4 m is presented in Fig.8. We can easily confirm from this figure there exist two layers. The first layer constitutes the fresh air. It is located between 0 m and 0.73 m heights. The second layer presents the hot smoke. It appears under the ceiling between the height levels of 0.73 m and 0.89 m. This parameter is defined as follow:

$$S_{nw} = \frac{T_{ul,avg} - T_{ll,avg}}{T_{avg} - T_0} \tag{10}$$

Where $T_{ul,avg}$ is the average temperature calculated in the hot layer between the height level of 0.73 m and 0.89 m. It is defined as bellow:

$$T_{ul,avg} = \iint \left[T - T_{inrf} \right] \, d\sigma = \sum_{jk} \left[T_{jk} - T_{inrf} \right] \Delta Y \Delta Z \tag{11}$$

$T_{ll,avg}$ is the average temperature calculated in the lower layer between the ground and 0.73 m height. It is defined as bellow:

$$T_{ll,avg} = \iint \left[T \quad T_0 \right] \, d\sigma = \sum_{jk} \left[T_{jk} - T_0 \right] \Delta Y \Delta Z \tag{12}$$

T_{jk} is the lonjitudinal component temperature calculated in each layer and σ is the cross-section of each considered upstream and downstream layer. T_{inrf} is the longitudinal component temperature calculated in the interface zone at 0.73 m. It constitute the temperature transformation for the downward state to the upward state. T_{avrg} presents the average temperature calculated along the two hot and cold layers. T_a is the ambient temperature.

Figure.9 shows the relationship of $\frac{\Delta T_{ul,I}}{\Delta T_{ul,o}}$ and S_{nw} . The domain can be divided in to two regions. $\frac{\Delta T_{ul,II}}{\Delta T_{ul,c}}$ increased firstly and then stabilized with increasing S_{nw}. When S_{nw} > 1.1, $\frac{\Delta T_{ul,II}}{\Delta T_{ul,t}}$ maintained as 1 indicating that is an interface between region 1 and region 2. The mean temperature for the lower layer of the corridor was approximately equal to the ambient temperature. The stratification is obvious, and the stratification state is in Region 1. Otherwise, the stratification is unclear, and the stratification state is in Region 2.

The distribution of the stratification parameter "S_{nw}" in the upstream "$S_{nw,up}$" and the downstream "$S_{nw,dow}$" directions of the duct is shown in Fig.10 for three different duct sections (0.04 m^2, 0.16 m^2 and 0.36 m^2). It can be observed that while the section increased, the "$S_{nw,up}$" increased significantly. It seems to be greater than 1.1. This result indicate that the smoke stratification is clear. In the downstream direction, the stratification is stable for the smaller duct since "$S_{nw,dow}$" is greater than 1.1. With the increase of the duct section, the distribution of "$S_{nw,dow}$" decays and the degree of stratification decreases significantly. This is because the mixing of hot smoke and cold air is important. For example, when s = 0.01 m^2 and for X/H = 6.5, $S_{nw} = 1$. For the largest cross section, the stratification of smoke became more disordered because "$S_{nw,dow}$" seems to be less than 1.1. We take for example the case of the dimension less length of the tunnel is equal to 6.6, $S_{nw} = 0.8$, which might due to the continuous heat loss from smoke to the surroundings during the process of longitudinal spread, resulting in lower smoke temperature. So, the smoke stratification is unclear.

The distribution of the stratification parameter "S_{nw}" in the upstream and the downstream direction of the duct is shown in Fig.11 respecting the variation of the duct height. The height level of 0.4 m, 0.6 m, 0.8 m and 1 m are selected here. Result show that the smoke stratification was stable in the upstream direction (Fig.11a) of the duct for all the listed tests since "$S_{nw,up}$" is greater than 1.1. This is because the mixing of hot smoke and cold air is lower and a small part of the surrounding air is entrained into the duct upstream. With the particles-diffusion beginning and the entrainment upstream, the mixing process increases and the smoke layer stability decreases as it is shown in the part (4.1). It is clearly seen that the smoke stable-stratification in the downstream direction of the duct becomes shorter as the duct height increasing. Fig.11b reveals that for H = 0.4 m and when $\frac{X}{H} \in [5.25 - 5.6]$, the "$S_{nw,dow}$" seems to be above the critical value were the stratification is clear. Then, it decreased significantly in the range from 5.7 to 6.7 of the less dimension $\frac{X}{H}$. It can be predicted that due to the longitudinal decay of the smoke temperature after a certain distance from the fire source, the "$S_{nw,dow}$" is bound to fall below 1.1. At this time, the smoke stratification state will change from Region I to Region II. With the increase of the duct height (H = 0.6, H = 0.8), the major point of the "$S_{nw,dow}$" seems to be below 1.1 indicating that the stratification was destroyed. For the case with the higher duct (H = 1 m), the "$S_{nw,dow}$" shows an important decreasing trend along the longitudinal less dimension of the length, which might due to the directly entrainment of the ambient air during the plug-holing effect. The temperature at upper height, approaches to the lower temperature layer and the smoke layer is completely destroyed. So, the smoke layer stratification became unstable.

V. CONCLUSIONS

In this parametrical study, a set of numerical simulations were conducted to investigate the effect of the section and the height of a vertical duct system issue at the ceiling projection on natural smoke extraction efficiency in a corridor fires with Large Eddy simulation (LES). The analysis of these results has provided the following conclusions:

The duct height constitutes an essential factor to be considered. When the duct is very low, it becomes unable to exhaust the maximum smoke outlet; leading to a poor natural ventilation. With the height of duct increase, a stronger stack effect is formed. The reason is that when the vertical component of inertia force is large, the fresh air in the superficial region is immediately extracted and the phenomenon of plug-holing occurs. So, the natural smoke extraction is inefficient.

However, the section of the duct presents the major factor to achieve a better performance for natural ventilation. Evidently, the total efficiency is not reached even for the greater duct. This is the cause of the mixing process producing and the drawing effect of the diluted gas into the duct bottom. The weak vertical inertia force acts to ameliorate the indirectly dilution discharging of the smoke with the air throw the upper part of the duct, leading to a smoke exhausting decrease and consequently the efficiency of natural extraction process reduction.

So, for achieving an extracting HRR efficiency and consequently a natural ventilation performance, it must be used with precaution and alternatively a considerable duct section and height.

Figure and Figure Captions

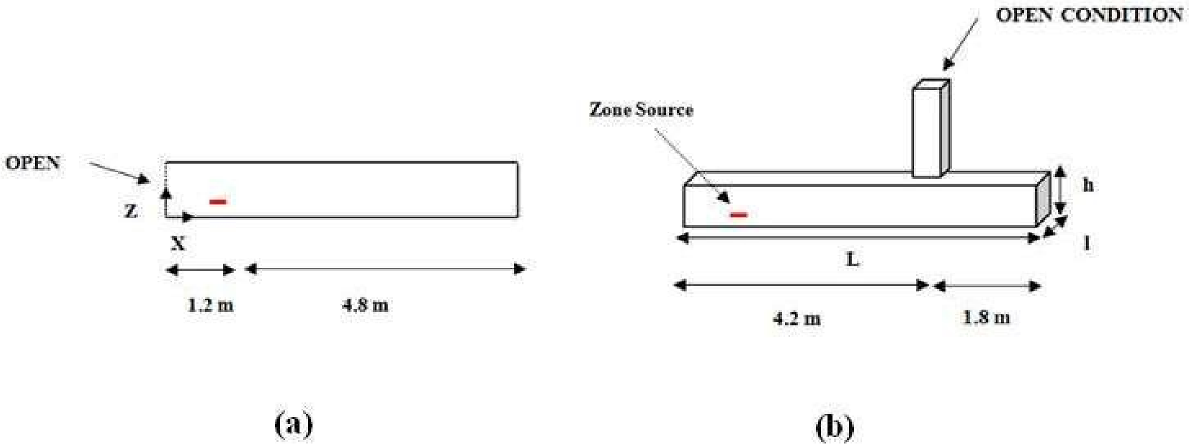

Fig. 1 The Schematic diagram of the model: (a) Corridor model; (b) Presence of the duct.

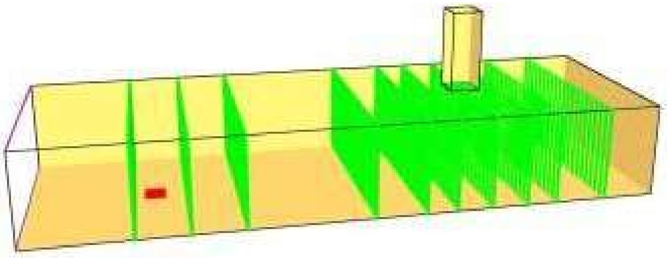

Fig. 2 Corridor topped by a duct system model established by FDS and the different transverse planes (The planes green are organized for the efficiency of the duct calculation) for several longitudinal X-displacements, with duct dimension of (0.3 m,0.3 m,0.8 m).

ISSN: 2961-6611

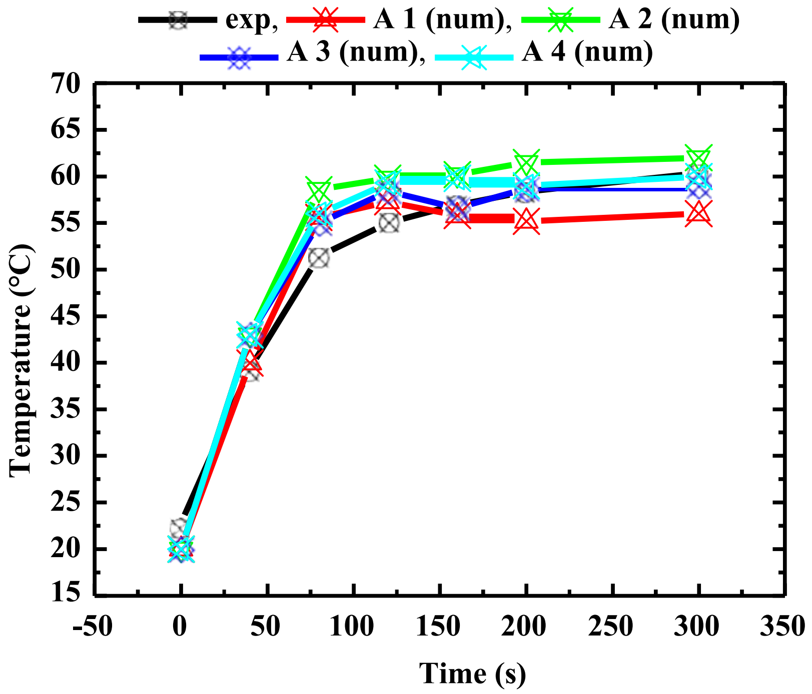

Fig. 3 The temperature distribution as a function of time (measured in the tunnel at 0.85 m height): Curve Validation & Sensitivity on the grid system with 0.2 m (mesh A1), 0.1 m (mesh A2) and 0.187 m (mesh A4).

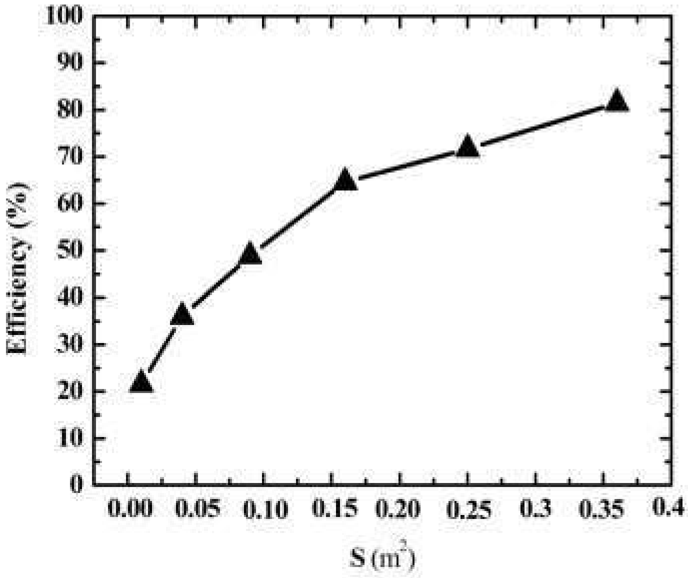

Fig. 4 Duct efficiency for different duct section.

Copyright © 2024
ISSN: 2961-6611

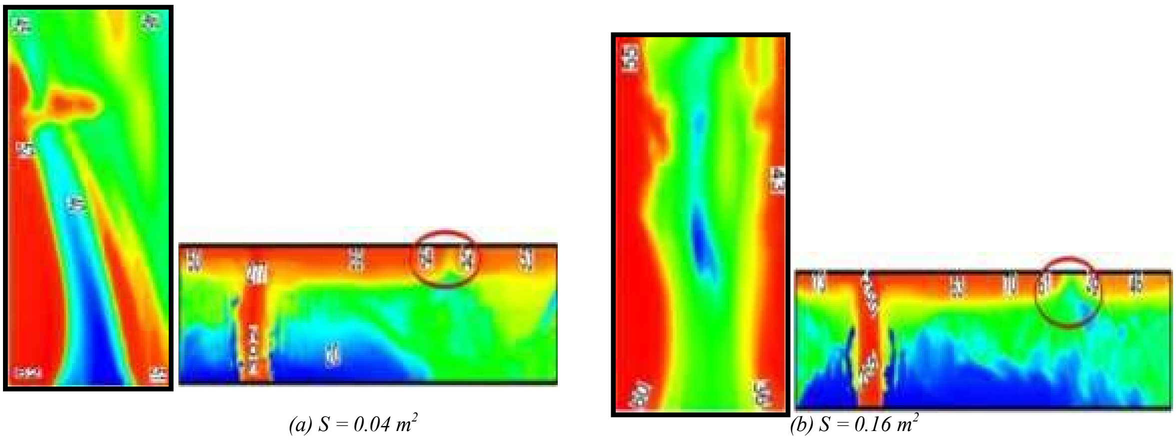

(a) S = 0.04 m^2 *(b) S = 0.16 m^2*

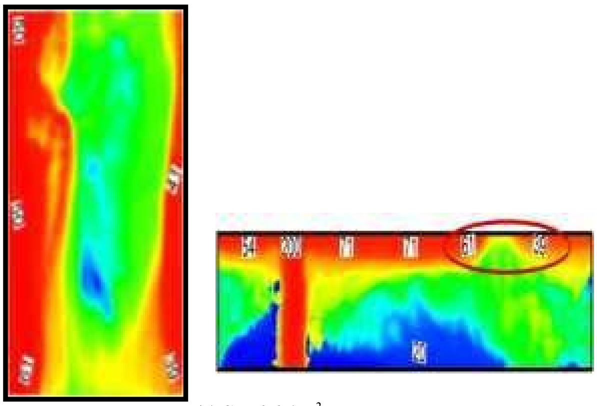

(c) S = 0.36 m^2

Fig. 5 Temperature Contour distribution for different duct section (5a: S = 0.04m^2, 5b: S = 0.16 m^2, 5c: S = 0.36 m^2) and in the lateral plan XZ (Y = 1) in the corridor (The zone sunken is circulated on red) and in the duct (In the left side: duct system; In the right side: the corridor).

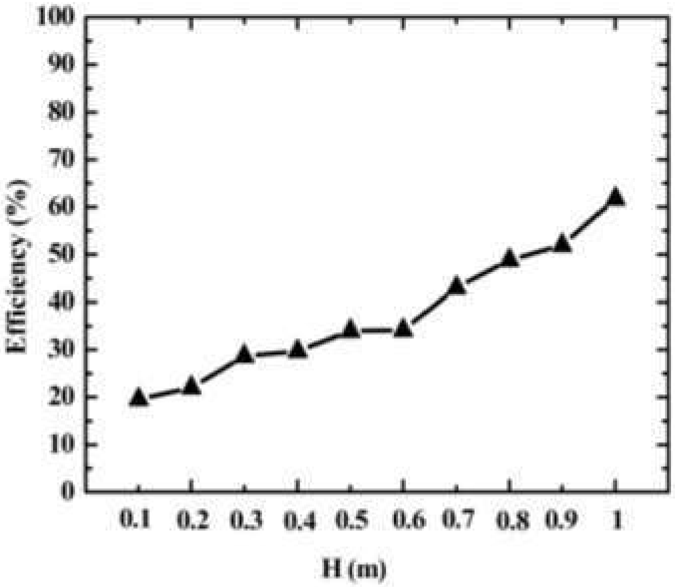

Fig.6 Duct efficiency for different duct height.

ISSN: 2961-6611

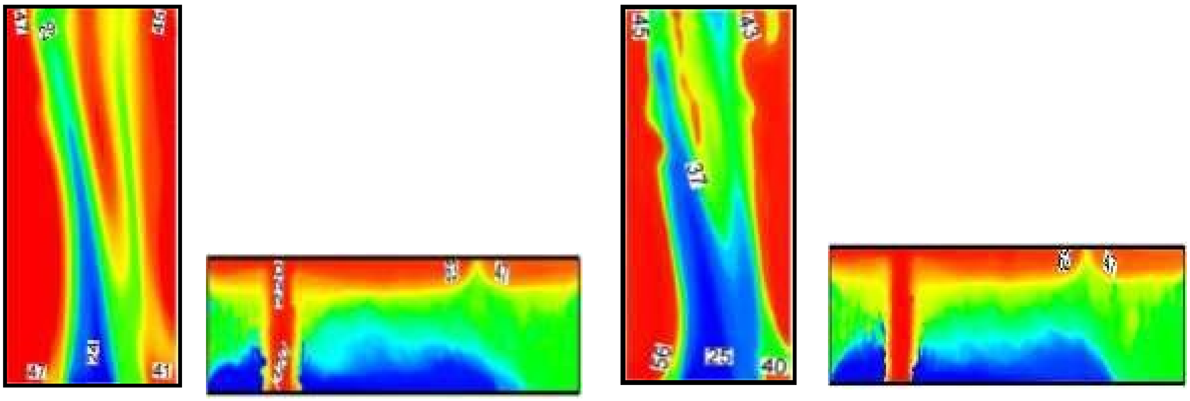

(a) H = 0.4 m

(b)H = 0.6m

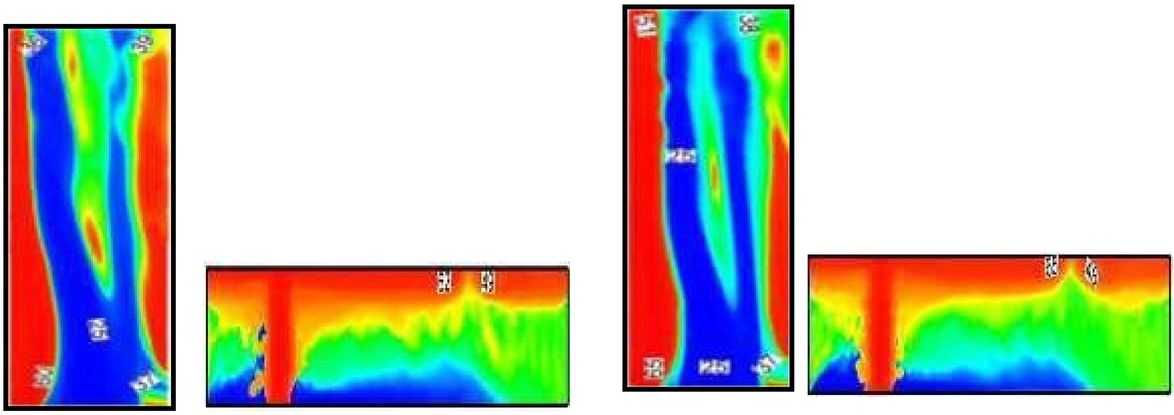

(c) H = 0.8 m

(d) H = 1 m

Fig. 7 Temperature contour distribution with various duct height (7a: H = 0.4 m,7b: H = 0.6 m, 7c: H = 0.8 m, 7d: H = 1 m) in the corridor and in the duct (In the left side: duct system; In the right side: the corridor).

ISSN: 2961-6611

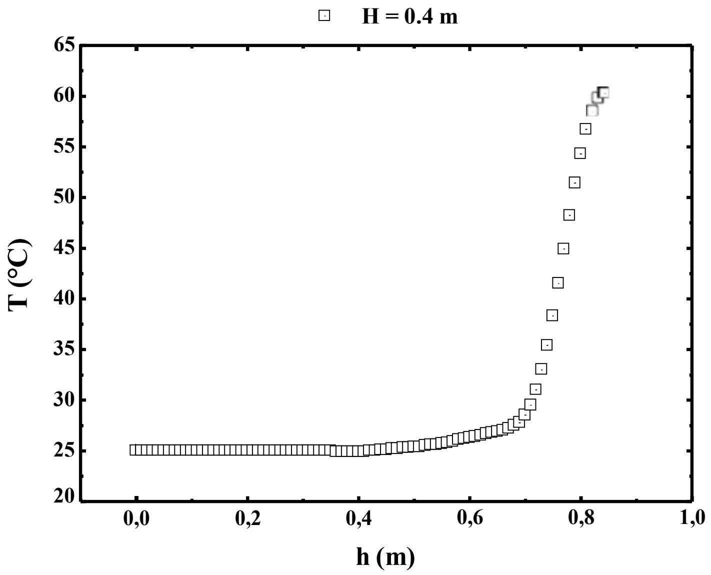

Fig. 8 Temperature distribution as a function of the corridor height: Illustration of the cold and the hot layers.

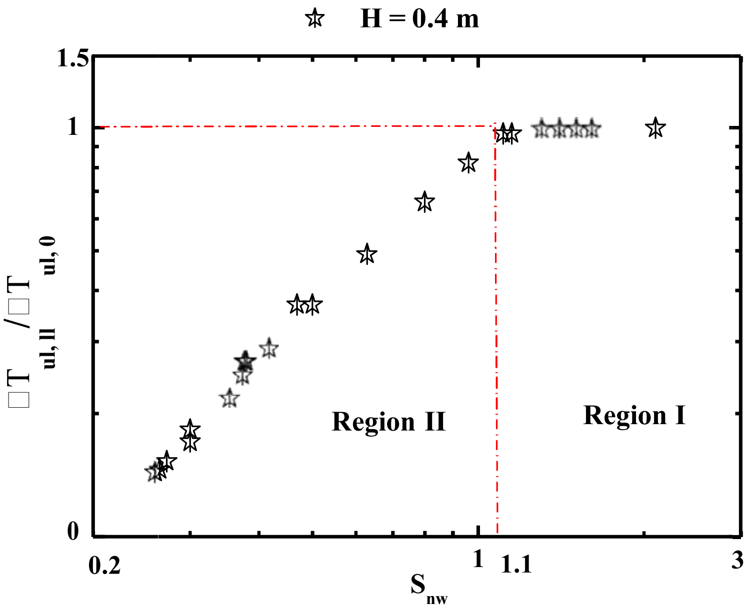

Fig. 9 Thermal stratification with a ceiling duct based on the new parameter $''S_{nw}'$:Illustration of the critical value

Copyright © 2024
ISSN: 2961-6611

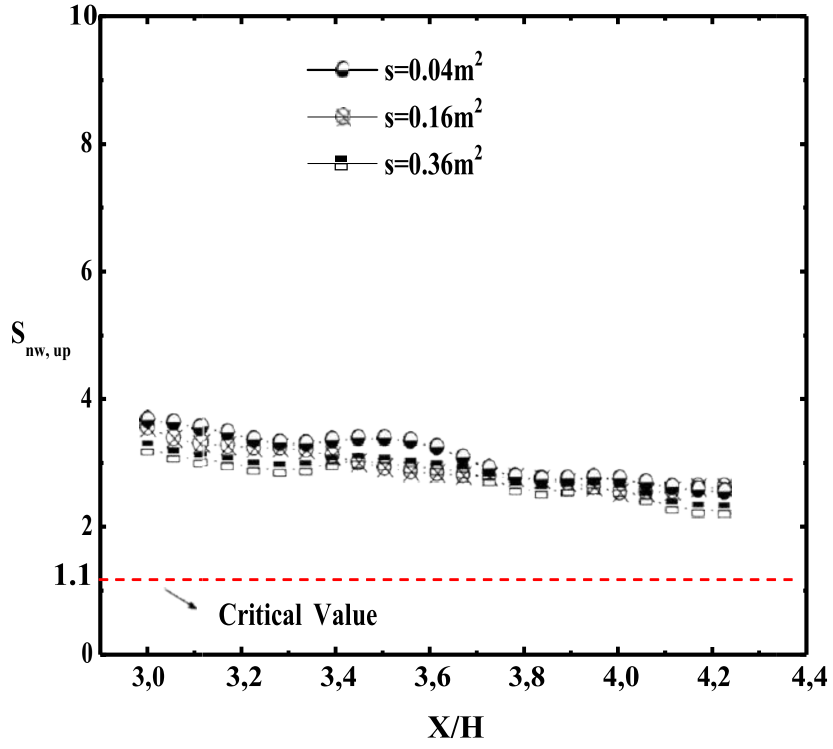

Fig. 10a The upstream evaluation of the new stratification parameter (the new model "S_{nw}") with the duct section variation.

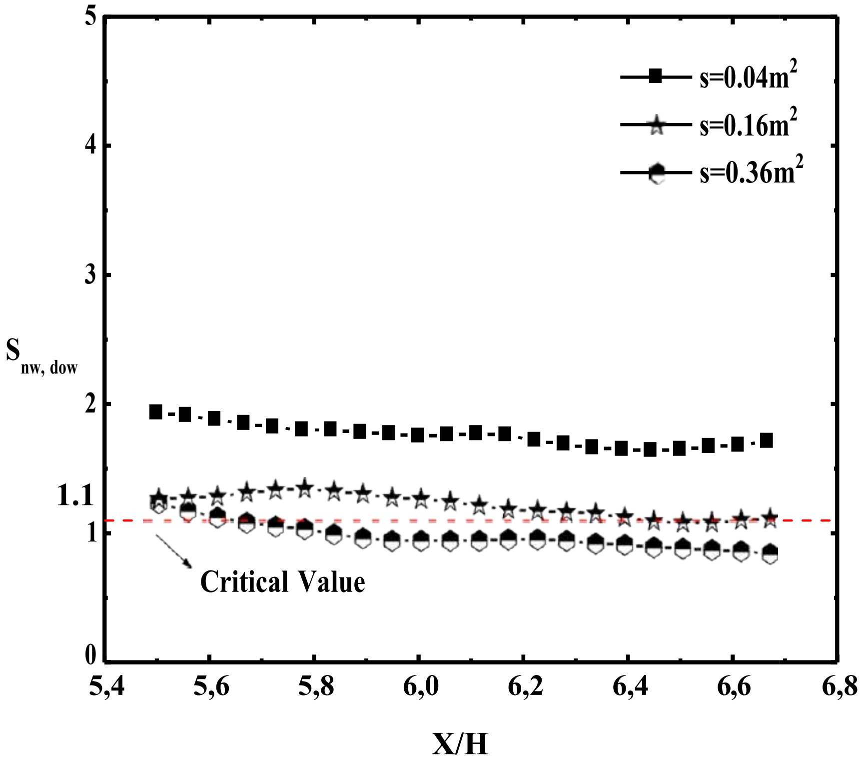

Fig. 10b The downstream evaluation of the new stratification parameter (the new model "S_{nw}") with the duct section variation.

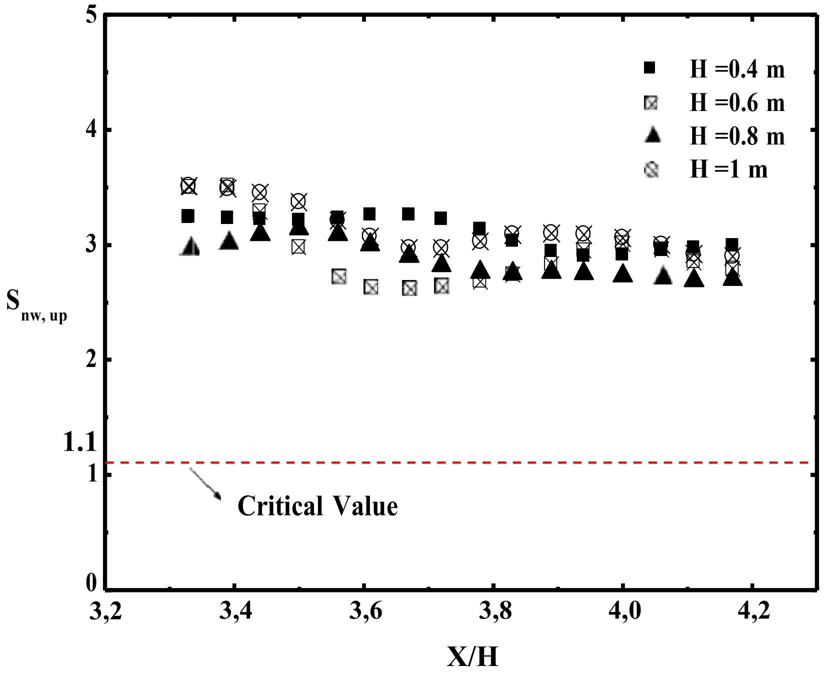

Fig. 11a: The upstream evaluation of the new stratification parameter (the new model "S_{nw}") with the duct height variation.

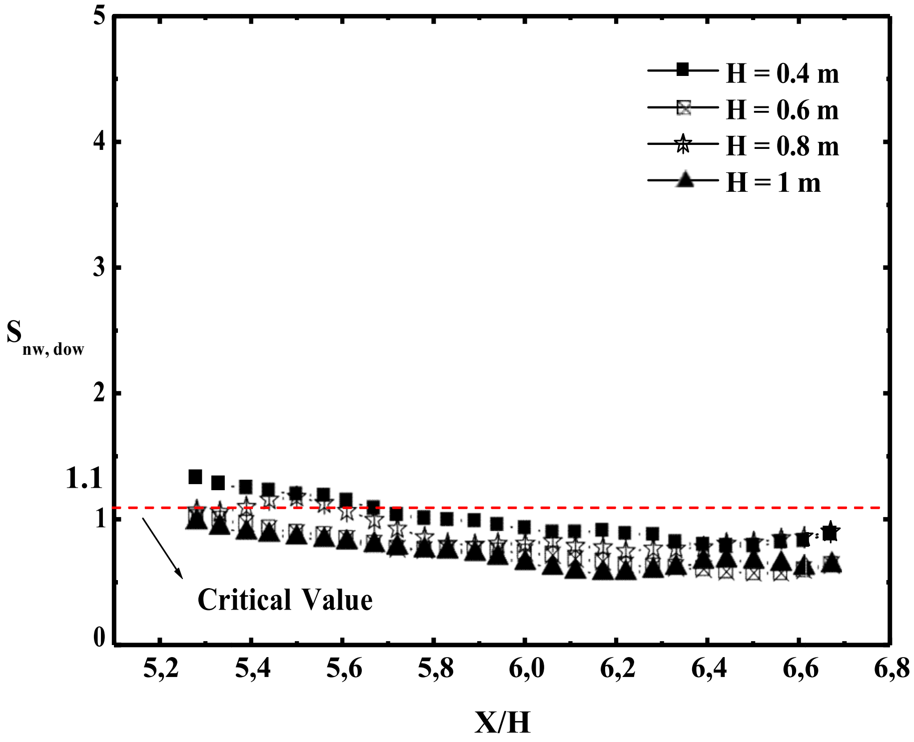

Fig. 11b: The downstream evaluation of the new stratification parameter (the new model "S_{nw}") with the duct height variation.

ISSN: 2961-6611

ACKNOWLEDGMENT

The main manuscript text and the prepared figure are written by Dr. Imen Ben Abdellaziz. Pr. Mourad Bouterra reviewed the manuscript.

REFERENCES

[1] C.H. Yoon, M.S. Kim, J. Kim, "The evaluation of natural ventilation pressure in Korean long road tunnels with vertical shafts," *Tunnelling Underground Space Technol*, vol. 21, pp. 3–4, 2006.

[2] J.F. Mao, J. Zhou, Y.L. Huang, Y.J. Yao, "Experimental study on temperature distribution under fire circumstance in natural ventilation city tunnel," *Refrigeration Air Conditioning & Electric Power Machinery*, vol. 1, pp. 1–4, 2009.

[3] J.Ji, Z.H. Gao, C.G. Fan, W. Zhong, J.H. Sun, "A study of the effect of plug-holing and boundary layer separation on natural ventilation with vertical shaft in urban road Tunnel fires," *Int. J. Heat Mass Transfer*, vol. 55, pp. 6032-6041, 2012.

[4] F. Vuilleumier, A. Weatherill, B. Crausaz, "Safety aspects of railway and road tunnel: example of the Lotschberg railway tunnel and Mont-Blanc road tunnel," *Tunnelling and Underground Space Technology*, vol. 17, pp. 153–158, 2002.

[5] L.F. Chen, L.H. Hu, W. Tang, L. Yi, "Studies on buoyancy driven two-directional smoke flow layering length with combination of point extraction and longitudinal ventilation in tunnel fires," *Fire Saf. J.*, vol. 59, pp. 94-101, 2013.

[6] J.Ji, L. Kaiyuanb, Z. Wei, H. Ran, "Experimental investigation on influence of smoke venting velocity and vent height on mechanical smoke exhaust efficiency," *J. Hazard. Mater*, vol. 177, pp. 209-215, 2010.

[7] C.C Hwang, J.C. Edwards, "The critical ventilation velocity in tunnel fires-a computer simulation," *Fire Saf. J.*, vol. 40, pp. 213-244, 2005.

[8] B. Kalech, Z. Mehrez, M.Bouterra, A. El Cafsi and A. Belghth, "Temperature Stratification in a Road Tunnel," *Thermal Science*, Vol. 20, pp. 223-237, 2016.

[9] O. Vauquelin, O. Mégret, "Smoke extraction experiments in case of fire in a tunnel," *Fire Saf. J*, vol. 37, pp. 525-533, 2002.

[10] J.Ji, J.Y. Han, C.G. Fan, Z.H. Gao, J.H., Sun, "Influence of cross-sectional area and aspect ratio of shaft on natural ventilation in urban road tunnel," *Int. J. Heat Mass Transfer*, vol. 67, pp. 420-431, 2013.

[11] W. Zhong, C.G. Fan, J. Ji, J.P. Yang, "Influence of longitudinal wind on natural ventilation with vertical shaft in a road tunnel fire," *Int. J. Heat Mass Transfer*, vol. 57, pp. 671-678, 2013.

[12] Lu He, Yuyang Ming, Ke Liao, Haojun Zhang, Chenhao Jia, Guoqing Zhu, Haowen Tao, "A study on the Behavior Characteristics of Air Supply during Tunnel Fires under Natural Ventilation with Multiple Vertical Shafts," *Fire*, vol. 6(10), pp. 393, 2023.

[13] F.Tang, L.J.Li, M.S.Dong, Q.Wang, F.Z.Mei, "Characterization of buoyant flow stratification behaviors by Richardson (Froude) number in a tunnel fire with complex combination of longitudinal ventilation and ceiling extraction," *Appl. Therm. Eng.*, vol. 110, pp. 1021-1028, 2017.

[14] Huang, D.F., Li, S.C., "An experimental investigation of stratification characteristic of fire smoke in the corridor under the effect of outdoor wind," *J. Wind Eng. Ind. Aerod*, vol. 179, pp. 173–183, 2018.

[15] A. Mos, B. Gay, "Phenomenological models for fire simulation in road tunnels," thesis, University of Claude Bernard-Lyon, 2005.

[16] K. Mc Grattan, R.M. Dermott, S. Hostikka, J. Floyd, "Fire Dynamics Simulator (version 5)-User's Guide, National Institute of Standards and Technology, Baltimore, Maryland, NIST Special Publication, 1019-5, 2010.

[17] K. Mc Grattan, S. Hostikka, J. Floyd, H. Baum, R. Rehm, W. Mell, R.M. Dermott, "Fire Dynamics Simulator (version 5)-Technical Reference Guide, National Institute of Standards and Technology, Baltimore, Maryland, NIST Special Publication, 1018-5, 2010.

[18] Hu, L. H., et al., "Modeling Fire-Induced Smoke Spread and Carbon Monoxide Transportation in a Long Channel: Fire Dynamics Simulator Comparisons with Measured Data," *J. Hazard. Mater*, vol. 140, pp. 293-298, 2007.

[19] Ying Zhen Li , Bo Lei, and Haukur Ingason, "Scale modeling and numerical simulation of smoke control for rescue stations in long railway tunnels," *Journal of Fire Protection Engineering*, vol. 22(2), pp. 101-131, 2012.

[20] J. Ji, Z.H. Gao, C.G. Fan, J.H. Sun, "Large Eddy Simulation of stack effect on natural smoke exhausting effect in urban road tunnel fires," *Int. J. Heat Mass Transfer*, vol. 66, pp. 531-542, 2013.

[21] J. Smagorinsky, "General circulation experiment with the primitive equations, I. The basic experiment," *Mon. Weather Rev.*, vol. 9, pp. 99-164, 1963.

[22] C.G. Fan, J. Ji, W. Wang, J.H. Sun, “Effects of vertical shaft arrangement on natural ventilation performance during tunnel fires,” *Int. J. Heat Mass Transfer*, vol. 73, pp. 158-169, 2014.

[23] J. Ji, C.G. Fan, Z.H. Gao, J.H. Sun, “Effects of vertical shaft geometry on natural ventilation in Urban road tunnel fires*,” J Civ Eng Manag.*, vol. 20, pp. 466–476, 2014.

[24] Y.Z. Li, H. Ingason, “Model scale tunnel fire tests with automatic sprinkler,” *Fire Saf J*, vol. 61, pp. 298–313, 2013.

[25] N.B. Kaye, G.R. Hunt, “Smoke filling time for a room due to a small fire: the effect of ceiling height to floor width aspect ratio,” *Fire Saf .J*, vol. 42 (2), pp. 329–339, 2007.

[26] F. Demouge, “Contribution to a numerical modeling of smoke stratification in case of a road tunnel fire,”doctoral thesis, University of Claude Bernard - Lyon 1, 2002.

Thermal and soluatl performance of micropolar nanofluid on a 3D enclosure saturated with porous media

Manaa Nessrin[#1], Abidi Awatef[*2], Mohammed Naceur Borjini[#3]

[#] *Research Laboratory of Metrology and Energy Systems, National Engineering School, Energy Engineering Department, Monastir University*
Monastir City, Tunisia.

[1]manaa_nessrin@outlook.com

[3]borjinimn@yahoo.com

[*]*Physics Department, College of Sciences Abha , King Khalid University,*
Abha City, Saudi Arabia.

[2]abidiawatef@yahoo.fr

***Abstract*— A numerical research on thermo-solutal natural convection of three-dimensional porous medium filled with microplar nanofluid. The Brinkman-Darcy model was employed. The finite volume method was chosen to discretized the governing equations. It found that when the micropolar model was present the heat and mass transfer rates decrease and the adding of nanoparticles favorites the flow fields. The enhancement of pertinent parameters such as Darcy and Rayleigh numbers, induces an increase on the flow intensity, the three-dimensional character and the average Nusselt and Sherwood numbers.**

***Keywords*—Thermo-solutal, natural convection, micropolar nanofluid, three-dimensional porous medium.**

I. INTRODUCTION

Usually, scientists and researchers are following to explore or find original method to improve heat and mass fields in thermal systems, by enhancement on the productivity of the heating systems, so reducing energy consumption and environment protection. In the recent years, convection heat transfer inside porous materials is more used in different systems. However, porous media was characterized with poor thermal conductivity, so this can cause limitations for the prospects of heat transfer enhancement in problems implicating fluid flow. Among the solutions found by researchers was adding solid nanoparticles to conventional liquids, it can help to increase fluid thermal conductivity. The nanoparticles dispersing into the ordinary fluid noted nanofluid. Therefore, the fusion of porous materials and nanofluids can be regarded as favorable approximation to reach substantial values of heat transfer. Alilat et al. [1] numerically investigated the free convection in an inclined porous cavity saturated by Cu-water nanofluid. They used the Aluminum foam such us the porous matrix material. The Darcy–Dupuit model was applied to characterize the flow in the porous media. They studied the effect of the governing parameters like Rayleigh number, nanoparticle volume fraction, the porosity, the inertial parameter, and the slope of the cavity. They obtained that the enhancement of nanoparticle volume fraction and the increase of porous medium porosity result a decrease in convection intensity. Jino and Kumar [2] performed a numerical work highlights the non-linear effects of natural convection on heat and fluid flow in a porous enclosure filled with nanofluid due to the effect of the magnetic field. They described the heat and nanofluid flow through an enclosure for a variety of parameters: Hartmann number, Darcy number, Rayleigh number, and nanoparticles volume fraction. Advancement in heat transfer is found for an enhancement in the permeability of cavity, nanoparticles volume fraction, and buoyancy force effect. Moreover, many studies are conducted in order to comprehend the phenomena associated to the improvement of nanofluid's thermal conductivity, with respect to the ordinary fluid's thermal conductivity. In addition, intensive research focused about nanoparticle microrotation appears to play an important role. This theory was called the theory of micropolar fluid, and it is studied at first by Enrigen [3-4]. There are different studies which investigated the convection heat transfer on cavity, especially on three-dimensional enclosure. Manaa et al. [5] investigated the double diffusive natural convection on 3D enclosure filled with micropolar nanofluid. They considered the impact of pertinent parameters on heat and mass transfer rates. They have found that the Nusselt and Sherwood numbers for the micropolar nanofluid model are smaller than those for a pure nanofluid model. Their

ISSN: 2961-6611

findings illustrate that the type of nanoparticles plays a significant role in heat and mass transfer rates. Manaa et al. [6] investigated a numerical study on 3D double-diffusive free convection in a 3D cavity filled with Cu-Al_2O_3/water micropolar hybrid nanofluid. They have resembled the efficiency improvement of micropolar hybrid nanofluid Cu-Al_2O_3/water with the micropolar simple nanofluid Cu/water. Manaa et al. [7] performed a computational analysis to solve the problem of three-dimensional double diffusive free convection in a 3D enclosure filled with micropolar CNT-water nanofluid stabilized lignin and sodium polycarboxylate as surfactants. They founded that the nanoparticles volume fraction represents a component to control heat rate and fluid flow. Significant efforts have been made to investigate heat transfer studies for the natural convection of micropolar nanofluid in porous environment. Ahmed and Rashad [8] performed a numerical study to study the free convection flow on rectangular enclosure saturated with anisotropic porous area filled with micropolar nanofluid. The authors gained that the heat transfer rate increases by the enhancement of the nanoparticle volume fraction. Furthermore, they observed that the increase in the permeability ratio results destruction on vortex strength, fluid activity, and the flow direction is changed. Rashad et al. [9] summarized a numerical study of MHD free convection flow and heat transfer in an inclined porous cavity filled with nanofluid. They obtained that the increase of nanoparticles volume fraction and Hartman number results a decrease on Nusselt number. This paper is therefore an original work attached to the comprehension of the variation of heat and mass transfer of a microplar nanofluid in porous medium. The temperature, concentration, velocity and fields for different effect of porous Rayleigh number, Darcy number, Rayleigh number, micropolar parameter, nanoparticles's volume, and porosity will be presented, detailed and discussed. The above literature clearly shows that there is no work in the literature on three-dimensional double-difusive natural convection for micropolar nanofuid. Thus, this is the novelty of the current work.

II. GOVERNING EQUATION AND DESCRIPTION MODEL

The considered geometry is a differentially heated cubic cavity, as illustrated in Figure 1. A homogenous, isotopic, micropolar Cu-water based nanofluid is enclosed in saturated porous medium. It is assumed that the two vertical walls are maintained at constants temperatures (T_H>T_C) and constants concentrations (C_H>C_L). It is also assumed that the other walls are adiabatic and impermeable. In this article the Cu/water nanofluid, is supposed laminar incompressible and Newtonian. From the physical point of view, the base fluid is in thermal equilibrium with nanoparticles. During the process of the free convection, the thermal properties of the fluid are unchangeable, apart from the density. It is changed spatially and is kept the Boussinesq approximation. In addition, the local thermal equilibrium (LTE) model is used in the current study.

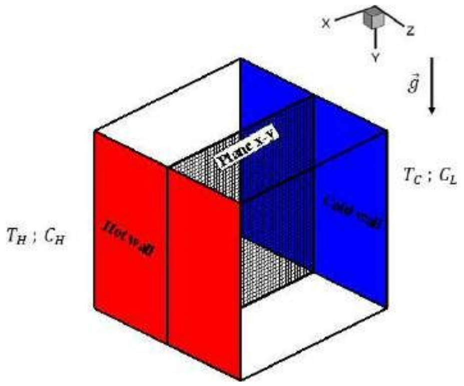

Fig. 1 Present model

The dimensionless governing equations are as following

$$\nabla\vec{U} = 0 \tag{1}$$

$$\left[\varepsilon\frac{\partial\vec{U}}{\partial t}+(\vec{U}.\nabla)\vec{U}\right] = -\varepsilon^2\frac{1}{\rho_{nf}}\nabla P + Pr\varepsilon\left(\frac{\mu_{nf}}{\mu_f}+K\right)\left(\frac{\rho_f}{\rho_{nf}}\right)\nabla\times\vec{U} - \varepsilon^2\frac{Pr}{Da}\left(\frac{\mu_{nf}}{\mu_f}+K\right)\left(\frac{\rho_f}{\rho_{nf}}\right)\vec{U} - \varepsilon^2 PrK\left(\frac{\rho_f}{\rho_{nf}}\right)\nabla\times\vec{H} + RaPr\varepsilon^2\left(\frac{(\rho\beta_T)_{nf}}{(\rho\beta_T)_f}\right)\left(\frac{\rho_f}{\rho_{nf}}\right)(T - NC) \tag{2}$$

$$\left(\varepsilon\frac{\partial \vec{H}}{\partial t}+(\vec{U}.\nabla)\vec{H}\right) - Pr\varepsilon\left(\frac{\mu_{nf}}{\mu_f}+\frac{K}{2}\right)\left(\frac{\rho_f}{\rho_{nf}}\right)\nabla^2\vec{H} + PrK\left(\frac{\rho_f}{\rho_{nf}}\right)(\nabla\times\vec{U}-2\varepsilon\vec{H}) \tag{3}$$

$$\sigma\frac{\partial T}{\partial t}+(\vec{U}.\nabla)T=\left(\frac{(\rho C_p)_f}{(\rho C_p)_{nf}}\right)\left(\frac{k_{mnf}}{k_f}\right)\nabla^2 T \tag{4}$$

$$\varepsilon\frac{\partial C}{\partial t}+(\vec{U}.\nabla)C=\frac{\varepsilon}{Le}\nabla^2 C \tag{5}$$

In the energy equations σ represents the heat capacity ratio $\sigma = (\varepsilon(\rho Cp)_f + (1-\varepsilon)(\rho Cp)_s)/(\rho Cp)_f$, where $(\rho Cp)_f$ and $(\rho Cp)_s$ are heat capacities for fluid and solid phases, respectively. κ_{mnf} is the effective thermal conductivity of the nanofluid saturated porous media given as $\kappa_{mnf} = (\varepsilon\kappa_{nf} + (1-\varepsilon)\kappa_s)$, where κ_{nf} and are thermal κ_s conductivities for fluid and solid phases, respectively.

The density, the heat capacity, the thermal expansion coefficient and the diffusivity of the nanofluid can defined as [10]

$$\rho_{nf} = (\varphi\rho_p + (1-\varphi)\rho_f) \tag{6}$$

$$(\rho Cp)_{nf} = (\varphi(\rho Cp)_p + (1-\varphi)(\rho Cp)_f) \tag{7}$$

$$(\rho\beta)_{nf} = (\varphi(\rho\beta)_p + (1-\varphi)(\rho\beta)_f) \tag{8}$$

$$\alpha_{nf} = \frac{\kappa_{nf}}{(\rho Cp)_{nf}} \tag{9}$$

The thermal conductivity of the nanofluid has been elaborated according to Maxwell model [11]:

$$\frac{\kappa_{nf}}{\kappa_f} = \frac{\kappa_p + 2\kappa_f - 2\varphi(\kappa_f-\kappa_p)}{\kappa_p + 2\kappa_f + \varphi(\kappa_f-\kappa_p)} \tag{10}$$

The effective dynamic viscosity has been elaborated according to the Brinkman model [12]:

$$\mu_{nf} = \frac{\mu_f}{(1-\varphi)^{2.5}} \tag{11}$$

In the equations system (1)-(5) , the dimensionless, micropolar *K,* Prandtl *Pr*, Darcy Da, Lewis *Le*, Rayleigh *Ra*, porous Rayleigh *Ra** numbers and buoyancy fraction *N* are respectively defined as

$$Pr = \frac{\mu_f}{\rho_f\alpha_f}, Da = \frac{K^*}{L^2}, Le = \frac{\alpha}{D}, Ra = \frac{g\rho_f\beta_{Tf}(T_H-T_C)L^3}{\mu_f\alpha_f}, Ra^* = RaDa. \quad K = \frac{k}{\mu_f} \text{ and } N = \frac{\beta_{Cf}(C_H-C_L)}{\beta_{Tf}(T_H-T_C)}$$

To exclude the pressure term, we have used in the present research the stream function-vorticity formulation. The stream function and vorticity are respectively determined as: $\vec{U} = \nabla\times\vec{\psi}$ and $\vec{\omega} = \nabla\times\vec{U}$.

The governing equations are rewritten in the subsequent form as:

$$\nabla^2\vec{\psi} = -\vec{\omega} \tag{12}$$

$$\begin{aligned}\frac{\partial\vec{\omega}}{\partial t_w}+(\vec{U}.\nabla)\vec{\omega}-(\vec{\omega}.\nabla)\vec{U}\\ = \varepsilon Pr\left(\frac{\mu_{nf}}{\mu_f}+K\right)\left(\frac{\rho_f}{\rho_{nf}}\right)\nabla^2\vec{\omega} - \varepsilon^2\frac{Pr}{Da}\left(\frac{\mu_{nf}}{\mu_f}+K\right)\left(\frac{\rho_f}{\rho_{nf}}\right)\vec{\omega} - \varepsilon^2 PrK\left(\frac{\rho_f}{\rho_{nf}}\right)\nabla^2 H\\ + \varepsilon^2 RaPr\left(\frac{(\rho\beta_T)_{nf}}{(\rho\beta_T)_f}\right)\left(\frac{\rho_f}{\mu_{nf}}\right)\left(\left[\frac{\partial T}{\partial z},0,-\frac{\partial T}{\partial x}\right]-N\left[\frac{\partial C}{\partial z},0,-\frac{\partial C}{\partial x}\right]\right)\end{aligned} \tag{13}$$

$$\left(\frac{\partial\vec{H}}{\partial t_w}+(\vec{U}.\nabla)\vec{H}\right)=\varepsilon Pr\left(\frac{\mu_{nf}}{\mu_f}+\frac{K}{2}\right)\left(\frac{\rho_f}{\rho_{nf}}\right)\nabla^2\vec{H}+PrK\left(\frac{\rho_f}{\rho_{nf}}\right)(\vec{\omega}-2\varepsilon\vec{H}) \tag{14}$$

ISSN: 2961-6611

$$\frac{\partial T}{\partial t_\sigma}+(\vec{U}.\nabla)T=\left(\frac{(\rho C_p)_f}{(\rho C_p)_{nf}}\right)\left(\frac{k_{mnf}}{k_f}\right)\nabla^2 T \tag{15}$$

$$\frac{\partial C}{\partial t_w}+(\vec{U}.\nabla)C-\frac{\varepsilon}{Le}\left(\frac{(\rho C_p)_{nf}}{(\rho C_p)_f}\right)\left(\frac{k_f}{k_{nf}}\right)\nabla^2 C \tag{16}$$

We defined the local (Nu) and average ($\overline{Nu}$) Nusselt numbers, local (Sh) and average ($\overline{Sh}$) Sherwood numbers on the isothermal walls as following:

$$Nu=\left.\frac{k_{mnf}\dfrac{\partial T'}{\partial x'}}{k_f\dfrac{T'_H-T'_C}{L}}\right)_{x'=0.1}=-\frac{k_{mnf}}{k_f}\left.\frac{\partial T}{\partial x}\right)_{x=0.1}\quad Sh=\left.\frac{D\dfrac{\partial C'}{\partial x'}}{D\dfrac{C'_H-C'_L}{L}}\right)_{x'=0.1}=\left.\frac{\partial C}{\partial x}\right)_{x=0,1} \tag{17}$$

$$\overline{Nu}=\iint_0^1 Nu\,dy\,dz\;\overline{Sh}=\iint_0^1 Sh\,dy\,dz \tag{18}$$

For each time step, the stopping convergence criterion is contented:

$$\sum_{1,2,3}\frac{\max|\psi^n-\psi^{n+1}|}{\max|\psi^n|}+\max|T^n-T^{n+1}|+\max|C^n-C^{n+1}|\leq 10^{-5} \tag{19}$$

III. RESULTS AND DISCUSSION

The variation of isotemperatures, isoconcentrations for different values of Darcy number *Da* for *K*=1 and 3, is presented respectively on **Figure 3** and **Figure 4**. In these figures, a smooth variation in isotemperatures and isoconcentrations surfaces shifted towards the lateral wall is recorded at *Da*=10^{-3}, and this displacement to the side walls increase with *Da*=10^{-1}. More distributed temperature and concentration is noted at higher *Da*=10^{-2} and 10^{-1}. A heat lines directed orthogonally to isotherms at low Darcy number Da= 10^{-3} indicates the conduction dominated heat transfer mode. The complete circulations achieved for heat-lines at *Da*=10^{-2} indicate the dominate impact of convection mode. Denser lines in the middle of the heat-lines and powerful circulations at *Da*=10^{-1} mean increased convective heat transfer significances.

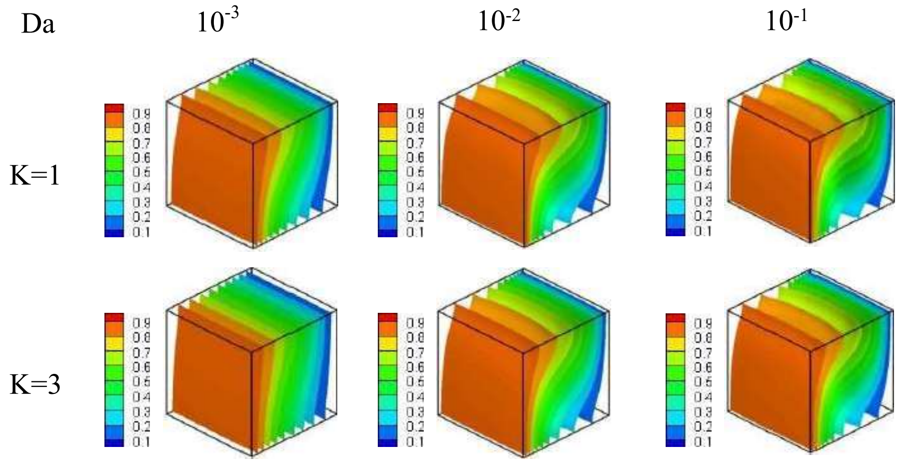

Fig.3: Influence of Darcy number and micropolar parameter on isotemperatures

ISSN: 2961-6611

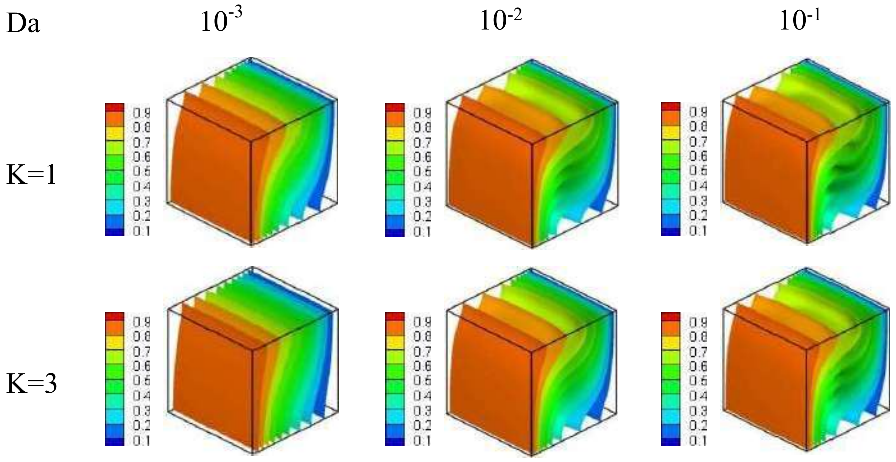

Fig.4: Influence of Darcy numberand micropolar parameter on isoconcentrations

The relation between average Nusselt and Sherwood numbers and the volume fraction of nanoparticles φ and Darcy number is investigated using the simulation results reported respectively in **Figure 11** and **Figure 12**. For a micropolar nanofluid, it is viewed that both Nu and Sh are becoming smaller relative to the pure nanofluid regardless of the value of Da selected. For a steady value of φ, the average Nusselt and Sherwood numbers decline with the increase of the vortex viscosity parameter (K). As the vortex viscosity parameter K is mainted steady, the average Nusselt and Sherwood numbers increase as the value of the volume fraction of nanoparticle. In this way, the addition of nanoparticles promotes the transfer of heat and mass. This can be explained that the enhancement of nanoparticle volume fraction induces the increase of thermal conductivity of fluid. In addition, it obtained that the heat and mass transfer decrease with the decrease of Darcy number.

IV. CONCLUSION

Three-dimensional numerical investigation was carried out to study the double diffusive natural convection of micropolar Cu-water nanofluids in a porous cubical enclosure. In this numerical work, it obtained that improving the micropolar parameter reduces the flow strength. Moreover, it observed, an improvement in average Nusselt and Sherwood numbers with increase in Darcy number. Besides, it's easy to see that the increases of micropolar parameter reduces heat and mass transfer characteristics. Finally, it obtained that the adding of nanoparticles favorites the heat and mass transfer.

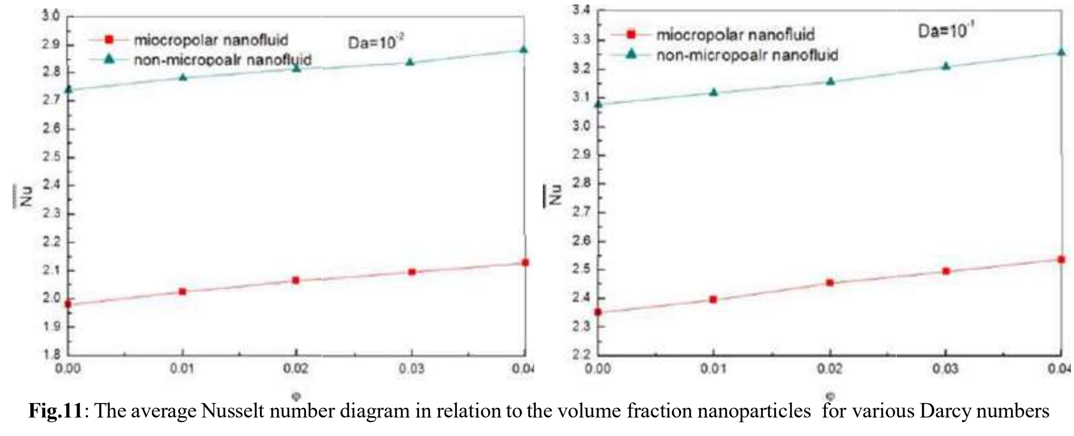

Fig.11: The average Nusselt number diagram in relation to the volume fraction nanoparticles for various Darcy numbers

ISSN: 2961-6611

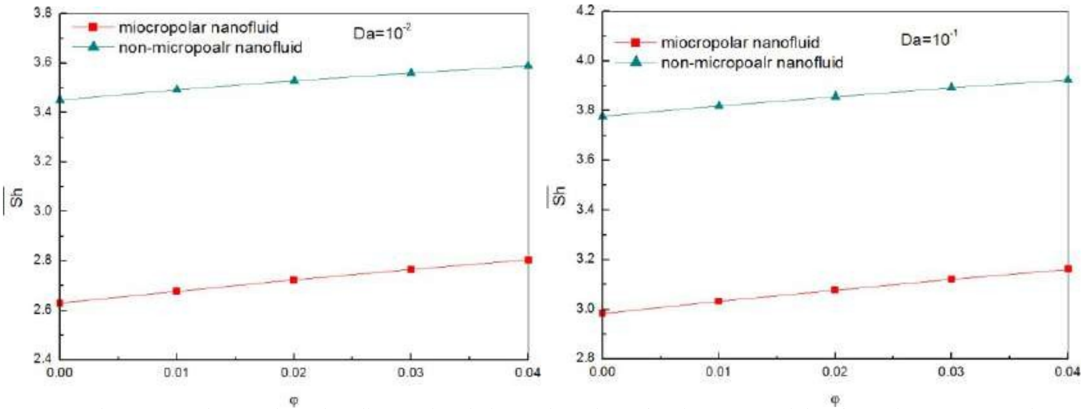

Fig.12: The average Sherwood number diagram in relation to the volume fraction nanoparticles for various Darcy numbers

REFERENCES

[1] Alilat D.,Alliche M.,Rebhi R., and Borjini M.,(2020), Inertial and Porosity Effects on Dupuit-Darcy Natural Convection of Cu-Water Nanofluid Saturated High Thermal Conductive Porous Medium.Special Topics and Reviews in Porous Media 11(5) DOI: 10.1615/SpecialTopicsRevPorousMedia.2020033717.

[2] Jino, L., & Kumar, A. V. (2021). *Cu-Water Nanofluid MHD Quadratic Natural Convection on Square Porous Cavity. International Journal of Applied and Computational Mathematics, 7(4).* doi:10.1007/s40819-021-01103-5.

[3] Eringen, A.C. Theory of micropolar fluids. J. Math. Mech. 1966, 16, 1–18.

[4] Eringen, A.C. Microcontinuum field Theories: II. Fluent Media; Springer Science & Business Media: Berlin/Heidelberg, Germany, 2001; Volume 2.

[5] Manaa N, Abidi A, Saleel CA, Al Makwash SM, Borjini MN. On Simulation of Double-Diffusive Natural Convection in a Micropolar Nanofluid Filled Cubic Cavity. Heat Transf Eng. 2020;https://doi.org/10.1080/01457632.2020.1756074.

[6] Manaa N, Abidi A, Ahamed SC, Madiouli J, Borjini MN. Three-Dimensional Numerical Analysis on Performance Enhancement of Micropolar Hybrid Nanofluid in Comparison with Simple Nanofluid. Heat Transf Eng. 2020; https://doi.org/10.1080/01457632.2020.1807106.

[7] Manaa, N., Abidi, A., Estellé, P., & Borjini, M. N. (2021). Numerical simulation of three-dimensional thermo-solutal convection of micropolar multi-walled carbon nanotubes water nanofluid stabilized by lignin and sodium polycarboxylate. Journal of Thermal Analysis and Calorimetry. doi:10.1007/s10973-

[8] Ahmed, S. E., & Rashad, A. M. (2016). Natural Convection Of Micropolar Nanofluids In A Rectangular Enclosure Saturated With Anisotropic Porous Media. Journal Of Porous Media, 19(8), 737–750. Doi:10.1615/Jpormedia.V19.I8.60.

[9] Rashad, A.M.; Armaghani, T.; Chamkha, A.J.; Mansour, M.A.: Entropy generation and MHD natural convection of a nanofuid in an inclined square porous cavity: Effects of a heat sink and source size and location. Chinese J. Physic **56**, 193–211 (2018).

[10] B. C. Pak and Y. I. Cho,” Hydrodynamic and heat transfer study of dispersed fluid with submicron metallic oxide particles”, Experimental Heat Transfer, vol. 11, pp. 151–170, 1998.

[11] J.C. Maxwell, “A Treatise on Electricity and magnetism,” second ed., clarendon press, (1881).

[12] H.C. Brinkman, “The viscosity of concentrated suspensions and solutions,” The Journal of Chemical al Physic, 20(4), (1952) 571-574.

ISSN: 2961-6611

Effect of Reynolds number and obstacle dimensions on laminar flow around single square obstacle -first part

Guemmadi Messaouda[#1], Brahimi Faiza[#2]

[#]Department of Mechanical Engineering, Faculty of Technology, University of Boumerdes, Algeria
[1]Laboratory of Mechanical Energetics and Engineering-University of Boumerdes, 35000, Algeria
[2]Laboratory of Dynamic Motors and Vibro-acoustic- University of Boumerdes, 35000, Algeria
[1] `m.guemmadi@univ-boumerdes.dz`
[2] `f.brahimi@univ-boumerdes.dz`

Abstract— This work aims to study the dynamic behavior of the flow around a square obstacle close to a wall. Two-dimensional flow in laminar regime for an incompressible fluid without heat transfer was simulated. We used the ANSYS Fluent software to solve the system of equations governing the flow. The analysis is done for different Reynolds numbers (Re= 5, 10, 30,…80) and different dimensions of the obstacle (D=0.5, D=1 and D=1.6) as well as the inclination of the obstacle. Streamlines, velocity contours, and the Strouhal number as a function of time in the unsteady case are determined in this study. We found that the effect of the inclination and the dimensions of the obstacle on the different flow parameters is very important. In particular, the dimensions of the obstacle and the Reynolds number strongly influence the structure of the fluid flow.

Keywords— *Square obstacles; Reynolds Number; Strouhal Number; Streamlines; CFD.*

I. INTRODUCTION

The study of rotating flows is motivated by the large number and diversity of applications, natural or industrial, in which they are encountered. They manifest themselves, for example, in the form of tornadoes in the geophysical field, and occur in chemistry in devices for mixing or separating constituents by centrifugation. In external aerodynamics, aircraft lift vortices, harmful to follower aircraft, constitute a well-known example which is the subject of much research at present. These flows are also very widespread in internal aerodynamics, particularly within turbojet engines and combustion systems.

The generic phenomena of which rotating flows are the seat are linked to the centrifugal force and the Coriolis force. The action of centrifugal force can lead to hydrodynamic instabilities; the Coriolis force generates the propagation of a regime of waves called inertia waves. These flows also harbor highly non-linear phenomena, of which vortex bursting is the most famous example. Vortex bursting refers to the sudden disorganization of a vortex, generally resulting in turbulent flow. In applications, we can seek to avoid it when it is associated with lift disturbances, as in the case of a wing, or, on the contrary, seek to provoke it, for example, to increase the mixing between fuel and oxidizer in the so-called “swirl” burner devices. Another example of the particularity of these flows concerns turbulence, the properties of which are modified in the presence of an overall rotation.

Rotating flows therefore present a wide variety of phenomena, some of which still remain unexplained. They also constitute formidable test cases for numerical simulation, mainly because of their high sensitivity to boundary conditions [9] and their particular turbulent properties, which defeat most classical turbulent closure models [8].

II. DESCRIPTION OF THE PROBLEM AND NUMERICAL MODELING

The study investigates flow past a square cylinder in a confined domain, as shown in figure 1. A square cylinder with edge length D is placed in the computational domain parallel to the flow at a distance of 32m from the inlet on the x-axis, and the outlet is 64m downstream, which is sufficiently large to minimize the exit effects [10]. The cylinder is placed at the center of the y-axis.

ISSN: 2961-6611

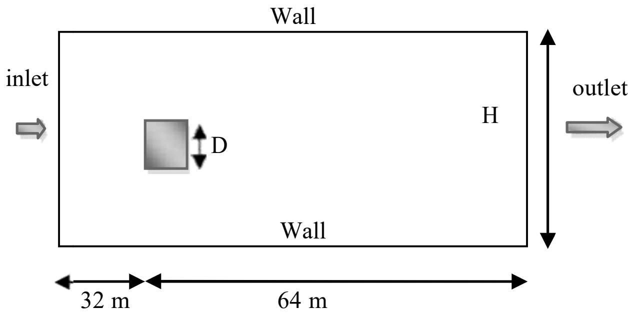

Fig.1 Calculation domain and Boundary Layer (angle θ=0°)

A Dirichlet type boundary condition, i.e., a uniform flow at the inlet (Fig. 1) with u = 1 and v = 0, is considered. An outflow boundary condition i.e., a fully developed flow, $\left(\partial u/_{\partial x} = \partial v/_{\partial x} = 0\right)$ is considered at the exit boundary (fig. 1). The channel boundaries and the square cylinder walls are imposed as rigid surfaces with a no-slip condition $(u = 0, v = 0)$. Steady and unsteady laminar incompressible flow is assumed for the present two-dimensional numerical model with dimensionless governing equations as given below:

$$\frac{\partial\rho}{\partial t} + \nabla.(V) = 0 \qquad (1)$$

$$\frac{\partial\rho}{\partial t} + \nabla\cdot(\mathrm{Vu}) = \nabla.(\nabla\mathrm{u}) - \nabla\mathrm{p.i} + \mathrm{Su} \qquad (2)$$

$$\frac{\partial\rho}{\partial t} + \nabla\cdot(\mathrm{Vv}) = \nabla.(\nabla\mathrm{v}) - \nabla\mathrm{p.j} + \mathrm{Sv} \qquad (3)$$

The source terms Su, Sv appearing in above equations, for a Newtonian fluid can be written as

$$S_u = f_u + \frac{\partial}{\partial x}\left(\mu\frac{\partial u}{\partial x}\right) + \frac{\partial}{\partial y}\left(\mu\frac{\partial v}{\partial x}\right) - \frac{2}{3}\frac{\partial}{\partial x}(\mu\,\nabla.\mathrm{V}) \qquad (4)$$

$$S_v = f_v + \frac{\partial}{\partial x}\left(\mu\frac{\partial u}{\partial y}\right) + \frac{\partial}{\partial y}\left(\mu\frac{\partial v}{\partial y}\right) - \frac{2}{3}\frac{\partial}{\partial x}(\mu\,\nabla.\mathrm{V}) \qquad (5)$$

For the transport of any scalar f, we have a general transport equation, which is given as follows:

$$\frac{\partial}{\partial t}(\rho\varphi) + \nabla.(\rho V\varphi) = \nabla.(\Gamma\nabla\varphi) + S_\varphi \qquad (6)$$

Comparing the u-momentum equation (2) to the general transport equation (6) we get $\varphi = u$, $\Gamma = \mu$, $S_\varphi = S_u - \partial p/\partial x$. Further in the present case, the viscosity (μ) and density (□) of the fluid are constant, and assuming that there are no body forces acting on the flow domain, the source terms S_u and S_v are zero. This can be shown by invoking the continuity equation for an incompressible fluid.
$\nabla.V = 0$ in eqs. 4 and 5. The Navier - Stokes equations are nonlinear (because of the convection term) and coupled (because the u-momentum equation has v velocity in it and vice versa). In order to solve these equations, we have to use finite volumes through the ANSYSY Fluent Software.

III. RESULTS AND DISCUSSION

In this work, we will study three cases by changing the diameter of the obstacle: d=0.2m, d=1m, d=1.6m, with a change in the angle of inclination of the obstacle (θ=0° and θ=45°).

A. Study of the effect of changing Reynolds number

When the Reynolds number is low (Fig. 2), viscous forces dominate and flow is generally laminar and smooth. As the Reynolds number increases, inertial forces become greater, and flows can become turbulent.

In the case of flow around a square obstacle, increasing the Reynolds number can lead to significant changes inthe flow characteristics. At low Reynolds numbers, flow can be laminar with well-defined streamlines. As the

Reynolds number increases, vortices and separation zones can form behind the obstacle, leading to increased pressure losses and drag forces.

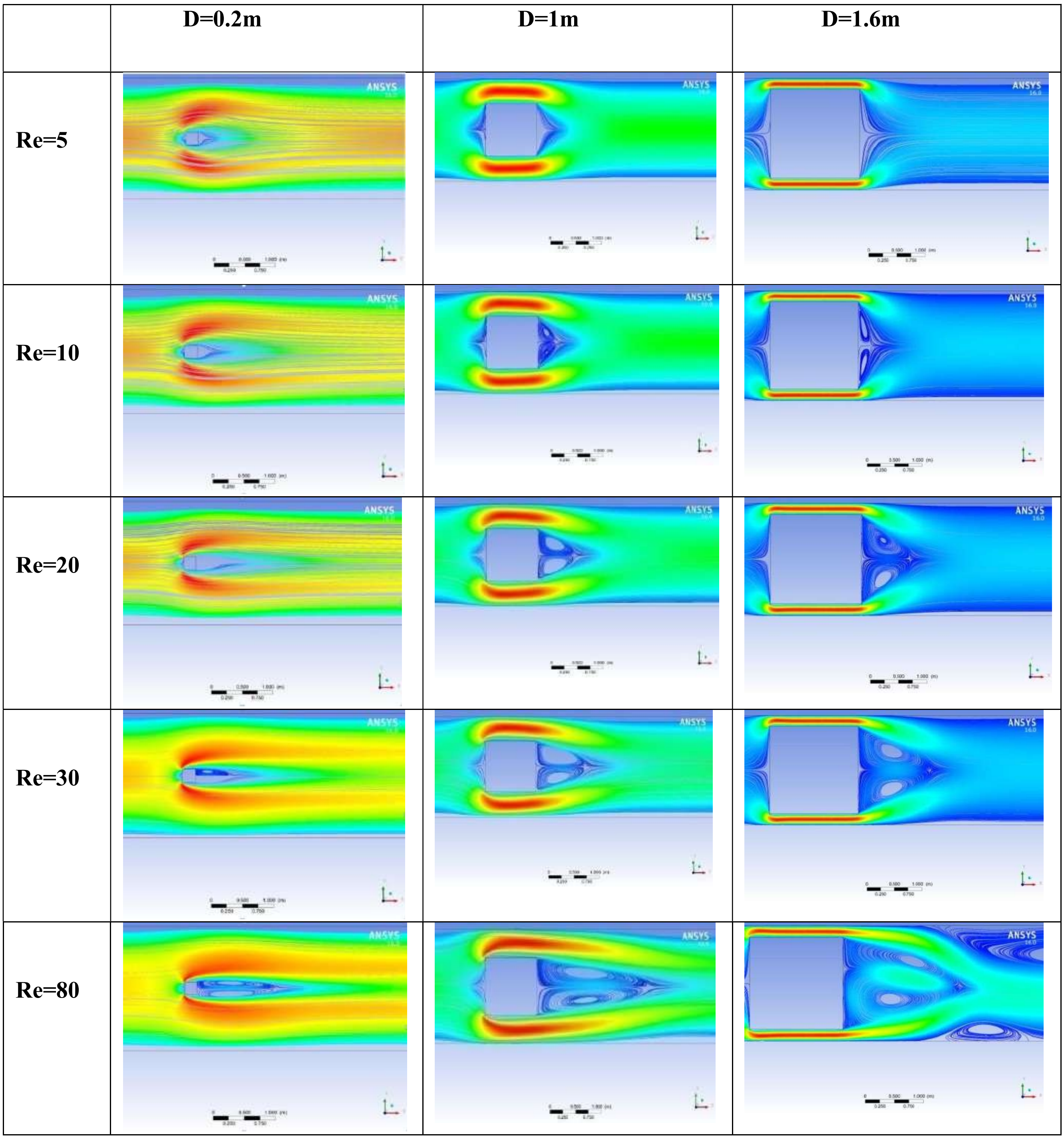

Fig. 2 Streamlines around a square obstacle with changing Reynolds number

ISSN: 2961-6611

B. Study of the effect of changing the diameter of the obstacle

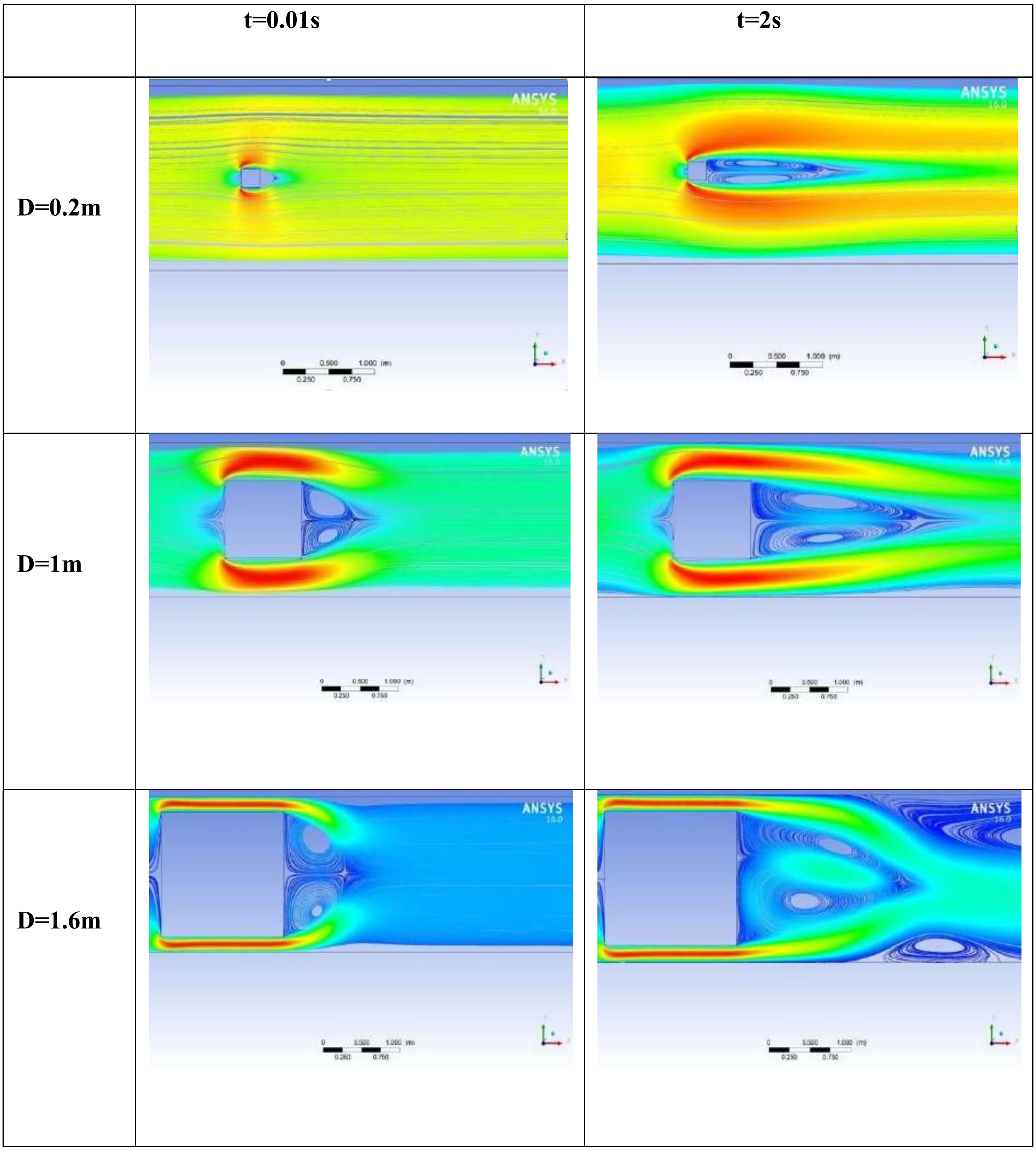

Fig. 3 The Streamlines around a square obstacle with change in diameter (D= 0.2 m, D=1m, D=1.6m)

We notice that when the diameter of the obstacle is smaller (Fig. 3), the flow can move around it more easily, creating a relatively stable flow zone. As the diameter increases, the obstacle creates more turbulence and swirl in the flow, which can have effects on the flow's drag, pressure, and velocity.

In general, a larger obstacle creates greater resistance to flow, which can result in a decrease in flow velocity upstream and an increase in turbulence downstream of the obstacle. This can also affect the formation of vortices and flow separation zones. It is important to note that these effects also depend on the flow speed, the viscosity, of

ISSN: 2961-6611

the fluid and the shape of the obstacle itself. Therefore, it is always necessary to consider all these factors to evaluate the effect of a change in obstruction diameter on a given flow.

C. Study of the effect of changing the inclination of the obstacle

When the obstacle is positioned with a 0-degree inclination relative to the flow, it is considered to be perpendicular to the direction of the flow. In this case, the flow can be essentially divided into two parts: the flow before the obstacle and the flow after the obstacle. The obstacle creates a separation zone where the flow slows down and forms a low-pressure zone on its rear side, which can lead to the formation of vortices and turbulence.

In contrast, when the obstacle is tilted at 45 degrees, it changes the flow direction more significantly. This creates a more complex interaction between the obstacle and the flow, which can generate aerodynamic phenomena such as the formation of vortices, the appearance of high-pressure zones, and changes in flow trajectory. The inclination of the obstacle can therefore have an effect on the overall behavior of the flow and on the forces exerted on the obstacle.

However, it should be noted that the specific effect of the change in inclination will depend on many factors (Fig. 4), such as the speed of the flow, the shape of the obstacle, the nature of the fluid, etc. Extensive experimental and/or numerical studies are often necessary to precisely evaluate the effect of tilt change in a specific situation.

	D=0.2m	**D=1m**	**D=1.6m**
Re=80	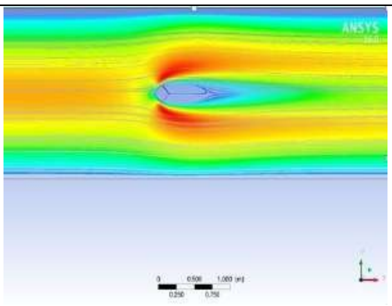	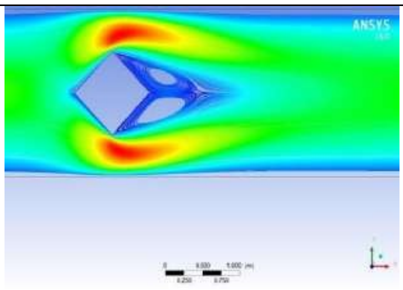	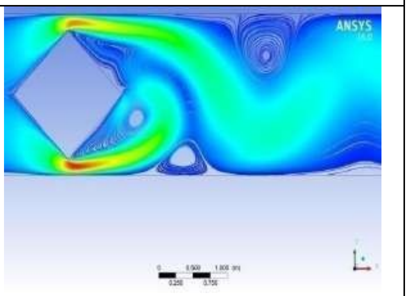

Fig. 4 The streamlines around a square obstacle (incline θ= 45°)

D. Change in the inclination of the obstacle in relation to the diameters

Changing the inclination from 0 to 45 of the obstacles in the case of flow around them can have a significant effect on the flow properties (Fig. 5). The inclination of the obstacle can affect the flow trajectory, speed, forces exerted, and turbulence phenomena.

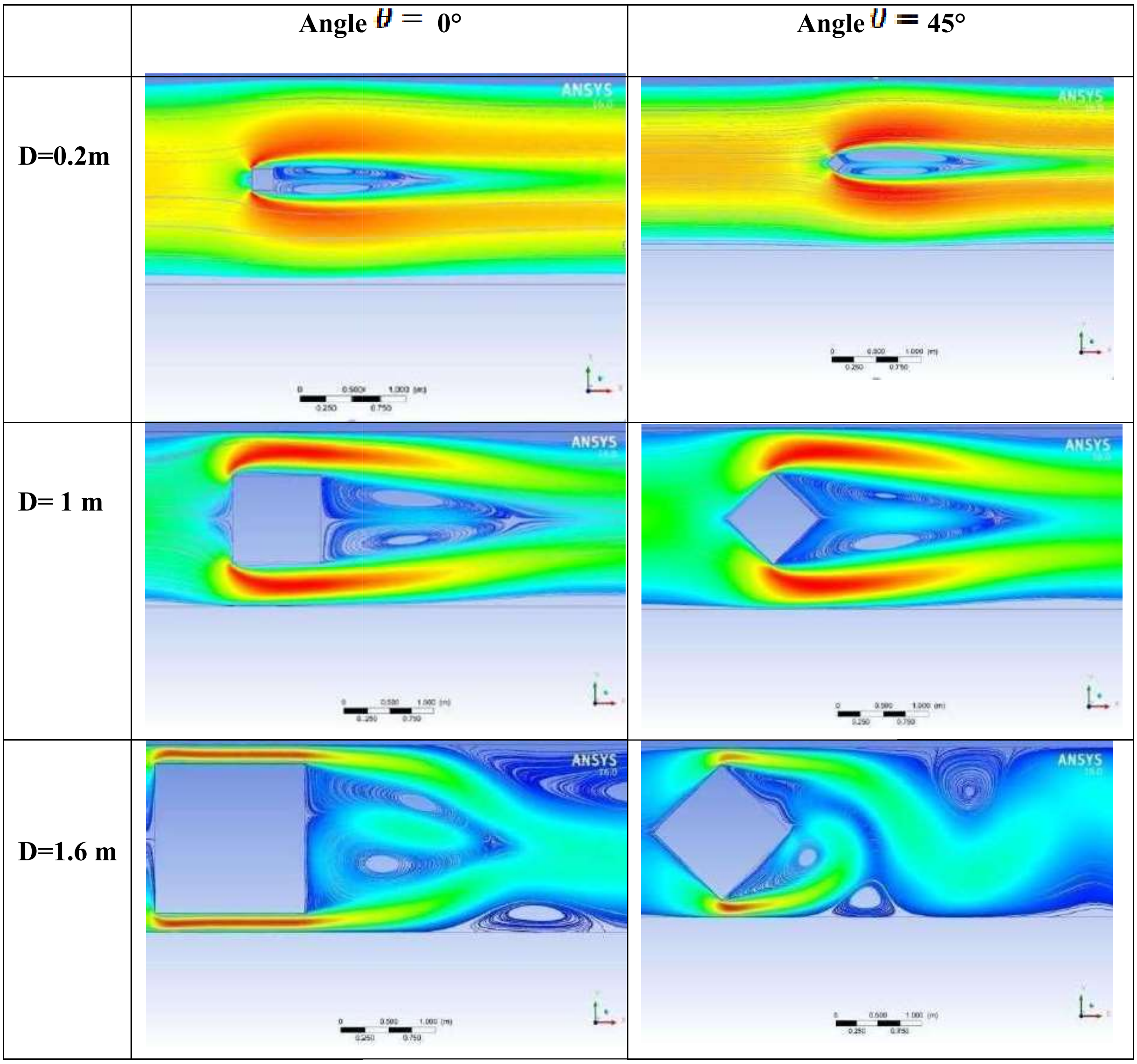

Fig. 5 The streamlines around a square obstacle with change in inclination θ= 0° and θ= 45° in relation to the diameters D=0.2m, D=1m, D=1.6m

E. Determining the length of the recirculation zone

The length of the recirculation zone (Lr) was measured by Zdravkovich (1997) if the blocking effect was eliminated. Then the empirical relationship is linear and given by:

$Lr/D = 0.05\ Re$ for $4.4 < Re < 40$.

$Lr/D = -0.065 + 0.0554\ Re$ for $5 < Re < 60$

Figures (6-a) and (6-b) summarize the calculated values for the recirculation length Lr/D for a square obstacle inside a channel as a function of the Reynolds number. First of all, we notice that if Re increases, the recirculation zone increases. These results are well explained in the previous figures. Then the agreement between the results obtained numerically by the present study and those of Breuer is explicitly visible.

ISSN: 2961-6611

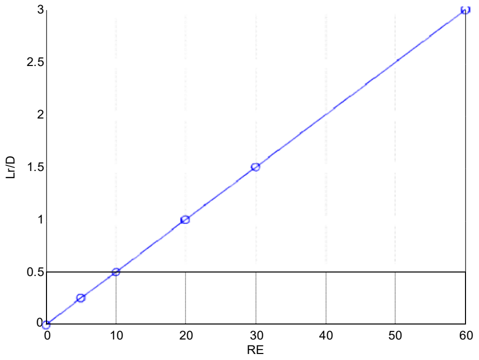

Fig. 6-a Length of the recirculation zone as a function of Reynolds (present work)

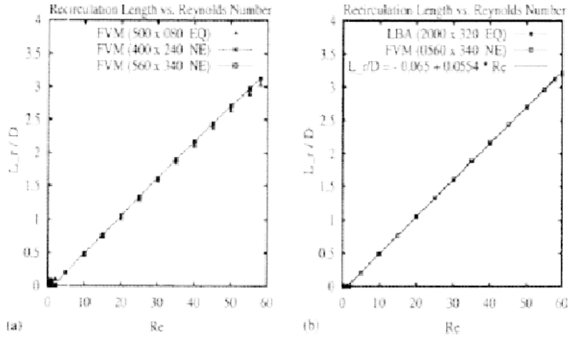

Fig. 6-b Length of the recirculation zone as a function of Reynolds (M.Breuer Results)

F. Calculation of the Strouhal Number

An important quantity taken into account in the present analysis is the Strouhal number St, calculated from the diameter of the cylinder D, the measured frequency of the vortex shedding f and the maximum speed umax at the entrance plane. St=f.D/umax. In figure (7), we notice that at the first moments, the flow is unsteady (St>1). After a few seconds, the flow becomes stationary (St<1). So we can say that for a margin of the Reynolds number <80 the flow is laminar and stationary. These results are confirmed by previous work cited in the first chapter of this dissertation. Figure (8) shows the importance of the influence of the dimensions of the obstacle on the Strouhal number and consequently on the instationarity of the flow.

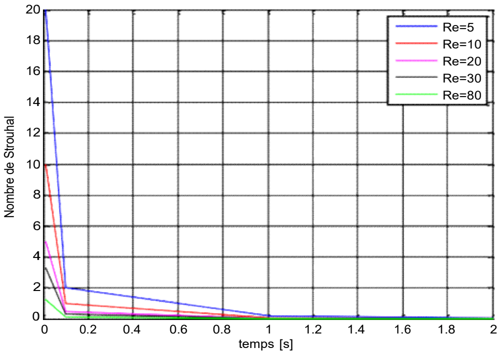

Fig. 7 Strouhal number as a function of time

Copyright © 2024
ISSN: 2961-6611

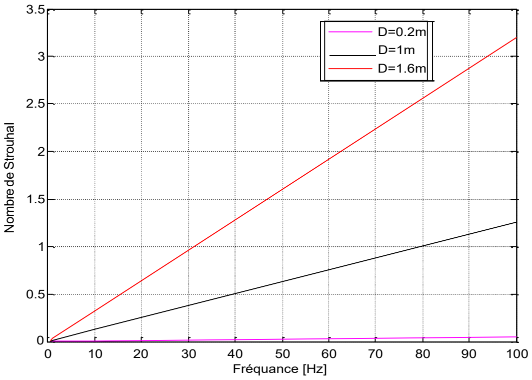

Fig. 8 Strouhal number as a function of frequency

VI. CONCLUSIONS

The study of laminar flows around obstacles near a wall was the objective of this work. Numerical simulation by ANSYS Fluent was adopted to solve the equations of the stationary and unsteady flow of a Newtonian and incompressible fluid in the laminar regime. This work allowed us to draw very rich observations for different Reynolds numbers in the laminar regime. Firstly, we compared our results with those obtained in the literature for a flow around a square obstacle [9]. At low Re < 5, creeping flow is examined. Then, from Re > 50, the instability begins to manifest itself in the wake zone, revealing an oscillatory flow with variable frequencies and progressive amplitudes in the geometry considered. This flow phenomenon is also called the Von-Karman vortex alley phenomenon. Then, we studied the effect of the Reynolds number and the dimension of the obstacle, as well as the inclination of the latter, on the flow. We found a vortex detachment. This detachment is responsible for creating large vortices at the wall. In the middle of the vortex zone, the speed and pressure are low compared to the end. We also noted that the dimension of the obstacle is very important in the flow disturbed by a square obstacle.

According to the numerical study carried out on the influence of the inclination of 0 and 45 degrees on a flow around a square obstacle, the following conclusions were reached:

0 degree tilt: When the obstacle is positioned perpendicular to the flow, a greater interaction between the flow and the obstacle is observed. This can result in areas of stagnation and recirculation of flow in the region immediately upstream and downstream of the obstacle. The presence of turbulence and drag forces may also be more significant.

45 degree tilt: When the obstacle is tilted at a 45 degree angle to the flow, an increase in flow velocity is generally observed compared to the 0 degree tilt. This increase in speed can be attributed to a reduction in the drag exerted by the obstacle on the flow. Additionally, the stagnation and recirculation zones can be minimized or moved to different positions relative to the obstacle.

It should be noted that these conclusions are based on numerical results and may vary depending on the specific conditions of the study, such as obstacle shape, flow velocity, fluid viscosity, etc.

The validity of the results obtained must also be questioned in terms of precision. Here, the mesh has a fairly weak influence on its resolution, which seems sufficient, but its geometry can be important. We must therefore always validate the simulation through experience and check the precision. It is therefore a perfect tool for the engineer and the researcher who know its shortcomings and maintain a critical spirit with regard to results that seem aesthetic in terms of their true physical appearance.

REFERENCES

[1] Benjamin Renaud, Instabilité de Bénard-Von Karman derrière un obstacle oscillant , Rapport de stage expérimental, Laboratoire de Physique et Mécanique des Milieux Hétérogènes, Paris, 2000.

[2] Khabbouchi, M.S. Guellouz. Ecoulement autour d’un cylinder circulaire proche d’une paroi, Effet de l’écoulement type jet. Laboratoire d’Etude des Systèmes Thermiques et Energétiques Ecole Nationale d’Ingénieurs Monastir, Tunisie, 2008.

[3]Benjamin Renaud, Instabilité de Bénard –Von Karman derrière obstacle oscillant. Rapport de stage expérimental, Laboratoire de Physique et de Mécanique des Milieux Hétérogènes, Paris, 2000

[4] Krishna Chaitanya, Dipankar Chatterjee, Effect of blockage on fluid flow past a square cylinder at low Reynolds numbers, Indian Academy of Sciences, Sådhanå (2022)47:4

[5] Zakaria Sari Hassoun and all, Effect of Obstacles on Turbulent Flows in a Rectangular Channel From their Front Sides, Thermal Science: Year 2023, Vol. 27, Special Issue 1, pp. S333-S341

[6] Moustafa Nooroullahi and all, Large eddy simulation of flow over a wall-mounted cube: Comparison of different semi dynamic subgrid scale models, Int. Jnl. of Multiphysics Volume 6 · Number 1 · 2012

[7] Benjamin Leclaire, Etude théorique et experimentale d'un écoulement tournant dans une conduite, Doctorat thesis 21 Décembre 2006.

[8] S. Jakirlic, K. Hanjalic, and C. Tropea. Modeling rotating and swirling turbulent flows : a perpetual challenge. AIAA J., 40(10) :1984–1996, 2002.

[9] D. O. Snyder and R. E. Spall. Numerical simulation of bubble-type vortex breakdown within a tube-and-vane apparatus. Phys. Fluids, 12(3) :603–608, 2

[10] Mittal S, Singh S P, Kumar B and Kumar R Flow past bluff bodies: effect of blockage. Int. J. Comut. Fluid Dyn. 20: 163–173-2006

[11] Breuer M, Bernsdorf J, Zeiser T, Durst F. Accurate computations of the laminar flow past a square cylinder based on two different methods: lattice-Boltzmann and finite-volume. International Journal of Heat and Fluid Flow 2000;21(2):186–96.

Numerical Study of Laminar and Turbulent Flow Around Two Side by Side Square Obstacles at Varying Gap Ratios

Guemmadi Messaouda[#1], Brahimi Faiza[#2], Oucali Hocine[#]

[#]*Department of Mechanical Engineering, Faculty of Technology, University of Boumerdes, Algeria*
[1]*Laboratory of Mechanical Energetics and Engineering-University of Boumerdes, 35000, Algeria*
[2]*Laboratory of Dynamic Motors and Vibro-acoustic- University of Boumerdes, 35000, Algeria*
`Email 1 - m.guemmadi@univ-boumerdes.dz`
`Email 2 - f.brahimi@univ-boumerdes.dz`
`Email 3- oukalihocine20@gmail.com`

Abstract- Turbulence is one of the most challenging problems of the modern physical and it is among the most complex and fascinating phenomena found in the nature. Due to several practical implications in different sectors, the number of researches related to the understanding and control of turbulent flows has become increasingly greater. An alternative for the treatment of flows at high Reynolds number can be done by scales separation. This separation can be accomplished through the decomposition process of the Navier-Stokes equations into a mean and a floating part, as proposed by Reynolds. In the present work, numerical simulations on Ansys-Fluent are performed for the study of two-dimensional, incompressible and isothermal flow around a pair of square obstacles arranged side by side. The influence of the spacing ratio is investigated for the two obstacles, and a comparison between laminar and turbulent flow is analyzed for different Reynolds Number. Also, the position effect of the obstacles (vertical or horizontal) for the side-by-side case is investigated. The streamlines and the time evolution of the vorticity fields, are presented.
Keywords: *Square obstacle, Reynolds number, Strouhal number; side-by-side arrangement; Turbulent flow; Laminar flow.*

I. INTRODUCTION

Flow around cylindrical structures of square cross section has various applications in different areas of architectural, mechanical and civil engineering. For instance, such type of structures can be seen in most of the architectural designs like buildings, beams, fences, bridges and many external and internal support components. In gas turbine blades and heat exchangers, the cylinders of square cross section are used as potential vortex generators for cooling purpose. The chips used in electronic devices mostly have square/rectangular cross sections. Another example of flow around a cylinder of square cross section is the flame holder of the combustor. By searching the literature related to the fluid interaction with solid structures, it can be found that numerous experimental investigations have been carried out to study the characteristics of flow around circular/square cylindrical structures. In the work of Norberg, [1] it was found that the vortex shedding around a circular cylinder starts at Reynolds number (Re) = 47. The flow remains two-dimensional till Re = 160 and after that three-dimensional effects start appearing in the range 160 < Re < 190. After Re = 190 the flow becomes completely three-dimensional. Price and al [2] experimentally visualized the flow around circular cylinder and divided it into four different regions regarding the behavior of shear layers and vortex generation mechanism. Wang and Tan [3] found in their experimental work that the vortex shedding and momentum exchange for the flow around square cylinders are slower as compared to circular cylinder. The vortex induced vibrations and oscillation mechanism of the flow around a square cylinder were also analyzed by Manzoor and al [4] Some experimental studies about characteristics of single cylindrical obstacle can also be found in Refs [5–7].

In the case of two or more cylinders, the gap spacing (g) significantly affects flow characteristics. This fact was also observed in many experimental studies. Deng and al [8] found that the placement of a second cylinder in the wake of a single cylinder, to a certain level of spacing, suppresses the three-dimensional instabilities. Sakamoto and al [9] observed significant changes in time-averaged forces of tandem (inline) square cylinders depending on g at Re =

ISSN: 2961-6611

27600. Kim and al [10] termed g = 2.5 as critical value of spacing and categorized the flow characteristics in two modes separated by critical spacing value. For the flow around three inline circular cylinders, Igarashi and Suzuki [11] divided the shear layers' behavior, depending on Re and g, in three categories: without reattachment, with reattachment and roll up. Liu [12] examined the dependence of flow induced forces on g and found that the drag coefficient (CD) of cylinders changes abruptly in the range between g = 3.5 and 4 due to existence of critical spacing value in this range. According to the study made by Hetz and al. [13], the Strouhal number (St) of five inline circular cylinders increases with increment in g. Some further experimental studies related to the fluid flow characteristics of two or more inline cylinders can be found in Refs [14–16].

Contrary to experimental measurements, numerical computations can quickly provide the information about important flow characteristics such as wake structure mechanism, temporal histories of flow induced forces, and sensitivity of force coefficients to different flow parameters. These characteristics are very difficult to obtain experimentally. In numerical simulations, the fluid flow parameters and conditions can be easily changed by suitable modification in the input parameters without any time or labor cost. Several numerical studies have been reported regarding the flow mode transitions from steady to unsteady state around single cylindrical obstacle.

From above discussion, it can be deduced that the transitions in flow states around the structures of square cross section are not investigated thoroughly yet. From the perspective of applications, the bluff bodies of square cross section are very important. Flow around such bodies differs from those of circular cross section in many aspects like flow structure mechanism, variation of flow induced forces, etc. Therefore, a detailed analysis of flow characteristics around bluff bodies of square cross section is very important in order to improve the design of structures and avoid losses. Keeping in view the above mentioned points, the current study will focus on: first the study of the flow around single square obstacle for different Reynolds number for Laminar flow and in the second part the transition in flow states around two square obstacles under the effect of Re, the effect of spacing on the transitional range of Re, comparison of transitional range for different positions of obstacles (horizontal and vertical).

II. GOVERNING EQUATIONS

In wind engineering, the flow fields treated are usually expressed by the continuity equation and incompressible Navier-Stokes equations.

$$div\, u = 0$$

$$\frac{\partial u}{\partial t} + u.\, grad\, u = -grad\, p + \frac{1}{Re} \Delta u$$

where u, p, t, Re denote the velocity, pressure, time and the Reynolds number, respectively. The above equations are non-dimensional and $Re = UL/\nu$.

U: characteristic velocity scale, L: characteristic length, ν: fluid kinematics viscosity factor.

III. COMPUTATIONAL DOMAIN AND BOUNDARY CONDITIONS

Arrangement for one and two square cylinders is shown in Fig. 1, together with the definition of fluid force coefficients. D is the square cylinder' s width. The below square cylinder is marked with (1) and the above square cylinder is marked with (2). This paper discusses side-by-side arrangement. We also simulate the flow around two square cylinders for G = 0.05, 0.1, 0.2 and 0.3. The computational domain and boundary conditions are shown in Fig. 1, we adopt non-uniform mesh, the mesh size adjacent to the square cylinder is 0.01, the interval for time advancement is equal to 0.02. The initial conditions are: u = Uo, v = 0.0, except at the surface of square cylinder; u = 0.0, v = 0.0. The Reynolds number is variable between 5 to 80 for Laminar flow and between 5000 to 22000 for turbulent flow.

IV. NUMERICAL MODELING

The study investigates flow past two square obstacles in a confined domain as shown in figure 1. The two square obstacles with edge length D are placed in the computational domain parallel to the flow. The two square obstacles are placed on the center of the y-axis and the spacing G is varied. The numerical simulations are carried out using a commercial software, Ansys-Fluent. It is based on a second order finite volume discretization and the SIMPLE pressure correction technique for enforcing the divergence-free condition of the velocity field. We must firstly; study the case of a single square obstacle. The results for different Reynolds number Re=5;10;20;30;80; are illustrated in Figure 2.

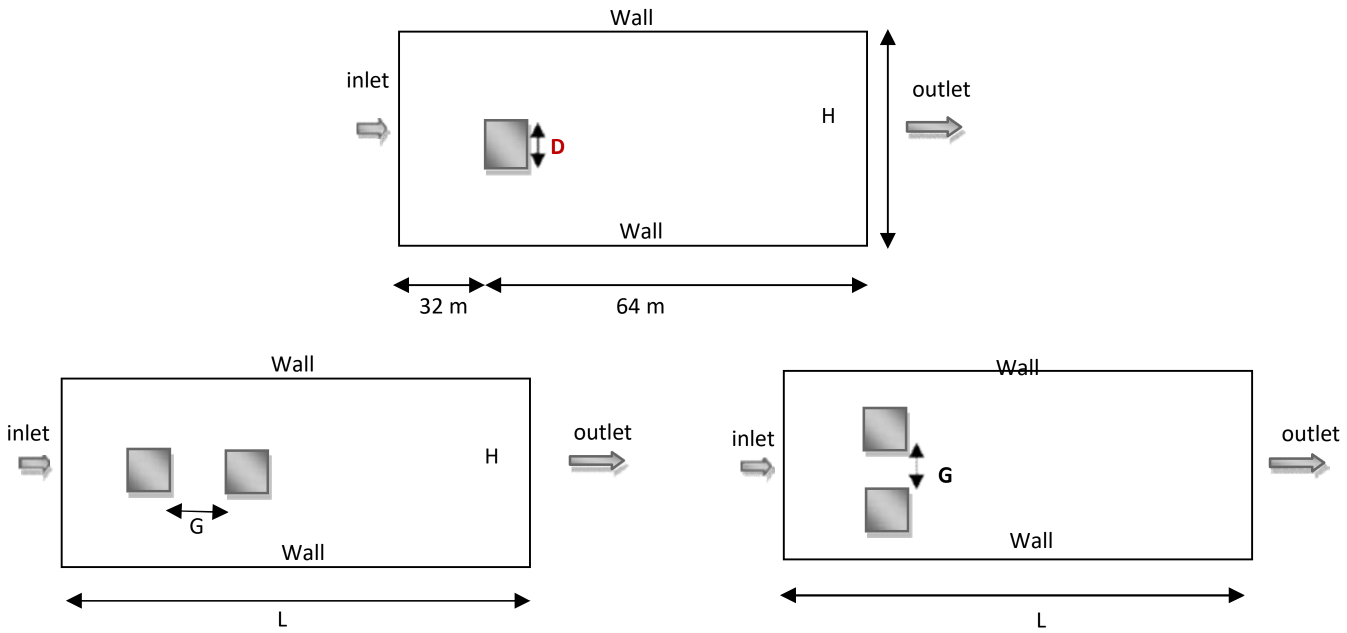

Fig 1. Computational domain for single square obstacle, for horizontal and vertical obstacles

A. *Study of laminar flow around of single square obstacle*

When the Reynolds number is low (Fig. 2), viscous forces dominate and flow is generally laminar and smooth. As the Reynolds number increases, inertial forces become greater, and flows can become turbulent. In the case of flow around a square obstacle, increasing the Reynolds number can lead to significant changes in the flow characteristics. At low Reynolds numbers, flow can be laminar with well-defined streamlines. As the Reynolds number increases, vortices and separation zones can form behind the obstacle, leading to increased pressure losses and drag forces.

In general, a larger obstacle creates greater resistance to flow, which can result in a decrease in flow velocity upstream and an increase in turbulence downstream of the obstacle. This can also affect the formation of vortices and flow separation zones. In Figure 3, we also see that, as it wears, the number of recirculation zones increases as a function of time as do these lengths. It is important to note that these effects also depend on the flow speed, the viscosity of the fluid and the shape of the obstacle itself. Therefore, it is always necessary to consider all these factors to evaluate the effect of a change in obstruction diameter in a given flow [21].

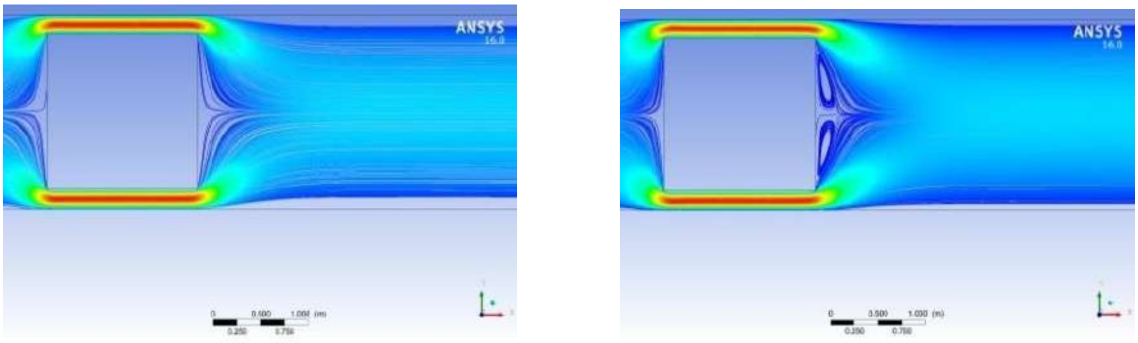

(a) :Re =5

(b) : Re=10

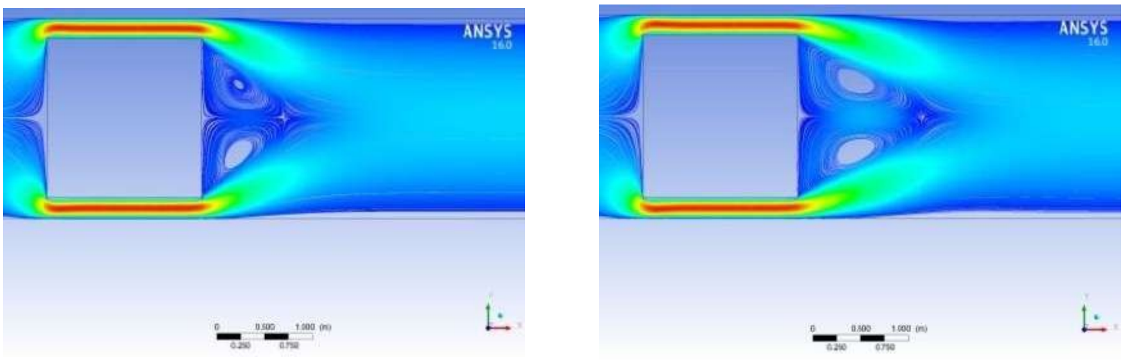

(c) : Re=20

(d) : Re=30

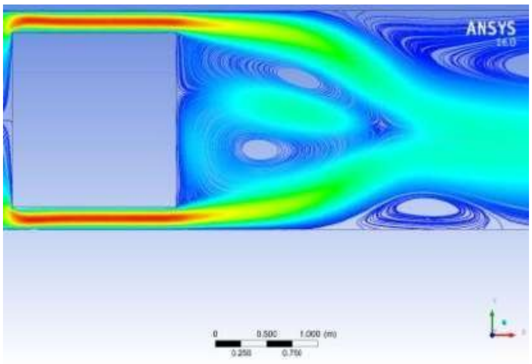

(e) : Re=80

Fig 2. The Streamlines around a single square obstacle with change in Reynolds Number

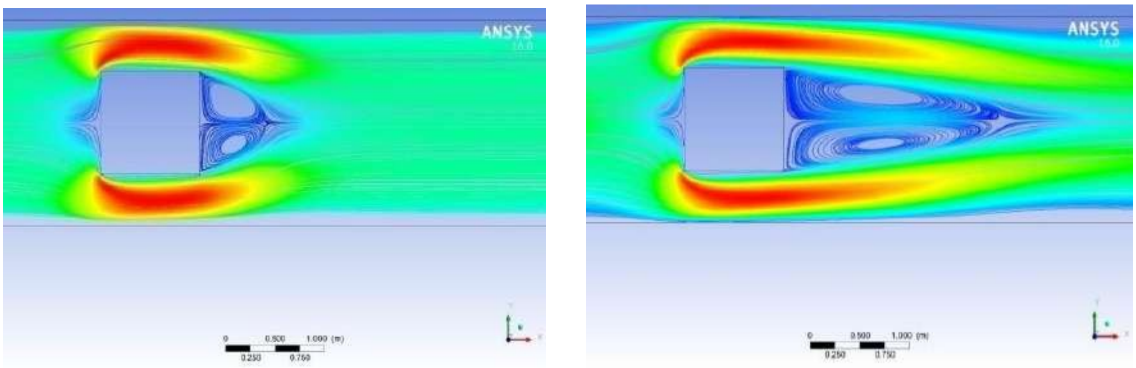

Fig 3. The Streamlines around a single square obstacle with change in time (0.01s to 2s)

Different values of Re are given in Figs. 2(a) ; 2(d) and 2(e) (only some representative cases shown). These figures indicate three different states of flow: the first one is steady state, the second one is transitional state and the third one is unsteady state. In steady state, the flow, after interacting with cylinder, moves steadily without any vortex formation (Fig. 2(d)), The main reason for steady state is low value of Re. Transitional state starts from Re = 80. Two recirculating eddies appear adjacent to the downstream position of cylinder (Fig. 2(b)). These eddies show that there is some unsteadiness appearing in flow. The increasing amplitude of lift cycles shows that the unsteadiness is dominating the steadiness of flow with passage of time fig (3). This transitional state indicates the weakening effect of viscous forces. This state ranges from Re = 30 to 80 and after that the flow becomes completely unsteady. The variation of streamlines in the wake of obstacle indicates the generation of vortices (Fig. 2(c)). From above, it can be concluded that the flow around a single square cylinder is steady in the range of Re 1 -30, transitional in the range of

ISSN: 2961-6611

Re 35- 60 and unsteady for Re = 80. Our findings agree well with those of Gera and al [19] and Sohankar and al [22] These observations indicate that the results obtained from the present code have good qualitative agreement with those of other researchers.

B. Study of turbulent flow around of single square obstacle

Figures (4-6), shows the instantaneous vortex contours around the square section. For different Reynolds numbers (5000-10000- 22000) at time t=5s. it can be seen from these figures that there were many vortex structures around the sections. The lower side was dominated by positive vortices. While negative vortices dominated the upper side. With the formation and development of vortices downstream, alternating vortex loss occurred in the wake region, and changing the corner recession did not change the vortex development tendency. The results are compared with the work of Zhang, Ling [38] and Sercan Yagmur et al,[39]. It is also noted that the length of the recirculation zone increases with increasing Reynolds number.

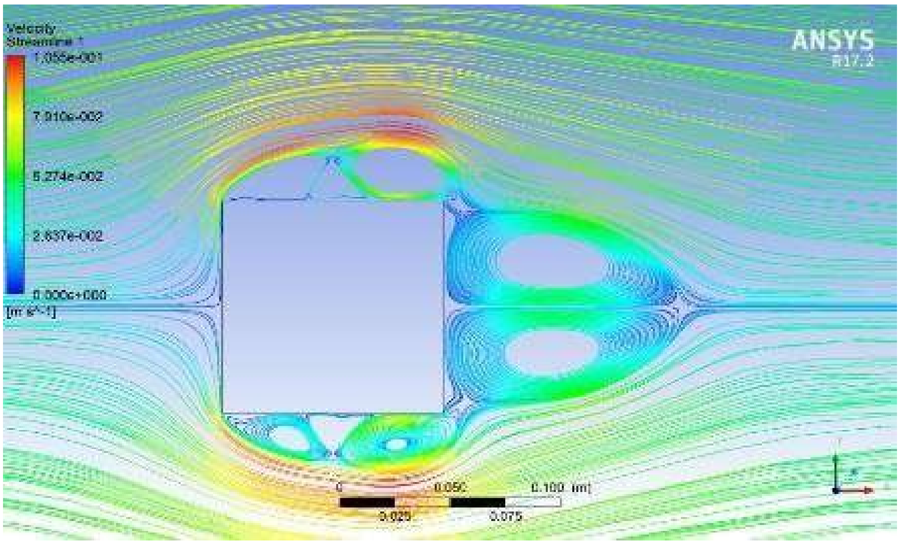

Fig 4. The Streamlines around a single square obstacle with Re= 5000 at t=5s

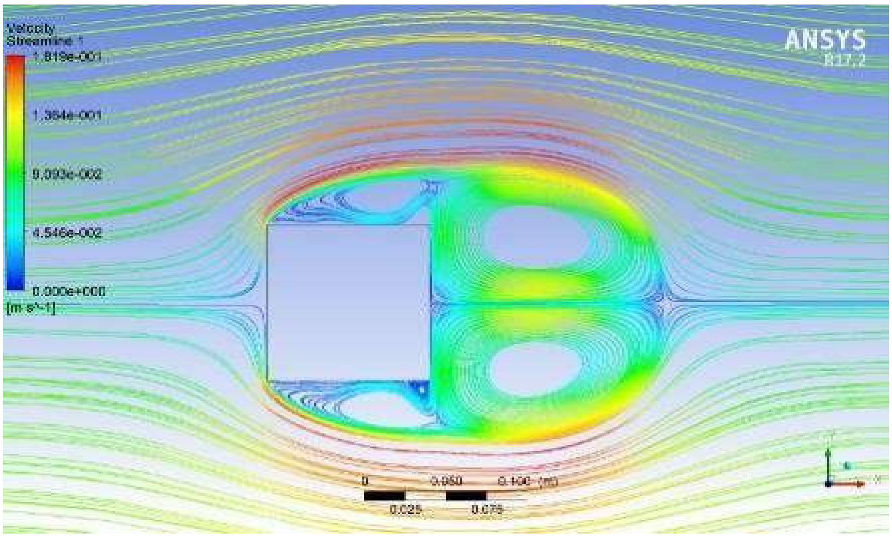

Fig 5. The Streamlines around a single square obstacle with Re= 10000 at t=5s

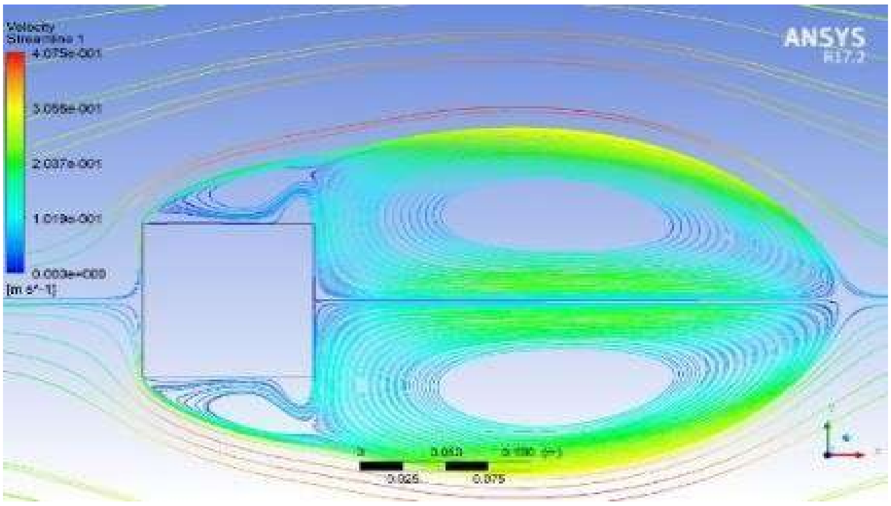

Fig 6. The Streamlines around a single square obstacle with Re= 22000 at t=5s

C. *Temporal evolution of the turbulent flow around a square obstacle*

Figure 7, shows the contours of the longitudinal velocity for different Reynolds numbers respectively. We notice a symmetrical flow which shows the presence of vortices at the separation. We note a specific change of vortex which develops by visualizing the Von-karman vortex path with an elongation of the wake zone. We thus witness the appearance of pairs of alternating vortices which detach behind the obstacles. The evolution of the velocity contours as a function of time shows that at the beginning of the flow it does not create recirculation zones neither before nor behind the obstacle. After a few seconds and from 2s; we clearly notice the appearance of recirculation zones.

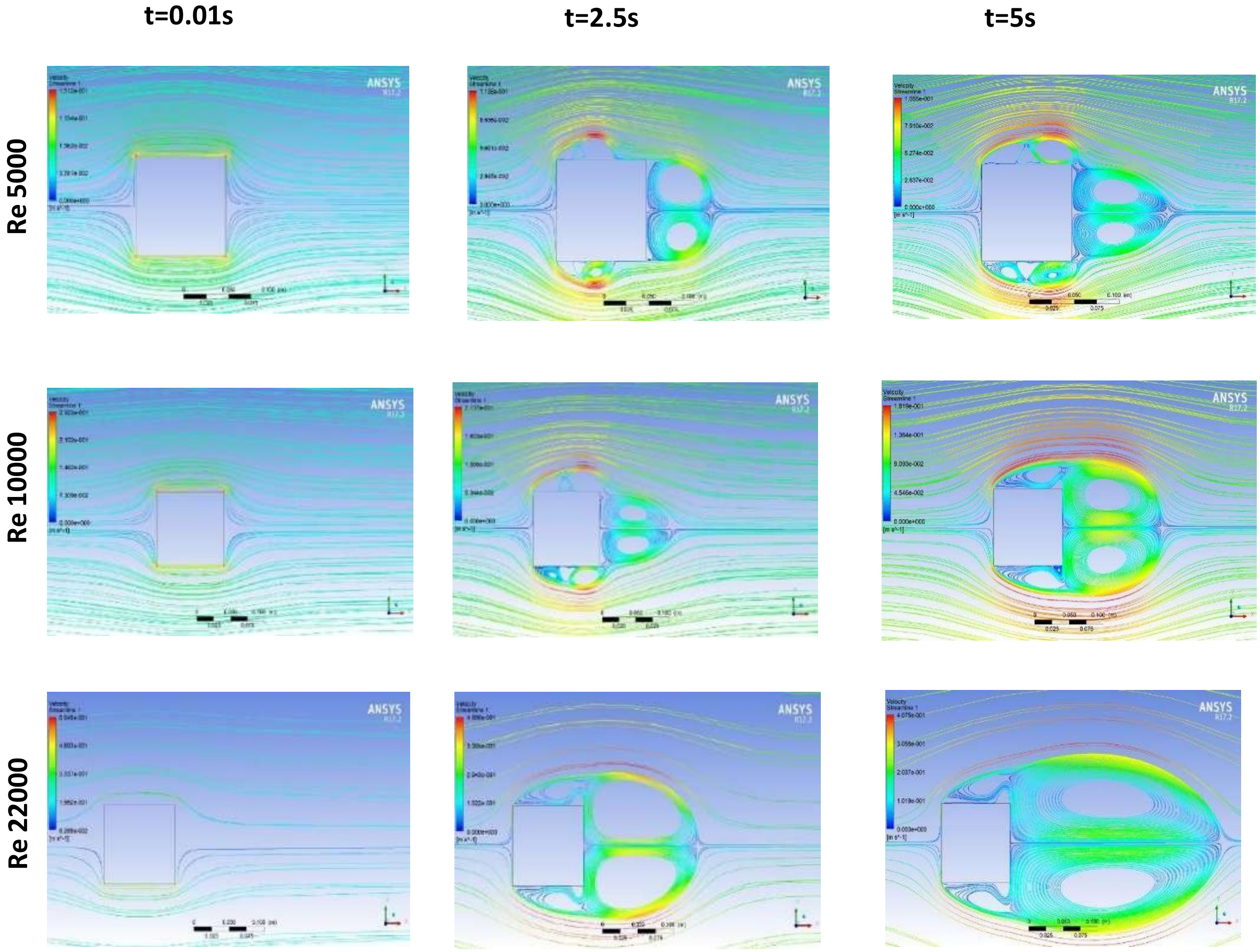

ISSN: 2961-6611

Fig 7. The Streamlines around a single square obstacle with change in Reynolds Number and temporal evolution

D. Study of turbulent flow around of two square obstacles-Horizontal case

Flow past tow square obstacles structures mostly depends on two parameters: Re and G. In this section, the variation of flow states around two side by side obstacles, under the effect of Reynolds numbers, will be discussed at four different gap spacings i.e., G = 0.05, G=0.1, G=0.2 and 0.3. As we have already seen from the above section that there are three main states of flow around a single cylinder: steady state, transitional state and unsteady state, and each state has its own range of Re, in this section we will investigate the range of Re, for these flow states, in the case of two obstacles in the flow field. Furthermore, from previous studies, it can be deduced that at G = 0.05 there is a strong proximity effect of multiple obstacles. The flow characteristics of each cylinder are influenced by other cylinders due to narrow space between these bodies. But at G = 0.05 the proximity effect becomes weaker and each cylinder in the flow field is able to shed its own vortices figures (8) and (11). That’s why we have selected these two spacing values in order to analyze the variation of flow states under the effect of Re at both small and high spacing between the cylinders.

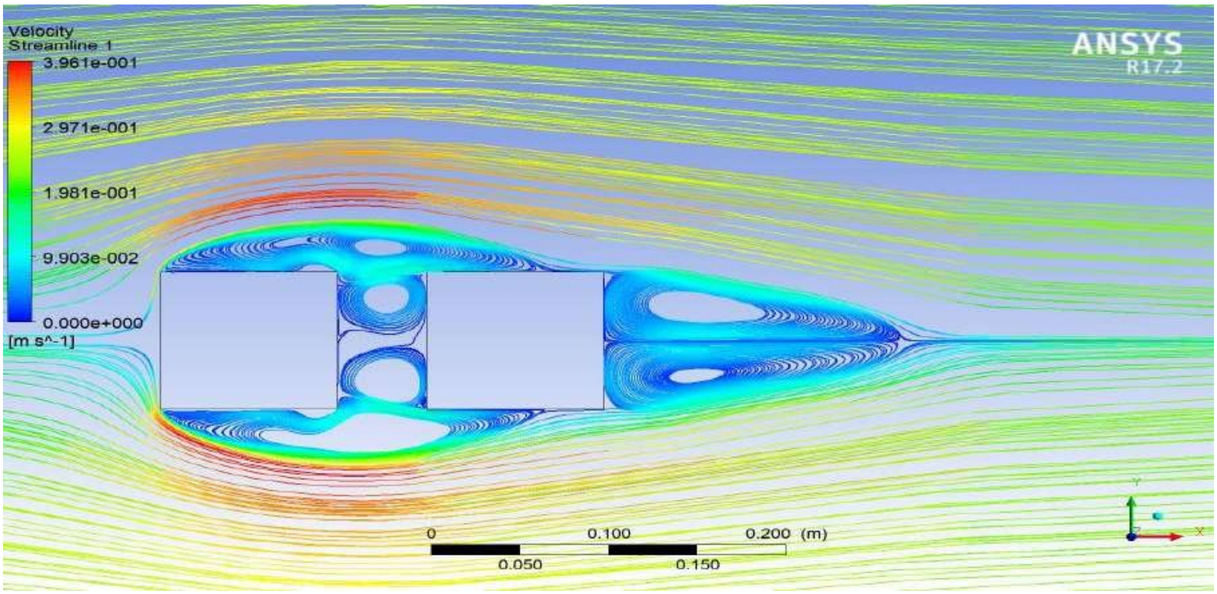

Fig 8. Streamline representation of flow around two horizontal square obstacles for the case of G=0.05 , t=2.5s , Re=22000

Copyright © 2024
ISSN: 2961-6611

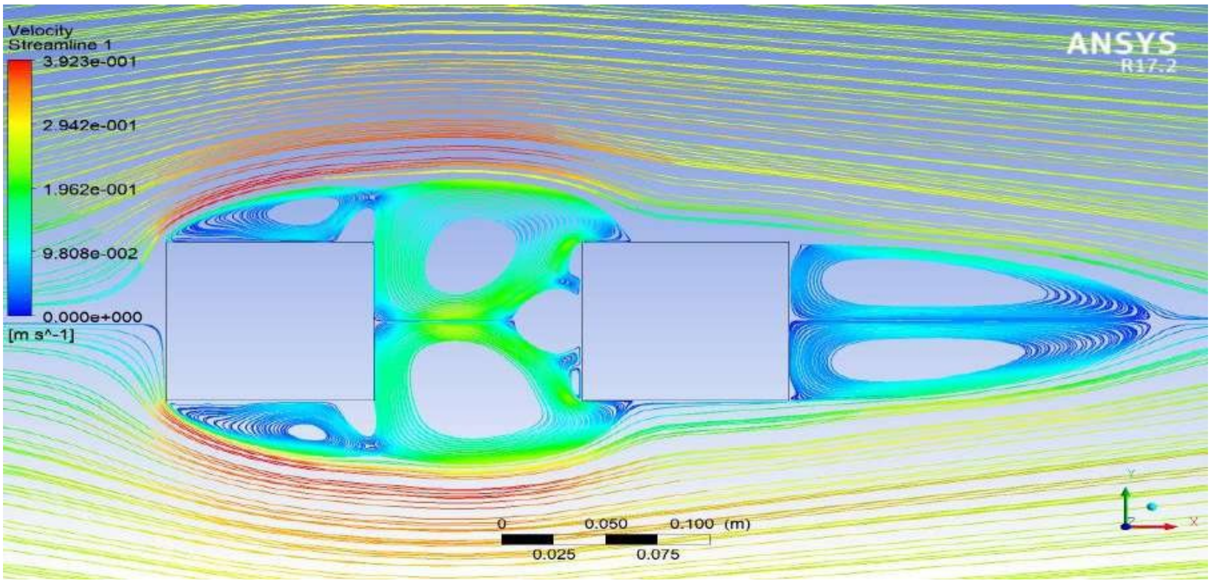

Fig 9. Streamline representation of flow around two horizontal square obstacles for the case of G=0.1 , t=2.5s , Re=22000

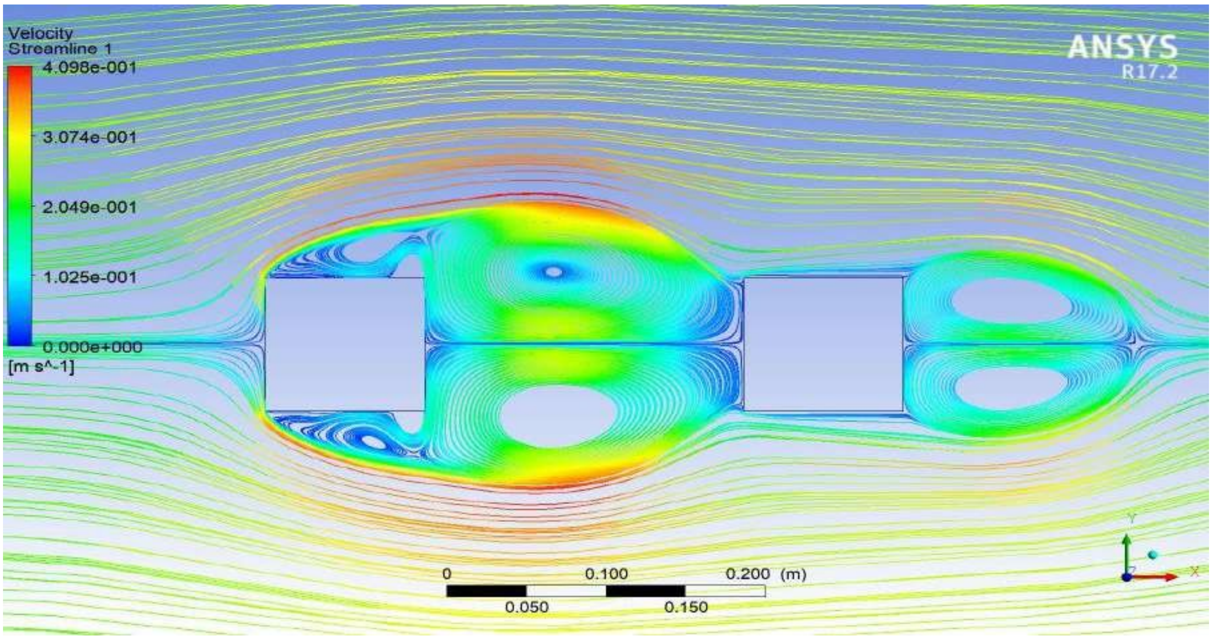

Fig 10. Streamline representation of flow around two horizontal square obstacles for the case of G=0.2 , t=2.5s , Re=22000

ISSN: 2961-6611

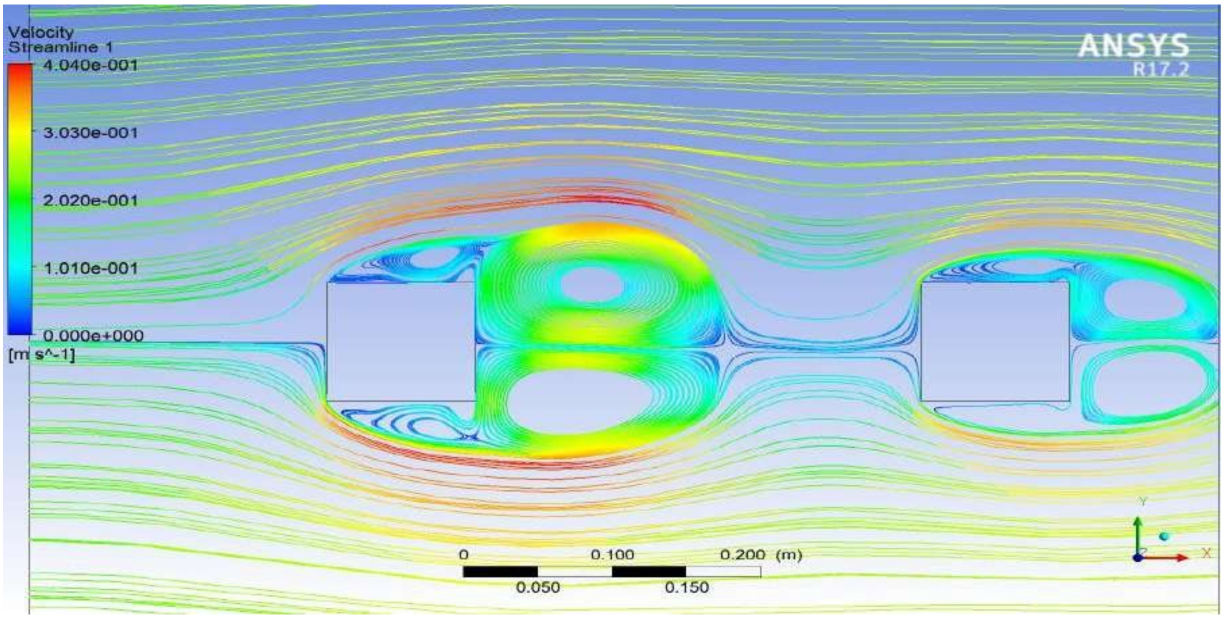

Fig 11. Streamline representation of flow around two horizontal square obstacles for the case of G=0.3 , t=2.5s , Re=22000

E. Study of turbulent flow around of two square obstacles-Vertical case

A representative case of transitional state of flow around two verticals square obstacles, at Re = 22000 and G = 0.05 to 0.3, is shown in Figures. 12 to 15. In this state of flow, the shear layers emerging from the first obstacle move till the exit position of computational domain (Fig. 15). This behavior of flow is different from the steady flow where we have seen only bubbles around the obstacles. Also the unsteadiness occurs in flow due to transverse oscillations in far wake region of obstacles. This unsteadiness can be witnessed from the temporal variation of lift coefficients. Unlike steady state flow, the lift coefficient is constant initially but after some time it becomes nonlinear which indicates transition in flow from steady to unsteady state. According to [25], the unsteadiness in flow around two or more square obstacles.

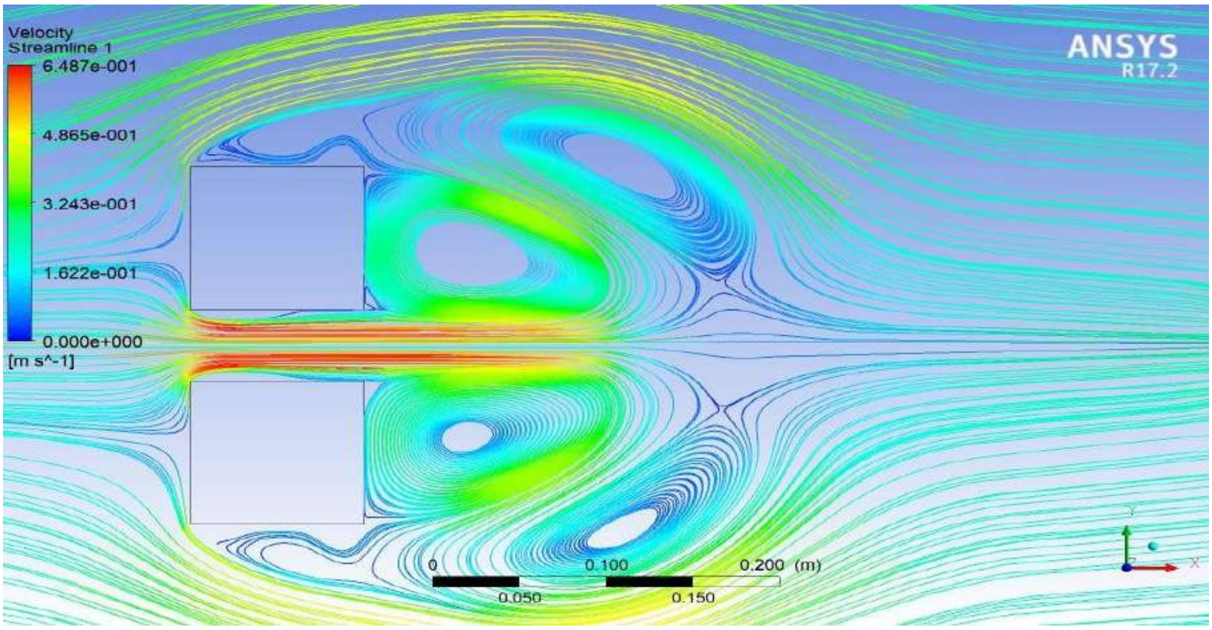

Fig 12. Streamline representation of flow around two vertical square obstacles for the case of G=0.05 ,t=2.5s ,Re=22000

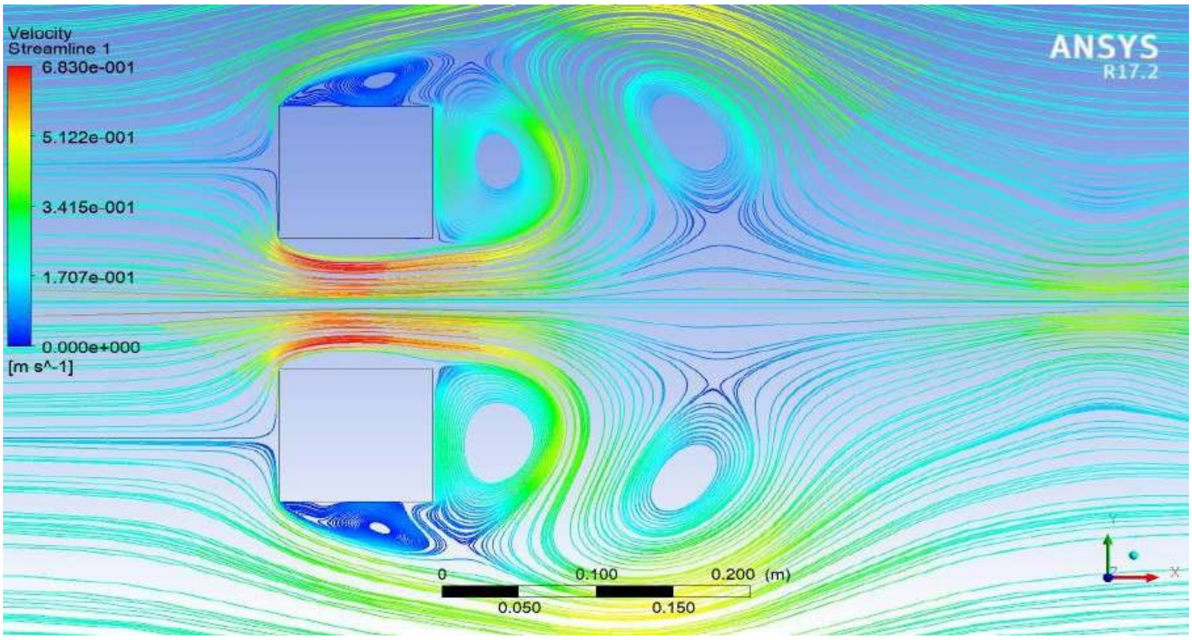

Fig 13. Streamline representation of flow around two vertical square obstacles for the case of G=0.1 ,t=2.5s ,Re=22000

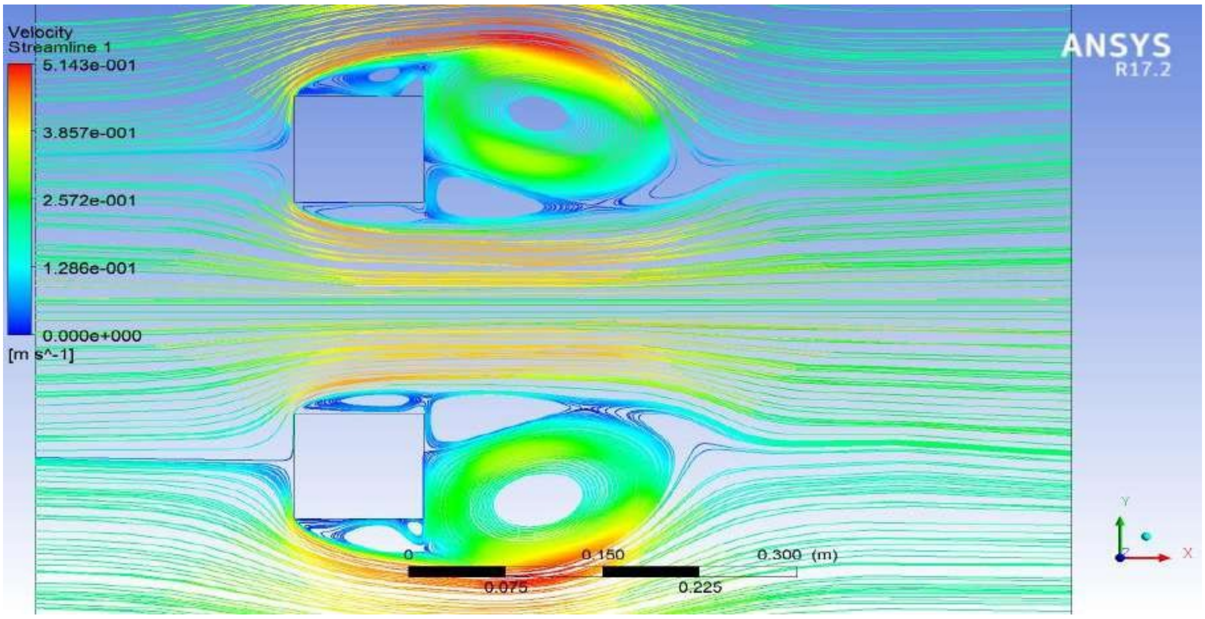

Fig 14. Streamline representation of flow around two vertical square obstacles for the case of G=0.2 ,t=2.5s ,Re=22000

ISSN: 2961-6611

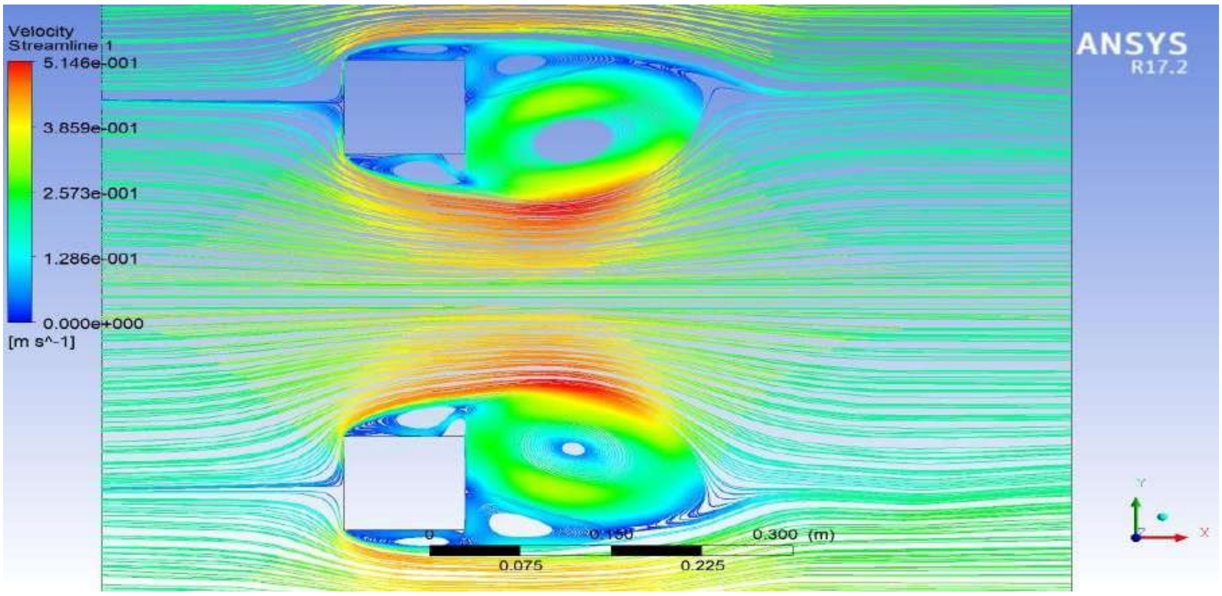

Fig 15. Streamline representation of flow around two vertical square obstacles for the case of G=0.3, t=2.5s ,Re=22000

V. CONCLUSION

The results indicated that the flow pattern is irregular and unstable for single obstacle and small arrangements (G ≤ 0.0.5) when the propagation of vortices does not have any tendency. This result agrees with the results of studies conducted by [4], [11] and [12]. Approximately the same for all our test cases except in G=0.1. In the cases where G is very low, e.g. G=0.1, the values of the average lift and drag coefficients for 1st obstacle were greater than for 2nd obstacle. However, in other cases, as the spacing between obstacles increases, the values of the average lift and drag coefficients decrease and gradually approach the value of the drag coefficient for the single cylinder when the G is high (approximately at 0.3). For higher G arrangements (G=0.3), the mean drag and the mean lift coefficients and the flow pattern for each obstacle are all similar to those for the single obstacle, indicating that the effects of shedding interactions are negligible, so we can say that the flow around the square obstacles is roughly independent.

REFERENCES

[1] Norberg C. Flow around a circular cylinder: Aspects of fluctuating lift. J Fluids Struct 2001;15(3–4):459–69.
[2] Price J, Sumner D, Smith JG, Leong K, Paidoussis MP. Flow visualization around a circular cylinder near to a plane wall. J Fluids Struct 2002;16(2):175–91.
[3] Wang XK, Tan SK. Comparison of flow patterns in the near wake of a circular cylinder and a square cylinder placed near a plane wall. Ocean Eng 2008;35(5–6):458–72.
[4] Manzoor S, Khawar J, Sheikh NA. Vortex-induced vibrations of a square cylinder with damped free-end conditions. Adv Mech Eng 2013;6:1267–91.
[5] Dutta S, Panigrahi PK, Muralidhar K. Effect of orientation on the wake of a square cylinder at low Reynolds numbers. Indian J Eng Mater 2004;11(6):447–59.
[6] Zdravkovich MM. Forces on a circular cylinder near a plane wall. Appl Ocean Res 1985;7(4):197–201.
[7] Shih WCL, Wang C, Coles D, Roshko A. Experiments on flow past rough circular cylinders at large Reynolds numbers. J Wind Eng Ind Aerodyn 1993;49(1):351–68.
[8] Deng J, Ren AL, Zou JF, Shao XM. Three-dimensional flow around two circular cylinders in tandem arrangement. Fluid Dyn Res 2006;38(6):386–404.
[9] Sakamoto H, Haniu H, Obata Y. Fluctuating forces acting on two square prisms in a tandem arrangement. J Wind Eng Ind Aerodyn 1987;26(1):85–103.
[10] Kim MK, Kim DK, Yoon SH, Lee DH. Measurements of the flow fields around two square cylinders in a tandem arrangement. J Mech Sci Tech 2008;22(2):397–407.
[11] Igarashi T, Suzuki K. Characteristics of the flow around three circular cylinders arranged in line. Bull JSME 1984;27:2397–404.

[12] Liu X. Wind loads on multiple cylinders arranged in tandem with effects of turbulence and surface roughness [dissertation]. Baton Rouge: Louisiana State University; 2003.
[13] Hetz AA, Dhaubhadel MN, Telionis DP. Vortex shedding over five in-line cylinders. J Fluids Struct 1991;5(3):243–57.
[14] Xu G, Zhou Y. Strouhal numbers in the wake of two inline cylinders. Exp Fluids 2004;37(2):248–56.
[15] Liu CH, Chen JM. Observations of hysteresis in flow around two square cylinders in a tandem arrangement. J Wind Eng Ind Aerodyn 2002;90(9):1019–50.
[16] Narashima S. Wind loads on multiple cylinders arranged in tandem: Applications to pipe rack structures [dissertation]. Baton Rouge: Louisiana State University; 1999.
[17] Park J, Kwon K, Choi H. Numerical solutions of flow past a circular cylinder at Reynolds numbers up to 160. KSME Int J 1998;12:1200–5.
[18] W. SARWAR ABBASI et al. 18. Rajani BN, Kandasamy A, Majumdar S. Numerical simulation of laminar flow past a circular cylinder. App Math Mod 2009;33 (3):1228–47.
[19] Gera B, Sharma PK, Singh RK. CFD analysis of 2D unsteady flow around a square cylinder. Int J App Eng Res 2010;1:602–10.
[20] Saha AK, Muralidhar K, Biswas G. Transition and chaos in twodimensional flow past a square cylinder. J Eng Mech 2000;126 (5):523–32.
[21] Breuer M, Bernsdorf J, Zeiser T, Durst F. Accurate computations of the laminar flow past a square cylinder based on two different methods: lattice-Boltzmann and finite-volume. International Journal of Heat and Fluid Flow 2000;21(2):186–96.
[22] Sohankar A, Davidson L, Norberg C. Numerical simulation of unsteady flow around a square two-dimensional cylinder Proceedingds of 12th Australasian fluid mechanics conference. 1995. p. 517–20.
[23] Benjamin Renaud, Instabilité de Bénard-Von Karman derrière un obstacle oscillant, Rapport de stage expérimental, Laboratoire de Physique et Mécanique des Milieux Hétérogènes, Paris, 2000.
[24] Khabbouchi, M.S. Guellouz. Ecoulement autour d'un cylinder circulaire proche d'une paroi, Effet de l'écoulement type jet. Laboratoire d'Etude des Systèmes Thermiques et Energétiques, Monastir, Tunisie, 2008.
[25] Benjamin Renaud, Instabilité de Bénard –Von Karman derrière obstacle oscillant. Rapport de stage expérimental, Laboratoire de Physique et de Mécanique des Milieux Hétérogènes, Paris, 2000
[26] Krishna Chaitanya, Dipankar Chatterjee, Effect of blockage on fluid flow past a square cylinder at low Reynolds numbers, Indian Academy of Sciences, Sådhanå (2022)47:4
[27] Zakaria Sari Hassoun and all, Effect of Obstacles on Turbulent Flows in a Rectangular Channel From their Front Sides, Thermal Science: Year 2023, Vol. 27, Special Issue 1, pp. S333-S341
[28] Moustafa Nooroullahi and all, Large eddy simulation of flow over a wall-mounted cube: Comparison of different semi dynamic subgrid scale models, Int. Jnl. of Multiphysics Volume 6 · Number 1 · 2012
[29] Benjamin Leclaire, Etude théorique et experimentale d'un écoulement tournant dans une conduite, Doctorat thesis 21 Décembre 2006.
[30] S. Jakirlic, K. Hanjalic, and C. Tropea. Modeling rotating and swirling turbulent flows : a perpetual challenge. AIAA J., 40(10) :1984–1996, 2002.
[31] D. O. Snyder and R. E. Spall. Numerical simulation of bubble-type vortex breakdown within a tube-and-vane apparatus. Phys. Fluids, 12(3) :603–608, 2
[32] Mittal S, Singh S P, Kumar B and Kumar R Flow past bluff bodies: effect of blockage. Int. J. Comut. Fluid Dyn. 20: 163–173-2006
[33] Gu, Z. On interference between two circular cylinders at supercritical Reynolds number. Journal of Wind Engineering and Industrial Aerodynamics, 62(2-3): 175-190. 1996
[34] Gu, Z.F., Sun, T.F., He, D.X., Zhang, L.L. Two circular cylinders in high-turbulence flow at supercritical Reynolds number. Journal of Wind Engineering and Industrial Aerodynamics, 49(1-3): 379-388. 1993
[35] Hamidreza Rahimi , Xiaonan Tang, Yaser Esmaeeli, Ming Li , Alireza Pourbakhtiar. Numerical Simulation of Flow Around Two Side-by-Side Circular Cylinders at High Reynolds Number. International Journal of Heat and Technology Vol. 38, No. 1, March, 2020, pp. 77-91
[36] Alice Rosa da Silva. Flow Dynamics around Two Side by Side Circular Cylinders with Alternating Movements. World Journal of Mechanics, Vol 13 pp 1-19, 2023
[37]Alice Rosa, Antonio Macros. Analysis of flow dynamics around tow rotating circular cylinders in tandem and side by side. International journal of Advenced Engineering research and science Vol-7, Issue-6, jun-2022
[38] Zhang, Ling, "Numerical Simulation of Flows past a Circular and a Square Cylinder at High Reynolds Number, and a Curved Plate in Transitional Flow". Engineering and Applied Science Theses & Dissertations. 264, 2017.
[39] Sercan Yagmur1, Sercan Dogan1, Muharrem H. Aksoy, Eyub Canli, Muammer Ozgoren Experimental and Numerical Investigation of Flow Structures around Cylindrical Bluff Bodies Selcuk University, Engineering Faculty, Mechanical Engineering Department, 42250 Konya, Turkey, 2015

Exploitation of Tunisian date palm sap as a promising carbon source for bioethanol production by a newly isolated yeast strain

Imen BEN ATITALLAH#1, Ioanna NTAIKOU*2, Georgia ANTONOPOULOU*3, Gerasimos LYBERATOS*4, Tahar MECHICHI#5

#*Laboratory of Biochemestry and Enzyme Engineering of Lipases, National School of Engineers of Sfax, University of Sfax, BP 1173, 3038 Sfax, Tunisia.*

1benatitallahimen@gmail.com

5Tahar.mechichi@gmail.com

**Institute of Chemical Engineering Sciences, 11 Stadiou st., Platani, Patras, GR 26504, Greece.*

2iwantaikou@chemeng.upatras.gr

3gerogant@chemeng.upatras.gr

***Abstract*— Among the so called clean fuels, bioethanol is considered to be one of the most promising, whereas it can also be used as fuel additive. However, in order to be sustainable bioethanol production has to be based on renewable carbon sources as well as robust microbial strains exhibiting advanced performance and high yields under various conditions. The present study investigated the efficient utilization of natural date palm sap (DPS) for direct, low cost bioethanol production. For all experiments the newly isolated yeast *Wickerhamomyces anomalus* X19 was used in batch and fed batch mode. Batch experiments were conducted using synthetic media and the DPS based medium at different initial substrate concentrations whereas the effect of low oxygen concentration on the performance of the stain was assessed under microaerobic or anaerobic conditions. Fed batch experiments with DPS were also conducted in order to improve ethanol yield. The scale-up of alcoholic fermentation was performed in batch mode under anaerobic non-pressurized condition. Growth, total and reduced sugars, ethanol and pH were monitored over time. It was shown that strain *W. anomalus X19* was able to grow sufficiently producing significant ethanol concentrations even in media with low pH values and initial concentration of sugars up to 200 g/L. The highest ethanol concentration achieved was 61 g/L, using DPS in batch-mode non-pressurized cultures of 48 hours incubation, whereas in all cases ethanol yields were quite high reaching up to 80 % of the theoretically estimated values. This study provides promising results for the possible exploitation of the DPS as a new renewable, non-cellulosic feedstock for bioethanol production.**

***Keywords*— Date palm sap, bioethanol, *Wickerhamomyces anomalus*, microaerobic and anaerobic fermentation, batch culture, fed-batch culture, scale-up.**

I. INTRODUCTION

The date palm trees are widely cultivated in various arid and semi-arid regions throughout the world, including North Africa and Arabian Gulf countries, where it plays significant socio-cultural, economic, and ecological roles. The cultivated surface of date palms in 2006 was estimated at 1.18 million hectares in the world. In Tunisia, for instance, date palm oases cover an area of about 46,000 hectares with around three million trees [1]. Tunisian date palm culture provides annually about 4 % of the total value of agricultural production and 13 % of the total value of agricultural exports. In addition to date fruits, palm trees offer several other derivatives (such as leaves, trunks, and seeds), which are used for various traditional and industrials activities such as roofing, fencing, basket making, and animal feeding [2]. Date palm sap (DPS), known in Tunisia as “legmi”, is one of the popular derivatives of date palm trees. During one tapping season, a date palm tree may offer a total sap yield up to 500L [3]. Composition analysis of fresh sap revealed that sugars are the major components (92 – 95 % dry matter basis) with the dominance of sucrose with small amounts of glucose and fructose [4]. In spite of the availability and the typical properties of DPS, the exploitation of this resource is still limited and no study has so far reported its potential as a promising carbon source for alcoholic fermentation. Thus, to the best of our knowledge, this is the first report describing the possible exploitation of the natural DPS extracted from palm trees as a renewable feedstock for direct bioethanol production. Batch experiments were conducted using DPS based medium under microaerobic or anaerobic conditions, followed by fed-batch and scale-up fermentations to evaluate growth and ethanol production

ISSN: 2961-6611

profile of the newly isolated yeast *W. anomalus* X19. The isolated strain was taxonomically characterized and its ability to grow and produce ethanol at various concentrations of sugars, at low pH and under anaerobic conditions was tested.

II. MATERIALS AND METHODS

1. Yeast isolation and molecular Identification

In the present study, the yeast strain *W. anomalus X19* (MH237950.1) was recently isolated from a sample of decaying wood collected from a forest located in the north west of Tunisia. The sample of decaying wood was transported in sterilized plastic bags and brought to the laboratory without further exposure to the external environment. 2 g of the sample were inoculated to 50 mL of yeast peptone dextrose medium (YPD) containing: 10 g/L yeast extract, 10 g/L peptone and 20 g/L glucose and incubated at 30 °C on an orbital shaker at 150 rpm. When growth was detected, successive serial dilutions was performed in sterilized physiological water (NaCl 0.9 %, w/v in water). Aliquots of each dilution (0.1 mL each) were spread on YPD agar (5 g/L yeast Extract, 5 g/L peptone, 10 g/L glucose and 20 g/L agar, pH 5.5) plates supplemented with 50 mg/L Chloramphenicol to avoid bacterial contamination and incubated for 48 h at 30 °C. The purified isolates were stored on YPD agar plates at 4 °C. For long-term preservation, the strain was stored in 20 % glycerol at − 80 °C.

The yeast isolate was identified by sequence analysis of the D1/D2 domain of the 26S rRNA and the ITS region [5]. The D1/D2 domain and the ITS region were amplified as described before by Kurtzman and Robnett [6] and Fell et al. [7]. Sequencing of the PCR products was done by Seqlab GmbH, Göttingen, Germany. The generated sequences were compared to the sequences of related species retrieved from the NCBI database using BLAST search in GenBank.

2. Feedstock used

The DPS was tested in this study as a suitable substrate for bioethanol production. Fresh DPS was kindly provided from palm trees planted in the region of Gabes “South east of Tunisia” in March 2017. The juice was collected from a shallow depression scooped out at the top. The samples were immediately stored in an ice box (4 °C) to avoid fermentation during transportation to the laboratory. Prior to use, the juice was centrifuged at 8000 rpm for 15 min at 4 °C to remove solid particles and the supernatant was sterilized for 121 °C for 20 min then stored at 4 °C until further use.

3. Bioethanol production

3.1 Inoculum preparation

One loopful of a single colony of the yeast *W. anomalus* X19 was transferred from the agar plate into 50 ml of sterile YPD proliferation media containing: 20 g/L glucose, 10 g/L yeast extract and 10 g/L peptone. The inoculum was cultivated overnight in 250 ml Erlenmeyer flask on a rotator shaker (150 rpm) at 30 °C.

3.2 Small scale batch and fed batch experiments

The fermentation was carried out comparatively in batch and fed-batch systems. In both fermentation systems, experiments were carried out in 160 mL serum vials with an initial working volume of 25 mL at 30 °C with orbital shaking at 150 rpm.

In batch experiments, the efficiency of the isolated yeast *W. anomalus* X19 to produce ethanol was assessed in various defined media containing 30 - 120 g/L of sugars (i.e. sucrose, sucrose /D-glucose mixture, D-xylose, D-xylose/D-glucose mixture, L-arabinose, L-arabinose/D-glucose mixture, cellobiose and cellobiose/D-glucose mixture) with 2 g/L of yeast extract or NH4Cl supplementation. The fermentations were performed during 96 h.

DPS based medium was evaluated as economic culture medium. The effect of diluted oxygen on the performance of the yeast strain was assessed in batch mode using this substrate under microaerobic and anaerobic conditions. Aerobic experiments were performed in 100 ml flasks plugged with hydrophobic cotton and incubated at 30 °C with mechanical agitation at 150 rpm. For anaerobic fermentations under pressurized condition, experiments were carried in serum vials sealed with rubber stoppers. While anaerobic fermentations under non-pressurized condition were conducted in serum vials capped with rubber stoppers pierced with a needle to allow the release of the carbon dioxide produced during the fermentation.

The fed-batch fermentation was performed under anaerobic non-pressurized condition with sterile DPS based medium. The feeding regime used was stepwise feeding. Feeding of the DPS was performed as described in Table 1. The initial total sugars concentration and initial cell mass concentration were the same in all the experiments. The fermentations were performed during 144 h.

TABLE I
ADDITION OF FRESH MEDIUM IN FED-BATCH MODE DURING THE FERMENTATION OF DPS

	Starting batch	First feeding	Second feeding	Third feeding	Forth feeding
	0 h	24 h	48 h	72 h	96 h
FB1	25 ml DPS	+ 5 ml DPS	+ 5 ml DPS	+ 5 ml DPS	+ 5 ml DPS
FB2	25 ml DPS	-	+ 10 ml DPS	-	+ 10 ml DPS
FB3	25 ml DPS	-	-	+ 20 ml DPS	-

In all experiments, cells were harvested from pre-culture of the yeast *W. anomalus* X19 equal to 5 % inoculum by centrifugation at 6000 rpm for 10 min, suspended in mineral salt solution containing the following nutrients (g/L): NH_4Cl, 2.0; KH_2PO_4, 0.05; and $MgSO_4.7H_2O$, 0.05. The initial pH of DPS was not adjusted for fermentation. At selected time intervals, samples withdrawn from the fermentations were centrifuged at 6000 rpm for 10 min, filtered through 0.7 µm filters and then analyzed for ethanol and sugars quantification. Microbial growth and pH were monitored over time. All experiments were carried out aseptically and analyses were performed in duplicate.

3.3. Scale-up batch experiment

In order to investigate the scaling up of alcoholic fermentation, experiments were performed in batch mode under anaerobic non-pressurized condition using a 1.2 L bioreactor with 200 mL working volume.

The substrate and the bioreactor were sterilized at 121 °C for 20 min before inoculation. Inoculum was prepared with centrifuged cells from pre-culture of *W. anomalus* X19 corresponding at 5 % v/v. NH4Cl, KH2PO4, and MgSO4.7H2O at concentrations of 2.0, 0.05 and 0.05 g/L respectively, were also added, for nutrients supplementation. pH of the DPS was not adjusted. During the fermentation, the temperature was set at 30 °C and the agitation was maintained at 150 rpm. Samples were periodically withdrawn at regular time intervals for analyses of sugars, ethanol contents and biomass. The pH values were also reported. Duplicate runs were performed and the average values of the two runs are reported.

4. Analytical methods

Total solids (TS), volatile solids (VS) and Total Kjeldahl Nitrogen (TKN) quantified according to Standard Methods [8]. Crude protein content was determined by multiplying TKN by a factor of 6.25 [9]. Phosphorous content was determined by vanadomolybdophosphoric acid method [8]. Total sugars concentration was measured by the phenol-sulfuric acid method described by DuBois et al. [10]. Reducing sugars concentration was determined in the growth media according to the DNS (3, 5-dinitrosalicylic acid) method as described by Miller [11] and was expressed as glucose. The minerals Na, K, Mg, Ca, Cu, Zn, Co and Fe were quantified by atomic absorption spectrometry. In order to estimate biomass, optical density (OD) was measured at 600 nm and subsequently biomass concentration (Cbiomass) was determined through the equation:

$$C_{biomass}\ (g/L) = 1.0858 * OD - 0.1376\ (R^2 = 0.993).$$

Ethanol was quantified via HPLC-RI (Shodex) with an Aminex HPX–87H column (Biorad) at 600C and a Cation H micro-guard cartridge (biorad Laboratories), with H_2SO_4 0.006N mobile phase at a flow rate of 0.7mL.min-1. The standard curve for ethanol was plotted using standard ethanol sample. Bioethanol yield (Y), volumetric productivity and fermentation efficiency (FE) were determined using the following equations as described by Laopaiboon et al. [12]:

$$\text{Fermentation Efficiency (FE, \%)} = \frac{\text{Obtained yield (g)}}{\text{Theoretical yield (g)}} \times 100$$

$$\textit{Volumetric productivity (g/l.h)} = \frac{\text{Maximum bioethanol concentration (g/L)}}{\text{Fermentation time (h)}}$$

$$\text{Bioethanol yield (Y, g/g)} = \frac{\text{Bioethanol concentration (g/L)}}{\text{Total utilised sugar (g/L)}}$$

ISSN: 2961-6611

III. RESULTS AND DISCUSSION

1. Identification of the isolated yeast: molecular characterization and taxonomy

The selected yeast strain X19 was identified by analysis of the sequence of its 26S rRNA D1/D2 domain and compared with sequence of type strains from the database of the NCBI (accession number indicated in Fig 1. Alignment results of the rRNA sequences of the isolate showed that the sequence of strain X19 (MH237950.1) have 100 % similarity with *Wickerhamomyces anomalus* strain H7 (KM655847.1). To confirm the position of each strain in phylogeny, a number of sequences were selected from the NCBI database and the phylogenetic tree was contracted using the MEGA7 software. As shown in Fig. 1 the isolate X19 share the same clade cluster of the phylogenetic tree of D1/D2 26S rDNA sequences corroborating all they belong to the genus *Wickerhamomyces*.

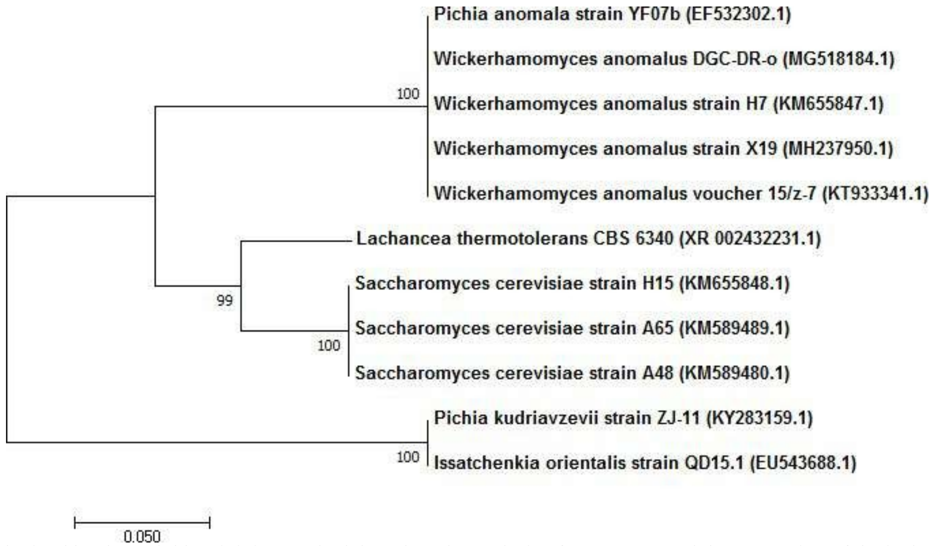

Fig 1. Phylogenetic tree obtained by the Neighbor-joining method, based on the analysis of 26S rDNA and the ITS region of the isolate strain X19. The strain was identified within the genus *Wickerhamomyces*. Access number type strain is in parentheses.

1. Composition of DPS

Chemical composition of DPS is shown in Table 2. It can be seen that DPS had high total sugar content. It is mainly composed of a mixture of sugars and other minor substances. It contained 92 total carbohydrates, 1.4 proteins and 2.56 mineral (g/100 g dry matter basis). Analysis revealed that dry matter represents 17.32 %. The pH of the sap was approximately 5.0. This result could explain the fact that the sap may be used as substrate for ethanol fermentation.

TABLE 2
PHYSICOCHEMICAL CHARACTERISTICS OF THE DATE PALM SAP USED IN THIS STUDY.

Characteristics	**Data**
pH	**4.8**
Dry matter (%)	17.32 ± 0.4
Ash (g /100 g dry matter)	2.56 ± 0.13
Reducing Carbohydrates (g/L)	18.345 ± 0.08
Total Carbohydrates (g/L)	200.013 ± 0.12
TNK (g /100 g dry matter)	0.224 ± 0.076
Protein (g /100 g dry matter)	1.4 ± 0.02
P *	40.14 ± 0.30
Na *	11.04 ± 0.19
Mg*	297.88 ± 0.21
K *	484.57 ± 0.03
Ca *	14.55 ± 0.08
Fe *	1.44 ± 0.41
Cu *	0.74 ± 0.12
Zn *	0.34 ± 0.07
Co *	< 0.01

Values are the means ± standard errors of three determinations. *mg /100 g dry matter basis.

2. *The batch and fed batch small scale experiments*

In order to study the ability of the yeast *W. anomalus* X19 to utilize DPS based medium as the sole renewable carbon source, we examined the effect of diluted oxygen concentration on the performance of the yeast for bioethanol production in batch culture under both anaerobic and microaerobic conditions. The results are shown in Fig. 2.

It can be noted that a similar ethanol production pattern was observed in anaerobic fermentation under both pressurized and non-pressurized condition and the amount of ethanol produced was also comparable. At the beginning of fermentation, there was a rapid increase in ethanol production and a rapid decrease in sugar concentration. This behavior can be attributed to two factors, first the active structure of the yeast which does not take much time to react, second the rich substrate that contains most of the nutrients which cause rapid adaptation and development of microorganisms. The maximum yields of ethanol concentrations were 61.08 and 61.07 g/L after 48 h of fermentation under anaerobic pressurized and non-pressurized fermentations respectively. For microaerobic fermentation, the ethanol concentration reaches its maximum value (51.62 g/L) after 48 h of fermentation and then showed a rapid decline.

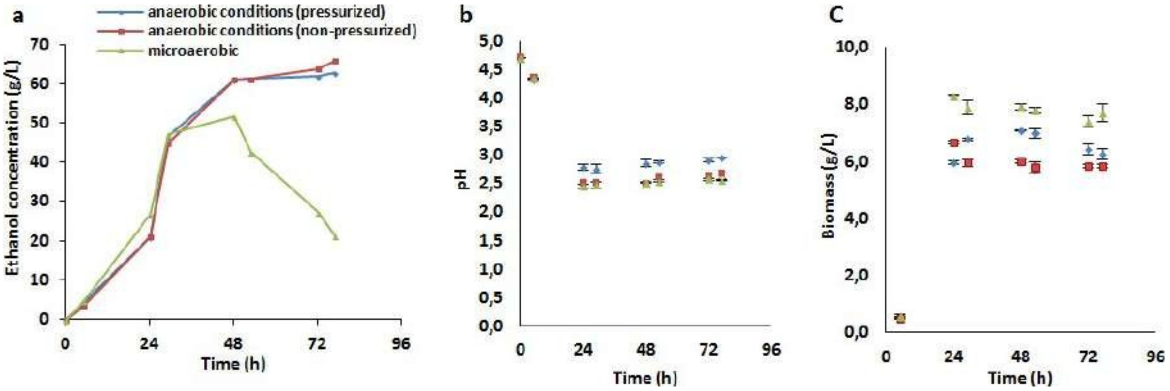

Fig 2. Kinetics of pH and cell growth during ethanol production from DPS based medium in batch mode under microaerobic and anaerobic conditions.

It is evident from Fig 2.C that the strain *W. anomalus* X19 is capable of growing both with and without oxygen supply, although the growth was much faster in aerobic condition when oxygen was present. The cell mass increased rapidly during the first 48 h of fermentation followed by a period of much slower growth. Maximum biomass values of 8.3 g/L were obtained after 24 h of fermentation under aerobic fermentation, while the respective value of biomass during growth of the strain was equal to 6.018 g/L and 7.035 g/L after 48 h of fermentation under anaerobic pressurized and non-pressurized fermentations respectively. Fig 2.b shows the effect of pH on ethanol production. It can be seen that the pH gradually decreases in all cultures during the 24 h. Then, it tends to fluctuate between 2.5 and 2.8.

Three fed-batch experiments under anaerobic non-pressurized conditions were performed with DPS based medium in order to improve ethanol yield. Cell growth, pH, sugar consumption and ethanol production results are shown in fig. 3. The effects of feeding on ethanol fermentation were investigated for fed-batch culture. All fermentations were compared at 96 h.

The fist fed-batch cultivation (FB-1) was performed by feeding 5 ml of DPS every 24 h. In this case, fig 3.a-1 shows that the ethanol production was 63.73 g/L giving 0.484 g/g bioethanol yield per consumed sugar. The fermentation efficiency reached 94.866 %. The second fed-batch culture was fed with 10 ml of DPS every 48 h. As observed in fig 3.a-2, the ethanol concentration was 70.1 g/L resulting from the maximum ethanol yield and fermentation efficiency of 0.5 g/g consumed sugar and 97.94 % respectively. The third fed-batch cultivation was fed with 20 ml of DPS after 72 h. Fig 3.a-3 shows that the ethanol yield was slightly lower compared to other fed-batch cultures.

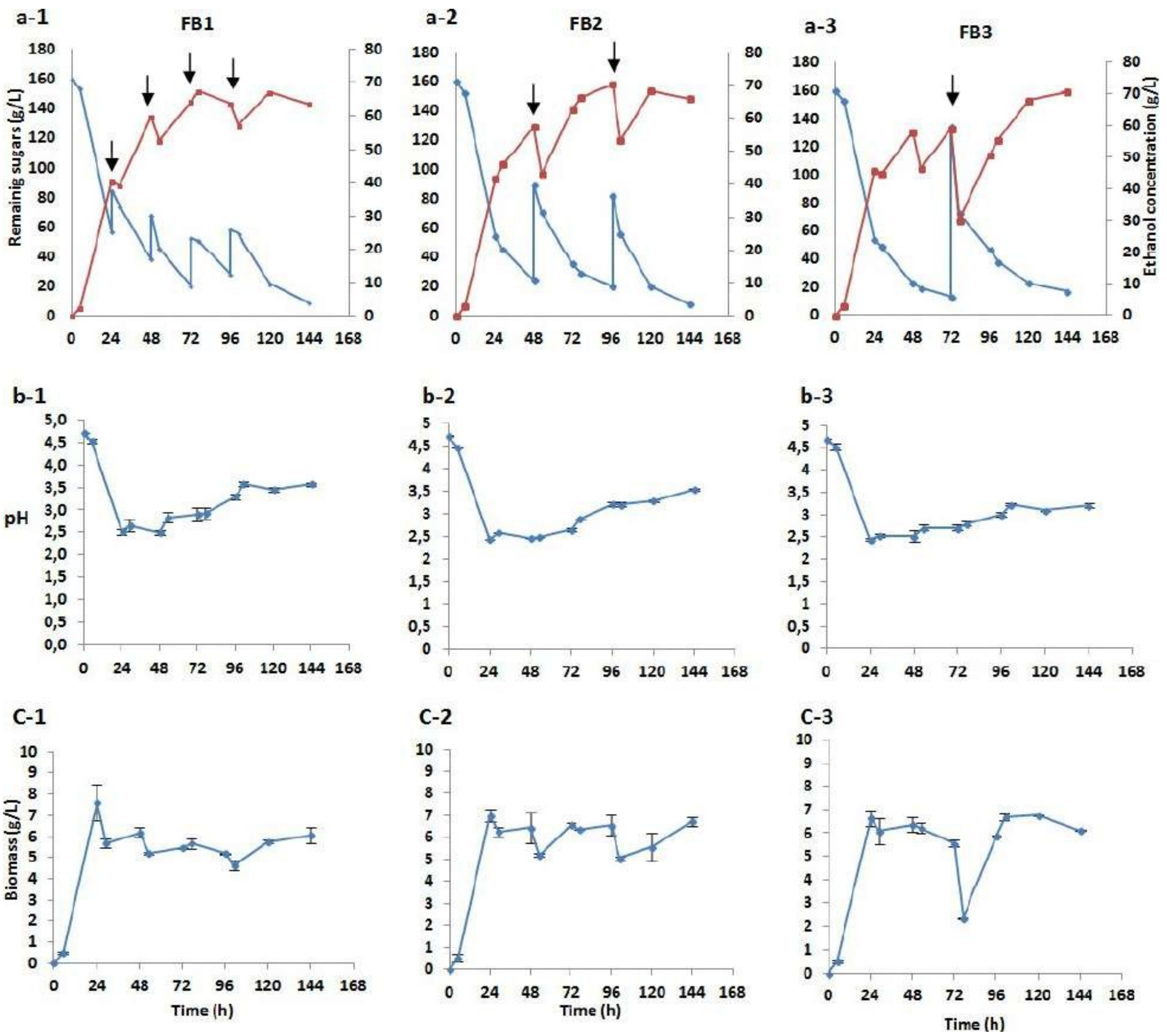

Fig 3. Kinetics of pH, cell growth, sugar consumption and ethanol production from DPS based medium in fed-batch fermentations.

3. The scale-up experiments

The experimental profile of bioethanol production by *W. anomalus* X19 cultivated in DPS based medium at scale-up condition under anaerobic non-pressurized condition is depicted in Fig 4.a it can be seen that bioethanol production started immediately from the first hours of fermentation. The ethanol concentration increased gradually until reaching a steady state after about 48 h of fermentation. The sugar consumption showed down and the fermentation medium becomes more acidic after the production of both ethanol and carbon dioxide. Higher bioethanol production (61.51 g/L) has been obtained after 48 h, giving 0.41 g/g bioethanol yield per sugar consumed.

The variation of pH during alcoholic fermentation is given in Fig 4.b. It showed a rapid decline from 5 to 2.5 during the first 24 h. Then, it tends to stabilize around 2.5. The decrease in the pH was due to the production of carbon dioxide that acidifies the medium, followed by ethanol formation and a small amount of carboxylic acids. The yeast *W. anomalus* X19 has great tolerance to low pH values which is in agreement with the description of the yeasts of the *Wickerhamomyces* genus.

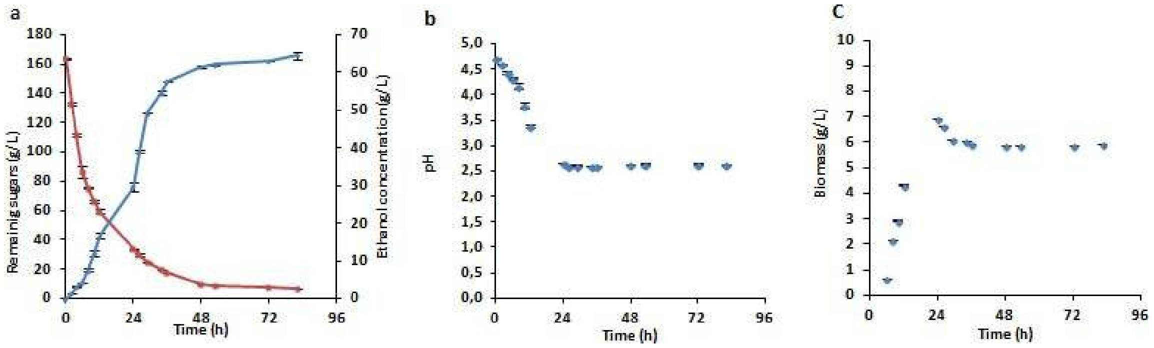

Fig 4. Kinetics of pH, cell growth, sugar consumption and ethanol production from DPS based medium in scale-up condition.

Kinetics of *W. anomalus* X19 were performed using DPS based media in scale-up condition and several parameters including ethanol concentration, ethanol yield and fermentation efficiency were estimated (Table 3).

TABLE 3
QUANTITATIVE DATA ORIGINATED FROM KINETICS OF *W. ANOMALUS* CULTIVATED IN DPS BASED MEDIUM AT SCALE-UP CONDITION.

Medium	**Fermentation parameters**			
	t (h)	**P_E (g/L)**	**$Y_{E/S}$ (g/g)**	**FE (%)**
DPS based medium	12	16.6	0.16	32.34
	24	29.67	0.23	45.9
	48	61.51	0.41	80.16
	72	63.00	0.41	81.01

Fermentation time (t, h), ethanol production (P_E, g/L), ethanol yield (YE/S, g/g) and fermentation efficiency (FE, %). Values represent the means of double independent experiments. Culture conditions: temperature, 30 °C ± 1 °C; agitation rate 150 rpm.

IV. CONCLUSIONS

This study provides that the newly isolated yeast strain *W. anomalus* X19 can be employed efficiently in bioethanol production. Results showed that promising ethanol yields obtained from different fermentation cultures of DPS based medium were quite high reaching up to 80 % of the theoretically estimated values. This demonstrated that the fresh DPS is a complete medium for alcoholic fermentation. In addition, the unnecessary pretreatment and enzymatic hydrolysis of the sap has promoted this substrate as an attractive feedstock. Therefore, a large amount of unexploited DPS could serve as a new renewable feedstock for bioethanol production.

REFERENCES

[1] FAOSTAT.: Agro-statistics database. Rome: Food and Agriculture Organization of the United Nations (2008).

[2] Besbes, S., Drira, L., Blecker, C., Deroanne, C., Attia, H.: Adding value to hard date (*Phoenix dactylifera* L.): Compositional, functional and sensory characteristics of date jam. Food Chemistry. 112, 406-411 (2009).

[3] Barreveld, W. H.: Date palms products. Rome: FAO. 101 (1993).

[4] Ben Thabet, I., Francis, F., De Pauw, E., Besbes, S., Attia, H., Deroanne, C., Blecker, C.: Characterisation of proteins from date palm sap (*Phoenix dactylifera* L.) by a proteomic approach. Food Chemistry. 123, 765-770 (2010).

[5] Brysch-Herzberg, M., Seide,l M.: Yeast diversity on grapes in two German wine growing regions. International journal of food microbiology. 214, 137-44 (2015).

[6] Kurtzman, C.P., Robnett, C.J.: Identification and phylogeny of ascomycetous yeasts from analysis of nuclear large subunit (26S) ribosomal DNA partial sequences. Antonie Van Leeuwenhoek. 73, 331–371 (1998).

[7] Fell, J.W., Boekhout, T., Fonseca, A., Scorzetti, G., Statzell-Tallman, A.: Biodiversity and systematics of basidiomycetous yeasts as determined by large-subunit rDNA D1/D2 domain sequence analysis. Int. J. Syst. Evol. Microbiol. 50, 1351–1371 (2000).

[8] APHA, AWWA, WPCF: Standard methods for the examination of water and wastewater, 17th edn. APHA, AWWA, WPCF, Washington (1989).

ISSN: 2961-6611

[9] Monlau, F., Barakat, A., Steyer, J.P., Carrere, H. Comparison of seven types of thermo-chemical pretreatments on the structural features and anaerobic digestion of sunflower stalks. Bioresour. Technol 120, 241–247 (2012)

[10] Dubois, M., Gilles, K.A., Hamilton, J.K., Rebers, P.A., Smith, F.: Colorimetric method for determination of sugar and related substances. Anal. Chem. 28, 350–356 (1956).

[11] Miller, G.L. Use of dinitrosalicylique acid reagent for determination of reducing sugar. Anal. Chem. 31, 426 - 428 (1959).

[12] Laopaiboon, L., Nuanpeng, S., Srinophakun, P., Klanrit, P., Laopaiboon, P.: Ethanol production from sweet sorghum juice using very high gravity technology: effects of carbon and nitrogen supplementations. Bioresour. Technol. 100, 4176–4182 (2009).

The design, development, and characterization of photovoltaic cells with a double passivation layer SiNx/SiO2

Mekedeme Abdellah[1,2] *, Boutouchent-Guerfi Nabila*[1] *, Maoudj Mohamed*[1]*, Benammar Samir*[2]

(1)Research Center in Semi-Conductors Technology for Energetic (CRTSE), 02, Bd Frantz Fanon, BP 140, Alger 7 Marseilles, 16200 Algiers, Algeria, direction@crtse.dz
(2)Laboratoire Dynamique des Moteurs et Vibroacoustique.Faculté de technologie Université M'hammed Bougara Boumerdes,umbb_ldmv@yahoo.fr

[1] mekedeme2004@gmail.com

***Abstract*— This work presents a project that involved the creation of a prototype solar cell with a double SiN_x/SiO_2 passivation layer, given that conventional processes employ a single passivation layer formed from silicon nitride (SiN_x). The protocol adopted was a comparative study of the electrical parameters between two batches of conventional cells Al-BSF. One batch was passivated with a single layer of SiN_x, while the other was passivated with a double layer of SiO_2/SiN_x. The results obtained using a solar simulator and the Qss-Sun Voc technique demonstrated that the double passivation layer of SiN_x/SiO_2 resulted in superior passivation, with a pseudo-Voc that was 98% higher than that of cells with a simple SiN_x layer. With regard to the fill factor, the SiN_x/SiO_2 passivation yielded a value of 80%, in comparison to 73.2% for the cells passivated with a mono-layer of SiN_x. It should be noted that the term 'pseudo' was employed in the context of the electrical parameters obtained by Sun-Voc, given that this technique does not account for the influence of the series resistance. The results obtained are of considerable interest**
***Keywords*— Solar energy, passivation layer, photovoltaic cells, single-crystal silicon**

I. INTRODUCTION

In recent years, the drive for cost reduction has led to a reduction in solar cell thickness, meaning that efforts to further improve device performance have shifted towards surface passivation. In this regard, dielectric coatings provide a comprehensive solution. Particular attention is now being paid to the quality of the passivation achieved by dielectric deposition [1]. In fact, it has been shown that the passivation quality of dielectric layers is altered during process fabrication of solar cells. Such treatment frequently involves a high temperature step, for example, annealing metal contacts within a cell in either an inert or reactive atmosphere. Alternatively, a secondary passivating species, commonly hydrogen, can be introduced. To address this issue, a hydrogenated SiNx-H/SiO2 stack is frequently employed. The characteristics of the materials in this double stack are mutually reinforcing, with the SiO2 film exhibiting a field effect passivation [2, 3], while the SiNx provide a chemical passivation [3, 4]. The advantages of using a SiNx/ SiO2 double layer for silicon surface passivation can be can be summarised as follows:

- SiO2/SiNx stacks are more thermally stable than SiNx layers, whose passivation performance degrades contact formation using high temperature process [4, 5].

- With the advent of advanced structures such as passivated emitter and rear cell (PERC), bifacial, and interdigitated back contact (IBC) designs using Cz-silicon p-type wafers with relatively high bulk lifetime, SiNx/SiO2 stack layers are required to achieve very low surface recombination velocity (SRV) [6, 7].

The objective of this study is to conduct a comparative analysis of the electrical parameters between two batches of conventional cells. One batch was passivated with a single layer of silicon nitride (SiNx), while the other was passivated with a double layer of silicon dioxide (SiO_2) and silicon nitride (SiNx). The findings obtained through the utilisation of a solar simulator and the Qss-Sun Voc technique illustrated that the double passivation layer of SiNx/SiO_2 resulted in enhanced passivation, exhibiting a pseudo-Voc that was 98% higher than that observed in

ISSN: 2961-6611

cells with a simple SiNx layer. With respect to the fill factor, the SiNx/SiO_2 passivation yielded a value of 80%, which is a notable improvement over the 73% achieved with a simple SiNx layer..

II. EXPERIMENTAL PROCEDURES

In this study, solar cells were made from monocrystalline silicon Cz <100> p-type with a resistivity of 1-3 Ωcm, passivated with a SiNx/SiO2 double layer. The process involved surface treatment of silicon wafers, creation of an n+/p emitter, deposition of the SiNx/SiO2 dielectric layer, metallization of the front and back faces, and annealing of the contacts. The cells were tested using a solar simulator and the QSS-Sun Voc technique

A. Chemical surface treatment of silicon plates

The initial thickness of the wafers we used in this study is about 410 µm. The first step in the technological process of the PV cells consists of a cleaning of the surface in chemical baths, allowing for the elimination of impurities and undesirable particles like dust, resins, and oils, as well as the crystalline defects induced by the mechanical stress during the stage of the cutting of the plates.
Thus, the chemical treatment that we have carried out before the realization of the n+/p emitter is summarized in three steps: degreasing, thinning, and stripping of the layer of silicon oxide (SiO2) called native oxide.

B. Formation of an n+/p emitter by phosphorus diffusion

The n+/p emitter is formed in a diffusion furnace from a liquid source of phosphorus oxychloride (POCl3) at relatively high temperatures to allow diffusion of the phosphorus atoms into the volume of the silicon wafer. This step is carried out at a temperature of 820°C and a pressure of 150 mbar; the diffusion is governed by:

$$4POCl_3 + 3O_2 \longrightarrow 2P_2O_5 + 6Cl_2$$

The chlorine is released, and the phosphorus pentoxide (P2O5) will diffuse in the furnace as a vapor, which will then coat the surface of the wafers.

$$2P_2O_5 + 5Si \longrightarrow 4P + 5SiO_2$$

Phosphorus is deposited on wafers, creating a P2O5 layer called phosphorus silicate glass (PSG).Drive-in stage involves stopping gas flow and maintaining 820°C for 15 minutes. This stage will allow the phosphorus atoms present in the (PSG) to penetrate inside the wafers according to the laws of Fick.

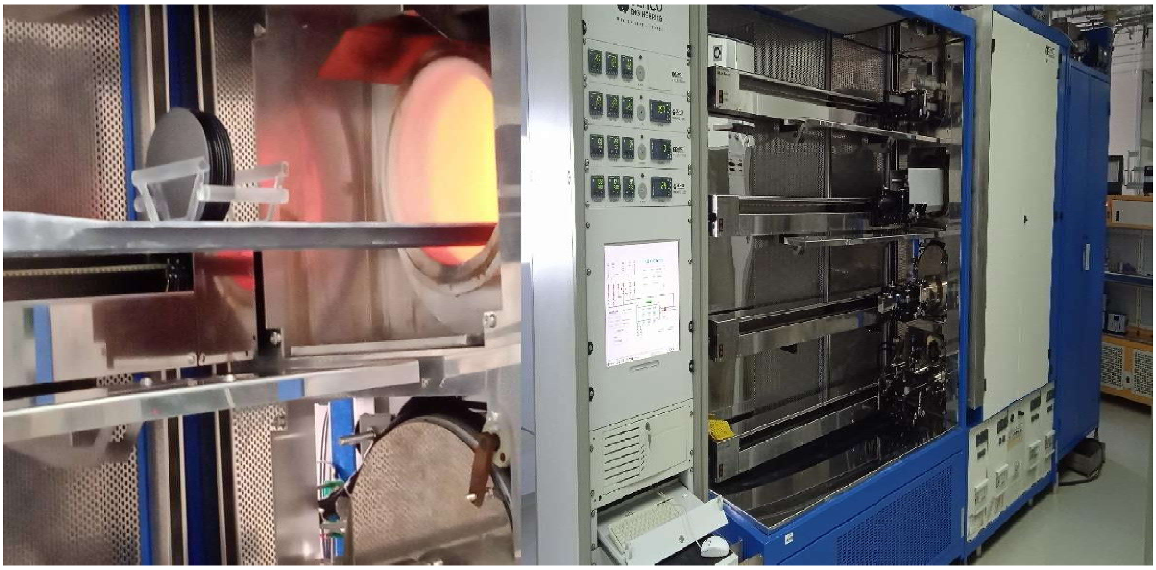

.FIG 1 : Photo of the SEMCO-Engineering diffusion furnace during the automatic entry of the quartz pod

C. Stripping of the parasitic junction of the edges

ISSN: 2961-6611

The emitter's elaboration creates a parasitic junction at the wafer edge, causing a short circuit. To remove this junction, a cylindrical plasma reactor is used. The reactor involves introducing wafers, ionizing carbon tetrafluoride (CF4), and applying high-frequency electric discharge. This ionization decomposes into reactive species, forming a plasma. The following reaction is involved:

$$4F^- + Si \longrightarrow SiF_4 \nearrow$$

Fluoride reacts with silicon to form silicon tetra fluoride which is a volatile gasAt the end of this step, the two emitters formed on the two sides of the wafer are isolated

D. Passivation and anti-reflective coating

In this stage of the process, we will passivate the surface with a single SiNx layer and a double SiNx/SiO2 layer in order to make a comparative study of the performance of the different wafers that have undergone the two passivation routes.

E. Plasma Enhanced Chemical Vapour Deposition (PECVD) of a SiNx anti-reflective film

After edge stripping, followed by R□ measurements, we performed the deposition of an 80 nm-thick silicon nitride (SiNx) layer on a batch of wafers on a PECVD reactor. The SiNx layer is obtained from a gas mixture of silane (SiH4) and ammonia (NH3). Silane is a source of silicon and hydrogen.
Ammonia, in addition to being a source of nitrogen, has the tendency to produce hydrogen-rich films. Deposition pressures range from a few hundred milliTorr to a few Torr. Deposition temperatures range from 250°C to 400°C. This silicon nitride layer not only plays a passivation role due to the presence of hydrogen but also provides an anti-reflection function due to its adjustable refractive index through the change of NH3/SiH4 gas ratios.

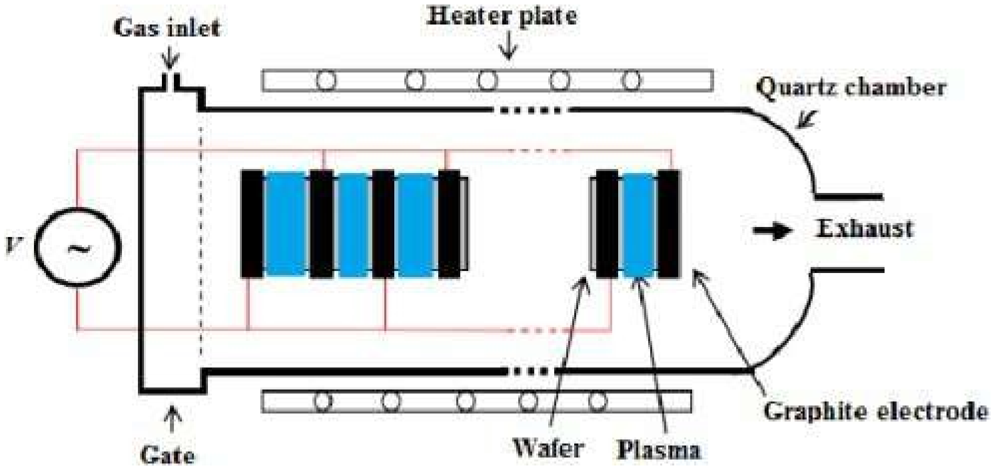

Fig.2: Illustration of PECVD reactor

F. Preparation of a SiNx/SiO2 double passivation layer

An additional 10 nm SiNx layer was deposited on top of a batch of wafers from Semco-Engineering furnace that had a quartz tube. On the control computer, oxidation parameters like temperature, gas flow rate, and time were inputted during the oxidation process.

- Oxidation temperature: 850°C,
- Gas flow rate: N2 =5000 sccm (5 L/min) and O2 =5000 sccm (5 L/min),
- Oxidation time: 13 min.

After that, a silicon nitride layer was deposited on top of the oxide layer, with the deposition duration being controlled by wavelength-dependent reflectance characterizations. It took 105 seconds to deposit the item.

G. Metallization: deposition of collector grid and rear contact by screen printing

The metallization process used in solar cell technology creates connections between the structure and external circuit during encapsulation. Careful metallization and heat treatment are essential. Through the process of screen printing, conductive paste is applied to a substrate, where it hardens, densifies, and forms a connection with the cell. The contact is created via the diffusion of metallic components into the semiconductor, such as silver for the front face and aluminum for the rear face.

III. RESULTS AND DISCUSSION

A. Characterization of the performance of manufactured solar cells using the solar simulator

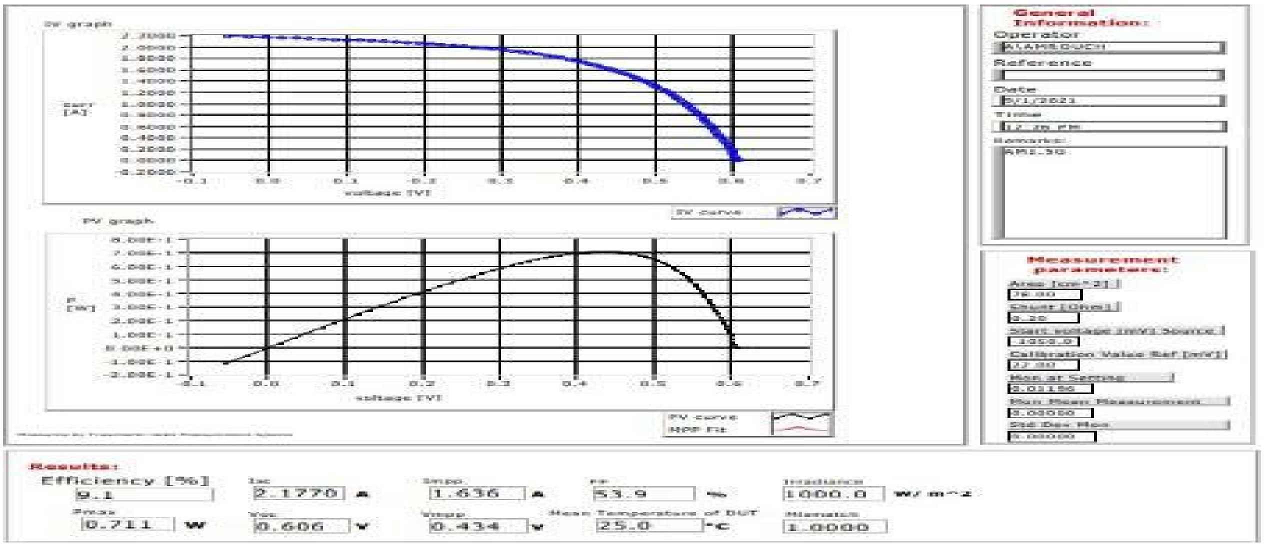

Efficiency [%] 9.1
Isc 2.1770 A
Impp 1.636 A
FF 53.9 %
Irradiance 1000.0 W/m^2
Pmax 0.711 W
Voc 0.606 V
Vmpp 0.434 V
Mean Temperature of DUT 25.0 °C
Mismatch 1.0000

Fig.3 : I-V characteristics of a sample of solar cells manufactured within the framework of this project with a SiNx/SiO2 double passivation layer. Measurements carried out under illumination in standard conditions.

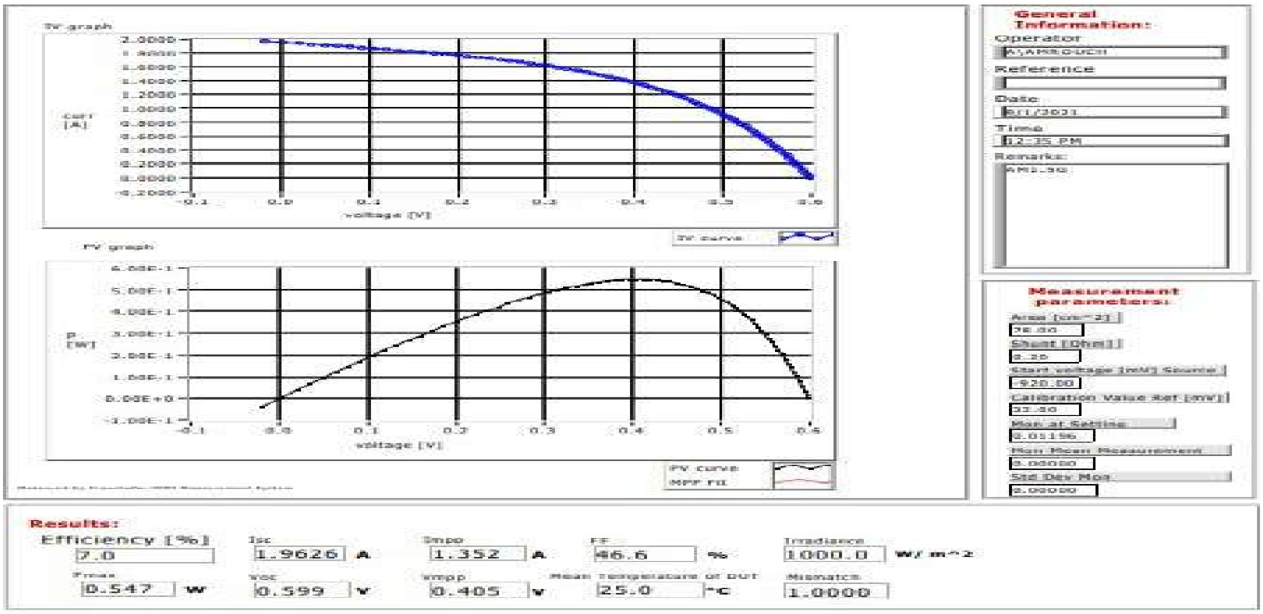

Efficiency [%] 7.0
Isc 1.9626 A
Impp 1.352 A
FF 46.6 %
Irradiance 1000.0 W/m^2
Pmax 0.547 W
Voc 0.599 V
Vmpp 0.405 V
Mean Temperature of DUT 25.0 °C
Mismatch 1.0000

Fig.4 : I-V characteristics of a sample of solar cells manufactured within the framework of this project with a simple SiNx passivation layer Measurements carried out under illumination in standard conditions.

Electrical characterization of the solar cells manufactured in this work, using an ORIEL solar simulator under illumination. Standard measurement conditions (1000 W/m2, 25°C) were adopted, using the AM1.5G spectrum. Before starting our measurements, we calibrated the instrument with a calibration cell.

Figures III-17 and III-18 illustrate, respectively, the electrical characteristics of the cells fabricated in our project, with a double passivation layer of SiNx/SiO2 and a single passivation layer of SiNx. As can be seen, the cell with a double SiNx/SiO2 layer has a better short circuit current Isc and open circuit voltage Voc than those obtained with the cells passivated with a single SiNx layer.

ISSN: 2961-6611

A current and voltage gain of 214.4 mA and 7 mV, respectively, were recorded on cells with a double SiNx/SiO2 layer. And so it can be stated that we have a gain of 9.84% with respect to the short circuit current Isc and 1.15% with respect to the open circuit voltage Voc.

In order to confirm these results, we carried out a characterization using the QSS-Sun Voc technique. This characterization gives the electrical parameters of a cell, neglecting the influence of series resistors. The results obtained are given in Table .1.

Table 1: Results obtained by QSS-Sun Voc, for the wafers manufactured as part of this project with a single SiNx passivation layer usually used and a double SiNx/SiO2 layer optimized in our study.

Cells type	Voc (mV)	FF (%)
SiNx/SiO2	610.1	79.7
SiNx	601.4	73.2

This reflects the effective contribution of the SiO2 layer in terms of passivation quality, the indicator parameter of which is the open circuit voltage; and therefore the comparison of this parameter between the wafers passivated with SiNx/SiO2 and SiNx indicates that we have a better passivation in favor of the SiNx/SiO2 double layer. Nevertheless, we notice that the form factor as well as the conversion efficiency remain low, this can be explained by a high series and parallel resistance, which can be clearly seen on the I (V) curves. This phenomenon is generally reflected in poor metal-semiconductor contact and leakage currents due to the RTP annealing process (high silver penetration, leading to junction breakthrough).

IV CONCLUSIONS

the results clearly demonstrate that the incorporation of a double sinx/sio2 layer led to a significant increase in the current and voltage of the solar cells. with a 9.84% increase in the short-circuit current isc and a 1.15% increase in the open-circuit voltage voc, it is evident that this approach holds considerable potential for enhancing solar cell performance. these promising results pave the way for future innovations in the field of solar

In view of this study, we propose to optimize the n+/p emitter based on the RTP annealing process in order to reduce the series resistance ‘Rs’ and increase the parallel resistance ‘Rshunt’, thereby achieving a better form factor and consequently a better conversion efficiency

V. REFERENCE

[1] R. S. Bonilla, I.Al-Dhahir1, M. Yu, P. Hamer, P. P. Altermatt, Charge Fluctuations at the Si-SiO_2 Interface and its Effect on Surface Recombination in Solar Cells, Solar Energy Materials and Solar Cells 215:110649215:110649, https://doi:10.1016/j.solmat.2020.110649

[2] R.S. Bonilla, B. Hoex, P. Hamer, and P.R. Wilshaw, Dielectric surface passivation for silicon solar cells: A review, Phys. Status Solidi A 1, 1 (2017). https://doi.org/10.1002/pssa.201700293.

[3] M. Maoudj, D. Bouhafs, N. Bourouba, A. El amrani, H. Tahi and A. Hamida-ferhat, Behavior of SiN_x/SiO_2 Double Layer for Surface Passivation of Compensated p-Type Czochralski Silicon Wafers, Journal of electronic materials, Vol.48, pp 4025–4032, (2019), https://doi.org/10.1007/s11664-019-07162-1

[4] S. Keipert-Colberg, N. Barkmann, C. Streich, A. Schutt, D. Suwito, P. Schafer, S. Muller, and D. Borchert, Investigation of a PECVD Silicon Oxide/Silicon Nitride Passivation System Concerning Process Influences, Proc. 26th EU PVSEC, 2BV.3.61, Hamburg (2011).

[5] J. Schmidt, M. Kerr, and A. Cuevas, Surface passivation of silicon solar cells using plasma-enhanced chemical-vapour-deposited SiN films and thin thermal SiO_2/plasma SiN stacks, Semicond. Sci. Technol.16, 164 (2001).

[6] F. Booka, T. Wiedenmann, G. Schubert, H. Plagwitz, Influence of the Front Surface Passivation Quality on Large Area n-Type Silicon Solar Cells with Al-Alloyed Rear Emitter, Energy Procedia 8 pp487–492 (2011).

[7] C. Schmiga, M. Rauer, M. Rüdiger, K. Meyer, J. Lossen et al. Aluminum Doped p+ Silicon for Rear Emitters and Back Surface Fields: Results and Potentials of Industrial n- and p-Type Solar Cells. Proc. 25th EU PVSEC, Valencia, p. 1163-8 (2010).

Utilizing Advanced Combined Thermodynamic Cycles for the Recovery of Residual Heat as a Clean Technology for Electricity Generation

F.Brahimi[1,2], M.Guemmadi[1,3], R.Boukaraou[2], S.Mohandi[2], , M.Mazari[1]
[1]Department of Mecanical engineering, Faculty of Technology, University M'hamed Bougara/Boumerdes, Algeria
[2]Laboratoire Dynamique des Moteurs et Vibro-acoustique, University M'hamed Bougara/Boumerdes, Algeria
[3]Laboratoire d'Energétique Mécanique et Matériaux, University of Tizi Ouzou, Algérie

f.brahimi@univ-boumerdes.dz
m.guemmadi@univ-boumerdes.dz
r.boukaraoun@univ-boumerdes.dz
s.mohandi@univ-boumerdes.dz
m.mazari@univ-boumerdes.dz

Abstract— **In this study, we demonstrate the capability of the Inverted Brayton Cycle (IBC) and the Air Brayton Cycle (ABC) to convert the energy from exhaust gases of gas turbines into mechanical energy. The gas turbine used operate according to the Joule Brayton Cycle (JBC). For this purpose, we analyzed three energy systems. The first system is the JBC, the second one is the IBC installed in series with a gas turbine, combining the Joule-Brayton cycle with the inverted Brayton cycle (JBC-IBC). The third system is the ABC installed in series with a gas turbine, combining the Joule-Brayton cycle with the air Brayton cycle (JBC-ABC). (JBC-IBC) and (JBC-ABC) constitute the first and second combined cycle respectively.**

Keywords— **gas turbine, energy conversion, inverted Brayton cycle, air Brayton cycle, exhaust gases.**

I. INTRODUCTION

Although renewable energies are considered the future of energy and the transition to these energy sources is crucial, it is important to emphasize that the development of renewable energies is still insufficient. This is due, in particular, to the high cost of the investments required for their operation, as well as the financial windfall that traditional energy sources represent for certain commercial groups or governments [1]. The complete transition to renewable energies will take time. During this transition period, it is crucial to improve existing thermal facilities that use fossil fuels to make them more environmentally friendly. This means reducing their environmental impact and promoting a more gradual transition. This involves adopting cleaner technologies. The recovery of exhaust gases from existing thermal installations, such as gas turbines, offers significant advantages in terms of energy recovery, reduction of greenhouse gas emissions, improvement of energy efficiency, reduction of air pollution, versatile use, and economic profitability [2]. This approach represents a significant step towards cleaner and more efficient energy production. It promotes the transition to a more sustainable economy and contributes to global efforts to combat climate change while meeting current energy needs, as we await the wider availability and economic viability of renewable energies [3-5]. In this context, two advanced combined cycles with exhaust gas recovery have been analyzed in this study. Unlike the conventional combined cycle (gas turbine and steam turbine), in the first analyzed combined cycle, the exhaust gases of the gas turbine operating on the simple Joule Brayton cycle (JBC) are recovered in an inverse Brayton cycle (IBC), thus forming the JBC-IBC combined cycle. In the second combined cycle, the exhaust gases from the same turbine are recovered in another Joule-Brayton cycle (ABC), forming the JBC-ABC combined cycle. The objective of this study is, firstly, to evaluate the benefits of exhaust gas recovery from gas turbines through advanced combined cycles in terms of energy performance. Secondly, to identify the combined cycle that best harnesses the potential of gas turbine exhaust gases and contributes the most to improving the performance of these gas turbines' simple cycle.

II. CYCLES DESCRIPTION

Fig. 1 (a) shows the simple gas turbine (JBC) composed of a compressor, a combustion chamber, a high pressure turbine and a low pressure turbine. The performance data at the standard conditions of the gas turbine used in this study is presented in Table 1. JBC is referred to as the topping cycle and IBC and ABC are called the bottoming cycles. The first combined cycle is schematically shown in Fig. 1 (b). Airflow enters the first compressor and is compressed. Then, it passes through the combustion chamber where heat is transferred to the airflow to increase its temperature to the maximum temperature of the cycle. The process within the combustion chamber is modeled as a simple heat transfer process. The energized airflow enters the high pressure turbine and expands to generate the power just is required for driving the first compressor. The exhaust gas leaving the high turbine enters the low pressure turbine to generate the power for the first generator. Then, the exhaust gas are expanded to sub-atmospheric pressure within the turbine in the bottoming cycle, this leads to generate the power in the second generator. The exhaust gas leaving the third turbine are cooled down within a heat exchanger before entering the second compressor in the bottoming cycle to increase the pressure and to discharge to the atmosphere. In the second combined cycle, schematically shown in Fig. 1 (c), the exhaust gas leaving the high turbine enters into the heat exchanger to heat air coming from the bottoming compressor and they are discharged into the atmosphere. At the exit of the heat exchanger air is conducted to the bottoming turbine where it is expanded to generate the power for the second generator and then it is discharged to the atmosphere.

TABLE I
PROPRIETIES OF AIR SIMPLE CYCLE (JBC)

Compressor inlet pressure (bar)	Compressor inlet temperature (°C)	Pressure ratio	Compressor isentropic efficiency(%)	Turbine isentropic efficiency (%)	Combustion efficiency (%)	Air mass flow rate (kg/s)	maximal turbine inlet temperature (°C)
1.01325	15	8.8	0.87	0.88	0.97	123.61	966

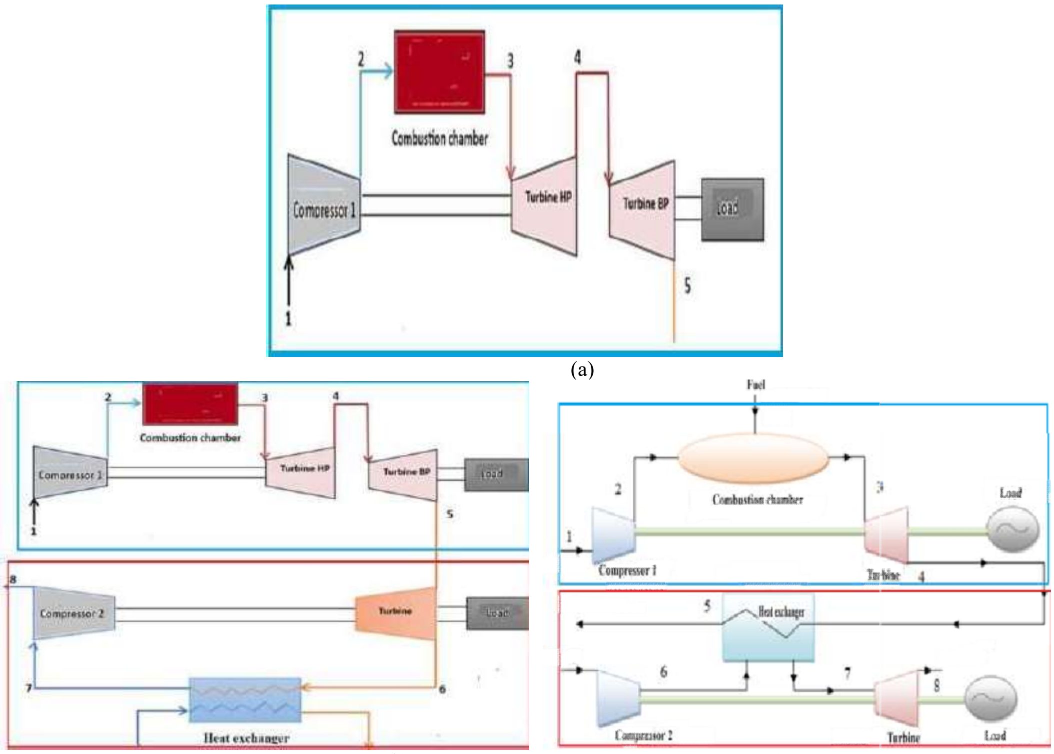

(a)

(b) (c)

Fig.1 Layout of (a): air simple cycle (JBC); the first combined cycle (JBC-IBC) and (c): the second combined cycle (JBC-ABC)

III. ENERGETIC ANALYSIS

Figure 2 shows the thermodynamic process in a temperature-entropy (T-s) diagram of a air simple cycle (JBC) (fig 2.a), the first combined cycle (JBC-IBC) (fig 2.b) and the second combined cycle (JBC-ABC) (fig 2.c). Energy analysis is conducted for the three configurations (JBC, JBC-IBC and JBC-ABC). The energy balance equations applied for each component of the topping and the bottoming cycles are listed from 1 to 9. The thermodynamic model establishment is based on some adopted assumptions. The flow system is considered in a steady-state, turbines and compressors have given isentropic efficiencies, pressure losses in the heat exchangers are ignored and variations of kinetic and potential energies of the fluid in all cycle components are negligible.

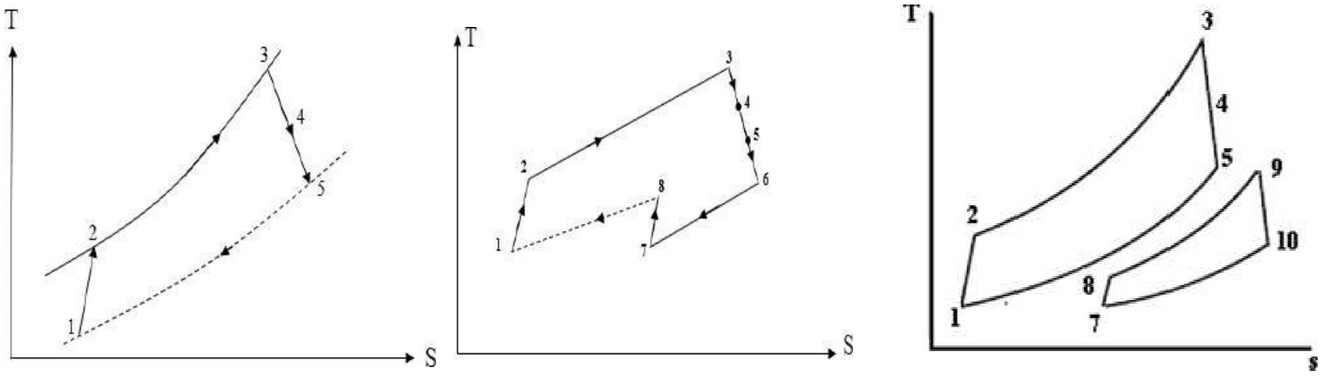

(a) (b) (c)

Fig. 2 Operating cycle of (a): air simple cycle; (b): the first combined cycle and (c): the second combined cycle

The mass conservation equation for a steady process states that the total mass flow rate entering a control volume is equal to the total mass flow rate leaving it:

$$\sum \min = \sum mout \qquad (1)$$

Energy equation for air compressor in the topping cycle is:

$$P_{C1} = \dot{m}a. C_{p\,air}\left(T_{out,air}\right) \times \left(T_{out,air}\right) - C_{p\,air}\left(T_{in,air}\right) \times \left(T_{in,air}\right) \qquad (2)$$

Energy equation for exhaust gas compressor in the bottoming cycle is:

$$P_{C2} = \dot{m}exhg. C_{p\,exhg}\left(T_{out,exhg}\right) \times \left(T_{out,exhg}\right) - C_{p\,exhg}\left(T_{in,exhg}\right) \times \left(T_{in,exhg}\right) \qquad (3)$$

Energy equation for a typical turbine is also:

$$P_T = (\dot{m}exhg. C_{p\,exhg}\left(T_{out,exhg}\right) \times \left(T_{out,exhg}\right) - C_{p\,exhg}\left(T_{in,exhg}\right) \times \left(T_{in,exhg}\right) \qquad (4)$$

Energy equation for combustion chamber is: $Pcc = m_f .PCI.\square_H$ (5)

Energy equation for heat exchanger in the first combined cycle is

$$P_{HEX} = m_{exhg} C_{pexhg} \square_{HEX} \left(T_7 \square T_6\right) \qquad (6)$$

Energy equation for heat exchanger in the second combined cycle is

$$P_{HEX} = m_{exhg} C_{pexhg} \square_{HEX} \left(T_5 \square T_4\right) \qquad (7)$$

Based on the first law of thermodynamics, energetic efficiency is defined by Eq. (8) for JBC and by Eq.(9) for JBC-IBC and JBC-ABC.

$$\square_{th,JBC} = \frac{P_{LPT}}{P_{CC}} \qquad (8)$$

$$\square_{th} = \frac{\left(P_{LPT} + P_{BT}\right) \square P_{C2}}{P_{CC}} \qquad (9)$$

IV. RESULTS

The available data of S. Besarati and al [6] are used to validate the model of the JBC. The results presented in fig.3, show the evolution of the thermal efficiency of JBC as a function of the compression ratio. We can see that the evolutions are similar and our results are very close to those of S. Besarati and al with a moderate difference of 4%.

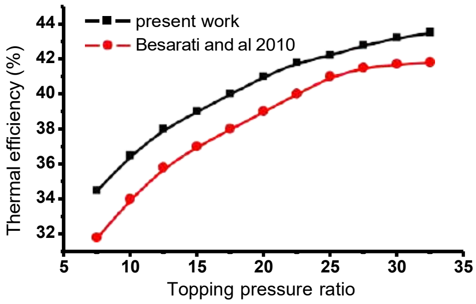

Fig.3 Comparison of the thermal efficiecy as a function of the topping pressure ratio

We have carried out a second comparison with the results of M. Goodarzi et al [7] who analyzed the simple Brayton cycle and the first combined cycle (JBC-IBC). The results of the simple cycle are presented in Fig.4 in terms of normalized heat amount, normalized net work and thermal efficiency. For JBC-IBC, the analysis was done for three different values of the topping compression ratio (TPR). The results are presented in Fig.5 in terms of heat exchanger outlet normalized temperature, normalized net work and thermal efficiency. We observe a good agreement of our results with those of M. Goodarzi et al. For both cycles, the difference between the results does not exceed 2%.

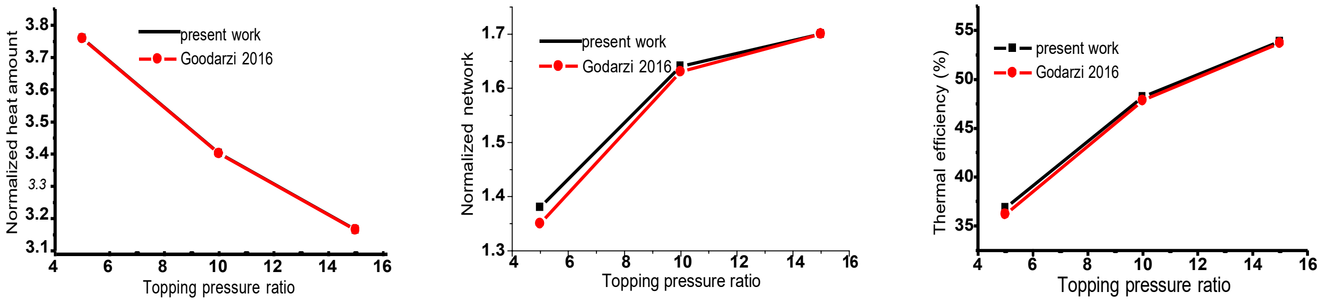

(a) (b) (c)

Fig.4 Comparison of the performances as a function of the topping pressure ratio (a): normalized heat amount, (b): normalized net work and (c) : thermal efficiency

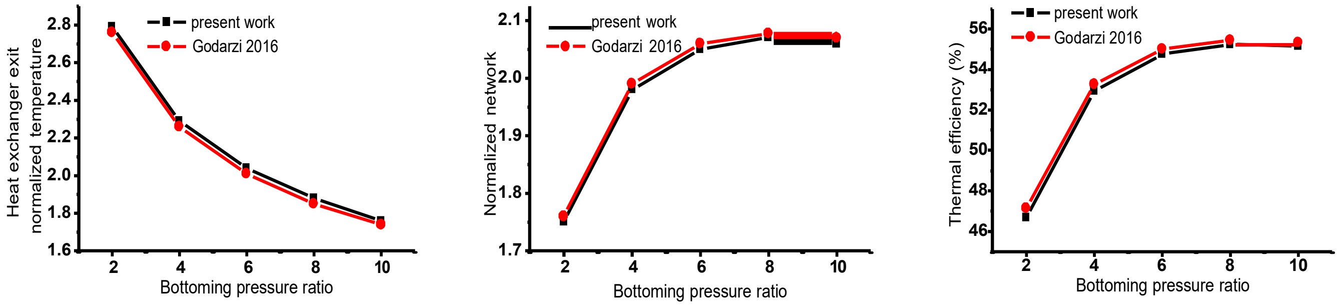

(a) : TPR = 5

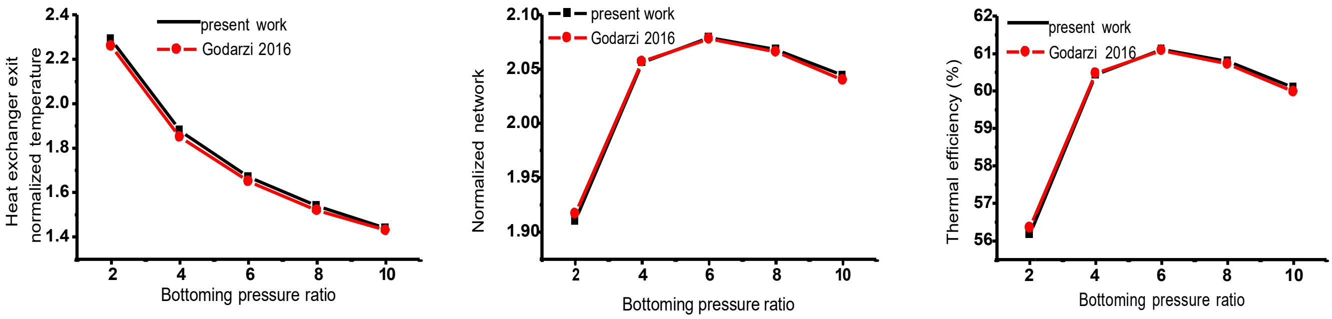

(b) : TPR = 10

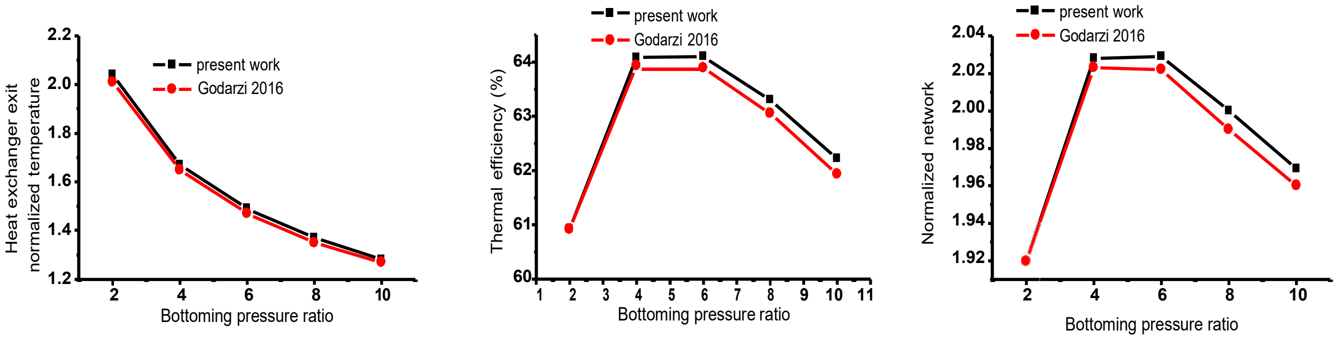

(c) : TPR = 15

Fig.5 Performances comparison according to the bottoming cycle pressure rate and for different pressure ratio of the topping cycle (TPR)

We have conducted a comparative analysis of the performance of the different cycles examined in this work. The goal was to demonstrate the potential of the IBC and ABC cycles to improve the performance of the simple gas turbine cycle (JBC) through the recovery of the exhaust gases.

The evaluated performances are the gain in the useful power and in the thermal efficiency. The increase in power output and in efficiency of the combined cycles is evaluated by comparing between the power output and thermal efficiency of JBC-IBC and JBC-ABC with those of JBC.

On Figs. 6 (a) and (b) we observe that the two advanced combined cycle provide significant gains in useful power and thermal efficiency. This highlights the advantages of these specific cycle configurations. The IBC and ABC connected to the outlet of the high-pressure turbine allow recovering the energy lost during the expansion in the JBC, leading to a reduction in thermal losses and an efficient use of the available energy, which allows, for the same heat power, to increase the useful power and the thermal efficiency. The performances of JBC- IBC are higher than those of JBC-ABC. Thus, it is obvious that JBC-IBC performs better.

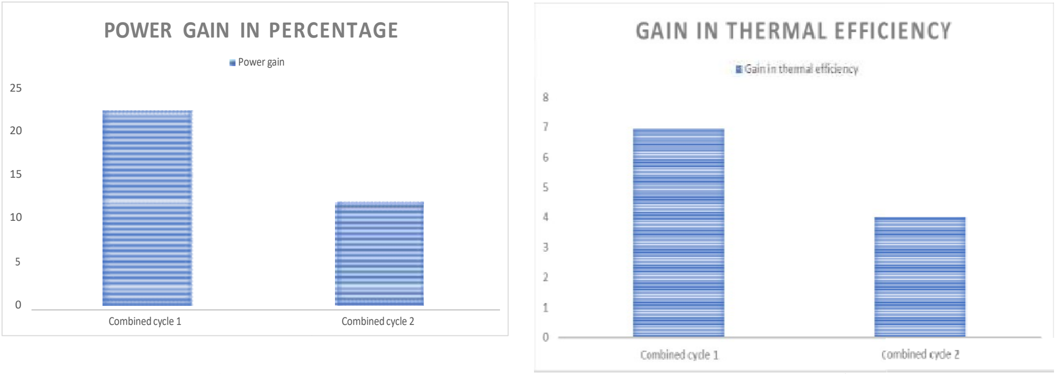

(a) (b)

Fig.6 Comparaison of the gain in performances obtained with the two combined cycles (a): useful power; (b) : thermal efficiency

ISSN: 2961-6611

A sensitivity analysis is carried out to evaluate the effects of various parameters on the thermodynamic results for the two combined cycles considered in this paper, including the effects of the bottoming compressor pressure ratio, ambient temperature, and heat exchanger efficiency. The thermodynamic performances of JBC-IBC and JBC-ABC are analyzed by varying the compressor pressure ratio at the limit of 1-10, the ambient temperature at the limit of 273-308 K and the heat exchanger efficiency at the limit of 0.7-0.9. When one specific parameter is studied, other parameters are kept constant.

Figs. 7 (a) and (b), showing the net output power and the thermal efficiency gains change of JBC-IBC and JBC-ABC with the pressure ratio, reveal that for each cycle, a maximum net output power can be achieved and the efficiency goes through a maximum value by increasing the pressure. In both cycles, the net output power and the thermal efficiency gains increase firstly with increasing pressure ratio until its maximum that is attained at an optimum pressure ratio. Afterward, it diminishes slightly with the addition of the pressure ratio. This is mainly resulting from the sharp rise in power consumption in the compression process. As can be seen from Figs. 7, the optimum pressure ratio for JBC-IBC and JBC-ABC is determined to be 3, it also yields to the maximum efficiencies of the cycles. It is also clear that the net output power and the thermal efficiency gains of JBC-IBC are always higher than those of JBC-ABC whatever the pressure rate.

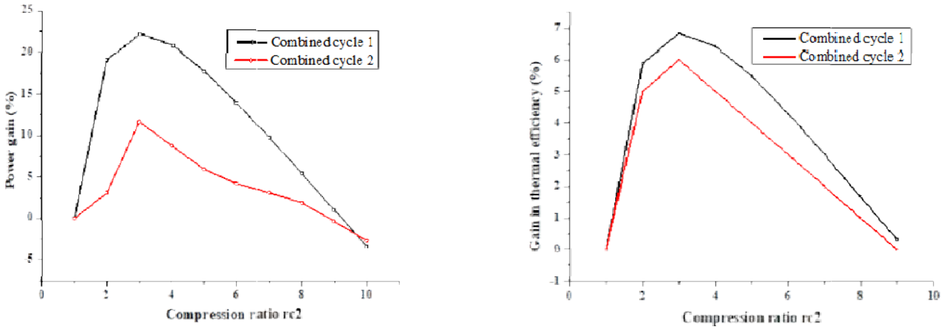

(a) (b)

Fig.7 Power and thermal efficiency gains obtained with the combined cycles as a function of the bottoming pressure ratio

Figs. 8 (a) and (b) show the sensitivity degree of JBC-IBC and JBC-ABC net output power and thermal efficiency gains, according to the ambient temperature which increases from 273 to 308 K. When the ambient temperature varies, JBC-ABC performances are directly affected because the inlet air of both topping and bottoming compressors is at atmospheric conditions. Unlike JBC-ABC where the net output power and thermal efficiency gains decrease with increasing the ambient temperature, in JBC-IBC, these performances increase. In Fig. 8 (a), it is noticed that for low temperatures, the thermal efficiency gain difference between the two cycles is weak and their efficiencies are very close, but improving an air simple cycle by JBC-ABC seems better. At 276 K, JBC- ABC and JBC-IBC give the same thermal efficiency. For a temperature of more than 276 K there is a sudden increase for JBC-IBC and a decrease for JBC-ABC in the net output power and thermal efficiency gains. When the compressor inlet temperature is high, it is seen that JBC-IBC performs relatively better. JBC-ABC performances degradation is due to the decrease of air density simultaneously in the topping and bottoming cycles each time the inlet air temperature increases. Low density means a low mass flow rate and this involves a less recovered heat amount in the heat exchanger. For JBC-IBC, the behavior is not similar because the temperature change concerns only the topping flow rate. It is shown that JBC-IBC would have a thermodynamic benefit compared to JBC-ABC, especially for high ambient temperatures. In contrast, for very low temperatures, the JBC-ABC performances are considered better.

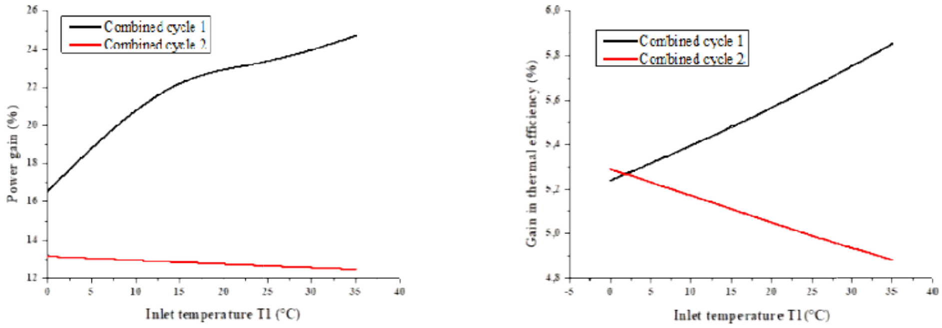

(a) (b)

Fig.8 Power and thermal efficiency gains obtained with the combined cycles as a function of the ambient temperature

Figs 9 (a) and (b) illustrate the variation in the performance of the two combined cycles as a function of the effectiveness of the heat exchanger. It is clear that increasing the effectiveness of the heat exchanger has a positive and significant impact on the performance of the two cycles. In terms of net power, the two cycles produce similar power outputs, but in terms of thermal efficiency, it is the JBC-ABC cycle that is the most advantageous.

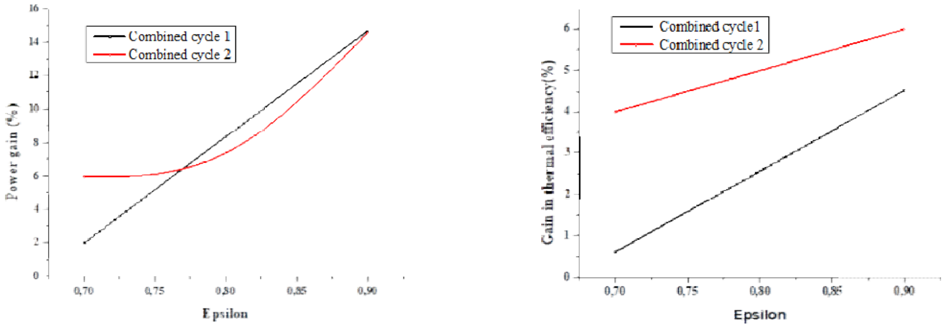

(a) (b)

Fig.9 Power and thermal efficiency gains obtained with the combined cycles as a function of the heat exchanger efficiency

V. CONCLUSIONS

This study illustrated the potential of two advanced combined cycles JBC-IBC and JBC-ABC to improve the performance of simple cycle gas turbines (JBC) via waste heat recovery.

The comparison of the performance of the two cycles shows that the JBC-IBC cycle allows for interesting gains in terms of net power and thermal efficiency.

The results assert that JBC-IBC is the appropriate option and a promising technology for gas turbine waste heat recovery to produce additional power. According to this analysis, pressure ratio, ambient temperature and heat exchanger efficiency are identified as factors affecting the performance of the two combined cycles. Furthermore, an environmental and economic analyses will enrich this work and will provide valuable information that can be used to make the best decision in selecting between the two cycle options.

REFERENCES

[1] Zhihang Chen et al, Modeling and Simulation of an Inverted Brayton Cycle as an Exhaust-Gas Heat- Recovery System, Journal of Engineering for Gas Turbines and Power, Vol. 139, pp. 081701-1 -081701-7, 2017.
[2] Ian Kennedy et al, Inverted Brayton Cycle With Exhaust Gas Condensation, Engineering for Gas Turbines and Power, vol. 140, pp. 111702-9, 2018.
[3] Ian Kennedy et al, Experimental investigation of an inverted Brayton cyclee for exhaust gas energy recovery, Engineering for Gas Turbines and Power, pp. 1-31, 2018.
[4] Rohan Sureshbhai Jayswal et al, Review paper on inverted Brayton cycles, Science and Technology, vol. 5, pp. 2456-5660, 2020.
[5] M. Goodarzi et al, Energy and exergy analysies of a new atmospheric regenerative Brayton and inverse Brayton cycle, Energy Reports, vol. 7, pp. 4530–4539, 2021.
[6] S. Besarati et al, Multi-objective thermodynamic optimization of combined Brayton and inverse Brayton cycles using genetic algorithms, Energy Conversion and Management, p. 212-217, 2010.
[7] M. Goodarzi et al, Usefulness analysis on regenerator and heat exchanger in Brayton and inverse Brayton cycles at moderate pressure ratio operation, Energy Conversion and Management, vol. 126, pp. 982-990, 2016.

ISSN: 2961-6611

Optimization of Nanostrutured TiO_2/CdS/CIGS Solar Cells via SCAPS-1D Software Package for Highly Photovoltaic Efficiency

Awatef Naffouti
Fluid Mechanics Laboratory, Faculty of Sciences of Tunis, Department of Physics, 2092 University El Manar 2, Tunis, Tunisia
Department of Physics, University of Hafar Al-Batin, Kingdom of Saudi Arabia
awatefnaffouti84@gmail.com

Abstract— **This study involves the numerical optimization and analysis of TiO_2/CdS/CIGS solar cell structure using one-dimensional Solar Cell Capacitance Simulator (SCAPS-1D) software package. It examines the electrical properties and photovoltaic performance of CIGS thin-film solar cells with a Molybdenum back contact. The research explores the effect of TiO_2 film thickness on the solar cell performance. The simulation is carried out by varying TiO_2 thickness in the range [50-500] nm. A photovoltaic efficiency of about 16.64 % was obtained for a thickness in the order of 200 nm. This result may be promising for the development of advanced high-performance CIGS solar cell technology based on titanium dioxide (TiO_2) compound.**

***Keywords*— SCAPS-1D package, solar cell, photovoltaic efficiency, film thickness**

I. INTRODUCTION

Metal oxides are formed when metal ions create coordination bonds with oxygen, resulting in a densely packed structure. These materials are highly attractive due to their exceptional physical and chemical properties. The diverse structures and properties of metal oxides make them valuable in various technological applications, including medical science, gas sensing, energy storage, and surface coatings. Thin films of metal oxides, such as ZnO, SnO_2, CdO, and TiO_2, have garnered significant interest from both the scientific community and industry in recent years. Among them, titanium dioxide (TiO_2) has emerged as a leading material in photoelectrochemical and photovoltaic applications due to its significant scientific and technological benefits [1-3].

Sun provides the most plentiful source of energy all renewable resources. In just two minutes, the earth receives from the sun an amount of energy equals to the total annual energy consumption of humanity. This vast potential can be harnessed by solar cells, which convert solar energy into electrical power through the photovoltaic effect [4].

Numerical simulation is a powerful tool that enhances our understanding of solar cells, identifies performance parameters, and aids in designing new experimental production structures. Thus, several numerical packages have been employed in order to evaluate the performance of solar cells. Among them, results, obtained using one-dimensional Solar Cell Capacitance Simulator (SCAPS-1D), are consistent with experience [5]. Thus, it is used in order to simulate various electrical parameters such as: short circuit density (Jsc), fill factor (FF), power conversion efficiency (PCE, η) and open-circuit voltage (Voc).

Therefore, this paper presents a detailed numerical analysis using Solar Cell Capacitance Simulator in one dimension (SCAPS-1D) package in order to examine the impact of TiO_2 film thickness on the efficiency of TiO_2/CdS/CIGS solar cell.

II. COMPUTATIONAL DETAILS

Various simulation packages, including SILVACO ATLAS [6], WAMPS [7], and SCAPS [8,9], are used to assess the efficiency of different types of solar cells. Among them, SCAPS-1D (version 3.3.0.7, developed by the University of Gent, Belgium) demonstrates a strong correlation between simulation results and experimental data. It is based on Poisson equation in one-dimensional form, along with the hole and electron continuity equations, to model charge transport in semiconductors [10]. It establishes the relationship between electrostatic potential and charge density in order to calculate the steady-state band diagram, recombination profile, and carrier transport in one dimension.

ISSN: 2961-6611

Fig. 1 illustrates a schematic diagram of the studied simulated solar cell (TiO_2/CdS/CIGS). It is structured as heterojunctions composed of various semiconductor materials.

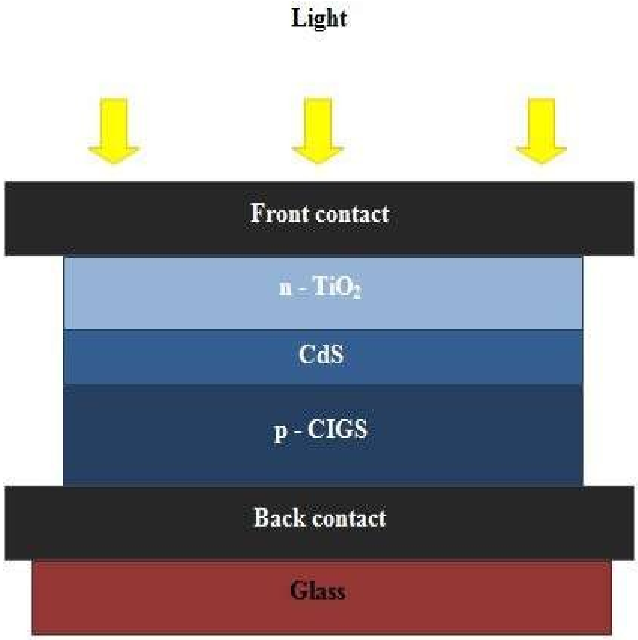

Fig. 1 Structural representation of TiO_2/CdS/CIGS solar cell.

In fact, it includes an n-type TiO_2 layer as the optical window with a thickness varying from 50 to 500 nm. An n-type CdS (cadmium Sulfide) thin film is used as the buffer layer with a thickness in the order of 50 nm. A 3000 nm p-type Copper Indium Gallium Selenide (CIGS) film plays the role of the absorber layer. The physical parameters of each layer are summarized in Table I.

TABLE I
LIST OF PHYSICAL PARAMETERS FOR SIMULATION OF TIO_2/CDS/CIGS SOLAR CELLS.

Term	**Parameters**	**TiO_2**	**CdS**	**CIGS**
Thickness	d (nm)	Variable	50	3000
Band gap	Eg (eV)	3.2 [11]	2.4	1.1
Electron affinity	χ (eV)	4 [11]	4.2	4.5
Relative permittivity	ε_r	9 [11]	10	13.6
Electrons/ holes' mobility	μ_n/μ_p (cm^2/s)	20/10 [11]	10/2.5	10/2.5
Donor density	N_d (cm^{-3})	10^{16} [11]	10^{17}	1
Acceptor density	N_a (cm^{-3})	0 [11]	0	2.10^{16}
Density of defects	N_t (cm^{-3})	5.10^{15} [11]	$1.77.10^{17}$	$1.77.10^{13}$

The proposed solar cell was modeled under an AM 1.5 light spectrum with an intensity of 1000 W/m². By incorporating various material parameters into SCAPS-1D, several aspects of solar cell performance such as open-circuit voltage (Voc), short-circuit current density (Jsc), fill factor (FF) and conversion efficiency can be analyzed.

III. RESULTS

It is evident that the optical window plays a critical role in ensuring maximum light absorption by protecting the PV materials, enhancing light trapping, managing heat, and providing electrical insulation. Its design and material choice, significantly, impact the overall efficiency and longevity of the solar cell. High transparency is essential for maximizing the amount of sunlight that can be converted into electrical energy.

The thickness of this layer is a key factor in optimizing the solar cell's efficiency. In fact, the thickness of optical window impacts how much light can pass through and reach the photovoltaic material. Thus, an optimal thickness ensures maximum light absorption; reduce the reflection of light away from the cell, and allow more light to be utilized for energy conversion, thereby, enhancing the solar cell efficiency.

In order to enhance the performance of TiO_2/CdS/CIGS, the effect of varying of titanium dioxide (TiO_2) layer thickness between 50 and 500 nm is investigated while the other layer parameters are kept constant. Fig. 2 displays the effect of TiO_2 film thickness on the performance of TiO_2/CdS/CIGS solar cell, including open-circuit voltage (Voc), fill factor (FF), short-circuit current density (Jsc), and efficiency (η).

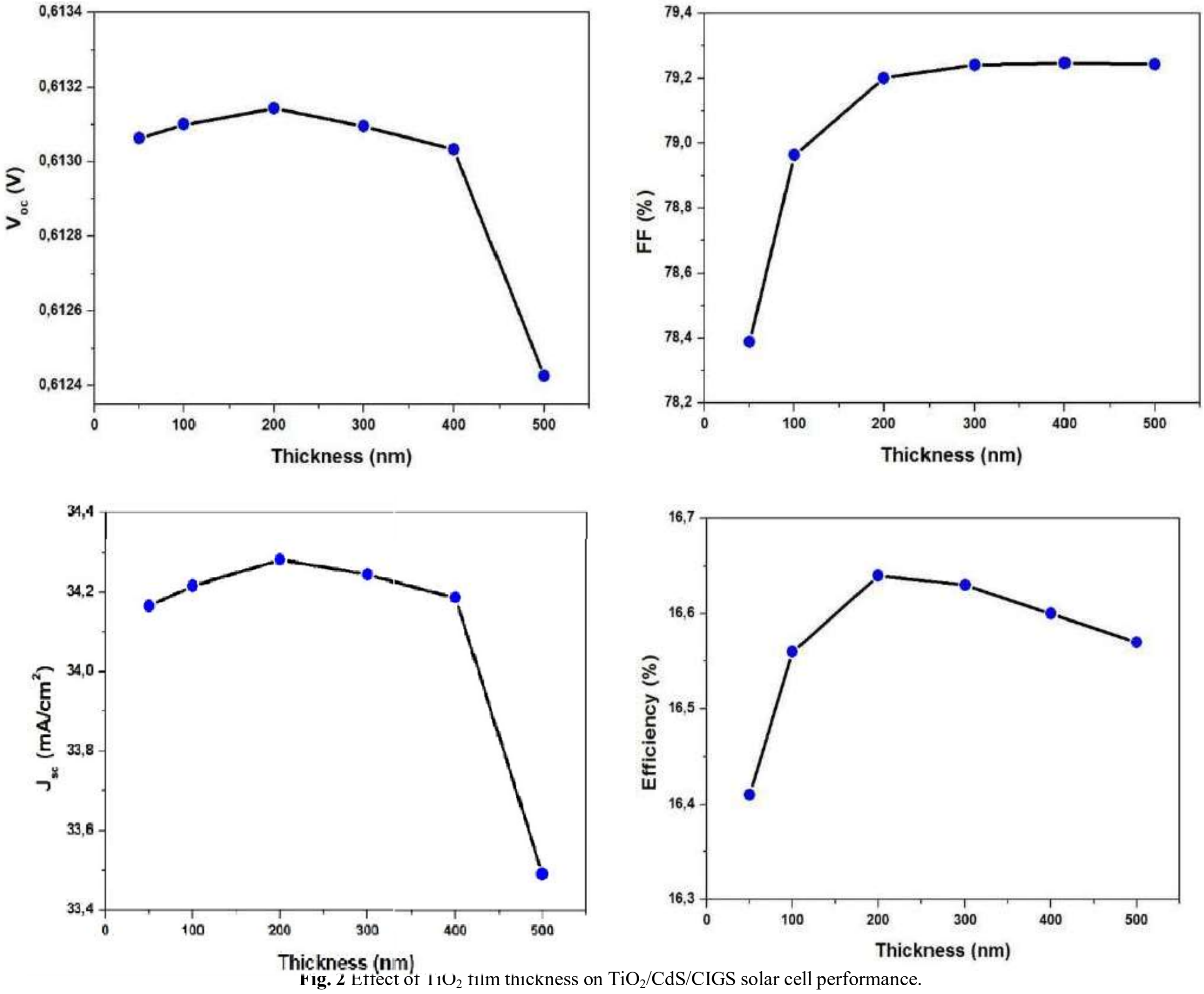

Fig. 2 Effect of TiO_2 film thickness on TiO_2/CdS/CIGS solar cell performance.

The obtained results indicate that Voc and Jsc increase, slightly, when TiO_2 film thickness increases from 50 to 200 nm. Then, they decrease, drastically, for further film thickness increment. Moreover, the Full Factor (FF) is found to increase, rapidly, with TiO_2 layer thickness increment until 200 nm, and then it starts to stabilize. It is in the order of 79 %. Concerning the efficiency (η) of the simulated solar cell, as it can be seen from Fig. 2, it increases with thickness rising to reach the highest value which is about 16.64 % in the case of TiO_2 layer thickness in the order of 200 nm. For further thickness increment, there is an outstanding decrease of η. Thus, it is evident to signal that a thickness of about 200 nm for TiO_2 layer ensures the highest photovoltaic efficiency of TiO_2/CdS/CIGS simulated solar cell. Similar behaviour has been observed by Mohammed F. Al-Mudhafer et al. [12].

In fact, this behaviour may be explained by the fact that a very thin optical window layer may not absorb or transmit enough light to the active layer of the solar cell. This means that a significant amount of the incident light might be reflected or absorbed by the optical window layer itself, reducing the amount of light that reaches the active layer where it can be converted to electricity.

As TiO_2 layer thickness increases, it can absorb and transmit more light effectively. This allows more light to reach the active layer, enhancing the generation of electron-hole pairs and, thus, increasing the efficiency of the solar cell. However, if TiO_2 layer becomes too thick, it can start to absorb too much light before it reaches the active layer. Additionally, excessive thickness can increase the distance that charge carriers need to travel, which can lead to higher recombination losses and reduced efficiency. This investigation may be useful guidelines for the development of solar cells based on TiO_2 material as optical window.

IV. CONCLUSIONS

SCAPS-1D software was employed in order to analyze the structure of TiO_2/CdS/CIGS solar cell. The study focused on the impact of titanium dioxide (TiO_2) layer thickness on the photovoltaic efficiency of the simulated solar cell. Indeed, the simulation revealed that a thickness of about 200 nm ensured the highest photovoltaic efficiency. A promising value of, approximately, 16.64 % was found. The short current density (Jsc), the open circuit voltage (Voc) and the Fill Factor (FF) are found to be about 34.28 mA/cm^2, 0.61 V and 79.20 %, respectively. These findings are crucial for the enhancement of solar cell performance.

ACKNOWLEDGMENT

We extend our gratitude to Mr. Marc Burgelman and his colleagues from the University of Gent, Belgium, for providing the SCAPS-1D package.

REFERENCES

[1] Shunhao Ge, Dandan Sang, Liangrui Zou, Yu Yao, Chuandong Zhou, Hailong Fu, Hongzhu Xi, Jianchao Fan, Lijian Meng and Cong Wang, *Nanomaterials* 2023, 13, 1141. https://doi.org/10.3390/nano13071141.
[2] Altamash Shabbir , Zain Hussain, Zuhair S. Khan, Wajahat Qasim, *Optical Materials,* Volume 146, December 2023, 114525.
[3] El-Rahman, A.M.A., Rabia, M. & Mohamed, S.H, *J Mater Sci: Mater Electron* **34**, 1149 (2023).
[4] L. Et-taya, A. Benami, T. Ouslimane, *Sustainability,* 14 No 3, 1916 (2022).
[5] L. Et-taya, T. Ouslimane, A. Benami, *Sol. Energy* 201 No 1, 827 (2020).
[6] M. Belarbi [a], M. Beghdad [b], A. Mekemeche, *Solar Energy,* Volume 127, April 2016, Pages 206-215.
[7] Muhammad Raheel Khan and Bozena Jarzabek, *Mater. Proc*. 2024, 17, 16. https://doi.org/10.3390/materproc2024017016.
[8] Mohamed Al-Hattab, L'houcine Moudou, Mohammed Khenfouch, Omar Bajjou, Younes Chrafih, Khalid Rahman, *Solar Energy*, Volume 227, October 2021, Pages 13-22.
[9] S. Abdelaziz [a], A. Zekry [a], A. Shaker [b], M. Abouelatta, *Optical Materials*, Volume 101, March 2020, 109738.
[10] R. Scheer, *Thin Solid Films*, (2011); vol. 519, no. 21, pp. 7472-7475.
[11] A. Benami, T. Ouslimane, L. Et-taya, A. Sohani, *Journal of nano and electronic physics*, Vol. 14 No 1, 01033(5pp) (2022).
[12] Mohammed F. Al-Mudhafer, Ahmed S. Al-Asadi, *Journal of Electronic Materials*, https://doi.org/10.1007/s11664-021-09020-5.

Nanostructured thin films coupled to single-junction solar cells: towards record efficiencies

Abdoulaye Sène, Césaire Ngor Ndiaye, Modou Kara Mbengue et Lamine Thiaw

Ecole Supérieure Polytechnique de Dakar, Université Cheikh Anta Diop de Dakar, SENEGAL

abdoulaye37.sene@ucad.edu.sn

cesairengor.ndiaye@esp.sn

modoukara1.mbengue@ucad.edu.sn

lamine.thiaw@ucad.edu.sn

Abstract— **Today, to address the environmental risks posed by fossil fuels and the greenhouse gases they emit, renewable energies offer a strong alternative to this problem. Among these renewable energies, the most widely used is photovoltaic solar. However, its performance remains below expectations despite its high potential. So to improve the efficiency of these solar cells, light trapping and the use of materials with a better absorption coefficient of the light spectrum are essential. It is in this context that the ternary $In_xGa_{1-x}N$ alloy is being intensively studied as a promising material for photovoltaic solar cells, thanks to its broad spectral coverage, good electrical characteristics and high power resistance. In addition, a synthesis method based on complex admittances has been used in our previous work to demonstrate the benefits of light confinement for electromagnetic field amplification in multi-dielectric structures. The aim of this work is to demonstrate the importance of coupling single-junction solar cells with nanostructured dielectric thin films. To this end, mathematical modeling of the $In_xGa_{1-x}N$-based single-junction cell was carried out in order to study its behavior when subjected to multispectral illumination in the static regime after its coupling with the resonant multidielectric structure. Next, the various electrical quantities of the coupled cell were simulated in Matlab/Simulink, after studying the influence of the various physical parameters (doping and sizing of the cell's n and p regions) on conversion efficiency. Promising results were obtained from these simulations, predicting record yields of 35.3% for the coupled cell, compared with 26.5% for the control cell.**

Keywords— **Coupling, nanostructures, multi-dielectric, solar cell, $In_xGa_{1-x}N$, static regime, multi-spectral illumination, resonant structure.**

I. INTRODUCTION

Today, there is a strong global demand for energy, both from industrialized and developing countries. All the primary energy consumed in the world comes from fossil fuels, causing global warming because of the greenhouse gases (GHGs) they emit. As a result, with fossil fuels running out and in order to protect the environment, “green” electricity needs to be increasingly present in our daily lives, particularly in our heating and transport systems, so that we can switch from fossil fuels to less polluting renewable energies [1]. One of these is photovoltaic solar energy, which has seen strong growth in recent years, offering a very practical solution for obtaining electricity anywhere. There are many expectations in this sector. These include conversion efficiency, which is still low in relation to availability.

On the one hand, since the photovoltaic conversion efficiency of a solar cell is intimately linked to the optical and electrical properties of semiconductor materials, solar cells are currently the focus of a great deal of research. With a view to improving energy efficiency in the photovoltaic sector, a number of research projects are focusing on the use of alternative materials that can exploit the full range of wavelengths in the solar spectrum, based on thin-film technology. These include technologies based on III-V materials, which are highly promising in terms of efficiency [2]. The In.Ga.N alloy is one of the most widely used alloys today for high-efficiency photovoltaic applications, thanks to its wide and adjustable energy gap ranging from 0.7 eV to 3.42 eV [3].

On the other hand, given that solar power generation is based on the principle of light absorption (photons) by the solar cell and the generation of electron-hole pairs, light trapping plays a particularly important role in improving light absorption to achieve record yields [4]. It is within this framework that a synthesis method based on complex

ISSN: 2961-6611

admittances, widely used to synthesize optical functions, has been implemented in our previous work [5], [6], [7]. So to help improve the electrical parameters of a photovoltaic cell and achieve record efficiency, the present work focuses on the coupling of single-junction solar cells with nanostructured dielectric thin films, thereby enhancing the optical field under multispectral illumination in the static regime.

II. SYNTHESIS METHOD

We'll now turn to the first point, which concerns the method for synthesizing multi-dielectric thin-film stacks that resonate under oblique illumination. The idea is to deposit alternating high-index (Ta_2O_5) and low-index (SiO_2) dielectric thin films between a superstrate (glass: BK7) and a substrate (air). To achieve total absorption, synonymous with amplification of the optical field in the structure, we'll start with the energy balance. Remember that, in an energy balance, the light absorbed, reflected, transmitted and scattered by a material must be equal to the incident field, as shown in equation 1.

$$A + R + T + D = 100\% \qquad (1)$$

With :

- A : l'absorption
- R : the reflection
- T : the transmission
- D : the distribution

On the one hand, in practice, the surfaces used have roughnesses of less than 500 nm [8] ; in which case we can consider diffusion to be zero. On the other hand, transmission is also zero, since we're working at oblique incidence under conditions of total internal reflection. So equation 1 reduces to : $A + R = 100\%$. Therefore, to have an absorption A equal to 100% in the multi-dielectric structure, the reflection R would have to be equal to 0. However, in the theory of complex admittances applied to nanostructured thin films under oblique illumination, reflection is given by equation 2 [9] :

$$R(\sigma_k) = 1 - A(\sigma_k) = \left|\frac{\tilde{n}_0 - Y_0(\sigma_k)}{\tilde{n}_0 + Y_0(\sigma_k)}\right|^2 = 0 \qquad (2)$$

where $\tilde{n}_0$ represents the effective index of the superstrate (glass : BK7), σ_k spatial pulsation and $Y_0(\sigma_k)$ represents the admittance between the superstrate and the first deposited layer, which can only be obtained from the effective index of the substrate, which is air. Therefore, to cancel this reflection, it would be necessary to $Y_0(\sigma_k) = \tilde{n}_0$. So, as shown in (Fig. 1), to reach this point Y_0, we start from Y_p which is identified with the substrate's effective index $\tilde{n}_s$ and using the recurrence relation between complex admittances (3) obtained from the transition matrix (4), we deduce Y_{p-1}. Knowing Y_{p-1} we deduce Y_{p-2} and one by one, you can find Y_0. As a result, we can cancel out the R reflection, giving us total absorption A=100%.

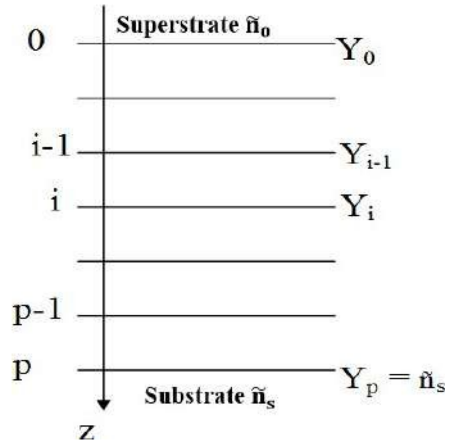

Fig. 1 Admittance Y_0 deduced by recurrence from the initial substrate admittance $Y_p = \tilde{n}_s$

$$Y_{j-1} = \frac{Y_j \cos(\delta_j) - i\tilde{n}_j \sin(\delta_j)}{\cos(\delta_j) - i\frac{Y_j}{\tilde{n}_j}\sin(\delta_j)} \qquad (3)$$

ISSN: 2961-6611

$$M_j = \begin{pmatrix} \cos(\delta_j) & -\frac{i}{\eta_j}\sin(\delta_j) \\ -i\eta_j\sin(\delta_j) & \cos(\delta_j) \end{pmatrix} \qquad (4)$$

The results of this synthesis method are shown for absorption and field strength (Fig. 2 and Fig. 3).

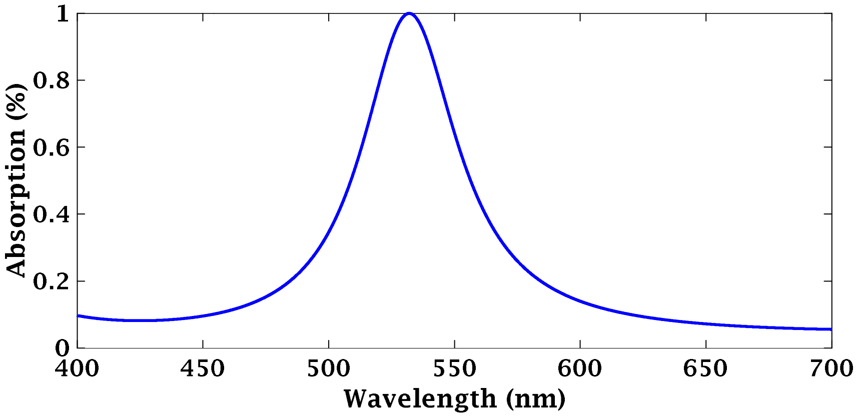

Fig. 2: Evolution of absorption as a function of wavelength

Figure 2 shows the evolution of absorption as a function of wavelength, with a maximum at around 532 nm.

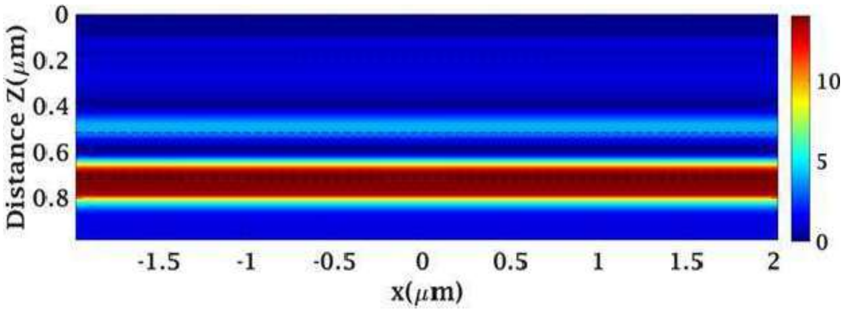

Fig. 3 Field mapping in the stack

In this figure, we visualize the evolution of the field in the stack, which is maximal in the last layer with an overintensification of the order of 14.

III. SOLAR CELL MODELING

To model the cell we're going to couple with the resonant structure, we've carried out a study of the material's spectral coverage, electrical characteristics and resistance to high power levels, in order to make the right choice of solar cell. And from the literature studies we've carried out, it follows that the model selected is an In.Ga.N-based single-junction cell consisting of an anti-reflective layer, a P-doped layer (emitter) and an N-doped layer (base), as shown in (Fig. 4).

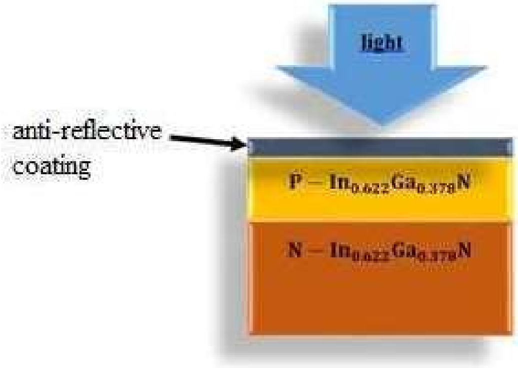

Fig. 4 InGaN-based single-junction solar cells [10]

ISSN: 2961-6611

This anti-reflective coating reduces the reflection of light on the front face, which is one of the main sources of losses that limit the conversion efficiency of solar cells.

This choice is based on its wide tunable spectral coverage, covering an energy range from 0,7 eV à 3,4 eV simply by changing the Indium composition and its high absorption coefficient of the order of 10^5cm^{-1}. The cell is modeled in the static regime under multi-spectral illumination, where the photocurrent for a given wavelength ($J_{ph}(\lambda)$) is obtained from the contribution of three current densities J_n , J_p et J_{ZCE} expressed as follows [11], [12] :

$$J_n(\lambda) = \left(\frac{qF(1-R)\alpha L_n}{\alpha^2 L_n^{\,2}-1}\right)\left(\frac{\left({}^{S_n\tau_n}/_{L_n}+\alpha L_n\right)-e^{-\alpha x_j}\left(\left({}^{S_n\tau_n}/_{L_n}\right)\cosh\left({}^{x_j}/_{L_n}\right)+\sinh\left({}^{x_j}/_{L_n}\right)\right)}{\left({}^{S_n\tau_n}/_{L_n}\right)\sinh\left({}^{x_j}/_{L_n}\right)+\cosh\left({}^{x_j}/_{L_n}\right)}-\alpha L_n e^{-\alpha x_j}\right) \quad (5)$$

$$J_p(\lambda) = \left(\frac{qF(1-R)\alpha L_p}{\alpha^2 L_p^{\,2}-1}e^{-\alpha(x_j+w)}\right)\left(\alpha L_p-\frac{\left({}^{S_p\tau_p}/_{L_p}\right)\left(\cosh\left({}^{H}/_{L_p}\right)-e^{-\alpha H}\right)+\sinh\left({}^{H}/_{L_p}\right)+\alpha L_p e^{-\alpha H}}{\left({}^{S_p\tau_p}/_{L_p}\right)\sinh\left({}^{H}/_{L_p}\right)+\cosh\left({}^{H}/_{L_p}\right)}\right) \quad (6)$$

$$J_{ZCE}(\lambda) = qF(1-R)e^{-\alpha x_j}(1-e^{-\alpha w}) \quad (7)$$

$$J_{ph}(\lambda) = J_n(\lambda) + J_p(\lambda) + J_{ZCE}(\lambda) \quad (8)$$

With

- $J_n(\lambda)$: the current density collected by the transmitter at a given wavelength.
- $J_p(\lambda)$: the current density collected by the base at a given wavelength.
- $J_{ZCE}(\lambda)$: the current density collected by the space charge zone at a given wavelength

.In order to compare the performance of the control cell with that of the coupled cell, we start from the calculation of photon current density and open circuit voltage in the multi-spectral case.

The total photocurrent density, J_{ph}, is obtained by integrating the current density, $J_{ph}(\lambda)$ over the entire range of the solar spectrum used ; i.e. from 0.32 µm to 1.32 µm [13], [14].

$$J_{ph} = \int_{\lambda_{min}}^{\lambda max} J_{ph}(\lambda)d\lambda = \int_{\lambda_{min}}^{\lambda max} J_n(\lambda)d\lambda + \int_{\lambda_{min}}^{\lambda max} J_p(\lambda)d\lambda + \int_{\lambda_{min}}^{\lambda max} J_{ZCE}(\lambda)d\lambda \quad (9)$$

The expressions for the open circuit voltage V_{co} depending on the inverse saturation current density J_0 are given by the equations [15], [16]:

$$V_{co} = \frac{K_B T}{q}\ln\left(\frac{J_{ph}}{J_0}+1\right) \quad (10)$$

$$J_0 = qn_i^2\left(\frac{D_n}{L_n N_A}+\frac{D_p}{L_p N_D}\right) \quad (11)$$

IV. SOLAR CELL/RESONANT STRUCTURE COUPLING

Here, we're going to couple these resonant components with the single-junction solar cell (Fig. 5). The aim is to collect as much energy as possible from the dielectric structure and inject it into the cell.

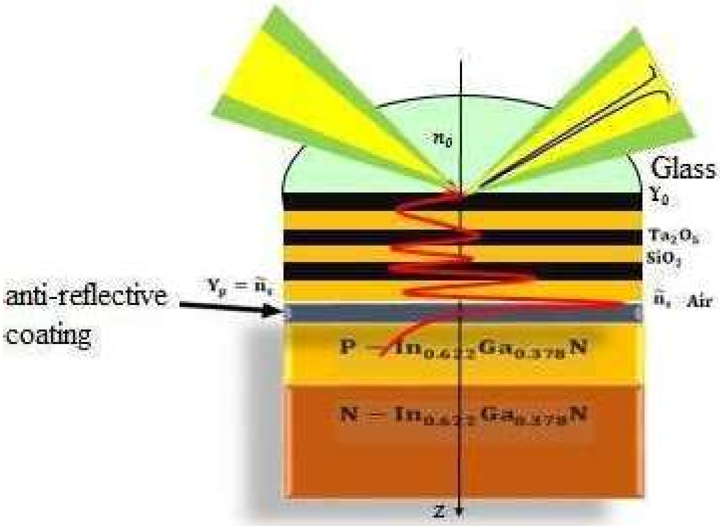

Fig. 5 Single-junction cell coupled with resonant structure

The results obtained for the absorption and field of the coupled cell are shown in Fig. 6 and Fig. 7.

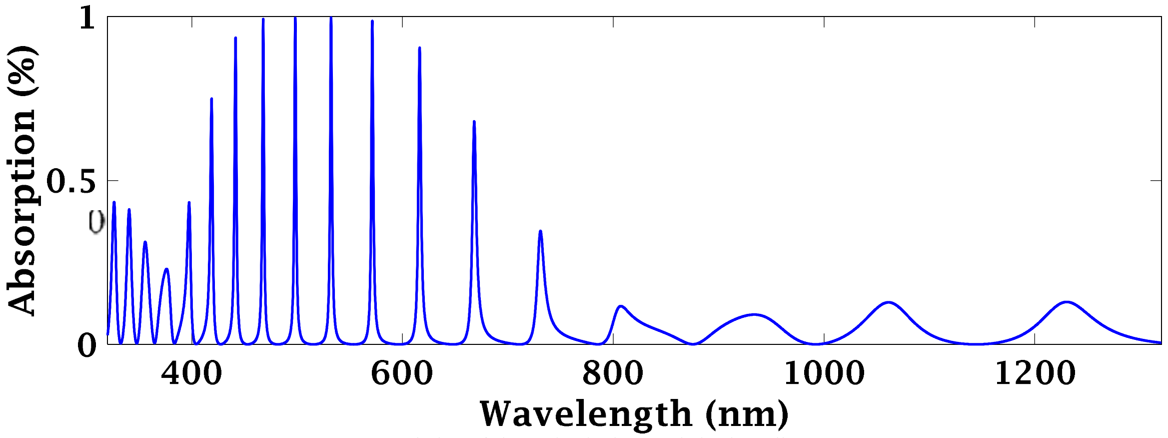

Fig. 6 Evolution of absorption in the coupled solar cell

The evolution of absorption shows that all wavelengths around 500 nm have more than 80% absorption, which translates into an amplification of the field around these wavelengths. However, this does not prevent other wavelengths from being absorbed naturally by the cell.

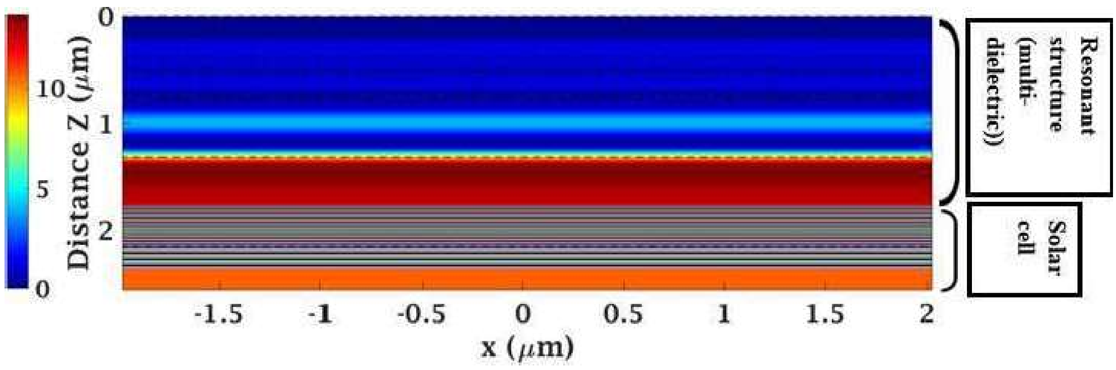

Fig. 7 Field mapping in the coupled solar cell

Remember that absorption is closely linked to field amplification. In Fig. 7, for example, if we represent the field mapping in the coupled solar cell, we obtain an amplification of the order of 10.

V. SIMULATION RESULTS AND DISCUSSION

In order to demonstrate the importance of adding the resonant structure to a conventional solar cell considered as a reference, we carried out a comparative study between the two structures (reference cell and coupled cell). For front illumination, simulation of the two cells gave us the output parameters shown in Fig. 8 and Fig. 9.

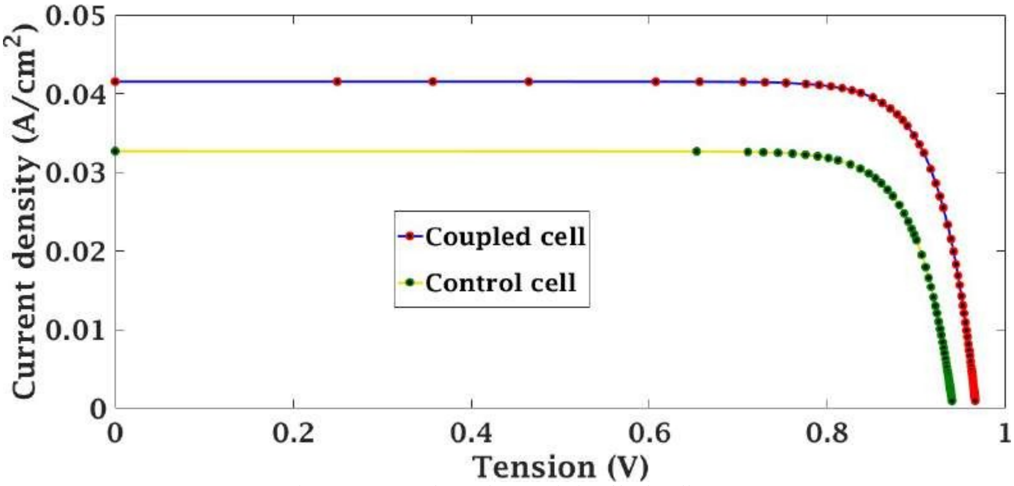

Fig. 8 Current-voltage characteristic of both cells

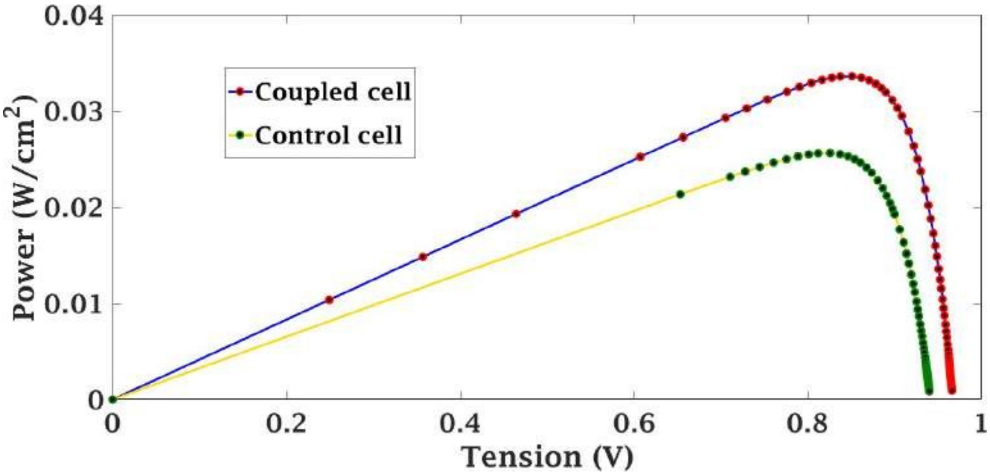

Fig. 9 Power-voltage characteristic of the two cells

These output parameters (short-circuit current, open-circuit voltage, maximum power and efficiency) are summarized in the following table :

TABLE I OUTPUT PARAMETERS FOR THE TWO CELLS

	Jcc (mA)	**Vco (V)**	**Jmax (mA)**	**Vmax (A)**	**Pmax (mW)**	**Ƞ (%)**
Control cell	**32.68**	**0.94**	**31.53**	**0.81**	**26.51**	**26.5**
Coupled cell	**41.55**	**0.97**	**39.5**	**0.85**	**33.61**	**35.3**

From this table, we can see that the output parameters of the coupled cell are better than those of the control cell, with an 8.79% increase in yield. This increase is due to the amplification of the optical field before it reaches the “front” of the cell.

ISSN: 2961-6611

VI. CONCLUSION

In this article, we were able to design a dielectric multilayer stack that enabled us to achieve total field absorption and thus field amplification.

Once the stack had been designed, modeling the single-junction cell in the static regime under multispectral illumination enabled us to couple it to the dielectric multilayer stack.

Using Matlab/Simulink software, we were also able to visualize the evolution of the absorption and field resulting from the coupling between the resonant structure and the single-junction cell. These results led to a giant optical amplification of the electromagnetic field, enabling us to simulate the electrical parameters of both cells (control and coupled).

As a result of this comparative study, a record yield of 35.3% was achieved for the coupled cell, compared with 26.5% for the control cell. Therefore, based on these results, we dare to hope that these resonant structures would be good candidates for the future solar cell market.

REFERENCES

[1] British Petroleum Company Limited, “Statistical Review of World Energy globally consistent data on world energy markets and authoritative publications in the field of energy,” *BP Energy Outlook*, vol. 70, p. 72, 2021.

[2] RADE, “Energies renouvelables, transition énergétique et enjeux climatiques en droit africain,” 2021.

[3] A. Adaine, S. Ould Saad Hamady, and N. Fressengeas, “Simulation study of a new InGaN p-layer free Schottky based solar cell,” *Superlattices Microstruct.*, vol. 96, pp. 121–133, 2016.

[4] “Comment fonctionnent l | Jokosun.” [Online]. Available: https://www.jokosun.com/blog/fonctionnement-cellule-photovoltaique. [Accessed: 31-May-2024].

[5] Michel Lequime et Claude Amra, *De l’Optique électromagnétique à l’Interférométrie Concepts et Illustrations*, EDP Scienc. 2013.

[6] A. Sene, C. N. Ndiaye, and L. Thiaw, “Absorption optimization in nano-structured optical thin films: Application to photovoltaic solar cells,” *2022 IEEE Int. Conf. Electr. Sci. Technol. Maghreb, Cist. 2022*, 2022.

[7] A. Sène, C. N. Ndiaye, and L. Thiaw, “Efficiency improvement in photovoltaic solar cells by giant optical amplification : metallic Vs multi-dielectric coupling,” *Int. J. Sci. Res. Eng. Technol.*, vol. 19, pp. 52–63, 2023.

[8] C. Poull *et al.*, “La rugosité des surfaces et ses applications To cite this version : HAL Id : hal-03892076 La rugosité des surfaces et ses applications,” 2022.

[9] C. Ndiaye, “Exaltation optique géante dans les filtres interférentiels : Modélisation, Optimisation et réalisation. Thèse de doctorat,” 2012.

[10] A. Mesrane, F. Rahmoune, A. Mahrane, and A. Oulebsir, “Design and Simulation of InGaN p-n Junction Solar Cell,” vol. 2015, 2015.

[11] T. Zdanowicz, T. Rodziewicz, and M. Zabkowska-Waclawek, “Theoretical analysis of the optimum energy band gap of semiconductors for fabrication of solar cells for applications in higher latitudes locations,” *Sol. Energy Mater. Sol. Cells*, vol. 87, no. 1–4, pp. 757–769, 2005.

[12] C. A. Hernández-Gutiérrez, A. Morales-Acevedo, D. Cardona, G. Contreras-Puente, and M. López-López, “Analysis of the performance of InxGa1−xN based solar cells,” *SN Appl. Sci.*, vol. 1, no. 6, 2019.

[13] S.-W. Feng, C.-M. Lai, C.-Y. Tsai, Y.-R. Su, and L.-W. Tu, “Modeling of InGaN p-n junction solar cells,” *Opt. Mater. Express*, vol. 3, no. 10, p. 1777, 2013.

[14] Y. Zhao *et al.*, “InGaN-Based Solar Cells for Space Applications,” vol. 1, pp. 954–957, 2017.

[15] P. François, K. Tagne, K. Kenfack, and A. Dimitri, “Journal of Renewable Energies,” vol. 24, pp. 25–39, 2021.

[16] Z. Li *et al.*, “Theoretical simulations of InGaN/Si mechanically stacked two-junction solar cell,” *Phys. B Condens. Matter*, vol. 414, pp. 110–114, 2013.

Title: Predicting Depression in Hemodialysis Patients: A Comparative Analysis of Regression and Boosting Algorithms

SAHRAOUI Leila[1],FRIH Hacène[2],ZERMI Narima[1]

[1]Badji Mokhtar University Bp 12 El Hadjar–Annaba- Algeria
Faculty of Technology/ Electronic Department/ Laboratory of Automatic and Signal Processing of Annaba (LASA)
[2]Badji Mokhtar University Bp 12 El Hadjar–Annaba- Algeria
Faculty of Science/ Department of Biology
sahraouil@yahoo.fr, leila.sahraoui@univ-annaba.dz
frihhacene@yahoo.fr
zermi.narimai@gmail.com

1. Introduction:

Chronic kidney disease (CKD) affects a significant portion of the global population, necessitating hemodialysis in advanced stages. Depression, commonly seen in hemodialysis patients, adversely affects quality of life and increases morbidity. Traditional detection methods are often subjective, underscoring the need for objective predictive tools like machine learning.

This study evaluates the effectiveness of machine learning algorithms, including logistic regression, CatBoost, Adaboost, and XGBoost, to predict depression in hemodialysis patients. By assessing various predictors such as demographic, clinical, and psychosocial data from 127 patients, the study identifies key factors influencing depression and compares algorithmic performances in terms of accuracy, sensitivity, and precision.

2. Methods:

Data Collection: Data on 127 hemodialysis patients from Annaba, Algeria, were analyzed, including demographic characteristics and responses to several psychological questionnaires.

Analytical Approach: Logistic regression was used as a baseline for comparison with advanced algorithms such as CatBoost, Adaboost, and XGBoost. Model performance was evaluated based on standard metrics including the area under the ROC curve.

3. Results:

Model Performance: Logistic regression showed the highest accuracy (88.5%), with CatBoost also performing well (80.8% accuracy). Adaboost and XGBoost had similar but lower accuracies (61.5%).

Predictor Importance: Key predictors included age, weight, GHQ_12 scores, ISI scores, and blood group, highlighting their relevance in influencing depression risks.

Discussion conclusion:

The study confirms the effectiveness of machine learning in predicting depression, with logistic regression and CatBoost showing significant promise. The analysis reveals the importance of both psychological measures and physical health indicators. The findings advocate for integrating machine learning tools into clinical practices to enhance early detection and personalized management of depression among hemodialysis patients. Machine learning models, especially logistic regression and CatBoost, are effective in predicting depression in hemodialysis patients, suggesting their potential utility in clinical settings. Continued research is necessary to refine these models and validate findings across broader populations.

Future studies should focus on longitudinal designs to better understand the temporal dynamics of depression in this demographic. Expanding the scope to include a larger sample size and additional predictive variables could further enhance model accuracy and applicability in diverse clinical settings.

REFERENCES

[1] Levey, A. S., Atkins, R., Coresh, J., Cohen, E. P., Collins, A. J., Eckardt, K.-U., Nahas, M. E., Jaber, B. L., Jadoul, M., Levin, A., Powe, N. R., Rossert, J., Wheeler, D. C., Lameire, N., &Eknoyan, G. (2007). Chronic kidney disease as a global public health problem: Approaches and initiatives – a position statement from Kidney Disease Improving Global Outcomes. Kidney International, 72(3), 247-259. https://doi.org/10.1038/sj.ki.5002343

[2] Kovesdy, C. P. (2022). Epidemiology of chronic kidney disease: an update 2022. Kidney International Supplements, 12(1), 7-11. https://doi.org/10.1016/j.kisu.2021.11.003

[3] Kimmel, P. L., Weihs, K., & Peterson, R. A. (1993). Survival in hemodialysis patients: the role of depression. Journal of the American Society of Nephrology, 4(1), 12-27. https://doi.org/10.1681/ASN.V4112

[4] Finkelstein, F. O., Wuerth, D., & Finkelstein, S. H. (2009). Health related quality of life and the CKD patient: challenges for the nephrology community. Kidney International, 76(9), 946-952. https://doi.org/10.1038/ki.2009.307

[5] Kovacs, A. Z. et al. (2011). Sleep disorders, depressive symptoms and health-related quality of life—a cross-sectional comparison between kidney transplant recipients and waitlisted patients on maintenance dialysis. Nephrology Dialysis Transplantation, 26(3), 1058–1065. https://doi.org/10.1093/ndt/gfq476

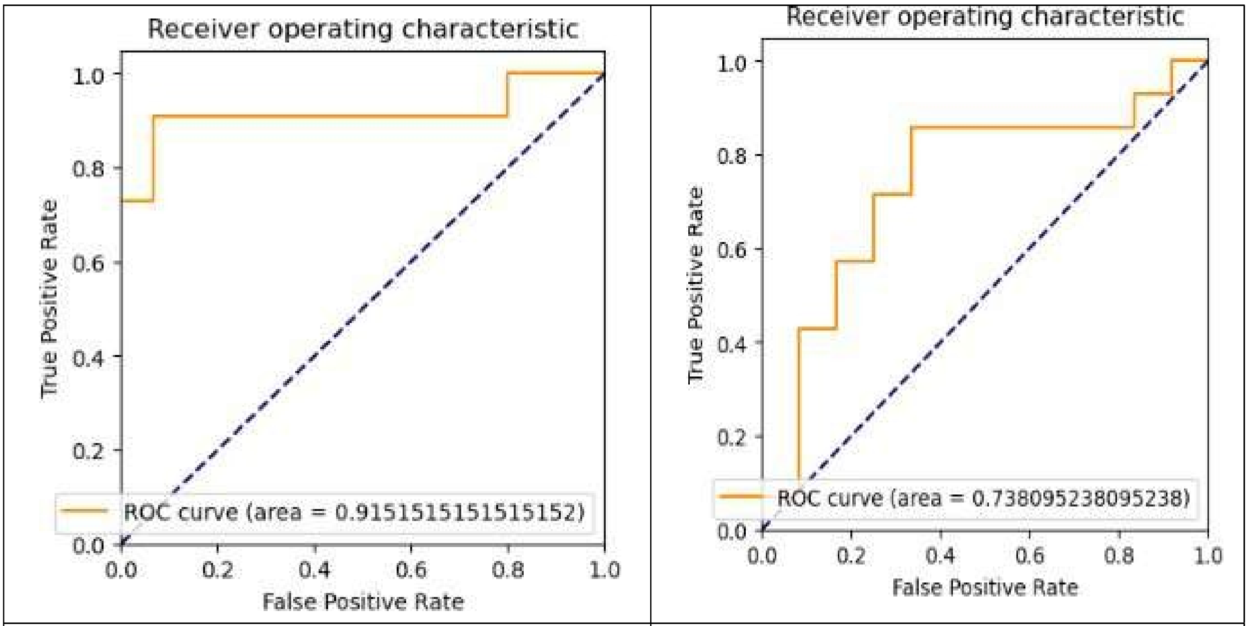

a/ CatBoostClassifier b/XGBClassifier

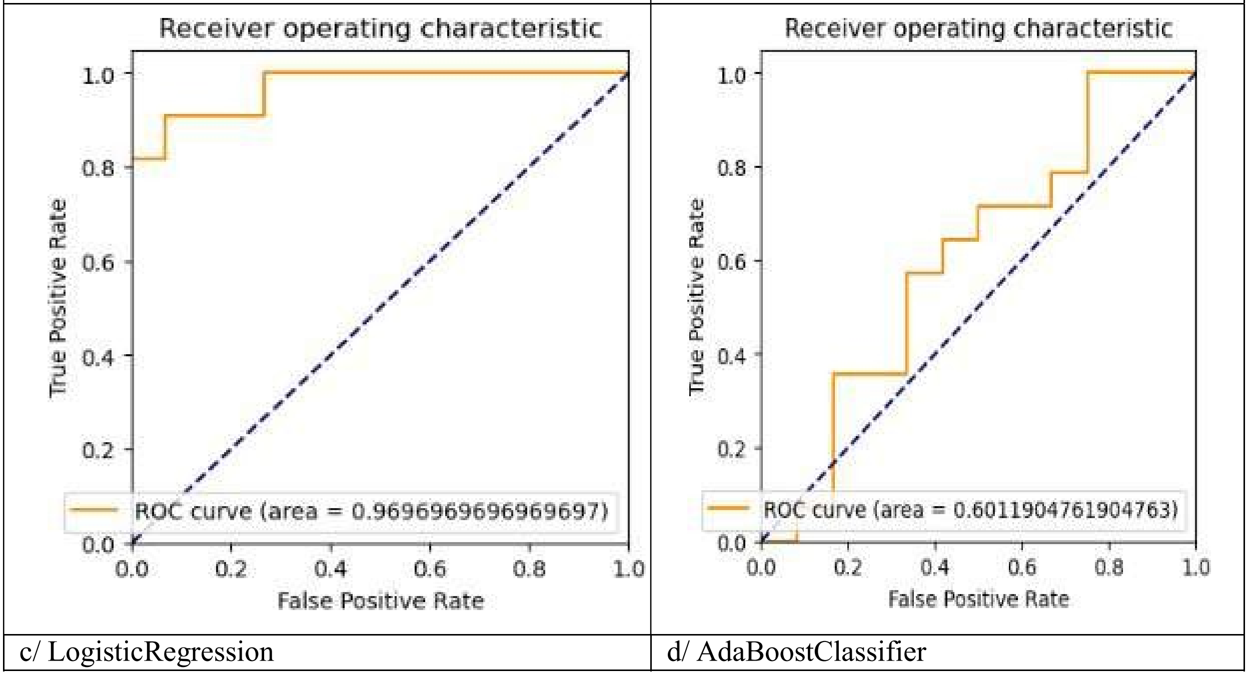

c/ LogisticRegression d/ AdaBoostClassifier

Figure 01 :ROC curve : a/CatBoostClassifier, b/XGBClassifier, c/ LogisticRegression, d/ AdaBoostClassifier.

ISSN: 2961-6611

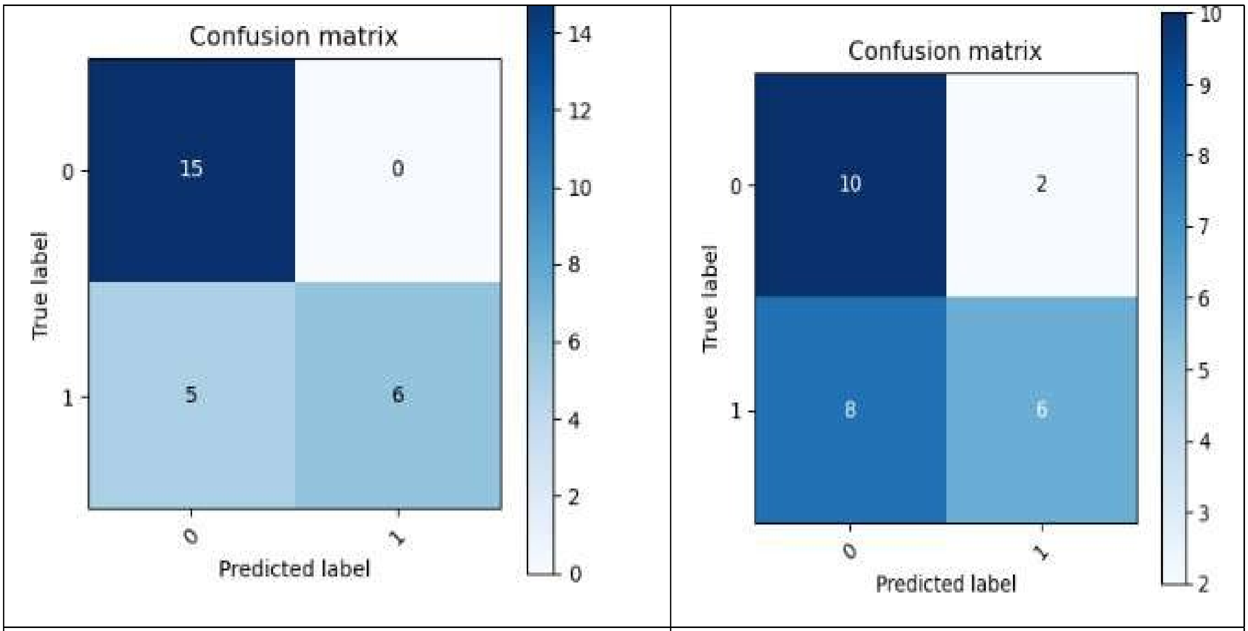

a/ CatBoostClassifier

b/XGBClassifier

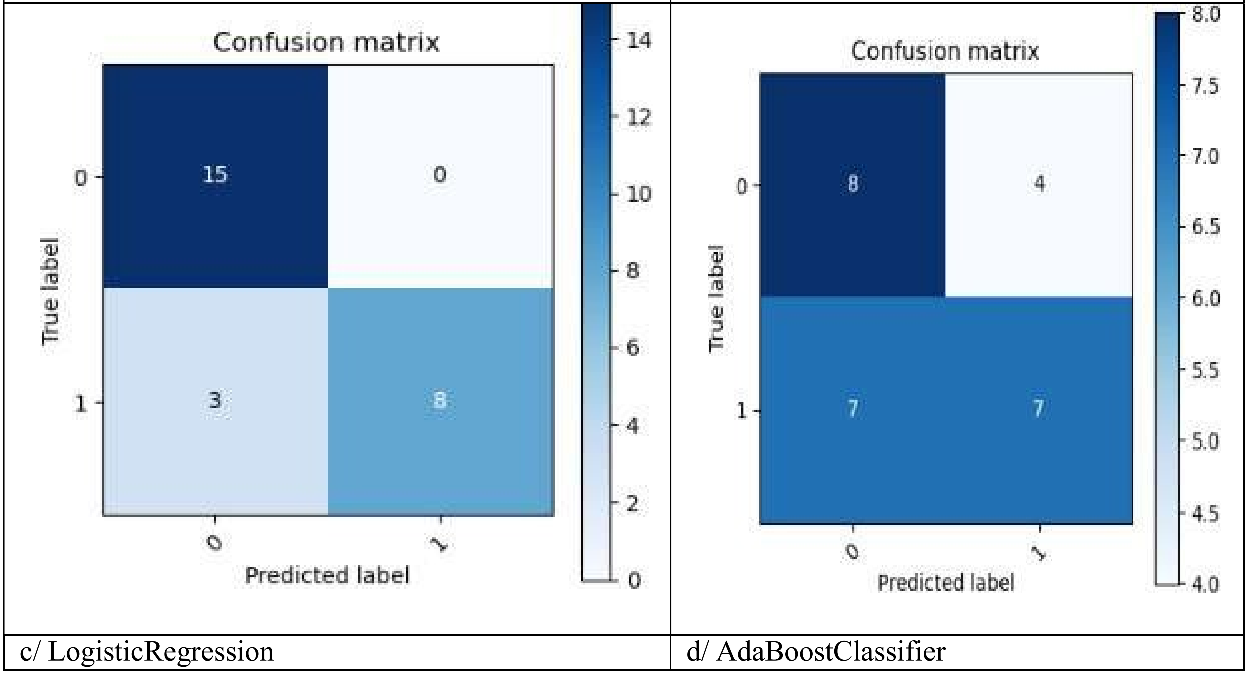

c/ LogisticRegression

d/ AdaBoostClassifier

Figure 02 : Confusion matrix : a/CatBoostClassifier, b/XGBClassifier, c/ LogisticRegression, d/ AdaBoostClassifier.

ISSN: 2961-6611

The impact of Entrepreneurial orientation on Performance Company: The Moderating Effect of the External Environment: Tunisian case

Author name: Soufien Zouari

e-mail: zouarysoufien@yahoo.fr

ID ORCID : 0009-0008-0308-8518

Author affiliation: University of economics and management sciences- SFAX TUNISIA.

ISSN: 2961-6611

Abstract

Although entrepreneurial orientation (EO) has been shown to play a key role in increasing firm performance (FP), the effects of EO have been extremely over simplified. The plethora of empirical studies on EO and FP suggest that the EO-FP relationship is linearly positive regardless of the amount of EO investment. The results show that EO increases FP at the bounded level. We argue that the excessive use of EO and organizational incapability may contribute to the non-linearity of such effects. We also find that highly dynamic environments enhance the EO-FP relationship. We present prescriptive implications to practitioners on the antecedent conditions for EO practices.

***Keywords*: Inverted U-Shaped, entrepreneurial orientation, performance, environment, SMEs.**

1. Introduction

A nation's economic development largely depends on new firm creation and innovation in existing firms (Schumpeter 1934; Audretsch, Keilbach, and Lehmann 2006). When we discuss new firm creation and innovation in existing firms, the core of the academic literature pays attention to entrepreneurship. Not only academics but also policy makers and practitioners are interested in this important sociological, economical, psychological, historical and managerial aspect of theory, as the latter are keen to know how to make society entrepreneurial. Firms that plan and manage innovations well will survive and stay competitive. Firms that rarely develop and introduce new products in the market will find long-term survival challenging (Arrow 1962). Therefore, firms must practice some form of entrepreneurial orientation (EO), which is exemplified as engagement in technological change, risky investments and pioneering activities in an effort to introduce new and innovative products/services.

Researchers have predominantly agreed on defining firm-level entrepreneurship as EO(Lumpkin and Dess 1996; Dess and Lumpkin 2005; Covin and Lumpkin 2011). The underlying assumption is that a positive link exists between a firm's EO and firm performance (FP).A conceptual understanding of this relationship has been emphasized (see Miller 1983; Guth and Ginsberg 1990; Covin and Slevin 1991; Lumpkin and Dess1996) and empirically tested in different cultural, geographical and business contexts (see Kraus, Rigtering, Hughes, and Hosman 2012; Lee, Lee, and Pennings 2001; Moreno and Casillas 2008; Wiklund and Shepherd 2005; Zahra and Covin 1995; Zahra and Garvis 2000). The main body of empirical research of has reported a positive EO-FP relationship (see Rauch, Wiklund, Lumpkin, and Frese 2009).

Because of the relative newness of the field, many phenomena related to EO are unknown. The EO-FP relationship is at the forefront of such disputes (see Rauch et al. 2009). EO researchers have seemingly oversimplified the EO-FP relationship as completely linear (Guth and Gingsberg 1990; Covin and Slevin 199; Lumpkin and Dess 1996). However, we cannot simply follow such logic without carefully considering a firm's resources, organizational capabilities and surrounding environment (see Man, Lau, and Chan 2002; Zahra and Garvis 2000). For example, R&D investment can be inefficient, not linear (see Huang and Liu 2006), and the imbalance of product portfolio management due to organizational incapability may deteriorate the suggested EO-FP relationship. Innovation usually comes from technological innovation and new business model (Chesbrough 2003). EO requires many resources, which are consumed in innovative activities (Covin and Slevin 1991; Tang, Tang, Marino, Zhang, and Li 2008). The failure to launch new products and generate profits from them can translate into unproductive resources (mostly R&D and production-related resources),which may be useless for other businesses (Dess and Lumpkin, 2005). Studies also have reported an inverted U-shaped relationship between R&D intensity (i.e., innovation) and FP (Miller and Friesen 1984; Huang and Liu 2006). Such investments can also be substituted as opportunity costs that are incurred from not investing in other businesses, which can also lead to a product portfolio imbalance issue (Cooper, Edgett, and Kleinschmidt, 2000). Because of organizational incapability, firms invest too many resources in new product development without considering the need for a properly balanced product portfolio, and they maybe more likely to perform poorly as a result of portfolio failure (Cooper, Edgett, and Kleinschmidt 2001). We argue that, compared with a linear relationship, a curvilinear (i.e., inverted U-shaped) EO-FP relationship more accurately reflects reality (e.g., Tang et al. 2008; Zahra and Garvis 2000; Su 2011). Therefore, firms face a paradoxical dilemma in terms of being entrepreneurial or being managerial.

Recently, contingency-based EO research has received ample attention (Lyon, Lumpkin, and Dess 2000; Zahra and Garvis 2000; Lumpkin and Dess 2001; Stam and Elfring 2008). Such research argues that the EO-FP relationship is not homogeneous and that, in certain environments, this relationship can be strengthened or weakened. The moderating effects of such contingencies are mainly studied through external environments, such as market dynamism and market hostility (Covin and Slevin 1991; Zahra and Covin 1995; Lumpkin and Dess 1996). Although the theoretical understanding of Covin and Slevin, 1991) claims that dynamic and hostile market conditions have a positive impact on the EO-FP relationship, a number of researchers have found that market dynamism and hostility play an insignificant moderating role (e.g., Wiklund 1999; Lumpkin and Dess 2001; Wiklund and Shepherd 2003, 2005; Frank, Kessler, and Fink 2010). These inconsistent results call for researchers to conduct more empirical studies to establish a generally grounded theory on a contingency-based model of EO-FP relationship (Lyon et al. 2000). Every contingency is unique because of national and regulatory differences and diverse incentives and rules of competition. Therefore, contingency-based EO-FP testing is needed in many different contextual settings. This study investigates the confounding EO-FP relationship and examines the moderating effects of environmental dynamism and hostility on the EO-FP relationship in the context of Tunisian manufacturing SMEs.

2. Theory and Hypothesis

2.1 Entrepreneurial orientation and firm performance

Entrepreneurship researchers have long been encouraged to prove how entrepreneurship is developed, deployed and sustained within organizations and to help them become more innovative, take on riskier projects and act proactively (Miller 1983; Covin and Slevin 1991; Zahra and Covin 1995; Lumpkin and Dess 1996), thus ultimately outperforming others in the market. Zahra and Covin's(1995)[1]definition of EO paints the most comprehensive picture of what can be operationalizin entrepreneurial firms:

> *...top management risk taking with regard to investment decisions and strategic actions in the face of uncertainty; the extensiveness and frequency of product innovation and the related tendency toward technological leadership; and the pioneering nature of the firm as evident in the propensity to aggressively and proactively compete with industry rivals.*(p.44)

In their guest editor's note in a strategic management journal, Guth and Ginsberg (1990) emphasize the direct relationship between firm-level entrepreneurship (i.e., EO) and FP. Covin and Slevin (1991) also insist on the direct positive effect of EO on FP, which can be moderated by internal (e.g., resources, culture, and structure), external (e.g., market dynamism and hostility) and strategic (e.g., grow, maintain, and harvest) variables. Further conceptual work can be found in Lumpkin and Dess (1996), who argue that environmental and organizational factors influenced the direct positive effect of EO on FP. A few researchers have found that EO has a positive direct effect on FP (Lee et al. 2001; Wiklund and Shepherd 2003;Li, Huang, and Tsai 2009). Rauch et al. (2009) conducted a vital meta-analysis of the EO-FP relationship based on 51 EO studies. They found that the EO-FP relationship is reasonably positive (where, r > .242), but it varies depending on the contexts (e.g., nations and measures) and contingencies (e.g., firm size, industry, and environment) in question.

A few researchers have probed the sustainability of EO's effect on FP. Based on longitudinal data on 108 U.S. manufacturing firms, Zahra and Covin (1995) found that EO had an increasingly positive effect on the performance indicator over a 7-year period. They used a composite performance value for the return on assets (ROA), the return on sales (ROS) and the growth rate, which was factor analyzed and multiplied by each score of the participating firms. In a study of 132 Swedish small firms, Wiklund (1999) tested the EO level using two years of performance data, mostly on the scale of

ISSN: 2961-6611

growth, i.e., “sales growth, employment growth, sales growth compared to competitors, and market value growth compared to competitors” (p.41). Similar to Zahra and Covin (1995), Wiklund contended that the effect of EO would increase gradually. In a similar vein, many other studies have reported a positive EO-FP relationship (Zahra and Garvis 2000; Lee et al. 2001; Wiklund and Shepherd 2005). Thus, we hypothesize the following:

Hypothesis 1: A direct positive relationship level of EO and FP.

Lyon et al. (2000) cautioned against the prevailing belief of EO’s positive effect of FP and argued that a deeper understanding of EO-FP relationship was needed. For example, in examining 164 Dutch software venture firms, Stam and Elfring (2008) found no direct positive effect of EO on perceived FP or sales growth. In addition, Moreno and Casillas (2008) reported an insignificant relationship between EO and FP. Kraus and al. (2012) tested the effect of each EO dimension on FP and found that two EO dimensions—innovativeness and risk taking had no significant effect on FP. Zahra and Garvis (2000) had also previously found a non-linear (inverted U-shaped) relationship in their study of international entrepreneurship and FP. More recently, Tang et al. (2008) and Su (2011) have attempted to take a more complex but realistic view of the EO-FP relationship. They claimed that the EO-FP relationship is positive but non-linear. In the context of Chinese venture capital and established firms, they found a curvilinear (i.e., an inverted U-shaped) relationship between EO and FP. Tang et al. (2008) argued that such phenomena could result from the lack of institutional support and role formalization, whileSu (2011) argued that the liability of newness, the lack of resources and social ties and role ambiguity could be potential causes.

Although we agree with Tang et al. (2008) and Su (2011), this perspective and their results are relatively new and limited in scope (only Chinese context). We further argue that excessive use of EO and a lack of organizational capabilities may contribute to the insignificant and negative effects reported thus far (Dess and Lumpkin 2005; Stam and Elfring 2008). A genuine entrepreneurial firm usually aggressively develops new products and services ahead of its competitors (Miller 1983; Lumpkin and Dess 1996). Such firms require ample resources for consumption and better

ISSN: 2961-6611

organizational capabilities(Wiklund 1999; Tang et al. 2008). A firm without such resources and capability can be at risk of failure. Because firm resources are not infinite, firms cannot invest in every opportunity that they identify (Bessant and Tidd 2007; Tang et al. 2008). For example, product portfolio management, which is mostly handled by senior management, can also affect the EO-FP relationship. Firms that invest too many resources into new product development and do not recognize the need for a balanced portfolio due to organizational incapability are likely to encounter financial instability (Cooper et al. 2000). Therefore, inefficiency in R&D investment (EO) and organizational incapability may have a negative impact on FP. We argue that the performance of EO initiatives will increase up to a certain point and then decrease. Based on rationale above, we propose the following:

Hypothesis2:An inverted U-shaped relationship exists between the level of EOand FP.

2.2 Moderating role of external environments

Lyon et al. (2000) noted the inconsistent results regarding the EO-FP relationship can be attributable to contingency factors. They divided such contingencies into two types: organizational and environmental factors. Lyon et al. (2000) stated "organizational factors include internal contingencies such as organizational size, structure and strategy, and the characteristics of the top management team. Environmental factors include external forces such as industry trends, growth rates and business cycles, as well as the power of a firm's customers, suppliers and competitors" (p.1077). Among these contingencies, researchers have shown particular interest in the external environment for its moderating role in the EO-FP relationship (Covin and Slevin 1989; Zahra and Garvis 2000; Lumpkin and Dess 2001; Wiklund and Shepherd 2005; Frank et al. 2010). Due to the cultural, regulatory, legislative and political differences across nations, the external environmental conditions for business practices are not identical. Business practitioners across different countries can view these diverse environmental conditions as either opportunities or threats. Therefore, the environmental factors affecting the EO-FP relationship must be tested in a specific country or continent (the proximity, similarity and familiarity of social, cultural and business practices must be considered).

Zahra (1996) classified market environments as dynamic, hostile and heterogeneous. In dynamic and hostile environments, the EO-FP relationship has been found to be strengthened (Kraus et al. 2012). Miller and Friesen (1983) defined market dynamism as “the amount and unpredictability of change in customer tastes, production or service technologies, and the modes of competition in the firm's principal industries” (pp.233). Firms in dynamic environments face frequent changes in technologies, customer needs and competitors’ strategic moves. The greater uncertainty in particular industries(high-tech industries) requires firms to develop new products faster than their competitors to keep up with such changes. Lumpkin and Dess (2001) found that the EO-FP relationship is positively moderated by dynamic market conditions. However, Wiklund and Shepherd (2005) found a negative moderating effect of market dynamism on the EO-FP relationship in Swedish firms. Frank et al. (2010)found no evidence for the moderating role of market dynamism on the EO-FP relationship.

Miller and Friesen (1983) defined market hostility as “price, product, technological and distribution competition, severe regulatory restrictions, shortages of labor or raw materials, and unfavorable demographic trends” (pp.233). In hostile environments, firms are more threatened by frequent regulatory changes, the difficulties in acquiring needed resources and the lack of new business opportunities (Zahra and Garvis 2000). Firms in hostile environments are continuously challenged to survive. These harsh environmental conditions require strong entrepreneurial mindsets (McGrath and MacMillan 2000). EO may be needed more in hostile environments than in benign ones because the risk and uncertainty is greater in the former. Zahra and Covin (1995) tested the role of market hostility in the context of U.S. manufacturing firms and found that market hostility had a positive effect on the EO-FP relationship. Covin and Slevin (1989) also found a positive moderating effect of market hostility on the relationship between EO and FP. However, in their study of 94 U.S. firms, Lumpkin and Dess (2001) found no significant moderating effect of environmental hostility on the EO-FP relationship. Although many have asserted the positive moderating roles of market dynamism and hostility (Covin and Slevin 1991; Zahra and Garvis 2000), contingency-based entrepreneurship research continues to reveal inconsistent results, which stem from the context specific nature of such research. As such, further empirical research is necessary. Based on rationale above, we propose the following:

Hypothesis 3: In a dynamic environment, the EO-FP relationship will be strengthened.

Hypothesis 4: In a hostile environment, the EO-FP relationship will be strengthened.

3. Research Methods

3.1 Sample and data collection

The data were gathered from Tunisian manufacturing SMEs. First, to meet the criteria for SMEs, we chose firms that had fewer than 150 employees. To reduce selection bias, we then used a random sampling method to select firms that can be normally distributed regardless of the region and industry. The total sampling frame consisted of 483 firms. The sample was drawn from an SME database provided by the Tunisian government. We then conducted on-site to assess the questionnaire's face validity. We conducted our survey from September 2020 to November 2020. We used a two-step data collection process. We first contacted all the firms in the sample to ask if they would be willing to participate in the survey; we then sent an email survey to entrepreneurs and executives. We obtained a final usable sample of 146, and this two-step method significantly improved response rate (30.22 %). Among the participating firms, the average number of employees was 35, and the average firm age was 19. Following data collection, we checked for non-response bias; we used t-tests to compare a number of employees in our response group and in our non-response group. The results indicated no statistically significant difference between these groups.

3.2 Measures

Entrepreneurial orientation was measured by asking entrepreneurs and executives to evaluate their perceptions of their firms' innovativeness, risk taking and proactiveness. First, we measured EO as a "composite weighting"of the level of innovativeness (Miller 1983, p.771), risk taking and proactiveness. Many empirical studies consider EO unidimensional rather than multidimensional (Rauch et al. 2009). All nine EO items were adopted from Naman and Slevin's (1993) questionnaire, based on 7-point Likert type scale. Three items were used to measure the firm's innovativeness: (1) its propensity for technological leadership and innovation, (2) its introduction of new products, and (3) its product line changes. Another three items were used to measure the firm's risk-taking tendencies: (1) its propensity for high-risk projects, (2) its fearless acts to achieve its goals, and (3) its boldness in exploiting potential opportunities. The remaining three items measured the firm's proactiveness: (1) its ability to act before its competitors do, (2) its attempts to become the first mover in the market, and (3) its possession of a competitive posture to beat out its competitors.

Firm performance was measured using four items adopted from Tang et al. (2008). Three items measured the firm's relative performance compared to that of its competitors in terms of (1) revenue growth, (2) market share growth, and (3) profit growth. The remaining item measures the firm's overall performance. All items were anchored on 7-point Likert type scale.

Market dynamism and hostility were moderating variables in this study. Market dynamism and hostility were measured based on the scale used in Miller and Friesen (1983). Three items were adapted to measure market dynamism. To measure market dynamism, we asked the executives about (1) the predictability of their competitors' activities, (2) the changes in customers' tastes and (3) the speed of their firms' innovation in terms of new products/processes. To measure market hostility, we asked them (1) whether their industry was predictable, (2) whether their competitor's activities were aggressive and (3)which competitor activities affected their business. All items were anchored on 7-point Likert type scale.

We controlled for firm size, firm age and the radicalness of new product innovations in this study. Compared with smaller firms, larger firms have more available resources for new product development, which affects the degree to which EO can be pursued (Lyon et al. 2000). A logarithm for the number of employees was computed to reflect firm size. Firm age was measured by the number of years that the participating firms had been in existence, and a natural log value was computed to reflect age. Younger firms may be more likely to act innovatively and boldly because they are disadvantaged in the market because of the "liability of newness" (Freeman, Carroll, and

Hannan 1983). Finally, we controlled for the innovative radicalness of new product development using four items measured on a 7 point-Likert scale, as suggested by Gatignon, Tushman, Smith, and Anderson (2002). These four items asked executives whether their firms' new products were perceived as (1) slight improvements from the previous technology (reversed), (2) breakthrough innovations, (3) difficult to replace with substitutes from older technology, and (4) major technological advancements in subsystem (Gatignon et al. 2002, pp.1112). If firms develop new products with highly sophisticated features, subsystems and embedded technologies, they will be more likely to possess an innovative posture.

4. Analysis and Results

We tested the validity and reliability of the data. As suggested in the literature, all the items were loaded on each construct to determine construct validity. All the items used in the testing model had Eigen values greater than 1.0 and factor loadings greater than 0.4, indicating a good convergent validity (Stevens 1992). All the items showed high coefficient alphas (Cronbach $\alpha > 0.6$), indicating good data reliability (Nunnally 1978). Table 1 provides descriptive statistics and the correlation matrix for all variables. The correlation between the independent variables was relatively low. Furthermore, the variance inflation factors (VIFs) for the variables ranged from 1.1 to 1.8 and fell well below the cut-off value of 10, indicating no multicollinearity issues.

We used hierarchical regression analysis to test our hypotheses. The results of the tests are presented in Table 2. In the first step, we used control variables in Model 1. The effect of EO and the moderators were included in Model 2. In Model 3, we added the squared term of EO. In Model 4, we included the interaction items. The adjusted R^2 for Model 1 was 0.057, and the f-statistic was highly significant ($p<0.01$). We found that firm age had a negative effect on FP among Tunisian manufacturing SMEs (β=-0.266, $p<0.01$). Model 2 had an adjusted R^2 of 0.896, and the f-statistic was highly significant ($p<0.01$). We found that the number of employees, the radicalness of new product innovation and environmental dynamism had a positive significant direct effect on FP.

Model 3 had an adjusted R^2 of 0.898, with high statistical significance ($p<0.01$). We found a strong positive effect of EO on FP ($\beta = 1.040$, $p < 0.01$), thus supporting Hypothesis 1. We also found that the squared term of EO had a negative significant effect on FP ($\beta = -0.309$, $p < 0.01$), thus supporting Hypothesis 2. Hypothesis 3 and 4 tested the interaction effect of environmental dynamism and hostility on the EO-FP relationship. The results showed that, as an interacting variable, environmental dynamism had a positive effect on the EO-FP relationship ($\beta = 0.271$, $p < 0.05$).However, as an interacting variable, environmental hostility was not found to have a significant effect on the EO-FP relationship ($\beta = -0.158$, n.s.). Therefore, the results supported Hypothesis 3 but led us to reject Hypothesis 4. We plotted the relationship between EO and FP in Figure 1.

5. Discussion

Research suggests that practicing EO has a direct positive effect on FP. However, this unduly bright forecast may mislead managers who strongly believe that their success lies in a strategy of being entrepreneurial at all times. However, we have observed the failures of the most innovative products and the firms that have been regarded as highly entrepreneurial. Although many entrepreneurial firms have experienced enormous success, innovation is a necessary but insufficient condition for success. Although the failures of such products and firms cannot be generalized to reflect the ineffectiveness of EO, researchers should examine EO's effects on performance in greater depth. In this paper, we argue that excessive use of EO (the inefficiency of R&D investment) and organizational incapability may contribute to the non-linearity of such effects. In this study, we further scrutinized the effects of EO. This study sought to investigate the curvilinear effect of EO on performance. We found an inverted U-shaped relationship between the EO and FP of Tunisian manufacturing SMEs. The results indicate that a positive relationship exists between EO and FP at the bounded level. This finding lends supports to the recent arguments and findings of Tang et al. (2008) and Su (2011). We do not intend to deny the positive effect of EO (Innovative/risky/bold activities) on FP. As found in this study, EO plays a key role in increasing FP. Research and history have proven that innovation is vital in creating competitive advantage and helping firms stay in the market. However, the findings here provide a few practical implications. We suggest that firms must measure their entrepreneurial competencies and organizational capabilities when setting their entrepreneurial goals. Pursuing EO without considering entrepreneurial competencies, organizational capabilities and calculated risks, FP can be beyond the control of the entrepreneurs/executives, who must then rely on luck or external conditions. EO research can be problematic when it over simplifies the EO-FP relationship and considers exante conditions, such as entrepreneurial competencies and organizational capabilities, as constants. We need to delve into the ways in which the level of EO implementation varies according to these exante EO conditions and the optimal level of EO for particular firms. Man et al. (2002) also argued that particular factors, such as the competitive environment, entrepreneurial competencies and organizational capabilities, are critical for achieving SMEs' entrepreneurial goals.

This study also investigated the moderating roles of environmental dynamism and hostility in the EO-FP relationship. We found that the impact of EO on performance increases as the external environment becomes more dynamic, which implies that firms operating in highly uncertain and fast-changing environments require more EO. Such environments are often found in high-tech industries. However, we found no support for the positive role of environmental hostility in the EO-FP relationship. The lack of business opportunities, difficulties in acquiring necessary resources and severe regulations shape the conditions for hostile environments, which are predominantly observed in saturated/mature markets and infrastructure industries. When confronted with innovation saturation, strong rival groups and industrial structures planned by governments or regulatory authorities in these industries, entrepreneurs will find making their businesses succeed extremely difficult through their efforts alone (Osenton 2004). Regulation has been found to have a negative impact on entrepreneurship (Baumol 1990; Lee and Peterson 2000). Therefore, in hostile environments, we argue that EO may not lead to superior performance (Lumpkin and Dess 1996),depending on nation-specific laws, regulations, policies, etc. Further research is needed in this important area.

This study is not without limitations. First, we focused on Tunisian manufacturing SMEs. Given the cultural, political and institutional differences of this context, the findings of this study should be interpreted and generalized with caution. Contextual differences across nations can significantly affect entrepreneurial attempts, processes and practices. Therefore, similar studies must be conducted in diverse national contexts. Second, this study focused on general manufacturing industries without targeting specific industries. To gain a more thorough understanding of industry variation in implementing EO, future research should focus on a particular industry. Classifying industrial sectors as high-tech, medium-tech and low-tech would be beneficial in cases in which the surrounding business environment is quite diverse.

REFERENCES

Arrow, K. (1962), ‘Economic Welfare and the Allocation of Resources for Innovation’, in *The Rate and Direction of Inventive Activity*, ed. R.R. Nelson, Princeton, NJ: Princeton University Press, pp.609-625.

Audretsch, D.B., Keilbach, M.C., and Lehmann, E.E. (2006), *Entrepreneurship and Economic Growth,* New York, NY: Oxford University Press.

Baumol, W.J. (1990), ‘Entrepreneurship: Productive, Unproductive, and Destructive’, *Journal of Political Economy*, 98, 893–921. doi:10.1086/261712.

Bessant, J., and Tidd, J. (2007), *Innovation and Entrepreneurship*, Chichester, UK: John Wiley & Sons.

Chesbrough, H. (2003), *Open Innovation:the New Imperative for Creating and Profiting from Technology*, Boston, MA: Harvard Business School Press.

Cooper, R., Edgett, S., and Kleinschmidt, E. (2001), ‘Portfolio Management for New Product Development: Results of an Industry Practices Study’, *R and D Management,* 31, 361-380. doi:10.1111/1467-9310.00225.

Cooper, R.G., Edgett, S., and Kleinschmidt, E. (2000), ‘New Problems, New Solutions: Making Portfolio Management More Effective’, *Research Technology Management*, 43, 18-33.

Covin, J.G., and Lumpkin, G.T. (2011), ‘Entrepreneurial Orientation Theory and Research: Reflections on a Needed Construct’, *Entrepreneurship Theory and Practice*, 35, 855–872. doi:10.1111/j.1540-6520.2011.00482.x.

Covin, J.G., and Slevin, D.P. (1989), ‘Strategic Management of Small Firms in Hostile and Benign Environments’, *Strategic Management Journal*, 10, 75-87. doi:10.1002/smj.4250100107.

Covin, J.G., and Slevin, D.P. (1991), ‘A Conceptual Model of Entrepreneurship as Firm Behavior’, *Entrepreneurship Theory and Practice*, 16, 7–25.

Dess, G.G., and Lumpkin, G.T. (2005), 'The Role of Entrepreneurial Orientation in Stimulating Effective Corporate Entrepreneurship', *Academy of Management Perspectives*, 19, 147-156. doi:10.5465/AME.2005.15841975.

Frank, H., Kessler, A., and Fink, M. (2010), 'Entrepreneurial Orientation and Business Performance: A Replication Study', *Schmalenbach Business Review*, 62, 175-198.

Freeman, J., Carroll, G.R., and Hannan, M.T. (1983), 'The Liability of Newness: Age Dependence in Organizational Death Rates', *American Sociological Review*, 48, 692-710. doi:10.2307/2094928.

Gatignon, H., Tushman, M.L., Smith, W., and Anderson, P. (2002), 'A Structural Approach to Assessing Innovation: Construct Development of Innovation Locus, Type, and Characteristics', *Management Science*, 48, 1103-1122. doi:10.1287/mnsc.48.9.1103.174.

Guth, W.D., and Ginsberg, A. (1990), 'Guest Editors' Introduction: Corporate Entrepreneurship', *Strategic Management Journal*, 11, 5-15.

Huang, C.J., and Liu, C.J. (2006), 'Exploration for the Relationship between Innovation, IT and Performance', *Journal of Intellectual Capital*, 6, 237-252.

Kraus, S., Rigtering, J.P.C., Hughes, M., and Hosman, V. (2012), 'Entrepreneurial Orientation and the Business Performance of SMEs: A Quantitative Study from the Netherlands', *Review of Managerial Science*, 6, 161-182. doi:10.1007/s11846-011-0062-9.

Lee, C., Lee, K., and Pennings, J.M. (2001), 'Internal Capabilities, External Networks, and Performance: A Study on Technology-Based Ventures', *Strategic Management Journal*, 22, 615–640. doi:10.1002/smj.181.

Lee, S.M., and Peterson, S.J. (2000), 'Culture, Entrepreneurial Orientation, and Global Competitiveness', *Journal of World Business*, 35, 401–416. doi:10.1016/S1090-9516(00)00045-6.

Li, Y., Huang, J., and Tsai, M. (2009), 'Entrepreneurial Orientation and Firm Performance: The Role of Knowledge Creation Process', *Industrial Marketing Management*, 38, 440-449. doi:10.1016/j.indmarman.2008.02.004.

Lumpkin, G.T., and Dess, G.G. (1996), 'Clarifying the Entrepreneurial Orientation Construct and Linking It to Performance', *Academy of Management Review*, 21, 135-172.

Lumpkin, G.T., and Dess, G.G. (2001), 'Linking Two Dimensions of Entrepreneurial Orientation to Firm Performance', *Journal of Business Venturing*, 16, 429-451. doi:10.1016/S0883-9026(00)00048-3.

Lyon, D.W., Lumpkin, G.T., and Dess, G.G. (2000), ‘Enhancing Entrepreneurial Orientation Research: Operationalizing and Measuring a Key Strategic Decision Making Process’, *Journal of Management*, 26, 1055-1085. doi:10.1177/014920630002600503.

Man, T.W.Y., Lau, T., and Chan, K.F. (2002), ‘The Competitiveness of Small and Medium Enterprises: A Conceptualization with Focus on Entrepreneurial Competencies’, *Journal of Business Venturing*, 17, 123-142. doi:10.1016/S0883-9026(00)00058-6.

McGrath, R.G., and MacMillan, I.C. (2000), *The Entrepreneurial Mindset*, Boston, MA: Harvard Business School Press.

Miller, D. (1983), ‘The Correlates of Entrepreneurship in Three Types of Firms’, *Management Science*, 29, 770-791. doi:10.1287/mnsc.29.7.770.

Miller, D., and Friesen, P.H. (1983), ‘Strategy-Making and Environment: The Third Link’, *Strategic Management Journal*, 4, 221-235. doi:10.1002/smj.4250040304.

Miller, D., and Friesen, P.H. (1984), ‘A Longitudinal Study of the Corporate Life Cycle’, *Management Science*, 30, 1161-1183. doi:10.1287/mnsc.30.10.1161.

Moreno, A.M., and Casillas, J.C. (2008), ‘Entrepreneurial Orientation and Growth of SMEs: A Causal Model’, *Entrepreneurship Theory and Practice*, 32, 507–528. doi:10.1111/j.1540-6520.2008.00238.x.

Naman, J.L., and Slevin, D.P. (1993), ‘Entrepreneurship and the Concept of Fit: A Model and Empirical Tests’, *Strategic Management Journal*, 14, 137-153. doi:10.1002/smj.4250140205.

Nunnally, J.C. (1978), *Psychometric Theory* (2nd ed.), New York, NY: McGraw-Hill.

Osenton, T. (2004), *The Death of Demand: Finding Growth in a Saturated Global Economy,* Upper Saddle River, NJ: Prentice Hall.

Rauch, A., Wiklund, J., Lumpkin, G.T., and Frese, M. (2009), ‘Entrepreneurial Orientation and Business Performance: An Assessment of Past Research and Suggestions for the Future’, *Entrepreneurship Theory and Practice*, 33, 761-787. doi:10.1111/j.1540-6520.2009.00308.x.

Schumpeter, J. (1934), *The Theory of Economic Development*, Cambridge, MA: Harvard University Press.

Stam, W., and Elfring, T. (2008), ‘Entrepreneurial Orientation and New Venture Performance: The Moderating Role of Intra- and Extraindustry Social Capital’, *Academy of Management Journal*, 51, 97-111. doi:10.5465/AMJ.2008.30744031.

Stevens, J. (1992), *Applied Multivariate Statistics for the Social Sciences* (2nd ed.), Hillsdale NJ: Lawrence Erlbaum Associates.

Su, Z., Xie, E., and Li, Y. (2011), 'Entrepreneurial Orientation and Firm Performance in New Ventures and Established Firms', *Journal of Small Business Management*, 49, 558- 577. doi:10.1111/j.1540-627X.2011.00336.x.

Tang, J., Tang, Z., Marino, L.D., Zhang, Y., and Li, Q. (2008), 'Exploring an Inverted U-Shape Relationship between Entrepreneurial Orientation and Performance in Chinese Ventures', *Entrepreneurship Theory and Practice,* 32, 219–239. doi:10.1111/j.1540-6520.2007.00223.x.

Wiklund, J. (1999), 'The Sustainability of the Entrepreneurial Orientation-Performance Relationship', *Entrepreneurship Theory and Practice*, 24, 37-48.

Wiklund, J., and Shepherd, D. (2003), 'Knowledge-Based Resources, Entrepreneurial Orientation, and the Performance of Small and Medium-Sized Businesses', *Strategic Management Journal*, 24, 1307-1314. doi:10.1002/smj.360.

Wiklund, J., and Shepherd, D. (2005), 'Entrepreneurial Orientation and Small Business Performance: A Configurational Approach', *Journal of Business Venturing*, 20, 71-91. doi:10.1016/j.jbusvent.2004.01.001.

Zahra, S.A. (1996), 'Goverance, Ownership, and Corporate Entrepreneurship: The Moderating Impact of Industry Technological Opportunities', *Academy of Management Journal*, 39, 1713-1735. doi:10.2307/257076.

Zahra, S.A., and Covin, J.G. (1995), 'Contextual Influences on the Corporate Entrepreneurship-Performance Relationship: A Longitudinal Analysis', *Journal of Business Venturing,* 10, 43-58. doi:10.1016/0883-9026(94)00004-E.

Zahra, S.A., and Garvis, D.M. (2000), 'International Corporate Entrepreneurship and Firm Performance: The Moderating Effect of International Environmental Hostility', *Journal of Business Venturing*, 15, 469-492. doi:10.1016/S0883-9026(99)00036-1.

Tables

Table 1 Descriptive Statistics and Correlations (N = 146).

	1	2	3	4	5	6	7
Mean	4.32	3.89	3.59	3.55	3.78	3.32	3.56
SD	0.92	1.18	0.70	1.01	0.82	0.37	0.76
1. Performance	1						
2. EO	0.835^{**}	1					
3. Environmental Dynamism	0.031	-0.412^{**}	1				
4. Environmental Hostility	-0.067	-0.048	-.023	1			
5. Firm Size [a]	0.042	-0.257^{**}	$.481^{**}$	.001	1		
6. Firm Age[a]	-0.258^{**}	-0.173^{**}	-.029	$.233^{**}$	$-.240^{**}$	1	
7. Product Radicalness	0.028	-0.386^{**}	$.686^{**}$	-.094	$.482^{**}$	-.031	1

[a] Logarithm, $^{*}p < 0.05$, $^{**}p < 0.01$, two-tailed test.

Table 2 Results of Regression Analysis - Standardized Beta Coefficients

Factor	Model 1	Model 2	Model 3	Model 4
Firm Size (log)	-0.040	0.059*	0.071***	0.074***
Firm Age (log)	-0.266***	-0.054*	-0.062***	-0.044†
Product Radicalness	0.039	0.199***	0.204***	0.211***
Environmental Dynamism (ED)		0.293***	0.289***	0.122
Environmental Hostility (EH)		0.020	0.019	0.129†
EO		1.040***	1.346***	1.063***
EO^2			-0.309***	-0.197
EO × ED				0.271*
EO × EH				-0.158
R^2	0.068	0.898	0.901	0.904
Adjusted R^2	0.057	0.896	0.898	0.901
F-value	6.033***	360.04***	317.94***	254.03***
R^2 Change		0.830	0.003	0.003
F-test for R^2 Change		666.24***	7.321***	3.899*

$^{\dagger}p < 0.1$, $^{*}p < 0.05$, $^{**}p < 0.01$, $^{***}p < 0.001$.

Figure

Figure 1 Relationship between EO and FP in Tunisian manufacturing SMEs

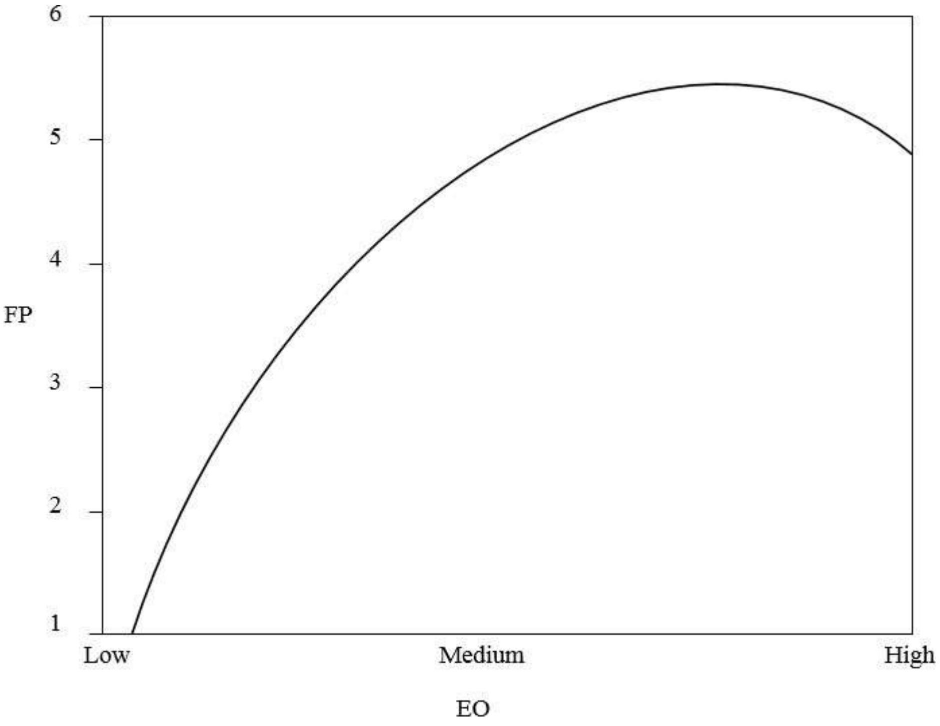

Geometrical parameters effect of the tower-chimney on the airflow behavior in a SCPP

Daimallah A[#1], Lebbi M [*2], Lounici M. S [#1]

[#1] *LEMI, FT, University M'hamed Bougara of Boumerdes, Boumerdes, Algeria*

[*2] *Unité de recherche appliquée en énergies renouvelables, URAER, Centre de développement des Energies Renouvelables, CDER ,47133,Ghardaia, Algeria*

[1] `a.daimallah@univ-boumerdes.dz`

***Abstract*— Solar chimney power plant (SCPP) is one of the cleanest systems that generate electric power from solar energy. The SCPP converts internal energy of the air into mechanical energy and then to electrical energy.**

The aim of this work is to conduct 2D numerical investigation on the effect of geometrical parameters of the tower chimney on the flow behavior. A 2D axisymmetric turbulent model is adopted, considering Manzanares prototype. The momentum and energy equations are solved using the finite volume method. A standard K-ε turbulent model is used. We analyse the influence of the radius and the height of the tower chimney. The obtained results indicate that geometrical parameters influence significantly the flow behaviour inside the solar chimney.

***Keywords*— Solar chimney, geometrical parameters, finite volume method, k-ε model, natural convection**

I. INTRODUCTION

The majority of electricity consumed in the world is produced from fossil resources. It is therefore necessary to develop means of exploiting renewable energies for the production of electricity.The SCPP concept was originally examined in 1903 by Cabanyes [1]. In 1931, Gunther [2] presented a description of a solar chimney power plant. In 1970s Schlaich achieved the basic study on the solar chimney. In 1981, his research team began the construction Manzanares prototype in, Spain [3-4]. In order to improve the performance of SCPP, extensive research has been carried out in this field. Pastohr et al. [5] conducted CFD simulation of SCPP. Von Backström et al. [6] investigated experimentally the pressure drop in a tall solar chimney with internal bracing wheels, to determine the bracing wheel loss coefficient. Then, Kebabsa et al. [7] studied numerically thermo-hydrodynamic behavior of an innovative solar chimney, named sloped collector entrance SCPP. They found that the new collector entrance design improve considerably the SCPP performance. Daimallah et al. [8] analysed the effect of the height and the radius of the collector on the flow behaviour in small solar chimney. They found that the mass flow rate is enhanced by about 27% for Rc = 12.5m and Hc = 0.25m. Kebabsa et al. [9] proposed novel concept of tower solar chimney which consists of annular tower solar chimney. They found that the total improvement in power output reaches 32% for the annular tower solar chimney. Ikhlef et al [10] analyzed the effect of environmental factors on the performance of a large/small scale prototype of a solar chimney with a thermal storage system for five regions of Turkey corresponding to different meteorological data. They obtained that the power output is affected by the global horizontal irradiance, the temperature, the relative humidity, and the wind velocity. They found that the best power production is for Antalya region according to the warmest and most irradiating site. The total annual power produced is 46.34E+6 kWh and 439.1E+3 kWh for large and small prototypes, respectively. Recently, Daimallah et al [11,12] investigated the influence of the radius ratio $Rt^* = Rtout/Rtinlet$ and the height of the tower-chimney, on the flow behavior inside the SCPP of Manzanares. They obtained an enhancement of mass flow rate by about 58.23% for the divergence of the tower-chimney.

Thus, it emerges that the tower chimney is incontestably a very important element of solar chimney power plant (SCPP). It is necessary to optimize the tower chimney dimensions in order to improve the performance of SCCP. The aim of this study is to investigate numerically the effect of the tower chimney height and radius on the flow behavior in a solar chimney.

ISSN: 2961-6611

II. MATHEMATICAL FORMULATION

A. *Physical model*

Figure 1 shows the physical model geometry of the studied solar chimney. This design has a collector radius (Rc =120m), collector height entrance (Hc = 1.7m), tower chimney height (Ht = 195m) and tower chimney radius (Rt = 5m). The values of $Rt^*=R/R_t$ and $Ht^*=H/H_t$ are varied as shown in Table 1.

TABLE I DIFFERENT CONFIGURATIONS OF THE SCPP

Ht(m)	Rt(m)	Ht^*	Rt^*
195	5	1; 0.75; 0.5; 0.25	1; 1.25 ;1.5;1.75; 2

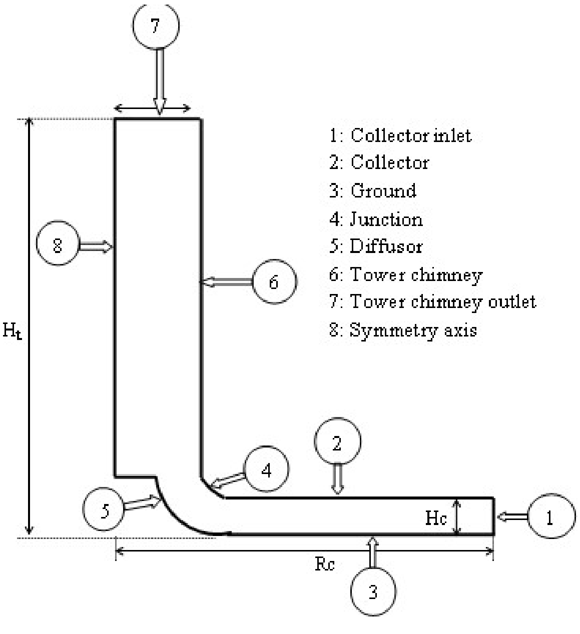

Fig. 1 Physical model of the problem

B. *Governing equation*

The airflow through the solar chimney power plant is prescribed by two-dimensional turbulent natural convection in cylindrical coordinates. The fluid is incompressible and satisfies the Boussinesq approximation, which implies that the density variation with temperature is negligible except in the motion equation for the buoyancy term. The governing equations that describe the flow are given by,

Continuity equation

$$\frac{\partial(\rho u)}{\partial x}+\frac{1}{r}\frac{\partial(r\rho v)}{\partial r}=0 \tag{1}$$

Momentum equations

$$\frac{\partial(\rho uu)}{\partial x}+\frac{1}{r}\frac{\partial(r\rho uv)}{\partial r}=-\frac{\partial p}{\partial x}+2\frac{\partial}{\partial x}\left[(\mu+\mu_t)\frac{\partial u}{\partial x}\right]+\frac{1}{r}\frac{\partial}{\partial r}\left[(\mu+\mu_t)r\left(\frac{\partial u}{\partial x}+\frac{\partial v}{\partial r}\right)\right]+(\rho-\rho_0)g \tag{2}$$

$$\frac{\partial(\rho uv)}{\partial x}+\frac{1}{r}\frac{\partial(r\rho vv)}{\partial r}=-\frac{\partial p}{\partial r}+\frac{\partial}{\partial x}\left[(\mu+\mu_t)\left(\frac{\partial v}{\partial x}+\frac{\partial u}{\partial r}\right)\right]+2\frac{1}{r}\frac{\partial}{\partial r}\left[(\mu+\mu_t)r\frac{\partial v}{\partial r}\right]-\frac{2(\mu+\mu_t)v}{r^2} \tag{3}$$

Energy equation

$$\frac{\partial(\rho uT)}{\partial x}+\frac{1}{r}\frac{\partial(r\rho vT)}{\partial r}=-\frac{\partial}{\partial x}\left[\left(\frac{\mu}{\Pr}+\frac{\mu_t}{\sigma_t}\right)\frac{\partial T}{\partial x}\right]+\frac{1}{r}\frac{\partial}{\partial r}\left[\left(\frac{\mu}{\Pr}+\frac{\mu_t}{\sigma_t}\right)r\frac{\partial T}{\partial r}\right] \tag{4}$$

Copyright © 2024
ISSN: 2961-6611

Turbulent kinetic energy equation

$$\frac{\partial(\rho k u)}{\partial x}+\frac{1}{r}\frac{\partial(r\rho k v)}{\partial r}=\frac{\partial}{\partial x}\left(\left(\mu+\frac{\mu_t}{\sigma_k}\right)\frac{\partial k}{\partial x}\right)+\frac{1}{r}\frac{\partial}{\partial r}\left(r\left(\mu+\frac{\mu_t}{\sigma_k}\right)\frac{\partial k}{\partial r}\right)+G_k+\beta g\frac{\mu_t}{\sigma_t}\frac{\partial T}{\partial x}-\rho\varepsilon \tag{5}$$

Dissipation of kinetic energy equation

$$\frac{\partial(\rho\varepsilon u)}{\partial x}+\frac{1}{r}\frac{\partial(r\rho\varepsilon v)}{\partial r}=\frac{\partial}{\partial x}\left(\left(\mu+\frac{\mu_t}{\sigma_\varepsilon}\right)\frac{\partial\varepsilon}{\partial x}\right)+\frac{1}{r}\frac{\partial}{\partial r}\left(r\left(\mu+\frac{\mu_t}{\sigma_\varepsilon}\right)\frac{\partial\varepsilon}{\partial r}\right)+G_k C_{1\varepsilon}\left(\frac{\varepsilon}{k}\right)-C_{2\varepsilon}\rho\frac{\varepsilon^2}{k} \tag{6}$$

Where: $\beta g\frac{\mu_t}{\sigma_t}\frac{\partial T}{\partial x}$ represents the effect of buoyancy;

μ_t is the eddy viscosity, expressed by: $\mu_t=\frac{\rho C_\mu k^2}{\varepsilon}$

G_k is the turbulence kinetic energy generation.

ρ_0 is the density of ambient air (kg/m^3).

C. Boundary conditions

- The boundary conditions for the computational domain are summarized in Table 2

TABLE II BOUNDARY CONDITIONS

Place	Type	Description
Centreline	Axis	Symmetry
Ground	wall	250 W/m^2 ≤ Q ≤ 1000 W/m^2
Collector	wall	T= 300 K
Tower	wall	Q = 0 W/m^2
Collector inlet	Pressure inlet	Gauge total pressure=0 Pa Turbulent intensity= 5% T = T$_0$=300K
Chimney Outlet	Pressure outlet	Gauge pressure=0 Pa Turbulent intensity= 5% Backflow turbulent viscosity ratio=4 Backflow temperature T=T$_0$=300K

III. NUMERICAL COMPUTATION

III.1 Numerical procedure

The finite volume method and the SIMPLE algorithm have been used to solve the flow governing equations (1)-(6). The second order upwind scheme is used to discretize the convective terms. The iterative solution is converged when the residuals across all nodes are less than 10^{-6}.

III.2 Mesh generation

A structured non-uniform grid with a more significant concentration on the inlet-outlet and junction regions was used. We adopt a (48X400) cells throughout the calculation domain since it has shown a negligible variation with a more refined grid (see figure 2).

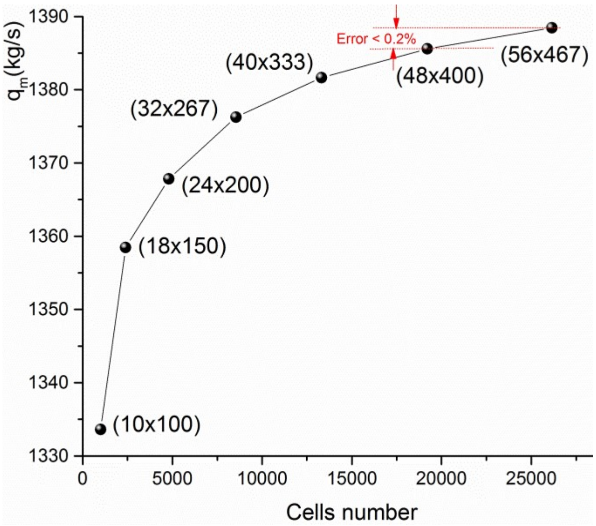

Fig.2 Mesh independence study

III.3 Validation

In order to validate the numerical code, we consider the Spanish SCPP of Manzanares as a model and we adopt the same working conditions of Pastohr et al. [5]. Figure 3 shows a comparison between our results and those of Pastohr et al. for velocity and temperature profiles, respectively, along the collector for x = 0.85 m. The obtained results indicate a good agreement between our results and those of Pastohr et al. [5].

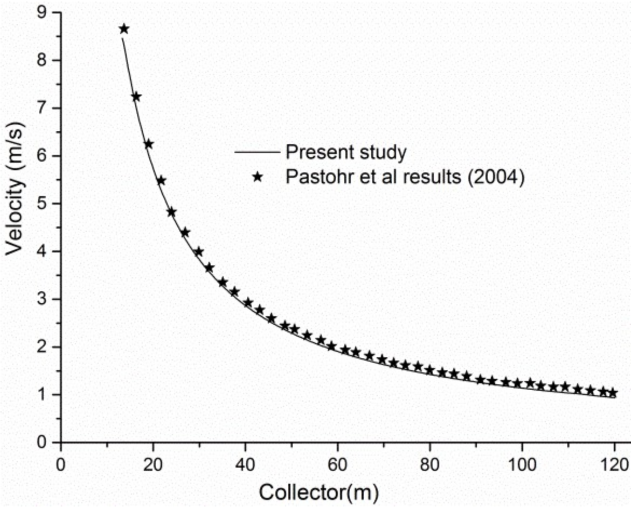

Fig. 3 Evolution of velocity profile along the collector at x = 0.85m

IV. RESULTS AND DISCUSSION

IV.1 Effect of geometrical parameters on the velocity contours for Ht= 1*

Figure 4 (a, b) illustrates the velocity contours for various values of Rt* et Q. It appears clearly that velocity increases versus the radius ratio Rt* and solar radiation. At the tower chimney entrance velocity reaches the value of 20.67 m/s for Rt* =1.5 and Q = 1000 W/m².

ISSN: 2961-6611

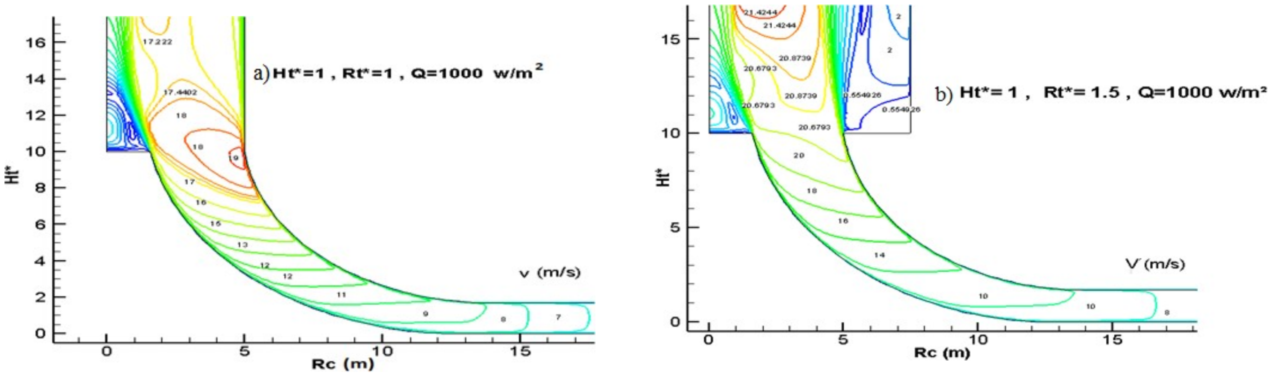

Fig. 4 Development of velocity contours for various Rt* for Ht* = 1

IV.2 Effect of geometrical parameters on the velocity contours for Ht= 0.5*

The analysis of the obtained results shown on figure 5 (a, b) indicate that velocity increases versus the radius ratio Rt* and solar radiation Q. A maximum velocity is recorded at the entrance of the tower chimney. Indeed, velocity increases from 12.39 m/s for Rt* = 1 and Q = 500 W/m² to 23.28 m/s for Rt* = 0.5 and Q = 1000 W/m².

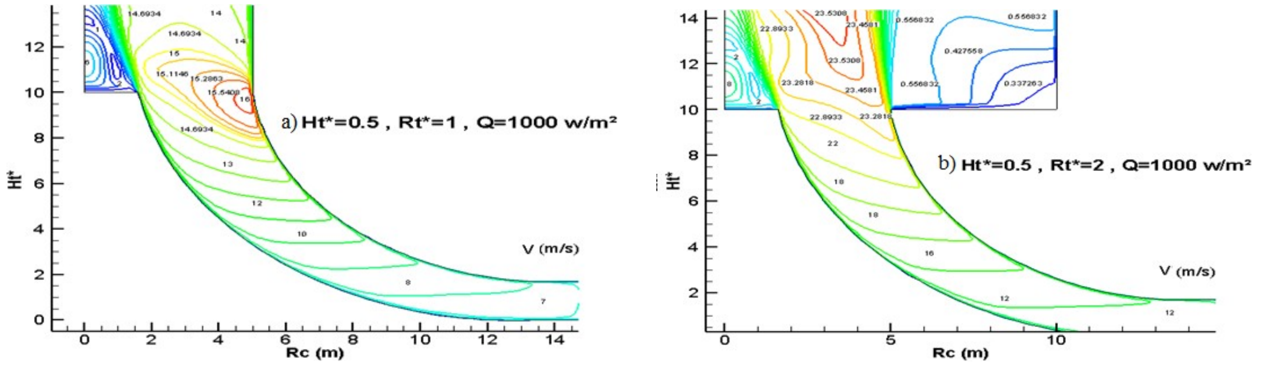

Fig. 5 Development of velocity contours for various Rt* for Ht* = 0.5

IV.3 Effect of geometrical parameters on the mass flow rate

Figure 6 shows the variation of mass flow rate versus radius ratio Rt* for various solar radiation and various Ht*.

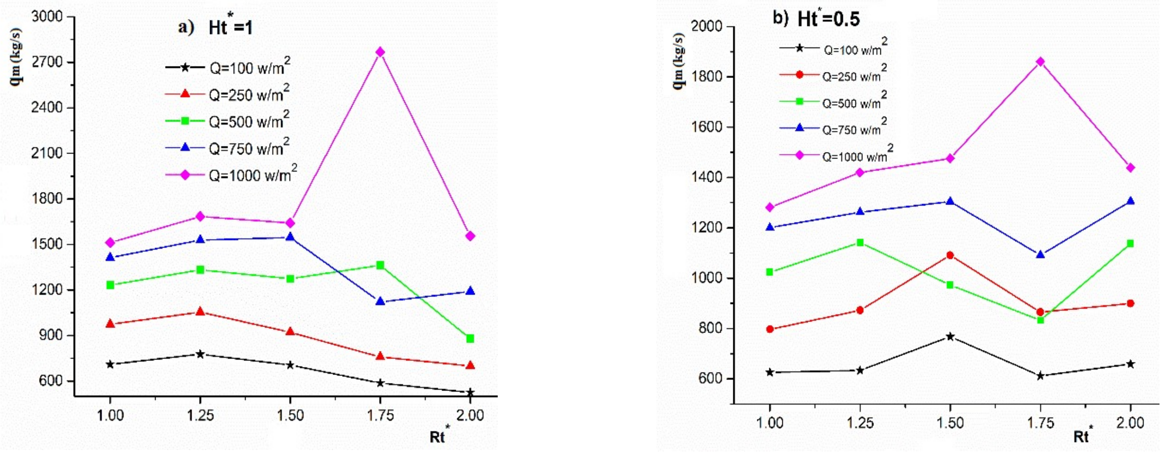

Fig. 6 Variation of mass flow rate versus Rt* for various Q and Ht*

From the results shown on figure 5, we note that mass flow rate is influenced by the radius ratio Rt*, height ratio Ht* and solar radiation Q. Il appears clearly that mass flow rate increases versus solar radiation Q and decreases versus height ratio Ht*. The height value of mass flow rate is reached for Rt* =1.5 and Ht* =1 which is 2767,889 kg/s. Indeed, the mass flow rate is improved by about 83.06%.

V. CONCLUSIONS

In this study, we investigate numerically the effect of geometrical parameters on the flow behavior inside the solar chimney power plant of Manzanares. The obtained results indicate that geometrical parameters influence significantly the flow behavior in the SCPP. We obtain that maximal velocity is reached at the entrance of the tower-chimney. Also, the flow rate is improved by the radius ratio Rt* and Ht* variation.

REFERENCES

[1] J. Lorenzo, “Las Chimneas solares: De una propuesta espanola en 1903 a de Mansanares. De Los Archivos Históricos De La Energia Solar,” http://www.fotovoltaica.com/chimenea.pdf.

[2] H. Günther, In hundred years-future energy supply of the world.: Kosmos, Franckh’sche Verlagshandlung : Stuttgart, 1931.

[3] W. Haaf, K. Friedrich, G. Mayer, J. Schlaich, “Solar chimneys, Part I : Principle and Construction of the Pilot Plant in Manzanares,” Int J Solar Energy, vol. 2, pp. 3-20, 1983.

[4] W. Haaf, K. Friedrich, G. Mayer, J. Schlaich, “Solar chimneys,” Int J Solar Energy, vol. 2, pp. 141–161,1984.

[5] Pastohr H., Kornadt O., Gürlebeck K., Numerical and analytical calculations of the temperature and flow field in the upwind power plant. Int. J. Energy Research 28, 495-510, 2004.

[6] Von Backström, T. W., Gannon, A. J. “Solar chimney turbine characteristics”, Solar Energy, 76 (1-3):235-41, 2004.

[7] Kebabsa, H., Lounici, M. S., Lebbi, M., Daimallah, A. “Thermo-hydrodynamic behaviour of an innovative solar chimney”, Renewable Energy 145 2074-2090, 2020

[8] https://doi.org/10.1016/j.renene.2019.07.121.

[9] A. Daimallah, M. Lebbi, M.S. Lounici, L. Boutina, “Effect of Thermal Collector Height and Radius on Hydrodynamic Flow Control in Small Solar Chimney”, Journal of Advanced Research in Fluid Mechanics and Thermal Sciences 71, Issue 2, 10-25, 2020.

[10] H. Kebabsa, M.S. Lounici, A. Daimallah, “Numerical investigation of a novel tower solar chimney concept”, Energy 214, 119048, 2021.

[11] I. Khaoula, U. İbrahim, L. Salah, O. Samir “Performance estimation of a solar chimney power plant (SCPP) in several regions of Turkey”, J Ther Eng; 8(2):202-220, 2022.

[12] A. Daimallah, M. Lebbi, M.S. Lounici, “Mass flow rate enhancement inside a solar chimney power plant”, Fourteen International Conference on Thermal Engineering: Theory and Applications, Yalova , Turkiye May 25-27, 2023.

[13] A. Daimallah, M. Lebbi, M.S. Lounici, “Effect of the tower-chimney form on the flow behavior inside a solar chimney power plant”, Topical Problems of Fluid Mechanics, Prague, République Tchèque February 16-18, 2022.

A 3D numerical modelling of heat and mass transfer in micropolar hybrid nanofluid

Awatef Abidi [a,b,c], , Nessrin Manaa[b], Mohammed Naceur Borjini [b]

[a] *Physics Department, College of Sciences Abha , King Khalid University, Saudi Arabia.*
[b] *Research Laboratory of Metrology and Energy Systems, National Engineering School, Energy Engineering Department, Monastir University , Monastir City, Tunisia.*
[d]*Higher school of Scienecs and Technology of Hammam Sousse, Sousse University, Tunisia.*
[d]*Univ Rennes, LGCGM, F-35000, Rennes, France.*
Email1 : abidiawatef@yahoo.fr
Email 2 : manaa_nessrin@outlook.com
Email 3 : borjinimn@yahoo.com

Abstract :

This paper presents numerical simulations of double diffusive natural convective heat and mass transport in a cubic cavity filled with micropolar nanofluid and micropolar hybrid nanofluid. The governing equations are stated in vorticity stream function formulations and numerically solved using the control volume approach. The effect of hybrid nanofluids and the significance of micropolar theory are investigated. Furthermore, the influence of nanoparticle volume fraction, Rayleigh number, Nusselt number, Sherwood number, buoyancy ratio, and micropolar vortex parameter on the flow field and the rate of heat and mass transfer is studied. The micropolar hypothesis played a role in lowering the Nusselt and Sherwood values. The rise in micropolar viscosity parameter affects the rates of heat and mass transfer, as well as the three-dimensional structure of the flow, which is more visible in regions dominated by thermal buoyancy. Heat and mass transfer rates rose when hybrid nanofluids were used instead of single nanofluids, but stayed constant when the Rayleigh number grew in regions dominated by thermal buoyancy. The kind of hybrid nanofluid has a considerable influence on heat and mass transfer rates, as well as the 3D aspect of the flow.

I. INTRODUCTION

Many fluids like water, ethylene glycol, kerosene, engine oil and acetone used in the industrial applications have low thermal conductivity. Due to this, the capital and operation costs of thermal systems become uneconomical. Hence highly thermal conductive nanoparticles are added to the afore-mentioned fluids to boost their thermal conductivities. Choi and Eastman [1] were the first who introduced this idea and used the term nanofluids to denote the fluids with suspended nanoparticles. Thereafter, a significant amount of research has been carried out on the nanofluids because of their important practical applications in microelectronics, solid-state lighting, detergency, and manufacturing. Heat transfer characteristics of the nanofluids are significantly improved because of an increase in surface area and heat capacity of the fluid, increase in thermal conductivity, interaction, and collision among nanoparticles, intensification in fluid turbulence, and flattening of the transverse temperature gradient across the fluid. Few investigators analyzed the convective heat transfer characteristics of nanofluids confined in enclosures with different models and those prominent researchers are When and Ding [2], Abouali and Falahatpishe [3], Jou and Tzeng [4], Abu Nada et al. [5], Kolsi et al. [6], Bouhalleb and Abbassi[7].Hybrid nanofluid is a new type of advanced working fluids, engineered with enhanced thermophysical properties. The hybrid nanofluids profit from the thermo-physical properties of more than one type of nanoparticles.

In the last few decades, many studies were being conducted to explore the preparation procedure, enhancement in properties, and challenges encountered in various stages of hybrid nanofluids preparation. Momin [8] experimentally investigated the mixed convection through Al_2O_3 water nanofluid inside an inclined copper tube surface by analysing the effects of nanoparticle concentration and power supply on the development of the thermal field under laminar flow condition. He also presented a fully developed laminar convective heat transfer through a uniformly heated circular tube using Al_2O_3–Cu/water hybrid nanofluid.

Afrand et al. [9] carried out an experimental investigation on the rheological behavior of Fe_3O_4–Ag/EG hybrid nanofluid with the influence of temperature and nanoparticles' concentration. Their results reveal that the dynamic viscosity of the hybrid nanofluid increases with the increase in nanoparticles' volume fraction and the same decreases

ISSN: 2961-6611

with the increase in temperature. Dalkılıç et al. [10] synthesized the hybrid nanofluids by dispersing silicon dioxide and graphite nanoparticles in distilled water and analyzed its viscosity variation with respect to nanoparticles' volume fraction ratio and temperature. It is found that the highest percentage increase in viscosity is 36.12% with nanoparticles' volume fraction ratio of 2 at 15 °C. Takabi and Salehi [11] numerically analyzed the laminar natural convection in a sinusoidal corrugated enclosure with a discrete heat source on the bottom wall, filled by pure water, Al_2O_3/water nanofluid, and Al_2O_3-Cu/water hybrid nanofluid. Their results indicate that hybrid nanofluid shows better heat transfer characteristics when compared to simple nanofluid.

The rotating micro-constituents' effects in nanofluids should be carefully analyzed to understand the nature of fluid flow effectively and the same was originally proposed by Eringen [12] to elucidate fluid particle's micro-motions which cannot be explained by the classical models. The model of micropolar fluid represents fluids consisting of rigid, randomly oriented (or spherical) particles suspended in a viscous medium where the deformation of the particles is ignored. Micropolar fluids have been well adhered to precisely simulate the flow characteristics of polymeric additives, geomorphological sediments, colloidal suspensions, haematological suspensions, liquid crystals, lubricants, etc. The main advantage of using a micropolar fluid model compared to other non-Newtonian fluids' models is that the former takes into account the rotation of fluid particles employing an independent kinematic vector called the microrotation vector. The above-mentioned applications demand critical research efforts on flow behavior and heat and mass transfer characteristics of micropolar fluids. Further, the findings of Eringen [12] were critically reviewed by Ariman et al. [13] and found it accurate. Lukaszewics [14] presented a detailed comprehensive analysis of micropolar fluids and their applications. It is vivid that the micropolar fluids have many engineering applications, such as liquid crystal solidification, colloidal and suspension solutions, exotic lubricants, animal blood, and polymer fluids extrusion.

Abidi and Borjini [15] analyzed the influence of micro-constituents in micropolar fluid on the three-dimensional double-diffusive natural convection. They established that the deterioration in three-dimensional features of the flow with a significant decrease in heat and mass transfer rates with an increase in the vortex viscosity parameter. The extensive use of colloidal suspensions in modern engineering industries along with the limitations of its modelling due to its non-Newtonian nature demands a more sophisticated micropolar nanofluid model.

Bourantas and Loukopoulos [16] proposed a theoretical micropolar model to investigate natural convection in nanofluidic suspensions based on a micropolar theory with its genuine validation. The presence of nanoparticles' microrotation well explains the controversial theoretical numerical results and experimental data on the natural convection of nanofluids (Putra et al. [17]). The results show that nanoparticles' microrotation decreases overall heat transfer rate with an increase in average Nusselt number. It was also observed that the variation of Rayleigh number and Nusselt number were in similar agreement for a constant microrotation number. Hussanan et al. [18] used five types of oxide nanoparticles on a vertical plate to explore the transient natural convection in a micropolar nanofluid. They concluded that the temperature of nano-fluid is much higher with graphene oxide.It is worth mentioning that the current literature does not give a substantial contribution to the analysis of flow and heat transfer in the micropolar hybrid nanofluid model. Mollamahdi et al. [19] studied the forced convection in Al_2O_3-Cu/water micropolar nanofluid in a porous channel under the effect of a magnetic field. The authors analyzed the consequences of utilizing hybrid nanofluid with the application of micropolar theory on flow field and heat transfer rate.

The focus of the present study is on the analyses of the influences of relevant parameters such as Rayleigh number, buoyancy ratio, nanoparticles' volume fraction, and vortex viscosity parameter on flow behavior and heat and mass transfer rates. The effects of type of hybrid nanoparticles on the rate of heat and mass transfer and flow structure are also analyzed.

II. MATHEMATICAL MODELING

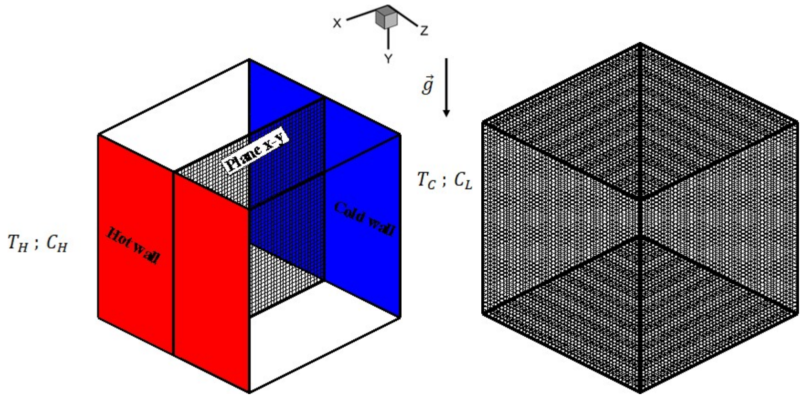

(a) **(b)**

Fig.1 (a) Schematic of the considered problem, **(b)** Mesh surfaces

ISSN: 2961-6611

A simple schematic view of the thermo-solutal natural convection problem under study is described in Fig. 1. The cube is filled with multi-walled CNT water-based micropolar nanofluid stabilized with two types of surfactants lignin and sodium polycarboxylate respectively. The two vertical walls parallel to the plane (y-z) are subject to constant temperatures ($T_H > T_C$) and constant concentrations ($C_H > C_L$). The other walls are supposed to be impermeable and adiabatic. The dynamic and thermal slips between nanoparticles and the base fluid are negligible. During the process of the natural convection, all the properties of the base fluid and nanoparticles are unchangeable except the density in the buoyancy term in momentum equation, its variations being modeled using Boussinesq approximation. The effects of Soret and Dufour are assumed to be negligible.

The vorticity–vector potential formulation is used in the present study to eliminate the pressure term and makes easier the numerical treatment. The vorticity and vector potential are respectively defined by the following two relations: $\vec{V} = \nabla \times \vec{\psi}$ and $\vec{\omega} = \nabla \times \vec{V}$.

The system of governing equations of the phenomenon is:

$$\nabla^2 \vec{\psi} = -\vec{\omega} \tag{7}$$

$$\begin{gathered}\frac{\partial \vec{\omega}}{\partial t} + (\vec{V}.\nabla)\vec{\omega} - (\vec{\omega}.\nabla)\vec{V} = Pr\left(\frac{\mu_{nf}}{\mu_f} + K\right)\left(\frac{\rho_f}{\rho_{nf}}\right)\nabla^2\vec{\omega} - PrK\left(\frac{\rho_f}{\rho_{nf}}\right)\nabla \times \vec{H} \\ + RaPr\left(\frac{(\rho\beta_T)_{nf}}{(\rho\beta_T)_f}\right)\left(\frac{\rho_f}{\rho_{nf}}\right)\left(\left[\frac{\partial T}{\partial z}, 0, -\frac{\partial T}{\partial x}\right] - N\left[\frac{\partial C}{\partial z}, 0, -\frac{\partial C}{\partial x}\right]\right)\end{gathered} \tag{8}$$

$$\left(\frac{\partial \vec{H}}{\partial t} + (\vec{V}.\nabla)\vec{H}\right) = Pr\left(\frac{\mu_{nf}}{\mu_f} + \frac{K}{2}\right)\left(\frac{\rho_f}{\rho_{nf}}\right)\nabla^2\vec{H} + PrK\left(\frac{\rho_f}{\rho_{nf}}\right)(\vec{\omega} - 2\vec{H}) \tag{9}$$

$$\frac{\partial T}{\partial t} + (\vec{V}.\nabla)T = \left(\frac{(\rho C_P)_f}{(\rho C_P)_{nf}}\right)\left(\frac{k_{nf}}{k_f}\right)\nabla^2 T \tag{10}$$

$$\frac{\partial C}{\partial t} + (\vec{V}.\nabla)C = \frac{1}{Le}\left(\frac{(\rho C_P)_{nf}}{(\rho C_P)_f}\right)\left(\frac{k_f}{k_{nf}}\right)\nabla^2 C \tag{11}$$

The local Nusselt and Sherwood numbers on the isothermal walls are defined by:

$$Nu = \left.\frac{k_{nf}\dfrac{\partial T'}{\partial x'}}{k_f\dfrac{T'_H - T'_C}{L}}\right)_{x'=0,1} = -\left.\frac{k_{nf}}{k_f}\frac{\partial T}{\partial x}\right)_{x=0,1} \tag{12}$$

$$Sh = \left.\frac{D\dfrac{\partial C'}{\partial x'}}{D\dfrac{C'_H - C'_L}{L}}\right)_{x'=0,1} = \left.\frac{\partial C}{\partial x}\right)_{x=0,1} \tag{13}$$

The average Nusselt and Sherwoood numbers, on the isothermal walls of the enclosure are defined as follows:

$$\overline{Nu} = \int_0^1\int_0^1 Nu\,\partial y\,\partial z \tag{14}$$

$$\overline{Sh} = \int_0^1\int_0^1 Sh\,\partial y\,\partial z \tag{15}$$

For each time step, the following convergence criterion is satisfied:

$$\sum_{1,2,3} \frac{\max|\psi^n - \psi^{n+1}|}{\max|\psi^n|} + \max|T^n - T^{n+1}| + \max|C^n - C^{n+1}| \leq 10^{-5} \qquad (16)$$

III. RESULTS AND DISCUSSION:

To highlight the influence of using Cu-Al$_2$O$_3$/water MHNF on HMT characteristics, the variations of $\overline{Nu}$ and $\overline{Sh}$ for different values of N for both Cu/water MNF and Cu-Al$_2$O$_3$/water MHNF are presented in Fig 6. It is increasingly obvious that both the cases have a quasi-similar pattern for different values of $\overline{Nu}$ and $\overline{Sh}$.

It is also seen that for both the cases, $\overline{Nu}$ and $\overline{Sh}$ decreases, as N value increases in the negative sense. And for N value above -1, $\overline{Nu}$ and $\overline{Sh}$ rises. However, when contrasted to Cu/water MNF in the thermally dominated zone, the values of $\overline{Nu}$ and $\overline{Sh}$ for Cu-Al$_2$O$_3$/water MHNF are larger. The values of $\overline{Nu}$ and $\overline{Sh}$ are lower for HN when compared with Cu/water MNF, conflicting to the thermally dominated region.

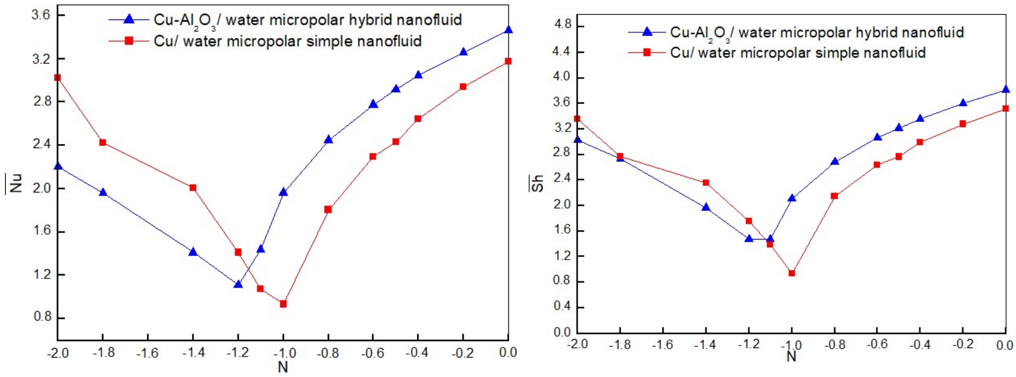

Figure 1 : $\overline{Nu}$ and $\overline{Sh}$ for different N using Cu-Al$_2$O$_3$/water MHNF and Cu/water MNF at$Ra=10^5$, $Le = 1$, $Pr = 6.2$, $\varphi = 0.01$, and $K = 1$.

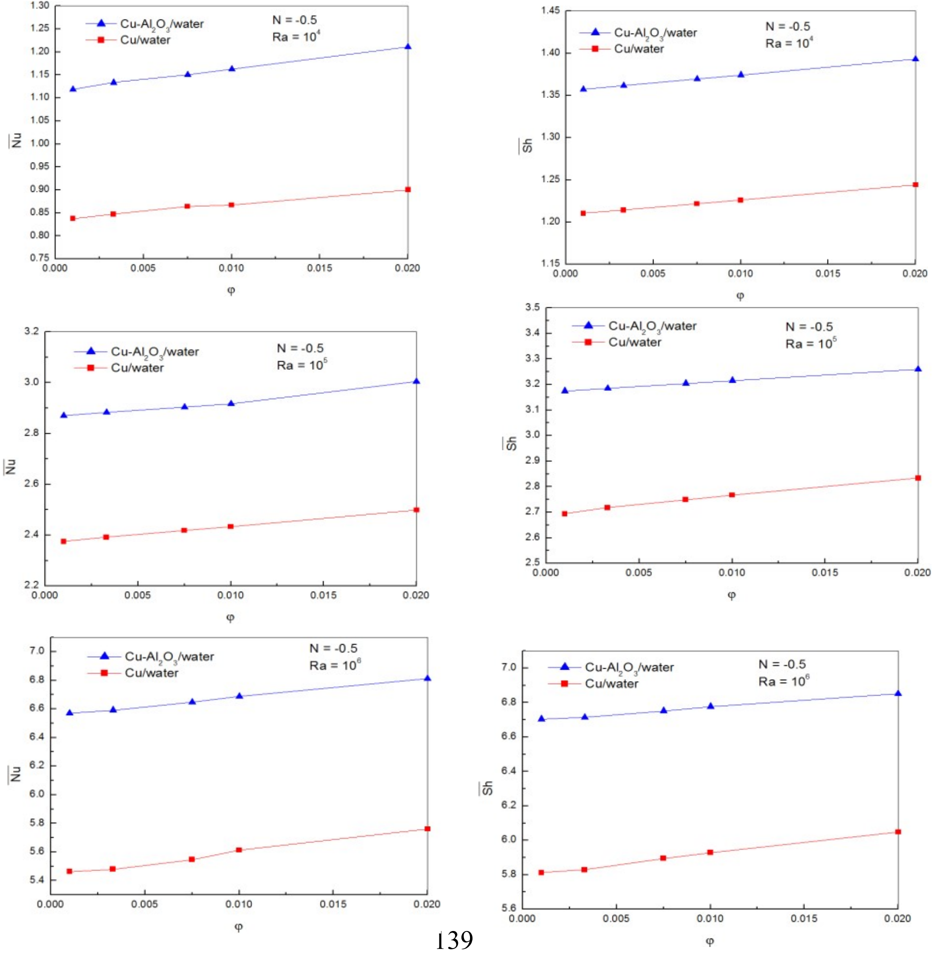

Figure 2: $\overline{Nu}$ and $\overline{Sh}$ variations versus volume fraction of nanoparticles (φ) for Cu-Al_2O_3/water MHNF and Cu/water MNF at N = - 0.5 at Le = 1, Pr = 6.2, φ = 0.01, and K = 1.

It can also be noticed that a lowest value for $\overline{Nu}$ and $\overline{Sh}$ exists for Cu/water MNF at N ≈ −1. By using Cu-Al_2O_3/water MHNF, this minimum value moves towards the left side of the y axis (N ≈ 0) and is equal to -1.2. As an interesting result in Figure 6, when using Cu-Al_2O_3/water MHNF, the heat and mass transfer in the thermally dominated region of the cavity is highest. Therefore, it can be inferred that both N and the hybridity may be important in the performance of heat and mass transfer within the cavity.

The variations of $\overline{Nu}$ and $\overline{Sh}$ versus volume fraction of nanoparticles for both classical nanofluid (Cu/water) and hybrid nanofluid (Cu-Al_2O_3/water) models are shown in Figure 2. For all cases, the increase of nanoparticles volume fraction increases $\overline{Nu}$ and $\overline{Sh}$ numbers for both working fluids. Besides, the hybrid nanofluid possesses better heat transfer characteristics for a given *Ra*. As expected, the influence of hybrid nanoparticles is more pronounced at high volume fractions due to high thermal conductivity. Therefore, the enhancement of heat and mass transfer characteristics using hybrid nanofluid becomes more prominent at high *Ra* cases.

IV. CONCLUSION:

Numerical investigation of heat and mass transfer in double-diffusive natural convection is performed in three-dimension. Single nanofluid (Cu /water) and hybrid micropolar nanofluid (Cu-Al_2O_3/water) filled in a cubic cavity is considered for the analysis. Following are the important conclusions arrived in this work:

1. The rates of heat and mass transfer considering the model of micropolar nanofluid is lower compared to the model of pure nanofluid.
2. The rates of heat and mass transfer are enhanced by using hybrid Cu-Al2O3/water compared to Cu /water nanofluid. These rates were true for any values of volume fractions of nanoparticles. However, these rates remained same at all Rayleigh numbers considered.

REFERENCES :

[1] D. Wen, Y. Ding, Formulation of nanofluids for natural convective heat transfer applications, Int. J. Heat and Fluid Flow 26 (6) (2005) 855–864.

[2] O. Abouali, A. Falahatpisheh, Numerical investigation of natural convection of Al2O3 nanofluid in vertical annuli, Int. J. Heat Mass Transf. 46 (1) (2009) 15–23.

R.Y. Jou, S.-C. Tzeng, Numerical research of nature convective heat transfer enhancement filled with nanofluids in rectangular enclosures, Int. Commun. Heat Mass Transf. 33 (6) (2006) 727–736.

[3] E. Abu-Nada, Z. Masoud, H.F. Oztop, A. Campo, Effect of nanofluid variable properties on natural convection in enclosures, Int. J. Therm. Sci. 49 (3) (2010) 479–491.

[4] L. Kolsi, A.A.A.A. Alrashed, K. Al-Salem, H.F. Oztop, M.N. Borjini, Control of natural convection via inclined plate of CNT-water nanofluid in an open sided cubical enclosure under magnetic field, Int. J. Heat Mass Transf. 111 (2017) 1007–1018.

[5] M. Bouhalleb, H. Abbassi, Numerical Investigation of Heat Transfer by CuO–Water Nanofluid in Rectangular Enclosures, Heat Transf. Eng. 37 (1) (2015) 13–23.

[6] G.G. Momin, Experimental investigation of mixed convection with water–Al2O3& hybrid nanofluid in inclined tube for laminar flow, Int. J. Scientific Technol. Res. 2 (2013), 195–202.

[7] M. Afrand, D. Toghraie, B. Ruhani, Effects of temperature and nanoparticles concentration on rheological behavior of Fe3O4 –Ag/EG hybrid nanofluid: An experimental study, Exp. Therm. Fluid Sci. 77 (2016) 38–44.

[8] A.S. Dalkılıç, Ö. Açıkgöz, B.O. Küçükyıldırım, A.A. Eker, B. Lüleci, C. Jumpholkul, S. Wongwises, Experimental investigation on the viscosity characteristics of water based SiO2-graphite hybrid nanofluids, Int. Commun. Heat Mass Transf. 97 (2018) 30–38.

[9] B. Takabi S. Salehi, Augmentation of the Heat Transfer Performance of a Sinusoidal Corrugated Enclosure by Employing Hybrid Nanofluid, Adv. Mechanical Eng. 6 (2014) 147059.

[10] A. Eringen, Theory of Micropolar Fluids, Indiana University Mathematics Journal, 16 (1) (1966) 1–18.

[11] T. Ariman, M.A. Turk, N.D. Sylvester, Applications of microcontinuum fluid mechanics, Int. J. Eng. Sci. 12 (4) (1974) 273–293.

[12] G. Lukaszewicz Birkhauser,Micropolar Fluids: Theory and Applications. 1999. 252 pp. ISBN 3 7643 4008 8. DM 14, J. Fluid Mechanics 401 (1999) 378–381.

[13] A. Abidi, M.N. Borjini, Effects of Microstructure on Three-Dimensional Double-Diffusive Natural Convection Flow of Micropolar Fluid, Heat Transf. Eng. (2018) 1–48.

[14] G.C. Bourantas V.C. Loukopoulos, Modeling the natural convective flow of micropolar nanofluids, Int .J. Heat Mass Transf. 68 (2014) 35–41.

[15] N. Putra, W. Roetzel, S.K. Das, Natural convection of nano-fluids, Heat Mass Transf. 39 (8–9) (2002) 775–784.

[16] A. Hussanan, M.Z. Salleh, I. Khan, and S. Shafie, Convection heat transfer in micropolar nanofluids with oxide nanoparticles in water, kerosene and engine oil, J. Mol. Liq. 229 (2017) 482–488.

[17] M. Mollamahdi, M. Abbaszadeh, G.A. Sheikhzadeh, Flow Field and Heat Transfer in a Channel with a Permeable Wall Filled with Al2O3-Cu/Water Micropolar Hybrid Nanofluid, Effects of Chemical Reaction and Magnetic Field, J. Heat Mass Transf. Res. 3 (2016) 101-114.

Some applications of Bratu integral equations in science and their numerical solutions

Somia GUECHI[#1]

[#] *Department of Mathematics, University of M'sila, 28000, Algeria.*
[1] somia.guechi @univ-msila.dz

Abstract— **Bratu's problem governs several important real life and various fields of science and engineering. A brief survey of the properties and different treatments of the one-dimensional Bratu's problems is presented, and a numerical method is stated for solving this problem via many numerical methods. In this paper, the problem is considered as a nonlinear integral equation and solutions are obtained using Nyström methods. Once more, the differential equation has been transformed into a numerically-solvable Hammerstein integral equation. The Nyström numerical method simplifies the integral problem to a system of algebraic equations.**

Keywords— **Bratu's problem, Integral equation, Numerical methods.**

I. INTRODUCTION

A mathematical model of the Bratu-type problem appears in a large variety of application regions, for example, fuel ignition model of thermal combustion, thermal reaction, chemical reactor theory and nanotechnology, radiative heat transfer, the Chandrasekhar model of the expansion of the universe [1–3]. It is possible to reduce this mathematical model to the nonlinear ordinary differential equation with a parameter in the boundary conditions

$$\begin{cases} \nabla\varphi - \lambda F(\varphi) = 0 & in\ \Omega \\ \varphi = 0 & on\ \ \partial\Omega \end{cases} \Leftrightarrow \begin{cases} \varphi''(t) - \lambda F(\varphi) = 0 \\ \varphi(0) = 0,\ \varphi(1) = 0. \end{cases} \tag{1}$$

where is λ a positive physical parameter, $F(\varphi)$ is non-linear function and $\Omega = [a, b]$ is a bounded domain with boundary .

The problem (1) is characterized by a nonlinear Fredholm integral equation of the second kind

$$\varphi(t) = \lambda \int_a^b G(t,x) e^{\varphi(x)} dx,$$

where $0 \leq t, x \leq 1$ and

$$G(t,x) = \begin{cases} \dfrac{(b-t)(x-a)}{b-a}, & x \leq t \\ \dfrac{(b-x)(t-a)}{b-a}, & t \leq x \end{cases}$$

which we consider in the space $C[0,1]$ of continuous functions on the closed interval $[0,1]$ with the usual sup norm $\|\cdot\|_\infty$. Numerous authors have studied this subject (see, [1,3]).

Several numerical techniques, like the Adomain decomposition method (ADM) [4], the one-dimensional differential transform method [5], the finite difference method, finite element approximation, weighted residual method [6], the shooting method [7] have been implemented independently to handle the Bratu model numerically.
The quadrature method is a simple and powerful method for solving a wide class of nonlinear differential and integral problems. Consider the nonlinear Fredholm integral equation of the second kind

ISSN: 2961-6611

$$\varphi(t) = f(t) + \int_G k(t,x,\varphi(x))\,dx, \quad t,x \in G.$$

For Fredholm integral equations, we take $G = [a,b]$, let $t_1 = a < t_2 < \cdots < t_n < t_{n+1} = b$ be an equidistant subdivision of a step $h = \frac{b-a}{n+1} = t_{j+1} - t_j$, for $1 \le j \le n+1$. Our objective we approximate the integral on the right-hand side of the last equation with $j = 1,\cdots,n+1$

$$\varphi(t_j) = f(t_j) + \sum_{i=1}^{n} \int_{t_i}^{t_{i+1}} k(t_j,x,\varphi(x))\,dx.$$

By the numerical integration formulas of trapezoidal rule, so we get

$$\varphi(t_j) = f(t_j) + \frac{h}{2}\left(k(t_j,t_1,\varphi(t_1)) + 2\sum_{i=2}^{n} k(t_j,t_i,\varphi(t_i)) + k(t_j,t_{n+1},\varphi(t_{n+1})) \right),$$

We get a nonlinear system of algebraic equations of the form

$$\varphi = T\varphi, \quad j = 1,\ldots,n+1$$

where $\varphi = (\varphi_1,\ldots,\varphi_{n+1})$, then we can use the method of fixed point for the resolution the system of nonlinear equations, then we passe to the following diagram of recurrence

$$\varphi^{K+1} = T\varphi^{K} \Leftrightarrow \varphi_j^{K+1} = f_j + \frac{h}{2}\left(k_{j,1,\varphi_1^K} + 2\sum_{i=2}^{n} k_{j,i,\varphi_i^K} + k_{j,n+1,\varphi_{n+1}^K} \right).$$

If we apply the method of Simpson; we will obtain another discretization compared to the variable of integration t as follows

$$\varphi_j = f_j + \frac{h}{3}\left(k_{j,1,\varphi_1} + 2\sum_{i=1}^{\frac{n}{2}} \left(k_{j,2i-1,\varphi_{2i-1}} + k_{j,2i,\varphi_{2i}} \right) + k_{j,n+1,\varphi_{n+1}} \right),$$

thus, this formula is a nonlinear system of $n+1$ equations with $n+1$ unknowns $\varphi_1,\ldots,\varphi_{n+1}$ can also to write in the form

$$\varphi = T\varphi, \quad j = 1,\ldots,n+1$$

with $\varphi = (\varphi_1,\ldots,\varphi_{n+1})$, then we can use the method of fixed point for the resolution the system of nonlinear equations, then we passe to the following diagram of recurrence

$$\varphi^{K+1} = T\varphi^{K} \Leftrightarrow \varphi_j^{K+1} = f_j + \frac{h}{3}\left(k_{j,1,\varphi_1^K} + 2\sum_{i=1}^{n} \left(2k_{j,2i-1,\varphi_{2i-1}^K} + k_{j,2i,\varphi_{2i}^K} \right) + k_{j,n+1,\varphi_{n+1}^K} \right).$$

Where K is the number of iteration. By recurrence, we can to calculate the vector of solutions in all points t_j for $j = 1,2,\ldots,n+1$. (See, [10-11]).

In the next section, we will present existence theorems for the solutions of nonlinear Fredholm integral equations.

II. EXISTENCE AND UNIQUENESS THEOREMS

Theorem *[8]: Suppose that* $k(t,x,\varphi)$ *is defined and continuous on the set* $[a,b]\times[a,b]\times\mathbb{R}$ *and that it satisfies a Lipschitz condition of the form*

$$|k(t,x,\varphi_1)-k(t,x,\varphi_2)|\le C|\varphi_1-\varphi_2|,$$

suppose further that $f\in C[a,b]$ *. Then the nonlinear Urysohn integral equation*

$$\varphi(t)=\lambda\int_a^b k(t,x,\varphi(x))\,dx+f(t)$$

has a unique solution on the interval $[a,b]$ *whenever* $|\lambda|<1/(C(b-a))$.

Theorem *[9] Consider the nonlinear Urysohn integral equation*

$$\varphi(t)=\lambda\int_a^b k(t,x,\varphi(x))\,dx+f(t), \qquad (a\le t\le b)$$

where $f(.)\in C[a,b]$ *. Assume that the function* $g(t,s,x)$ *satisfies the following conditions:*

$$\sup\left(|g(t,s,x)|,\left|\frac{\partial g}{\partial t}(t,s,x)\right|\right)\le V_1(t)V_2(s)\phi(|x|),\quad \left|\frac{\partial g}{\partial s}(t,s,x)\right|\le V_1(t)V_2(s)\psi(|x|)$$

where $V_1(.)\in C[a,b]$, $V_2(.)\in L^1[a,b]$, $\phi(.)$ *is positive and bounded over* $[0,+\infty[$ *and* $\psi(.)$ *is positive and continuous over* $[0,+\infty[$ *. Under the above conditions, Urysohn integral equation has a solution in* $C[a,b]$.

III. NUMERICAL EXAMPLES

Example 01**:** Consider the following nonlinear Bratu BVP

$$\begin{cases}\varphi''(t)-\pi^2 e^{\varphi(t)}=0\\ \varphi(0)=0,\quad \varphi(1)=0\end{cases}\qquad(2)$$

The problem (2) is characterized by a nonlinear Fredholm integral equation of the second kind

$$\varphi(t)=\pi^2\int_0^1 G(t,x)e^{\varphi(x)}dx\qquad(3)$$

where $0\le t,x\le 1$ and

$$G(t,x)=\begin{cases}(1-t)x, & x\le t\\ (1-x)t, & t\le x\end{cases}$$

To validate the application of some numerical methods to the integral equation (3), we will show numerical resultants by these methods, and we take K=20 and N=10, 20, 40.

N=10	**ES**	**AS via Simp**	**Err via Simp**	**AS via Trap**	**Err via Trap**
0	0	0.0000e+00	1.1102e-16	0.0000e+00	1.1102e-16
0.1	-2.6928e-01	-2.7984e-01	1.0562e-02	-2.6792e-01	1.3610e-03
0.2	-4.6234e-01	-4.6020e-01	2.1362e-03	-4.6033e-01	2.0090e-03
0.3	-5.9278e-01	-5.9904e-01	6.2573e-03	-5.9046e-01	2.3213e-03
0.4	-6.6837e-01	-6.6559e-01	2.7831e-03	-6.6591e-01	2.4623e-03
0.5	-6.9315e-01	-6.9832e-01	5.1698e-03	-6.9064e-01	2.5026e-03
0.6	-6.6837e-01	-6.6559e-01	2.7831e-03	-6.6591e-01	2.4623e-03
0.7	-5.9278e-01	-5.9904e-01	6.2573e-03	-5.9046e-01	2.3213e-03
0.8	-4.6234e-01	-4.6020e-01	2.1362e-03	-4.6033e-01	2.0090e-03
0.9	-2.6928e-01	-2.7984e-01	1.0562e-02	-2.6792e-01	1.3610e-03
1	0	0.0000e+00	2.2204e-16	0.0000e+00	2.2204e-16

TABLE **I:**Exactes solution, Approximation solutions and Absolute errors to Bratu integral equation (3);
for **N=10** by using the Nyström numerical methods.

N=20	**ES**	**AS via Trap**	**Err via Trap**	**AS via Simp**	**Err via Simp**
0	0	0.0000e+00	1.1102e-16	0.0000e+00	1.1102e-16
0.1	-2.6928e-01	-2.6893e-01	3.4696e-04	-2.6895e-01	3.3024e-04
0.2	-4.6234e-01	-4.6183e-01	5.1079e-04	-4.6182e-01	5.1587e-04
0.3	-5.9278e-01	-5.9219e-01	5.8926e-04	-5.9216e-01	6.2173e-04
0.4	-6.6837e-01	-6.6775e-01	6.2448e-04	-6.6769e-01	6.7681e-04
0.5	-6.9315e-01	-6.9251e-01	6.3453e-04	-6.9245e-01	6.9395e-04
0.6	-6.6837e-01	-6.6775e-01	6.2448e-04	-6.6769e-01	6.7681e-04
0.7	-5.9278e-01	-5.9219e-01	5.8926e-04	-5.9216e-01	6.2173e-04
0.8	-4.6234e-01	-4.6183e-01	5.1079e-04	-4.6182e-01	5.1587e-04
0.9	-2.6928e-01	-2.6893e-01	3.4696e-04	-2.6895e-01	3.3024e-04
1	0	0.0000e+00	2.2204e-16	0.0000e+00	2.2204e-16

TABLE **III:**Exactes solution, Approximation solutions and Absolute errors to Bratu integral equation (3);
for **N=20** by using the Nyström numerical methods.

N=60	ES	AS via Trap	Err via Trap	AS via Simp	Err via Simp
0	0	0.0000e+00	1.1102e-16	0.0000e+00	1.1102e-16
0.1	-2.6928e-01	-2.6924e-01	3.8783e-05	-2.6924e-01	3.6045e-05
0.2	-4.6234e-01	-4.6228e-01	5.7049e-05	-4.6228e-01	5.6496e-05
0.3	-5.9278e-01	-5.9272e-01	6.5780e-05	-5.9272e-01	6.8230e-05
0.4	-6.6837e-01	-6.6830e-01	6.9693e-05	-6.6830e-01	7.4359e-05
0.5	-6.9315e-01	-6.9308e-01	7.0808e-05	-6.9307e-01	7.6268e-05
0.6	-6.6837e-01	-6.6830e-01	6.9693e-05	-6.6830e-01	7.4359e-05
0.7	-5.9278e-01	-5.9272e-01	6.5780e-05	-5.9272e-01	6.8230e-05
0.8	-4.6234e-01	-4.6228e-01	5.7049e-05	-4.6228e-01	5.6496e-05
0.9	-2.6928e-01	-2.6924e-01	3.8783e-05	-2.6924e-01	3.6045e-05
1	0	0.0000e+00	2.2204e-16	0.0000e+00	2.2204e-16

TABLE IIII:Exactes solution, Approximation solutions and Absolute errors to Bratu integral equation (3); for **N=60** by using the Nyström numerical methods.

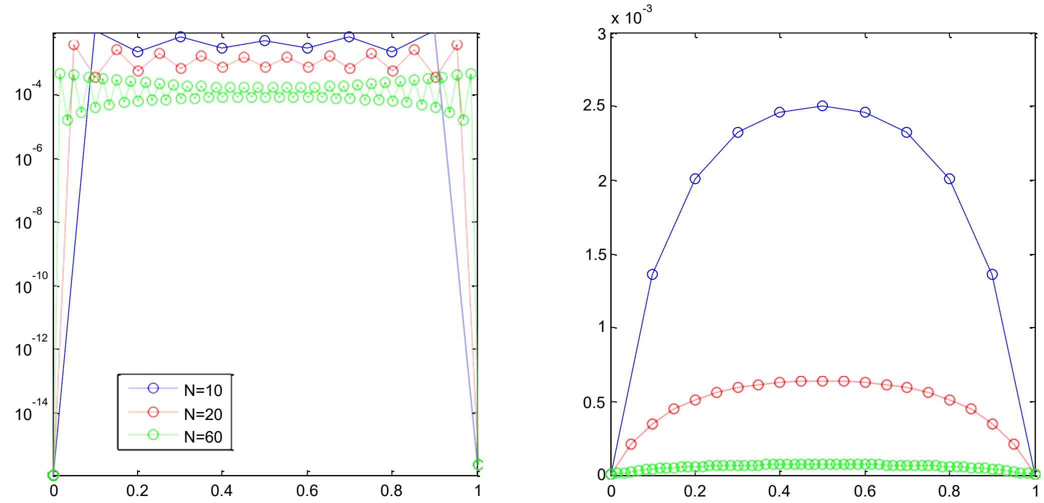

Fig. 1 Absolute errors to Bratu integral equation (3); for **N=10,20,60** by using the trapezoidal and Simpson numerical methods.

We tested the quadrature methods for solving Bratu integral problm by using some an example. It is observed that the errors in the solutions are tabulated in tables (1), (2) and (3) which show that numerical results were acceptable and the two methods converge and the absolute error has approached zero which was shown that numerical results were acceptable. Then, the most accurate scheme is Simpson method.

IV. CONCLUSIONS

In this paper, we gave approximating solution of Bratu problem (nonlinear Volterra integral equations). The Nyström method has been applied to the nonlinear Bratu integral equation. The approximate solution to this equation has been successfully arrived at, by comparing the exact solution and the numerical solution; we can see that the results are closed and accurate by choosing different values for **N**. The recommendation in this study is we can to use trapezoidal method, Simpson method or any other simple type of perturbation method.

REFERENCES

[1] Gelfand, I.M., Some problems in the theory of quasilinear equations, Amer. Math. Soc.Transl., 29(1963), 295-381 (Usp. Mat. Nauk, 14(1959), no. 2, 87-158).
[2] Frank-Kamenetskii, D.A., Di_usion and Heat Exchange in Chemical Kinetics, Princeton Univ. Press, 1955.
[3] Wazwaz, A.M. Adomian decomposition method for a reliable treatment of the Bratu-type equations, Applied Mathematics and Computation 166, 652–663, 2005.
[4] Chang, S.H. and Chang, I. L. A new algorithm for calculating one-dimensional differential transform of nonlinear functions, Appl. Math. Comput. 2007,doi:10.1016/j.amc.2007.05.026.
[5] Aregbesola, Y. Numerical solution of Bratu problem using the method of weighted residual, Electronic Journal of Southern African Mathematical Sciences Association 3 (01), 1–7, 2003.
[6] Ascher, U.M., Matheij, R. and Russell, R.D. Numerical solution of boundary value problems for ordinary differential equations (SIAM, Philadelphia, PA, 1995).
[7] Zemyan, S.M. The Classical theory of integral equations. A concise treatment. SpringerScience+Business Media, LLC, 2012.
[8] Karoui, A. On the existence of continuous solutions of nonlinear integral equations. Applied Mathematics Letters, 18 (2005) 299.305.
[9] Guechi S., Guechi, M. (2023). Effective technique for converting ill-posed volterra equation to integro-differential equation and solving it. Mathematical Modelling of Engineering Problems, 10(2), 458-462.
[10] Guechi, S. (2024). Numerical solution of Volterra-Hammerstein integral equation of the first kind by finite difference method decomposition with Nyström method. Mathematical Modelling of Engineering Problems, Vol. 11, No. 4, pp. 1029-1036.